

MICROTECHNOLOGY AND MEMS

H. Ukita

Micromechanical Photonics

 Springer

MICROTECHNOLOGY AND MEMS

MICROTECHNOLOGY AND MEMS

Series Editor: H. Fujita D. Liepmann

The series Microtechnology and MEMS comprises text books, monographs, and state-of-the-art reports in the very active field of microsystems and microtechnology. Written by leading physicists and engineers, the books describe the basic science, device design, and applications. They will appeal to researchers, engineers, and advanced students.

Mechanical Microsensors

By M. Elwenspoek and R. Wiegerink

CMOS Cantilever Sensor Systems

Atomic Force Microscopy and Gas Sensing Applications

By D. Lange, O. Brand, and H. Baltes

Micromachines as Tools for Nanotechnology

Editor: H. Fujita

Modelling of Microfabrication Systems

By R. Nassar and W. Dai

Laser Diode Microsystems

By H. Zappe

Silicon Microchannel Heat Sinks

Theories and Phenomena

By L. Zhang, K.E. Goodson, and T.W. Kenny

Shape Memory Microactuators

By M. Kohl

Force Sensors for Microelectronic Packaging

By J. Schwizer, M. Mayer and O. Brand

Integrated Chemical Microsensor Systems in CMOS Technology

By A. Hierlem

CCD Image Sensors in Deep-Ultraviolet

Degradation Behavior and Damage Mechanisms

By F. M. Li and A. Nathan

Micromechanical Photonics

By H. Ukita

H. Ukita

Micromechanical Photonics

With 285 Figures



Springer

Prof. Dr. Hiroo Ukita
Ritsumeikan University
Faculty of Science and Engineering
Department of Photonics
Nojihigashi, Kusatsu 1-1-1
525-8577 Shiga, Japan
Email: ukita@se.ritsumei.ac.jp

Series Editors:

Professor Dr. Hiroyuki Fujita
University of Tokyo, Institute of Industrial Science
4-6-1 Komaba, Meguro-ku, Tokyo 153-8505, Japan

Professor Dr. Dorian Liepmann
University of California, Department of Bioengineering
6117 Echteverry Hall, Berkeley, CA 94720-1740, USA

ISSN 1615-8326

ISBN 10 3-540-31333-8 Springer-Verlag Berlin Heidelberg New York

ISBN 13 978-3-540-31333-5 Springer-Verlag Berlin Heidelberg New York

Library of Congress Control Number: 2006920112

This work is subject to copyright. All rights are reserved, whether the whole or part of the material is concerned, specifically the rights of translation, reprinting, reuse of illustrations, recitation, broadcasting, reproduction on microfilm or in any other way, and storage in data banks. Duplication of this publication or parts thereof is permitted only under the provisions of the German Copyright Law of September 9, 1965, in its current version, and permission for use must always be obtained from Springer-Verlag. Violations are liable for prosecution under the German Copyright Law.

Springer-Verlag is a part of Springer Science+Business Media

springer.com

© Springer-Verlag Berlin Heidelberg 2006
Printed in The Netherlands

The use of general descriptive names, registered names, trademarks, etc. in this publication does not imply, even in the absence of a specific statement, that such names are exempt from the relevant protective laws and regulations and therefore free for general use.

Typesetting by the author and SPI Publisher Services using a Springer L^AT_EX macro package
Cover concept: eStudio Calamar Steinen

Cover production: *design & production* GmbH, Heidelberg

Printed on acid-free paper 57/3100/SPI-543210

Preface

The recent remarkable development of microsystems dates back to 1983 when Richard P. Feynman of California University delivered a speech to a large audience of scientists and engineers at the Jet Propulsion Laboratory. He presented the concept of sacrificed etching to fabricate a silicon micromotor, and pointed out the need for a friction-less, contact sticking-free structure, due to the relative increase of the surface effect in such microsystems and devices. A micromotor fabricated by Fan *et al.* in 1988 caused a tremendous sensation and opened the way for Micro-Electro-Mechanical-System (MEMS) technology. The diameter of the rotor was $120\text{ }\mu\text{m}$, its rotational speed was 500 rpm, and the gap between the rotor and the stator was $2\text{ }\mu\text{m}$. Today, many successful examples of MEMS products can be found: MEMS such as accelerometers, pressure sensors, microphones and gyros are used commercially, and various branches of industry are already including MEMS components in their new products.

Furthermore, optical MEMS, or micromechanical photonics, are evolving in interdisciplinary research and engineering fields to merge independently developed technologies based on optics, mechanics, electronics and physical/chemical sciences. Manufacturing technologies such as semiconductor lasers, surface-micromachining and bulk-micromachining are promoting this fusion of technologies. In addition, new devices such as optical MEMS including optical sensors, optical switches, optical scanners, optical heads, near-field probes, optical rotors and mixers, actuators, and microsystems for diagnosis and treatments, and new conceptual frameworks such as micromechanical photonics including an optical encoder, a tunable laser diode with a microcantilever and Nano-Electro-Mechanical-Systems (NEMS) are appearing.

Rapidly emerging interdisciplinary science and technology are expected to provide new capabilities in sensing, actuation, and control. Advances such as MEMS, optical MEMS, micromechanical photonics and microfluidics have led not only to a reduction in size but also be the merging of computation, communication and power with sensing, actuation and control to provide new functions. By integrating smart optoelectronics and antennas for remote control with a microstructure, the ability of microsystems to interpret and control

its environment will be drastically improved. Much further work, however, is required to develop this new field to the stage of commercial production.

The purpose of this book is to give the engineering student and the practical engineer a systematic introduction to optical MEMS and micromechanical photonics not only through theoretical and experimental results, but also by describing various products and their fields of application. Chapter 1 begins with an overview spanning topics from optical MEMS to micromechanical photonics and the diversity of products using them at present and in the near future. Chapter 2 demonstrates extremely short-external-cavity laser diodes, tunable laser diodes, a resonant sensor and an integrated optical head. The chapter deals with laser diodes closely aligned with a microstructure including a diaphragm, a microcantilever and a slider. Chapter 3 addresses optical tweezers. This new technology is employed to manipulate various types of objects in a variety of research and industrial fields. The section first analyzes the trapping efficiency by geometrical optics and then compares the theory with the results obtained experimentally, finally presenting a variety of applications. Chapter 4 deals with the design and fabrication of an optical rotor and evaluates its improved mixing of micro-liquids for future fluidic applications such as micrototal analysis systems (μ -TAS). In Chap. 5, the fundamentals and applications of the near field are described for the future development of micromechanical photonics. This technology enables us to observe, read/write and fabricate beyond the wavelength resolution by accessing and controlling the near field. The chapter deals with near-field features, theoretical analyses, experimental analyses and applications mainly related to optical recording.

This work was created in conjunction with many coworkers at NTT and professors and graduate students in Ritsumeikan University. I would like to thank many friends at NTT Laboratories: T. Toshima, K. Itao, and K. kogure for their helpful discussions; Y. Uenishi, Y. Katagiri, E. Higurashi for their long-term co-operation; H. Nakata for bonding an LD-PD on a slider; Y. Sugiyama and S. Fujimori for the fabrication of phase-change recording media; R. Sawada, H. Shimokawa, O. Oguchi, and Y. Suzuki for the preparation of experimental devices; T. Maruno and Y. Hibino for their help with the fabrication of a PLC grating sample; K. Kurumada, N. Tuzuki, and J. Nakano for the preparation of InP laser diodes; and T. Ohokubo and N. Tamari for their help with the experiments.

Professors Y. Ogami, H. Shiraishi, and S. Konishi of Ritsumeikan University and O. Tabata of Kyoto University also deserve many thanks for their co-operation. In addition, I would also like to thank many graduate students of Ukita Laboratories: K. Nagatomi, Y. Tanabe, A. Okada, K. Nagumo, Y. Nakai, T. Ohnishi, Y. Nonohara and Y. Note for their theoretical analyses; S. Tachibana, T. Saitoh, M. Idaka, H. Uemi, M. Kanehira, K. Uchiyama, and K. Takada for their help with the experimental analysis; A. Tomimura, M. Oyoshihara, M. Makita, T. Inokuchi, Y. Itoh, and D. Akagi for their preparation of optical rotor and microcantilever samples; Y. Takahashi, T. Tagashira, Y. Ueda, M. Sasaki, and N. Tamura for their experiments on super-RENS.

I would like to thank J. Tominaga of the National Institute of Advanced Industrial Science and Technology for preparation and discussion of the super-RENS optical disk, and S. Hiura and K. Yamano of Denken Engineering Co. for the trial manufacture of a micro-photoforming apparatus, and K. Horio of Moritex Co. for the trial manufacture of a micro-energy-conversion apparatus.

I would also like to thank Dr. Claus E. Ascheron and Ms. Adelheid Duhm for supporting our book project.

Finally, I wish to thank my wife Misako for her continuous support. I would like to offer her this book as a gift for our 30th wedding anniversary.

Lakeside Biwako
February 2006

Hiroo Ukita

Contents

1	From Optical MEMS to Micromechanical Photonics	1
1.1	Micromechanical Photonics – An Emerging Technology	1
1.2	Fabrication Methods	2
1.2.1	Bulk and Surface Micromachining	3
1.2.2	Three-Dimensional Micromachining	5
1.2.3	Monolithic Integration – Micromachining for an LD	10
1.3	Miniaturized Systems with Microoptics and Micromechanics	11
1.3.1	Important Aspects for Miniaturization	11
1.3.2	Light Processing by Micromechanics	12
1.3.3	Kinetic Energy of Light	20
1.3.4	Micromechanical Control by Optical Pressure	20
1.4	Integrated Systems with LDs and Micromechanics	21
1.4.1	Tunable LD	21
1.4.2	Resonant Sensor	22
1.4.3	Optical Encoder	23
1.4.4	Integrated Flying Optical Head	24
1.4.5	Blood Flow Sensor	25
1.5	Future Outlook of Optical MEMS and Micromechanical Photonics	26
2	Extremely Short-External-Cavity Laser Diode	31
2.1	Background	31
2.2	Theoretical Analysis	32
2.2.1	Lasing Condition of a Solitary LD	32
2.2.2	Effective Reflectivity	34
2.2.3	Light Output	37
2.2.4	Wavelength	37
2.3	Experimental Analysis	41
2.3.1	Experimental Setup	42
2.3.2	Light Output	44
2.3.3	Wavelength and Spectrum Characteristics	45

X Contents

2.4	Applications	48
2.4.1	Tunable LD	50
2.4.2	Resonant Sensor	52
2.4.3	Optically Switched Laser Head	58
2.5	Designs for Related Problems of an ESEC LD	67
2.5.1	Enlargement of a Photothermal MC Deflection for a Tunable LD	67
2.5.2	Reflectivity Design of LD and Disk Medium for an OSL Head	76
3	Optical Tweezers	81
3.1	Background	81
3.2	Theoretical Analysis	85
3.2.1	Optical Pressure	85
3.2.2	Optical Trapping Efficiency	87
3.2.3	Effect of Beam Waist	93
3.2.4	Off-axial Trapping by Solitary Optical Fiber	97
3.3	Experimental Measurement and Comparison	103
3.3.1	Experimental Setup	103
3.3.2	Axial Trapping Power	104
3.3.3	Transverse Trapping Power	106
3.3.4	Optical Fiber Trapping	108
3.4	Applications of Optical Tweezers	112
3.4.1	Basic Research	112
3.4.2	Industry	118
4	Optical Rotor	121
4.1	Background	121
4.2	Theoretical Analysis I – Optical Torque	124
4.2.1	Optical Rotor Having a Dissymmetrical Shape (Shuttlecock) on its Side	124
4.2.2	Optical Rotor with Slopes on the Light Incident Surface	127
4.2.3	Enhanced Shuttlecock Rotors with Slopes	135
4.3	Theoretical Analysis II – Fluid Dynamics	136
4.3.1	Optical Rotor Having a Dissymmetrical Shape on its Side	138
4.3.2	Optical Rotor with Slopes on the Light Incident Surface	141
4.3.3	Mixing Performance in a Microchannel	144
4.4	Fabrication	148
4.4.1	Potolithography	148
4.4.2	Microphotoforming	151
4.5	Evaluation	152
4.5.1	Visualization of Microflow (Agitation)	153

4.5.2	Medium Density Pattern Tracking	158
4.5.3	Velocity Vector and Flux Amount Analyses	159
4.6	Mixer Application for μ -TAS	163
5	Near Field	167
5.1	Background	167
5.2	Theoretical Analysis	169
5.2.1	FDTD Method	169
5.2.2	Numerical Examples of Near Field Analysis	173
5.3	Experimental Analysis	179
5.3.1	Comparison of Near-Field Probes	179
5.3.2	Photocantilever Probe	180
5.3.3	Gold Particle Probe	184
5.4	Future Applications	193
5.4.1	Conventional Superresolution	193
5.4.2	Near-field Recording	196
5.4.3	Super-RENS Optical Disk	198
6	Answers, Hints and Solutions	215
References		227
Index		243

1

From Optical MEMS to Micromechanical Photonics

Micromechanical photonics is evolving in interdisciplinary research and engineering fields and merging independently developed technologies based on optics, mechanics, electronics, and physical/chemical sciences. Manufacturing technologies such as those of semiconductor lasers, surface micromachining and bulk micromachining are promoting technology fusion.

This chapter presents an overview of the emerging technologies that feature new conceptual frameworks such as optical microelectromechanical systems (optical MEMS) including an integrated optical sensor, an integrated optical switch, an integrated optical head, an optical rotor, and a micrototal analysis system (μ -TAS); micromechanical photonics devices including an extremely short-external-cavity tunable laser diode (LD) with a microcantilever, a resonant sensor, an optical encoder and a blood flow sensor; nanoelectromechanical systems (NEMS) and system networks.

1.1 Micromechanical Photonics – An Emerging Technology

We have made substantial progress in individual areas of optics, mechanics, electronics and physical/chemical sciences, but it is insufficient to apply individual technologies and sciences to solve today's complicated technical problems. The start of semiconductor LD room temperature continuous oscillation in 1970 and micromachining technology [1.1, 1.2] based on photolithography and selective etching in the late 1980s resulted in the birth of optical MEMS [1.3]/micromechanical photonics [1.4] that combines/integrates electrical, mechanical, thermal, and sometimes chemical components through optics in the early 1990s.

Various kinds of optical MEMS have been developed for the fields of information, communication, and medical treatment. They include a digital micromirror device (DMD) [1.5] for both large projection display and color printing, optical switches [1.6, 1.7] for communication, microservo mechanisms

[1.8, 1.9] for optical and magnetic recording, and μ -TAS [1.10] for medical treatment.

Advanced lithography has been applied not only to silicon (Si) but also to thin film materials, including dielectric [1.11], polyimide [1.12], and metal [1.13] to offer unprecedented capabilities in extending the functionality and miniaturization of electro-optical devices and systems. Group III–V compounds, which include gallium arsenide (GaAs) [1.14] and indium phosphide (InP) [1.15], are attractive for integrating optical and mechanical structures to eliminate the need for optical alignment. In a tunable LD, the moving external cavity mirror has been integrated with a surface-emitting LD [1.16]. A moving cantilever has been integrated with edge-emitting LDs and a photodiode in a resonant sensor [1.17]. Monolithic integration technologies are expanding the field of micromechanical photonics.

Novel probing technologies such as the scanning tunneling microscope (STM) and optical tweezers have advanced our knowledge of surface science [1.18, 1.19] and technology, which are important in microscale and nanoscale mechanisms. Today's science and technology requires the focusing of multidisciplinary teams from engineering, physics, chemistry, and life sciences in both universities and industry. In this chapter, I first review fabrication methods of microstructures, then summarize some of the highlights in these attractive research fields, and then discuss the outlook for the future.

1.2 Fabrication Methods

There are common steps in fabricating optical MEMS/micromechanical devices: deposition, sputtering and etching, bulk micromachining including anisotropic etching and etch stop, and surface micromachining characterized by sacrificed layers that are etched away to leave etch-resistant layers. The fabrication methods of microstructures with optical elements are reviewed in [1.1, 1.2]. Miniaturization requires high aspect ratios and new materials. Reactive ion beam etching (RIBE) precisely defines the features and the spacing in deposited thin film and is of great importance in making high-aspect-ratio microstructures.

Si has been the most commonly used in micromachining, and its good electrical and mechanical properties have resulted in many commercially available sensors and actuators. A diaphragm is fabricated by bulk micromachining such as selective wet etching. Free-space micro-optical systems can be fabricated by surface micromachining; this is very promising and will greatly enrich the variety of integrated optical devices [1.20]. One choice is the silicon-on-insulator (SOI) technology [1.21]. Advantages of the SOI technology are its simplicity and small number of process steps.

Group III–V compounds, such as GaAs and InP, are attractive candidates for monolithic integration of optical and mechanical structures [1.14, 1.15]. Concrete examples are given later.

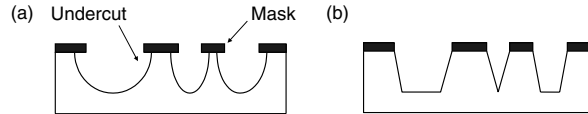


Fig. 1.1. Isotropic (a) and anisotropic (b) etchings for bulk micromachining

1.2.1 Bulk and Surface Micromachining

To fabricate structures by bulk micromachining, two etching methods can be used, isotropic and anisotropic etchings. In isotropic etching, etching proceeds at the same rate in all directions, which leads to the isotropic undercut shown in Fig. 1.1a. On the other hand, in anisotropic etching, etching proceeds at different rates depending on the crystal orientation, which leads to precise features, shown in Fig. 1.1b. Silicon V-grooves are fabricated by anisotropic etching of a (100) silicon substrate and are widely used in optical MEMS. The V-grooves are also used in packing of fiber and optoelectronic components.

To fabricate structures by surface micromachining, a sacrificed film is first deposited and patterned on the wafer. The film to be formed into the desired microstructure is next deposited and patterned, and the sacrificed layer is then etched away, undercutting the microstructure and leaving it freely suspended. There are two kinds of surface micromachining: photolithography for a thickness less than several $10\text{ }\mu\text{m}$, and electron beam lithography for a thickness of less than $1\text{ }\mu\text{m}$.

Photolithography

Photolithography is most widely used for the fabrication of a microstructure. The process steps shown in Fig. 1.2 include ultraviolet (UV) light exposure, development, etching, and resist stripping. This essentially 2-D process has the following characteristics:

1. difficulty in fabricating features smaller than the exposure light wavelength
2. high throughput by a mask process
3. relatively high aspect ratio.

The electrostatic micromotor [1.2] shown in Fig. 1.3, fabricated by Fan et al. of California University in 1988, caused a tremendous sensation and paved the way for the development of MEMS technology. The diameter of the microrotor was $120\text{ }\mu\text{m}$ and the gap between the rotor and the stator was $2\text{ }\mu\text{m}$. Both were made of polysilicon thin films. When pulse voltages are applied to stator poles with different phases, an electrostatic torque arises between the rotor and the stator, which leads to the rotation rate of 500 rpm. Two years later, Mehregany et al. [1.22] of the Massachusetts Institute of Technology fabricated a micromotor with a higher speed of 15000 rpm. Recently, commercially used MEMS such as pressure sensors, accelerometers, and gyros are fabricated by the successive photolithography.

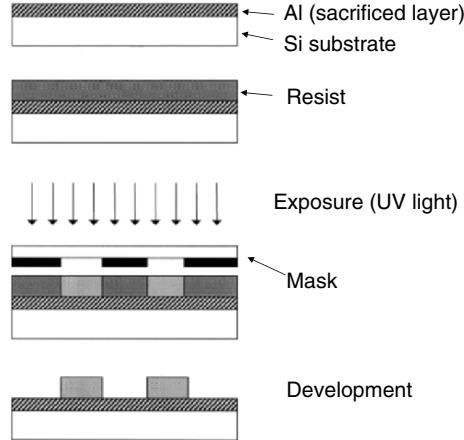


Fig. 1.2. Basic process of photolithography using a negative resist

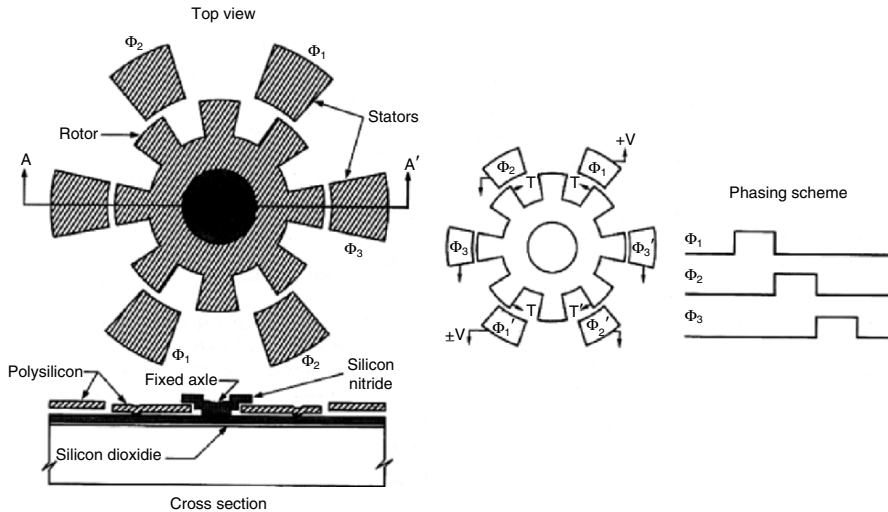


Fig. 1.3. Top view, cross-section, and the phasing scheme of a micromotor fabricated by surface micromachining [1.2] ©1988 IEEE

In the case of thick microstructures, SU-8 resists are widely used [1.23]. Physical properties of SU-8 can be found at <http://aveclafaux.freeservers.com/SU-8.html>. To view typical SU-8 applications, visit <http://www.mimotec.ch/>.

As an example of optical MEMS, the process for fabricating optical pressure rotors having anisotropic geometry on the side is shown in Fig. 1.4. First, the SiO_2 layer is deposited on a GaAs substrate, and then the SiO_2 is etched down to the GaAs substrate by reactive ion beam etching (not by UV light). The substrate is then immersed in a wet-etching solution to dissolve the GaAs

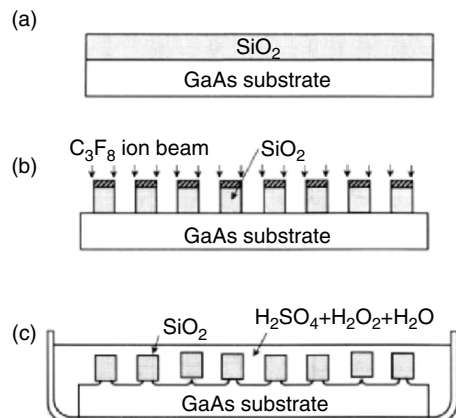


Fig. 1.4. Fabrication sequence, by photolithography, of an SiO₂ optical rotor (see Fig. 1.26). Deposition of SiO₂ layer by RF sputtering (a), etching of SiO₂ layer by reactive ion-beam etching (b), and stripping of SiO₂ by dissolution of the substrate (c)

layer. The resulting microrotors are washed and dispersed in water. Typical optical rotors are 20 μm in diameter and 10 μm thick, and are made of SiO₂ or polyimide or SU-8, which are transparent at the laser wavelength of 1.06 μm.

Electron Beam Lithography

In electron beam lithography (EBL), focused high-energy electrons with wavelengths less than that of UV light are irradiated onto electron-sensitive resist, as shown in Fig. 1.5. High-resolution patterning can be accomplished by scanning the e-beam two-dimensionally on the resist. Numerous commercial resists have been produced. EBL exhibits the following characteristics:

1. high-resolution patterning (less than 0.1 μm)
2. Easy and precise deflection by electrostatic or magnetic field
3. No need for mask process
4. Low throughput due to direct e-beam writing
5. Low aspect ratio (less than 1 μm thick).

1.2.2 Three-Dimensional Micromachining

LIGA

A surface-micromachined device has a thickness less than 100 μm. However, many micromechanical devices, particularly microactuators, require a thickness of few hundreds micrometers. Microstructures with a very large aspect

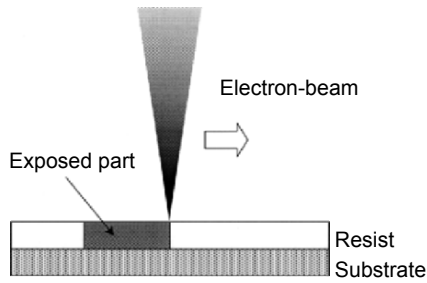


Fig. 1.5. Electron beam lithography (EBL) in which focused high-energy electrons are irradiated to the electron-sensitive resist

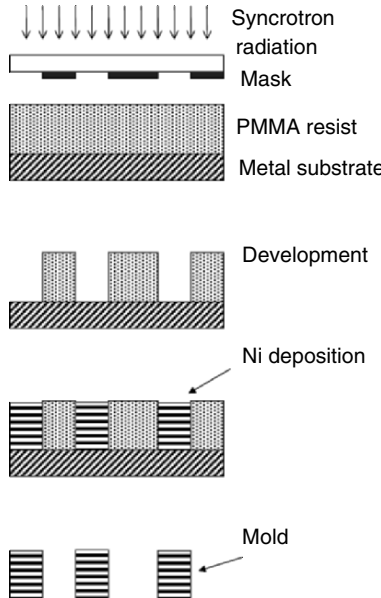


Fig. 1.6. Lithographie galvanoformung abformung (LIGA) involves X-ray lithography and electrodeposition processes

ratio (thickness-to-width ratio) can be fabricated by Lithographie galvanoformung abformung (LIGA), illustrated in Fig. 1.6. LIGA involves X-ray lithography, electrodeposition and molding process [1.24]. The aspect ratio that can be achieved using LIGA exceeds 300. LIGA exhibits the following characteristics:

1. high resolution
2. high aspect ratio
3. high throughput by mask and molding process
4. complicated mask production process.

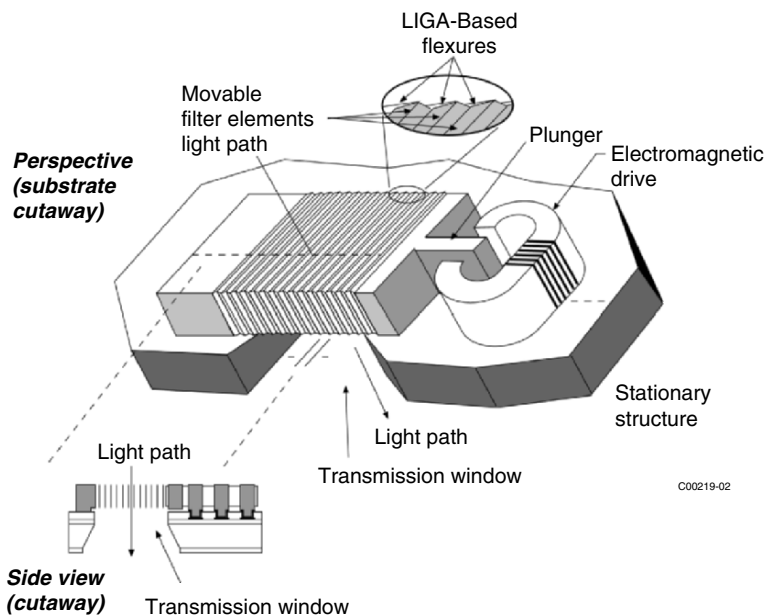


Fig. 1.7. LIGA-based tunable IR filter showing vertical parallel plate filter structure and linear magnetic drive actuator [1.25]. Courtesy of J. Allen Cox, Honeywell, USA

Figure 1.7 shows an LIGA-based tunable infrared (IR) filter [1.25]. Gratings with free-standing nickel walls as high as $50\text{ }\mu\text{m}$ with periods on the order of $10\text{ }\mu\text{m}$ were fabricated by LIGA. The linear actuator utilizes a permalloy electromagnet with an air gap because of the large power (0.1 mN) necessary to adjust the spacing of the grating. Furthermore, simple 3-D microstructures will be fabricated by the LIGA process [1.26].

Photoforming

Complicated 3-D microstructures have been fabricated by stacking preshaped layers made by solidifying a thin resin layer with UV light [1.27, 1.28]. There are two solidification methods: a free surface and a fixed surface solidification. In the case of the free surface, solidification occurs at the resin/air interface, leading to perturbation on the surface. On the other hand, in the case of the fixed surface, solidification occurs at the stable window/resin interface, leading to smoother structures. Photoforming exhibits the following characteristics:

1. complicated microstructures can be fabricated
2. laser beam can be deflected easily by scanning mirrors
3. no need for mask process
4. low throughput due to direct laser beam writing.

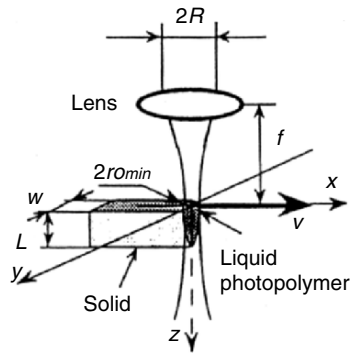


Fig. 1.8. Mechanism of photopolymerization using a focused laser beam. Reprinted from [1.27] with permission by K. Yamaguchi

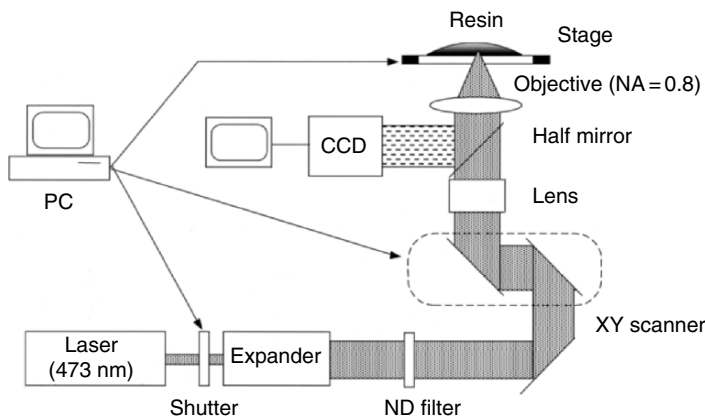


Fig. 1.9. 3-D microfabrication with photopolymerization using scanning focused laser beam

We also can directly fabricate a microstructure by scanning the laser beam in the resin. Figure 1.8 shows the mechanism of photopolymerization using a focused laser beam. Figure 1.9 shows the block diagram of such a point-by-point photoforming method. A focused blue laser beam (wavelength of 473 nm, output power of 10 mW) is used to solidify the resin. The scanning of the blue laser beam is controlled by adjusting mirrors according to the slice data of the microstructure. In this case, a 3-D structure is fabricated by scanning the focused spot in three dimensions inside the resin, rather than by using a layer-by-layer process. Although the spot diameter is small at the focal plane, the depth of focus is large, which leads to inferior resolution at depth.

In order to improve 3-D resolution, several photoforming methods have been proposed, as listed in Table 1.1. Photopolymerization stimulated by two-photon absorption was demonstrated using a Ti:sapphire laser and urethane-based resin (SCR-500), as shown in Fig. 1.10 [1.29]. Since the two-photon

Table 1.1. Comparison of proposed photoforming methods with high resolution

method	two-photon absorption	super IH process	spinner
light source			
laser	titan-sapphire laser	He-Cd laser	laser diode
wavelength (nm)	780	442	650
power	50 kW (peak)	1.5 mW	0.35 mW
resin	urethane based (SCR-500)	urethane based (Threshold)	aclyle based (DF-200N) ^a
cubic structure resolution (μm)	3-D scanning	3-D scanning	stacking
depth	2.2	3.0	2.0
lateral	0.62	0.5	1.0

^a Commercially available from Nippon Kayaku Corp.

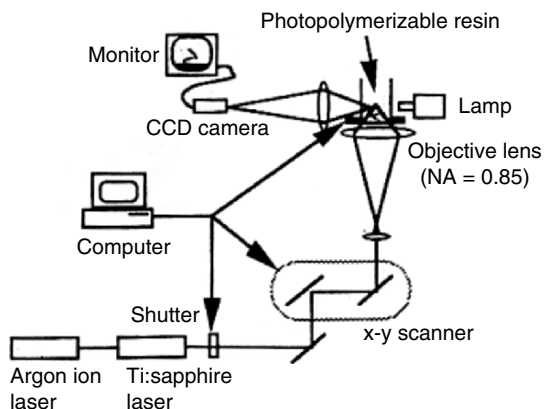
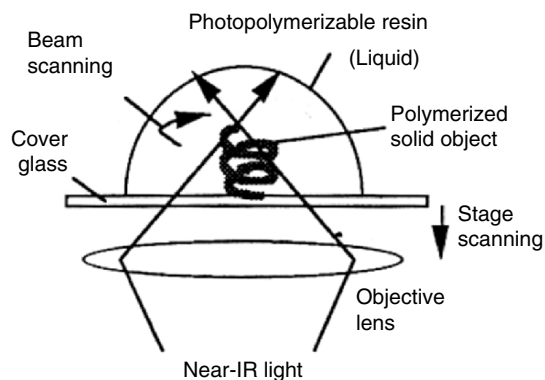


Fig. 1.10. Photopolymerization stimulated by two-photon-absorption using Ti:sapphire laser and SCR-500 resin. Reprinted from [1.29] with permission by S. Kawata, Osaka University, Japan

absorption rate is proportional to the square of the incident light intensity, a 3-D structure is fabricated by scanning the focused spot of a near-infrared-wavelength beam in three dimensions inside the resin. The lateral and depth resolutions are said to 0.62 and 2.2 μm , respectively. After that, they also succeeded in fabricating a micrometer sized cow with a resolution of 140 nm [1.30].

Replication

Replication from a mold is important technology for realizing lower cost and mass production. For optical MEMS applications, the use of sol-gels which become glass-like material upon curing is foreseen. ORMOCECER US-S4 is such a material. It is optically transparent over the wavelength from 400 to 1600 nm and has a refractive index of 1.52 at 588 nm. Obi et al. replicated many sol-gel micro-optical devices and optical MEMS including a sol-gel cantilever with a microlens on the top [1.31].

1.2.3 Monolithic Integration – Micromachining for an LD

Monolithic integration of micromechanics is possible not only on a Si substrate but also on a semiconductor LD substrate of GaAs [1.14] or InP [1.15]. A smooth etched surface and a deep vertical sidewall are necessary for good lasing characteristics of LDs.

For fabricating a resonant microcantilever (MC), for example, there are three micromachining steps (Fig. 1.11). (a) An etch-stop layer of AlGaAs is formed in an LD structure prepared by metalorganic vapor phase epitaxy (MOVPE). (b) The microstructure shape is precisely defined by a reactive dry-etching technique, which simultaneously forms the vertical etched

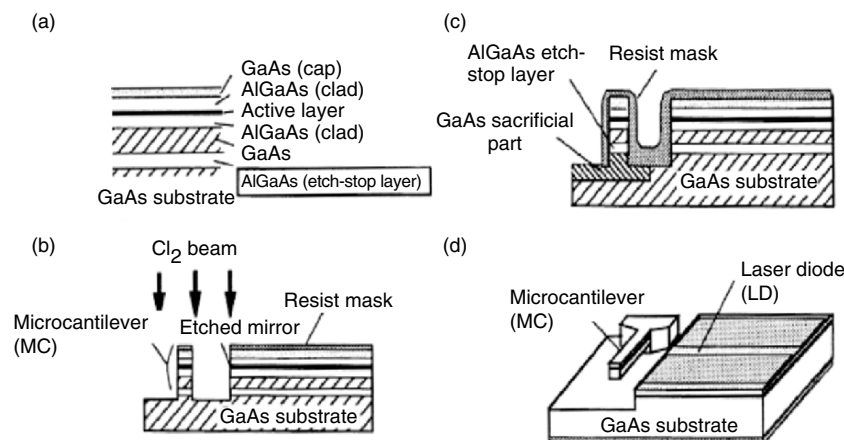


Fig. 1.11. Steps in the fabrication of a GaAs/AlGaAs resonant microcantilever (MC) integrated with a laser diode (LD)

mirror facets for LDs. (c) A wet-etching window is made with a resist, and the microcantilever is undercut by selective etching to leave it freely suspended.

These processes are compatible with laser fabrication, so an MC structure can be fabricated at the same time as an LD structure. Furthermore, because a single-crystal epitaxial layer has little residual stress, precise microstructures can be obtained without significant deformation.

Combined use of the above micromachining processes will be useful in the future. However, processing of electronics and MEMS must be compatible and should be held down to low costs. In many actual microsystems, microassembly, bonding, and packing techniques will also play important roles. Moreover, to apply the merit of the mask process to the MEMS with an arrayed structure, it is imperative to increase the yield rate.

1.3 Miniaturized Systems with Microoptics and Micromechanics

1.3.1 Important Aspects for Miniaturization

We see that the miniaturization techniques described earlier will provide many new optical MEMS that will environmentally friendly due to their smallness, reliable due to the integration process, and low in cost owing to mass production. However, new problems arise as a result of the miniaturization. Understanding the scaling laws and the important aspects of miniaturization will help readers in choosing the appropriate actuator mechanism and power source.

Feynman presented the concept of sacrificed etching to fabricate a silicon micromotor 20 years ago [1.32]. At the same time, he pointed out the necessity of friction-less and contact sticking-free structure for the MEMS because of the relative increase of the surface effect in such microdevices.

Figure 1.12 shows the general characteristics of scaling laws. As the object size $[L]$ decreases, the ratio of surface area $[L^2]$ to volume $[L^3]$ increases. Weight depends on volume, while drag force depends on surface area, which renders surface forces highly important in microstructures. Faster evaporation associated with larger surface-to-volume ratios has important consequences in analytical equipment such as μ -TAS.

Response time is proportional to [mass/frictional force], i.e., $[L^3/L^2] = [L]$, which leads to fast response. The Reynolds number is proportional to [inertia force/viscous drag force], i.e., $[L^4/L^2] = [L^2]$, which leads to laminar flow. Moving energy is proportional to [mass \times velocity 2], i.e., $[L^3 \times L^2] = [L^5]$, which leads to low energy consumption.

Almost all micromotors and microactuators have been built based on electrostatic actuation, nevertheless, electrostatic force is proportional to $[L^2]$, but electromagnetic force is proportional to $[L^4]$. This is because the plate for

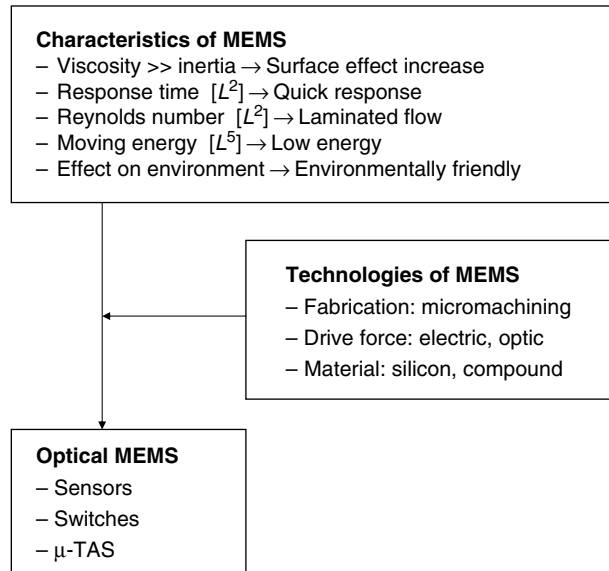


Fig. 1.12. General characteristics of scaling laws: the merits of miniaturization

generating electrostatic force is easier to fabricate in a limited space than the inductance coil that generates the magnetic field for actuation. Actually, to drive thick and heavy MEMS [1.25], electromagnetic force is used because the electrostatic driving force is too weak.

We deal mostly with micrometer-sized devices. In the micrometer regime, conventional macrotheories concerning electrical, mechanical, fluidic, optical, and thermal devices require corrections. Specific properties of the thin film material differ from those of bulk. Shape change due to thermal stress or fast movement occurs in the micromirror fabricated by surface micromachining, which degrades the optical quality of the laser beam.

1.3.2 Light Processing by Micromechanics

Since light can be controlled by applying relatively low energy, the electrostatic microstructures such as moving mirrors or moving gratings have been fabricated on the same wafer. Applications of moving mirrors in micro positioning have begun to appear recently, and many kinds of digital light switches have been demonstrated. These include a DMD [1.5], an optical scanner [1.33], a tunable IR filter [1.25], and a comb-drive nickel micromirror [1.34]. A nickel micromirror driven by a comb-drive actuator was fabricated by nickel surface micromachining. The micromirror was $19\text{ }\mu\text{m}$ high and $50\text{ }\mu\text{m}$ wide and the facet reflectivity was estimated to be 63%. A microstrip antenna was fabricated on a fused quartz structure that could be rotated to adjust spatial scanning of the emitted microwave beam [1.35].

Free-space Micro-optical Bench and Sensors

Vertical micromirrors can be fabricated by anisotropic etching on (100) silicon just like the V-groove described in Sect. 1.2.1. The (111) planes are perpendicular to the Si surface and atomically smooth. Therefore, high-aspect-ratio mirrors can be formed. Figure 1.13 shows an on-chip Mach-Zehnder interferometer produced by Uenishi [1.36]. Micromirrors are reported several μm s thick and 200 μm high.

Free-space micro-optical elements held by 3-D alignment structures on a silicon substrate have been demonstrated using a surface-micromachining technique in which the optical elements are first fabricated by a planar process and then the optical elements are folded, into 3-D structures, as shown in Fig. 1.14 [1.37]. Figure 1.15 shows the schematic of the out-of-plane micro-Fresnel lens fabricated on a hinged polysilicon plate (a), and the assembly process for the 3-D micro-Fresnel lens (b) [1.38]. A Fresnel lens stands in front of an edge-emitting LD to collimate its light beam.

To achieve on-chip alignment of hybrid-integrated components such as an LD and a micro-optical element, a micro-XYZ stage consisting of a pair of

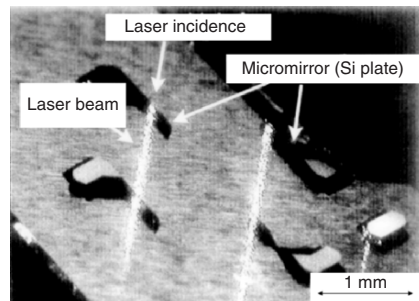


Fig. 1.13. An on-chip Mach-Zehnder interferometer produced by anisotropic etching on (100) silicon [1.36]. Courtesy of Y. Uenishi, NTT, Japan

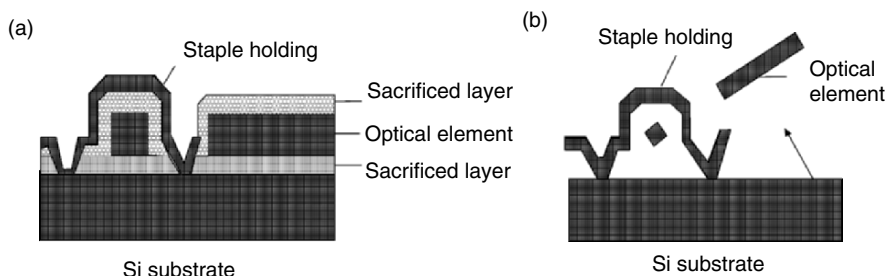


Fig. 1.14. Free-space micro optical elements held by 3-D alignment structures on a silicon substrate, fabricated using a surface-micromachining technique. Optical elements were first fabricated by planar process and then folded into 3-D structures [1.37]

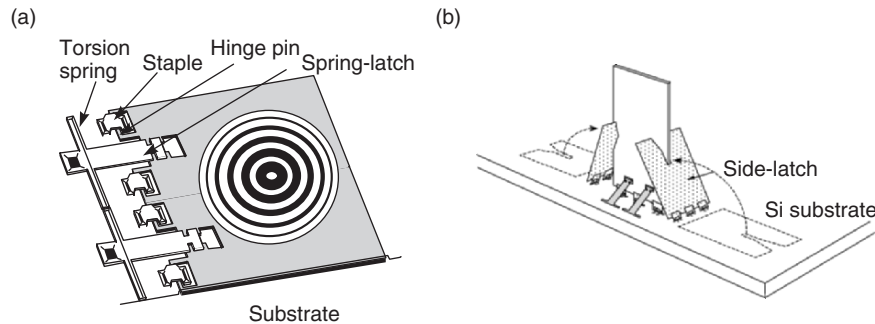


Fig. 1.15. Schematic of the out-of-plane micro-Fresnel lens fabricated on a hinged polysilicon plate (a), and the assembly process for the 3-D micro-Fresnel lens (b) [1.38]. Courtesy of Ming Wu, University of California, USA

parallel 45° mirrors has been demonstrated to match the optical axis of the LD with that of the micro-optical element [1.38]. Both the micro-XYZ stage and the free-space micro-optical elements are fabricated by the microhinge technique to achieve high-performance single-chip micro-optical systems.

Digital Micromirror Device (DMD)

A digital micromirror device (DMD) was developed by Texas Instruments in 1987. A standard DMD microchip has a 2-D array of 0.4×10^6 switching micromirrors. Figure 1.16 shows a DMD structure consisting of a mirror that is connected to a yoke through two torsion hinges fabricated by a CMOS-like process. Each light switch has an aluminum mirror that can be rotated ± 10 degrees by electrostatic force depending on the state of the underlying CMOS circuit [1.5].

The surface micromachining process to fabricate DMD is shown in Fig. 1.17. The illustrations are after sacrificial layer patterning (a), after oxide hinge mask patterning (b), after yoke oxide patterning (c), after yoke/hinge etching and oxide stripping (d), after mirror oxide patterning (e), and the completed device (f). “CMP” in (a) means “chemomechanically polished” to provide a flat surface.

Figure 1.18 shows the optical layout of a large-screen projection display using a DMD. The DMD is a micromechanical reflective spatial light modulator consisting of an array of aluminum micromirrors. A color filter wheel divided into three colors; red, blue, and green, is used for color presentation. A 768×576 pixel DMD was tested and a contrast ratio of 100 was reported.

Optical Switch

Analog and digital switches, tunable filters, attenuators, polarization controllers, and modulators are some of the devices required in optical

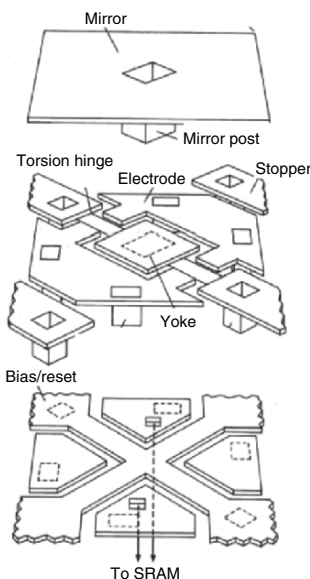


Fig. 1.16. Digital micromirror device (DMD) developed by Texas Instruments. A DMD structure, with a mirror connected to a yoke by two torsion hinges, is fabricated by a CMOS-like process [1.5] Courtesy of Larry J. Hornbeck, Texas Instruments, USA ©1993 IEEE

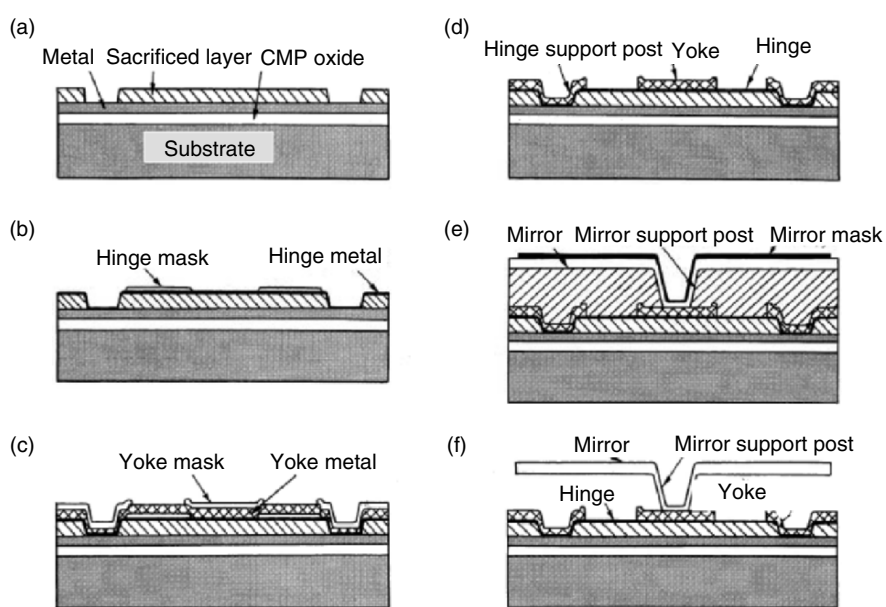


Fig. 1.17. Fabrication process of a digital mirror device (DMD) structure consisting of a mirror connected by two torsion hinges [1.5] ©1998 IEEE

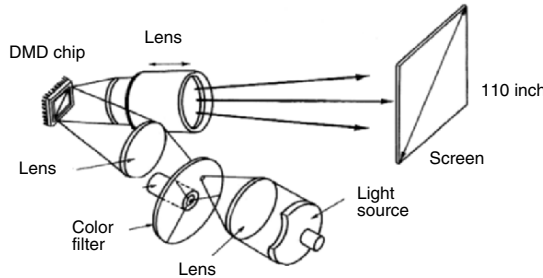


Fig. 1.18. Optical layout of a projector using a DMD [1.5]. Courtesy of Larry J. Hornbeck, Texas Instruments, USA ©1993 IEEE

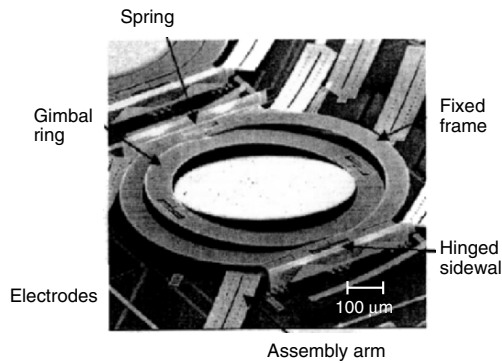


Fig. 1.19. Surface-micromachined beam-steering micromirror [1.7] ©2003 IEEE

communication. Optical MEMS has become a household word thanks to the enormous interest in fiber-optic switching technology. Micromirror-based all-optical switches are thought to be the only actual solution to wavelength division multiplexing (WDM) because they are independent of wavelength. Miniaturized optical switches can be changed to select different optical paths by adjusting the mirror tilt (without optic to electric transformation).

The micromirrors were fabricated based on the surface micromachining of polysilicon thin films (Fig. 1.19) in the first stage [1.6, 1.7]. Miniaturization methods enable the creation of arrays of tiny, high-capacity optical switches, such as those for switching 256 input light beams to 256 output fibers developed at Lucent Technologies [1.7]. An optical switch of 1152×1152 optical cross-connects was fabricated by Nortel. Free-space switching with a MEMS micromirror array between two stacked planar lightwave circuits (PLCs) is used to construct a wavelength-selective switch [1.39].

Recently, bulk micromachining of crystalline silicon has been revived (Fig. 1.20) [1.40, 1.41] because the conventional mirror surface (polysilicon) fabricated by surface micromachining is thin ($1\text{ }\mu\text{m}$) and deformable due to the presence of both residual stress and a metal film coating [1.42]. The use of

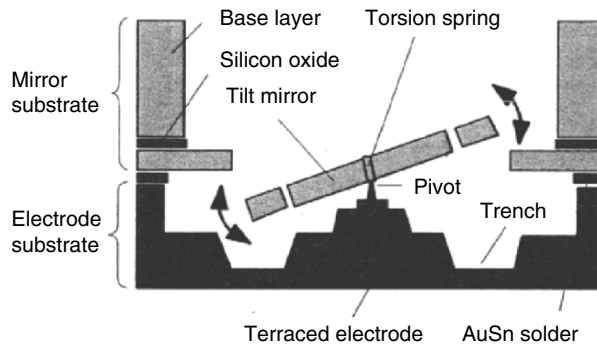


Fig. 1.20. Single-crystalline mirror actuated by electrostatic force applied via terraced electrodes. Reprinted from [1.40] with permission by T. Yamamoto, NTT, Japan

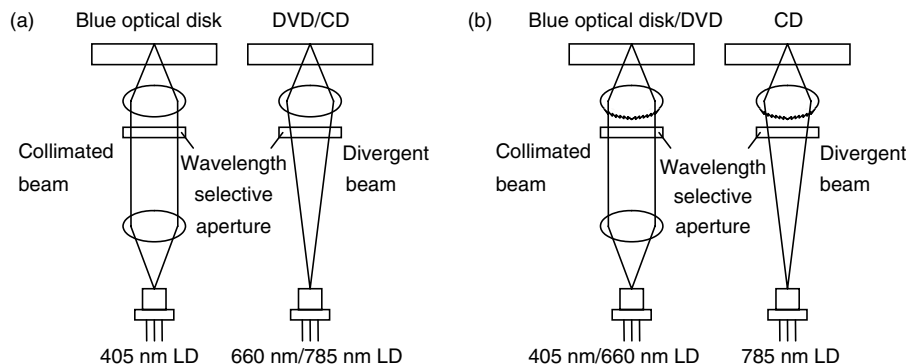


Fig. 1.21. Blue ray/DVD/CD compatible optical head technology. The compatibility principle is based on spherical aberration correction and objective NA control for each disk [1.45]. Courtesy of R. Katayama, NEC, Japan

silicon-on-insulator (SOI) substrates together with deep reactive ion etching (DRIE) is now an established technology for fabricating high-performance optical switches because of the flatness of the mirror [1.43].

Optical Heads

Various optical disk systems with a Blue ray/digital versatile disk (DVD)/compact disc (CD) compatible optical head, a free-space integrated optical head, and an electrostatic torsion mirror for tracking have been investigated for the advanced DVD [1.44]. Flying optical heads with various small-aperture probes are proposed for next-generation near-field recording.

Three kinds of light wavelength λ and objective lens NA are used for the optical heads of a Blue ray, a DVD and a CD: $(\lambda, \text{NA}) = (405 \text{ nm}, 0.8)$, $(650 \text{ nm}, 0.6)$, and $(785 \text{ nm}, 0.5)$, respectively. Compatibility of heads with different wavelengths and different NAs, is needed (Fig. 1.21) [1.45].

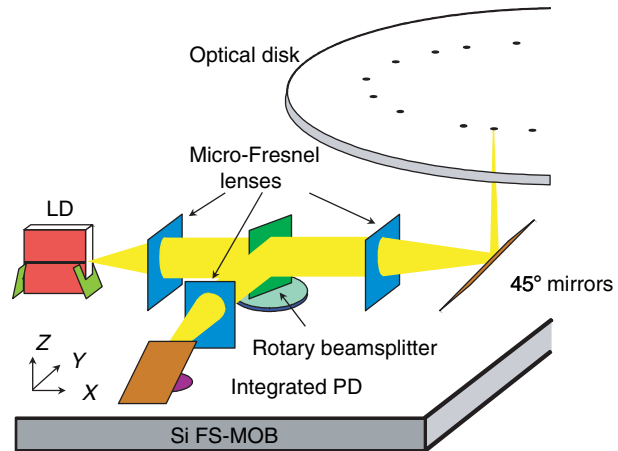


Fig. 1.22. A free-space optical pickup head integrated by surface micromachining [1.20]. Courtesy of Ming Wu, University of California, USA

The compatibility principle is based on spherical aberration correction and objective NA control for each disk. Optical MEMS technologies are applied to control NA (aperture) depending on the wavelength [1.45], to integrate optical components (Fig. 1.22) [1.20], and to track the optical disk groove [1.9]. Rotable microstages are implemented by a suspended polysilicon plate fabricated by micromachining.

In order to realize an ultrahigh-density optical disk, a tiny-aperture probe is needed. However, the optical transmittance decreases rapidly as the aperture diameter decreases below 100 nm. To increase the transmittance, a bow-tie probe with an actuator driven by electrostatic force was successfully fabricated (Fig. 1.23) [1.46]. The on-chip actuator provides not only a narrow gap to enhance the intensity of the near field but also precision alignment of the optical components.

μ-TAS/bio MEMS

Chip-scale technologies are diversifying into the field of microfluidics, such as a sample analysis system for physiological monitoring, sample preparation and screening, and a biomedical treatment application for a new surgical tool and drug delivery [1.47].

A micrototal analysis system (μ -TAS) [1.48] is expected to reduce inspection time or the amount of reagent needed. The system shown in Fig. 1.24 comprises inlets for the sample and reagent loading, microchannels with a mixing chamber and an analysis chamber, and outlets for sample wastes.

In a microchannel, mixing is performed mainly by diffusion owing to the small Reynolds number. To promote a diffusion effect by interweaving two fluids, mixing devices such as micronozzle arrays to increase the contact area,

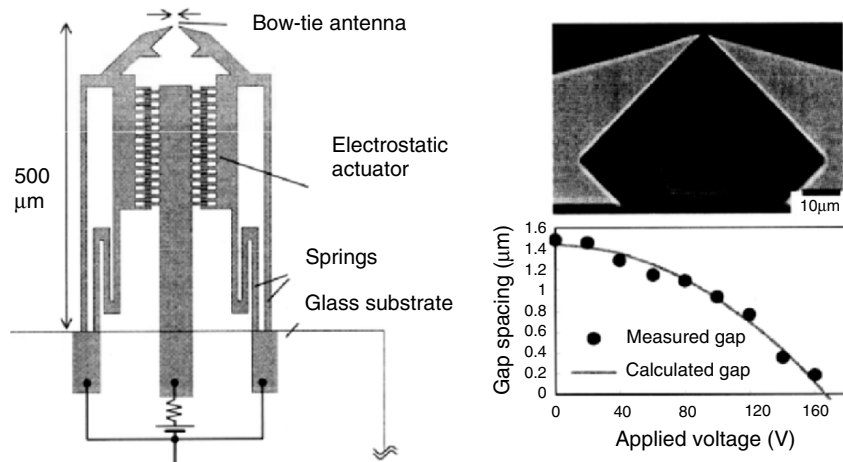


Fig. 1.23. A bow-tie probe with an actuator driven by electrostatic force is fabricated to provide a narrow gap that enhances the intensity of the near field. Reprinted from [1.46] with permission by M. Esashi, Tohoku University, Japan

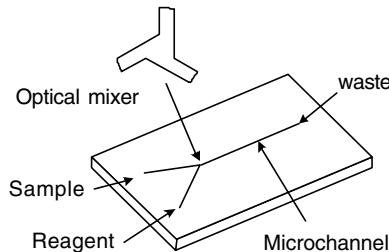


Fig. 1.24. Conceptual drawing of the future micrototal analysis system (μ -TAS) [1.50]

and intersecting channels [1.49] to induce chaotic behavior of a flow have been fabricated. An optically driven micromixer [1.50] has been proposed to stir a liquid directly, which is described in detail in Chap. 4. Highly sensitive detection methods [1.51] and high-performance micropumps [1.52] are also important because of the reaction between small liquids, as well as to drive liquids in microchannels.

Optical inspection of a human body is also a useful method for minimally invasive diagnosis and treatment. Figure 1.25 shows the microconfocal optical scanning microscope (m-COSM) [1.53]. The probe, 2.4 mm in diameter, consists of a 2-D electrostatic scanner which is placed in front of the end of the optical fiber. Light reflected by the tissue is collected by the same objective lens and reflected back into the same optical fiber. The field of view is $100\text{ }\mu\text{m} \times 100\text{ }\mu\text{m}$ and the resolution is $1\text{ }\mu\text{m}$ with an image feed speed of 4 frames s^{-1} .

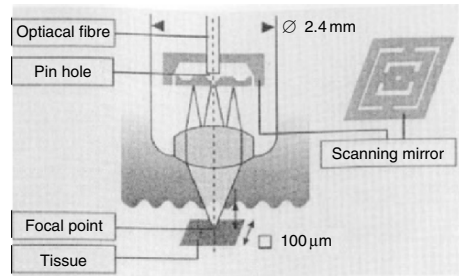


Fig. 1.25. Microconfocal optical scanning microscope fabricated for minimally invasive medical diagnosis and treatment (m-COSM). Reprinted from [1.53] with permission by M. Esashi, Tohoku University, Japan

1.3.3 Kinetic Energy of Light

Light is conventionally applied in optical data storage such as CDs and DVDs, in an optoelectronic information apparatus such as displays and printers, in optical communication devices such as optical fibers and LDs, and in optical measurements using various kinds of sensors. In these applications, we have utilized the electromagnetic aspect of light. On the other hand, in optical MEMS and in micromechanical photonics applications, the kinetic energy aspect of light becomes important.

Powering of miniaturized equipments or systems by a light beam has recently been rediscovered, and many kinds of transduction from light energy to kinetic energy have been developed. The photoelectric effect was used to make a photostrictional actuator driven by light-induced conformational change of a polymer, semiconductor or ceramic. The photothermal effect was used to make a tiny resonator [1.14], a micropump, a microgripper [1.54] and a waveguide switch [1.55]. A photoformed gripper, designed for handling micro-objects in a narrow space, is actuated by the volume change of fluid upon applying laser power. This photothermal energy will be useful as a driving force of miniaturized systems because of its high power density and good energy transfer efficiency. A photoelectrochemical effect was studied for the development of a storage battery [1.56].

A photovoltaic microdevice to cover the surface of a miniaturized system was developed for amorphous silicon thin films triple-stacked and series-connected to obtain a high voltage of 200 V [1.57]. A microdevice to transfer energy via light to a microwave by combining piezoelectric force and an antenna has been reported [1.58].

1.3.4 Micromechanical Control by Optical Pressure

Ashkin et al. demonstrated optical trapping in 1970. A great deal of theoretical and experimental knowledge and technology in this field has been

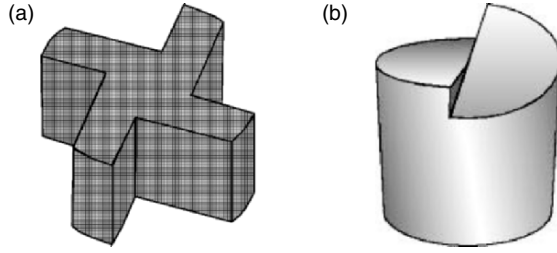


Fig. 1.26. Two kinds of optical rotors: a rotationally but not bilaterally symmetric rotor which uses optical torque exerted on its side surfaces (a), and a cylindrical optical rotor which has slopes for rotation on its upper surfaces (b)

accumulated. Today, such technology is used in various scientific and engineering fields to manipulate [1.59], align [1.60], and switch [1.61] many kinds of micro-objects. Optical tweezers is described in detail in Chap. 3.

Using a laser beam the rotation of artificial micro-objects fabricated by micromachining was demonstrated. Figure 1.26 shows two kinds of optical rotors: a rotationally but not bilaterally symmetric structured rotor to which optical torque is exerted on its side surfaces (a) [1.62], and a cylindrical optical rotor which has slopes for trapping and rotating on its upper surfaces (b) [1.63]. The rotation mechanism has been shown both experimentally and theoretically.

The use of optical rotors is expected to solve the problems of an MEMS motor, i.e., short lifetime due to friction and the requirement of electrical wires for the power supply. Applications of directional high-speed optical rotation may include an optical motor and a microgear for micromachines [1.64, 1.65] and a micromixer [1.66] for μ -TAS. These optical-rotor-related technologies could have a significant effect on developments in optical MEMS and micromechanical photonic systems. Optical rotation is described in detail in Chap. 4.

1.4 Integrated Systems with LDs and Micromechanics

In micromechanical photonics applications using LDs of group III–V compounds are predominant for monolithic integration of microstructures. They include a GaAs-based integrated tunable laser [1.16, 1.67], a resonant sensor [1.17], an optical encoder [1.68], an optical head [1.69], and an InP-based free-standing microstructure [1.15], and a portable blood flow sensor [1.70], which can be used to provide supersmall, cost-effective microdevices.

1.4.1 Tunable LD

Tunable LDs are desirable for use in WDM communications, multi-wavelength optical data storage, sensing systems, and a variety of scientific

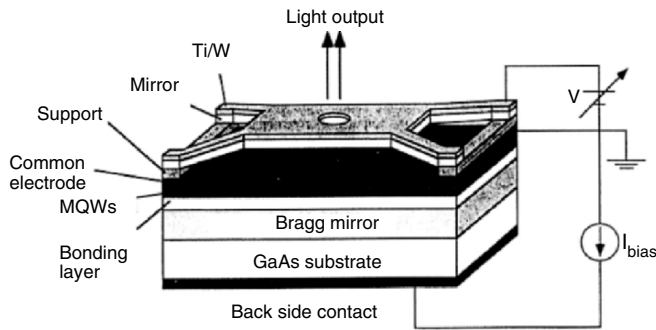


Fig. 1.27. A surface-emitting laser diode with a thin film mirror. A laser driver supplies current for light emission, and the bias applied moves the thin film mirror in the adjustment of the output wavelength [1.16]

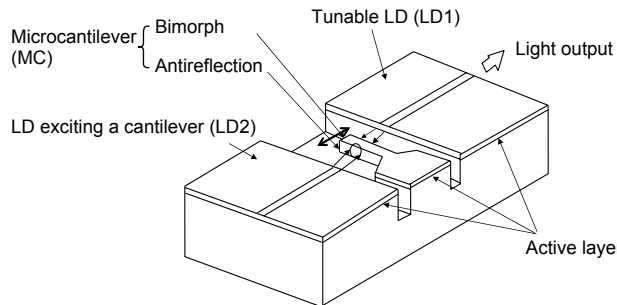


Fig. 1.28. Edge-emitting laser diodes (LDs) with a microcantilever (MC). The microcantilever is driven photothermally by one laser diode (LD2) to adjust the output wavelength from the other laser diode (LD1)

instrumentations. A surface-emitting LD or an LED with microstructure, as shown in Fig. 1.27, can be used for micromechanically tuned devices [1.16]. By varying the external cavity length, the laser wavelength can be easily changed.

Edge-emitting LDs that have an extremely short-external-cavity length are also applicable as tunable LDs [1.67], as shown in Fig. 1.28. The wavelength shift varies every $\lambda/2$. The tuning span was 30 nm around 1,300 nm, which was measured using an LD on a slider with an antireflection coating [1.71] on the LD facet facing the external mirror. To increase the monolithically integrated cantilever displacement driven by the temperature rise induced upon applying the LD, an antireflection-coated metal-dielectric bimorph structure was designed [1.72].

1.4.2 Resonant Sensor

A resonant sensor is a device that changes its mechanical resonant frequency as a function of a physical or chemical parameter such as stress or massloading.

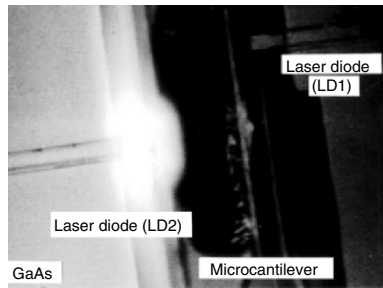


Fig. 1.29. Photograph of central part of a resonant sensor

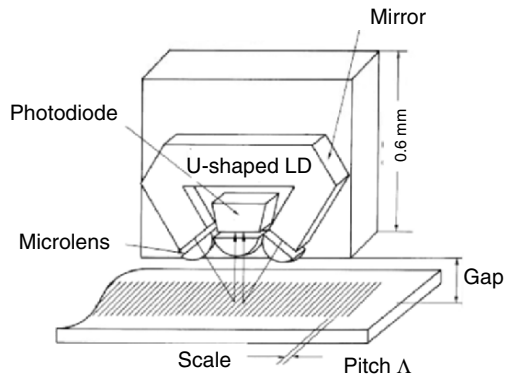


Fig. 1.30. Schematic drawing of an optical encoder consisting of a photodiode (PD), a U-shaped laser diode (LD), and microlenses [1.68]

A microcantilever (MC), LD, and a photodiode (PD) have been fabricated on the surface of a GaAs substrate, as shown in Fig. 1.29. Possible applications are resonant frequency detection sensors such as accelerometers, and mechanical filters such as those for synchronizing signal detection, which are described in Sect. 2.4.2 [1.17].

1.4.3 Optical Encoder

Elimination of bulky optical components, including a beamsplitter, a reflection mirror, a photodiode, and a collimating lens, will lead to adjustment-free, cost-effective small optical devices. An optical encoder consisting of a PD, a U-shaped LD, and microlenses, as shown in Figs. 1.30 and 1.31, was proposed. It has been evaluated to measure the relative displacement between a scale grating and the encoder itself with a resolution of $0.01 \mu\text{m}$ [1.68].

When the encoder moves a distance x relative to the grating, the phase shift of the light refracted at the grating of pitch Λ is $+2\pi x/\Lambda$ for one etched

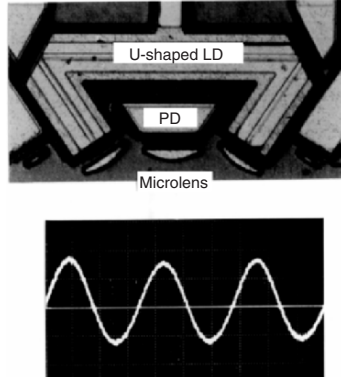


Fig. 1.31. Photograph of the optical encoder. Courtesy of R. Sawada, NTT, Japan

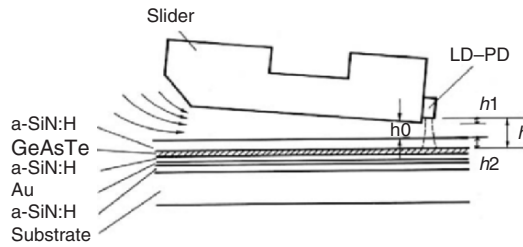


Fig. 1.32. A flying optical head with a laser diode. The optical head consists of a monolithically integrated laser diode (LD) and a photodiode (PD) attached to the slider

mirror and $-2\pi x/\Lambda$ for the other etched mirror. The intensity of interference caused by the refracted lights is expressed as a function of period $4\pi x/\Lambda$.

1.4.4 Integrated Flying Optical Head

Figure 1.32 shows a flying optical head with an integrated LD [1.69]. The flying optical head consists of a monolithically integrated LD and a PD attached to the slider. Autofocusing is accomplished by means of an air bearing, which maintains a spacing of $2\mu\text{m}$ and eliminates the need for a focusing servo system.

The sensing part of the head is an LD integrated with a PD, as shown in Fig. 1.33. To reduce the light beam width parallel to the junction plane, a taper-ridged waveguide was fabricated on the edge of the diode cavity by reactive ion beam etching (RIBE). The ridged waveguide is $1.3\mu\text{m}$ wide and the groove is $3\mu\text{m}$ deep, which is deeper than the active layer. The full widths half-maximum (FWHM) of the near-field pattern perpendicular and parallel to the junction plane are 0.65 and $0.85\mu\text{m}$, respectively, at the facet.

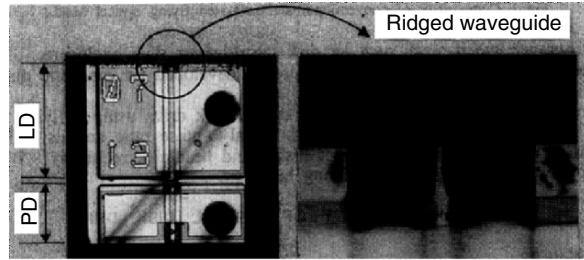


Fig. 1.33. Photograph of a laser diode (LD) integrated with a photodiode (PD). To reduce the beam width parallel to the junction plane, a taper-ridged waveguide is fabricated on the edge of the diode cavity by reactive ion beam etching (RIBE)

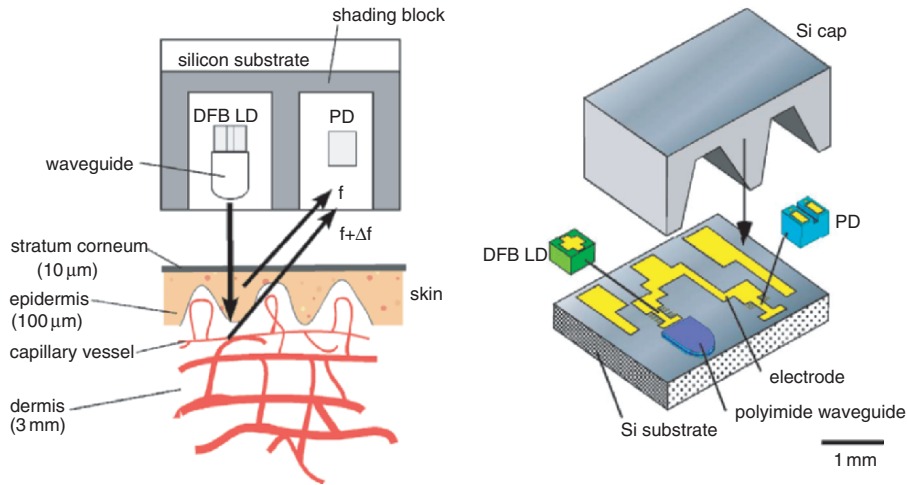


Fig. 1.34. The hybrid integrated structure of the blood flow sensor consists of an InGaAsP-InP distributed feedback laser diode (DFB-LD), a photodiode (PD) and a polyimide waveguide on a silicon (Si) substrate [1.70]. Courtesy of E. Higurashi, NTT, Japan

An LD used in an optical head forms a composite cavity with a recording medium. Light output of the LD is either a strong stimulated emission corresponding to the high-reflectivity part of the nonmark or a weak spontaneous emission corresponding to the low-reflectivity part of the mark. That is, the laser is switched according to the light fed back from the recording medium.

1.4.5 Blood Flow Sensor

A very small and lightweight blood flow sensor was constructed using surface mounting techniques, as shown in Fig. 1.34 [1.70]. The hybrid integrated structure of the optical system incorporates an edge-emitting InGaAsP-InP

distributed feedback laser diode (DFB LD) with a wavelength of $1.3\text{ }\mu\text{m}$, a photodiode (PD) and a polyimide waveguide on a silicon substrate.

Figure 1.34a shows the velocity measurement principle. The DFB LD in Fig. 1.34b illuminates the human skin and the lights scattered by the flowing blood and by the stationary tissue interfere on the PD. The beat frequency between the two depends on the average velocity of the blood flow. This integrated flow sensor can be positioned directly on a finger and permits real-time monitoring of the blood flow.

1.5 Future Outlook of Optical MEMS and Micromechanical Photonics

One advantage of the optical method in microdevices is that it is not affected by electromagnetic interference. This is particularly critical for highly integrated devices. Other advantages are its remote control and friction-free characteristics, which are of great value in optical tweezers and optical rotors. An earlier disadvantage was that the optical technique required lenses and fiber systems to guide the light to a PD or a moving mechanism, but recent micromachining technology has made it easy to eliminate these lenses and fiber systems, leading to the easy integration of optics, mechanics and electronics. In this section we present current and potential applications of the optical MEMS and micromechanical photonics.

Various kinds of optical MEMS/micromechanical photonics devices have been fabricated on Si substrates, polymers, and III–V compounds. They include a micrograting/micromirror with a rotating stage for optical interconnects, a micromirror scanner for displays and printers, a micromirror switch/tunable LD for wavelength division multiplexing (WDM) systems, information and communication apparatus, and sophisticated positioning systems at submicrometer and nanometer levels. Other applications may be in medical instruments such as micropumps for disposable drug delivery systems [1.52], medical microsystems for minimally invasive diagnosis and treatment [1.53] and μ -TAS [1.48].

Researchers have been using various types of controlling/driving methods: for example, optical, electrostatic, electromagnetic, and piezoelectric methods, as shown in Table 1.2. Optical force is classified into optical pressure, photoelectric, photothermal, and photo-electrochemical effects. Table 1.2 shows already proposed or commercialized optical MEMS/micromechanical photonics devices and systems classified according to the driving method and materials used. Refer to the fabrication method and reference number given after each device/system. In the table, we can see not only conventional sensors and actuators but also the recently developed tunable LDs, optical switches, scanners, mirrors, optical heads, near-field probes, control devices with nanometer precision, and medical microsystems [1.73] for diagnosis and treatment.

Table 1.2. Optical micro-electromechanical systems (optical MEMS) and micromechanical photonics devices. Waveguides and optoelectronics devices without mechanical structures are not shown

kinds of force	silicon	dielectric, quartz	polymer, polyimide, resin	metal	III-V compound (GaAs, InP)	others
optical						
optical pressure		rotor, M (1.62)	rotor, P (1.63)	near field probe, (1.19)		
			rotor, P (1.64)			
			rotor, P (1.65)			
			mixer, M (1.50, 1.66)			
photoelectric		solar cell, M (1.57, 1.58)	encoder, I (1.68)			
		near field probe, M (1.74)	blood flow sensor, I (1.70)			
photothermal		gripper, P (1.54)	switch, M (1.55)	tunable LD, I (1.67)		
				resonator, I (1.17)		
				optical head, I (1.69)		
photoelectrochemical				battery, O (1.56)		

Table 1.2. Continued

kinds of force							
electrostatic	silicon	dielectric, quartz	polymer, polyimide, resin	metal	III-V compound (GaAs, InP)	others	
	slider, M (1.8)	antenna, M (1.35)	pump, M (1.12)	DMD, M (1.5)	tunable LD, I (1.16)		
	optical head, I (1.20)			mirror, M	tunable PD, I (1.15)		
	bow-tie probe, M (1.46)						
	switch, M (1.6, 1.7)						
	switch, M (1.40)						
	focal length control						
	mirror, M (1.75)						
	shutter, M (1.76)						
	XYZ stage, M (1.38)						
	micro-pump, M (1.52)						
	diagnosis probe, M (1.53)						
electromagnetic	scanner, M (1.33)			tunable filter, L (1.25)			
piezoelectric	nano-tracking, M (1.9)						
	variable focal length						
	lens, M (1.77)						
	others			microchannels, M (1.49) μ -TAS, M (1.48)			

M: micromachining including lithography, etching, sputtering and deposition P: photoforming, L: LIGA,

I: monolithic integration of a laser diode, O: Others

The reduction of friction force and the adoption of contact sticking-free mechanisms are important in microscale operation. Therefore, microstructures without contact, for example, a micromirror suspended by two torsion hinges [1.5], a cantilever [1.17], a deformable membrane [1.16], and a flying slider [1.69] are preferably used to prevent friction and sticking.

Figure 1.35 shows the direction of development in these technical fields. The horizontal axis shows miniaturization (size) and the vertical axis shows the number of functions that characterize the optical MEMS/micromechanical photonics devices. To evaluate the number of functions, we first considered how optics, mechanics, and electronics are combined (1) simple assembly, (2) hybrid, and (3) monolithic. Second, in how many directions can the device/system move (1) 1D, (2) 2D, and (3) 3D. Finally, what kind of functions does the device/system have: measurement, feedback control, recognition, and remote power supply. We gave a point for each function. The maximum number of points becomes $3 + 3 + 5 = 11$. Many kinds of proposed optical MEMS and micromechanical photonics devices are seen, and the fabrication of molecular devices is the final goal in the figure.

It is apparent from the figure that there are two development directions owing to miniaturization. First, as the device/system size decreases, the number of functions decreases, for example, from an MDF (exchanger: main distributing frame) to an optical disk system to optical interconnection to an actuator and to a sensor. It is a natural direction and has led to the commercialization of many products (white circles), as seen in the figure. Second, as the device/system size decreases the number of functions increases, for example, from a sensor to an optical resonator to an electrostatic motor to an optical motor and to a molecular device. It is an ideal and a research-oriented

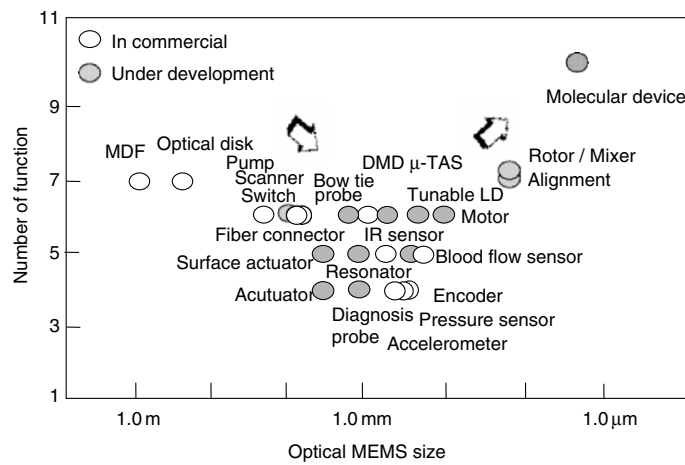


Fig. 1.35. Proposed and commercialized devices/systems fabricated using optical MEMS and micromechanical photonics. The horizontal axis is device/system size and the vertical axis is the number of functions

direction, in which many devices are under development (black circles), as seen in the same figure.

Much work is needed to reach the final goal. Good mechanical properties, high speed, and strong power are foreseen for microdevices. Microassembly, packing, and wiring techniques must be improved. Tribology on the microscale must be studied to realize smooth motion.

In the following chapters, we highlight key technologies in the development of future optical MEMS/micromechanical photonics devices and describe not only theoretical and experimental results but also their fields of application. Chap. 2 deals with LD closely aligned with a microstructure such as a diaphragm, a microcantilever and a slider. As examples, we examine extremely short-external-cavity LDs such as a tunable LD, a resonant sensor and an integrated optical head. Chap. 3 addresses optical tweezers. The new technology is employed to manipulate various types of objects in a variety of research and industrial fields. Chap. 4 deals with the design and fabrication of an optical rotor and the evaluation of the mixing performance of microliquids for a future fluidic applications such as μ -TAS. In Chap. 5, the fundamentals and applications of the near field induced on an object surface are described for the future development of micromechanical photonics. This technology enables us to carry out observing, reading/writing, and fabrication beyond the wavelength resolution by accessing and controlling the near field.

Problems

- 1.1.** Compare the methods of fabricating optical MEMS/micromechanical photonics devices.
- 1.2.** Explain the working mechanism of a sacrificed layer in the fabrication of microdevices.
- 1.3.** Explain the problems to be solved for a miniaturized device.
- 1.4.** Estimate the reduction of torque required to tilt a micromirror with a 50% reduction of the dimensions (the mirror is $a \times b$ in area and t thick).
- 1.5.** Why does response time become fast in a microsystem?
- 1.6.** Compare the methods of driving micromechanical photonics devices.
- 1.7.** Predict the future technical trend of micromechanical photonics.

Extremely Short-External-Cavity Laser Diode

In this chapter, we deal with laser diodes closely aligned with a microstructure including a diaphragm, a cantilever and a slider. New functional and sophisticated microdevices are given by closely aligning or integrating the microstructure with a laser diode, which does not require a lens system.

2.1 Background

Extremely short-external-cavity laser diodes (ESEC LDs) have been demonstrated for monitoring reflectivity [2.1] and displacement [2.2]. Tunable LD [2.3] are also demonstrated with an ESEC configuration. ESEC LDs include desirable properties for optical communication, optical data storage, spectroscopy, and a variety of sensing and measurement systems.

A surface-emitting LD with a micromechanical reflector has been used for tuned devices [2.4–2.6]. The structure is designed to have an air-gap of approximately one wavelength. When a voltage is applied to the membrane reflector, the electrostatic force reduces the air-gap, which changes the wavelength. An edge-emitting laser diode is also applicable for the micromechanically tunable laser [2.7,2.8]. By varying the external cavity length, the laser wavelength can be easily changed. However, to date the experimental data of the ESEC LD under various coupled conditions have been poor.

Some studies have reported special considerations for such a short-external-cavity LD based on butt coupling into an optical fiber [2.9]. In a short-external-cavity LD system, the feedback light must return to an approximately 1- μm diameter LD aperture, although it is difficult in practice to align the light beam with such micrometer-level accuracy, and it is more difficult to maintain this accuracy for a long period against external environmental perturbations [2.10]. One possible solution is automatic alignment using an air bearing slider which has the same flying mechanism as that of a magnetic hard disk drive (HDD).

In this chapter, we deal with LDs closely aligned with a microstructure including a diaphragm, a cantilever and a slider. By closely aligning or integrating the microstructure with an LD, which does not require a lens system, new functional and sophisticated microdevices can be developed.

In the following, we analyze the ESEC LD by introducing the effective reflectivity of the laser facet facing the external mirror. Then a measurement method that uses an LD attached to a flying slider and a semitransparent rotating disk mirror for an extremely short-external-cavity configuration is presented. Then as practical applications, a tunable LD, a resonant sensor, an integrated optically switched laser head are introduced from the viewpoint of their composition, principle, basic characteristics, and fabrication methods.

2.2 Theoretical Analysis

The lasing behavior for an ESEC LD with a feedback light has not yet been clarified because of the complexity of the many parameters involved [2.9, 2.11]. In this section, we analyze the composite resonant phenomena under the strong light feedback. We first analyze a solitary LD and then an ESEC LD by introducing the effective reflectivity facet facing the external mirror.

2.2.1 Lasing Condition of a Solitary LD

A laser diode (LD) consists of an active region of (n, β, g, α) and two mirrors with the reflectivities R_1 and R_2 separated at the length of L as shown in Fig. 2.1, where n is the refractive index, β is the propagation constant, g is the gain and α is the extinction coefficient. The active region with a pn junction semiconductor is in the state of population inversion in the energy levels. Among the photons emitted spontaneously in all directions, only the photons traveling along the axis of the resonator (incident to the mirrors

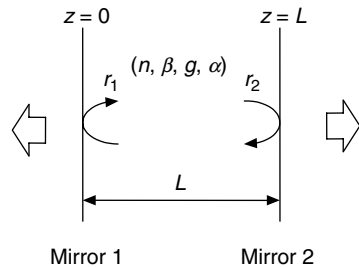


Fig. 2.1. A laser diode (LD) consists of an active region of (n, β, g, α) and two mirrors with reflectivities of R_1 and R_2 separated at the length of L , where n is the refractive index, β is the propagation constant, g is the gain and α is the extinction coefficient

vertically) are amplified per pass by

$$e^{2gL} \quad (2.1)$$

but they are decayed per pass by

$$e^{-2\alpha L} R_1 R_2. \quad (2.2)$$

The lasing condition is that the product of (2.1) and (2.2) is larger than 1, namely

$$e^{2gL} e^{-2\alpha L} R_1 R_2 \geq 1. \quad (2.3)$$

Therefore, the lasing threshold gain g_{th} is expressed as

$$g_{\text{th}} = \alpha + \frac{1}{2L} \ln \frac{1}{R_1 R_2}, \quad (2.4)$$

where $\alpha = 10 \text{ cm}^{-1}$, $L = 300 \mu\text{m}$, $R_1 = R_2 = 0.32$, then $g_{\text{th}} \geq 49 \text{ cm}^{-1}$

The light travels in the active region infinitesimally to establish a high value of radiation density. The lasing light in the resonator generates the standing wave fields. Since the integral multiple m of the half-wavelength equals the cavity length L

$$\frac{\lambda}{2n} m = L. \quad (2.5)$$

When $\lambda = 1.3 \mu\text{m}$, $n = 3.5$ and $L = 300 \mu\text{m}$, the integer m equals 1615. The wavelength difference $\Delta\lambda$ when m increases by 1 becomes

$$\Delta\lambda = -\frac{\lambda^2}{2n_{\text{eff}} L}, \quad (2.6)$$

where n_{eff} is the effective refractive index of the LD. In terms of wave numbers, the frequencies are separated by an interval of $1/\Delta\lambda$. The calculated mode interval of $\Delta\lambda$ equals 0.76 nm for $\lambda = 1.3 \mu\text{m}$, $n_{\text{eff}} = 3.7$, and $L = 300 \mu\text{m}$. The lasing-mode shift corresponds to the integral multiple of $\Delta\lambda$.

Example 2.1. Derive the mode interval $\Delta\lambda = -\frac{\lambda^2}{2n_{\text{eff}} L}$ from $\frac{\lambda}{2n} m = L$, where λ is the wavelength, n_{eff} is the effective refractive index, m is the integer, and L is the cavity length of the LD.

Solution. Assuming that refractive index n does not dependent on λ , (2.5) becomes

$$\lambda = \frac{2nL}{m}. \quad (\text{E2.1})$$

When m increases by 1, the wavelength becomes

$$\lambda + \Delta\lambda = \frac{2n}{m+1} L. \quad (\text{E2.2})$$

From (E2.1) and (E2.2), $\Delta\lambda$ is given as

$$\Delta\lambda = 2nL \left(\frac{1}{m+1} - \frac{1}{m} \right) \cong 2nL \left(-\frac{1}{m^2} \right) = -\frac{\lambda^2}{2nL}. \quad (\text{E2.3})$$

The mode interval is the absolute value of (E2.3). The refractive index n is expressed as

$$n(\lambda) = n(\lambda_0) + \frac{\partial n(\lambda)}{\partial \lambda} \Delta\lambda. \quad (\text{E2.4})$$

Similarly,

$$\lambda_0 = \frac{2n(\lambda_0)}{m} L \quad (\text{E2.5})$$

$$\lambda_0 + \Delta\lambda = \frac{2 \left(n(\lambda_0) + \frac{\partial n(\lambda)}{\partial \lambda} \Delta\lambda \right)}{m+1} L. \quad (\text{E2.6})$$

The mode interval $\Delta\lambda$ is given as (E2.6) – (E2.5), namely

$$\Delta\lambda = 2n(\lambda_0)L \left(\frac{1}{m+1} - \frac{1}{m} \right) + \frac{2 \frac{\partial n(\lambda)}{\partial \lambda} \Delta\lambda}{m+1} L. \quad (\text{E2.7})$$

From (E2.3)

$$2n(\lambda_0)L \left(\frac{1}{m+1} - \frac{1}{m} \right) = -\frac{\lambda_0^2}{2n(\lambda_0)L}. \quad (\text{E2.8})$$

From (E2.2),

$$\frac{2L}{m+1} = \frac{\lambda_0 + \Delta\lambda}{n(\lambda_0)} \cong \frac{\lambda_0}{n(\lambda_0)}. \quad (\text{E2.9})$$

Substitute (E2.8) and (E2.9) to (E2.7),

$$\Delta\lambda = \frac{\lambda_0^2}{2n(\lambda_0) \left(1 - \frac{\lambda_0}{n(\lambda_0)} \frac{\partial n(\lambda)}{\partial \lambda} \right) L}, \quad (\text{E2.10})$$

as n_{eff} is,

$$n_{\text{eff}} = n(\lambda_0) \left(1 - \frac{\lambda_0}{n(\lambda_0)} \frac{\partial n(\lambda)}{\partial \lambda} \right). \quad (\text{E2.11})$$

Finally, the mode interval $\Delta\lambda$ can be expressed as

$$\Delta\lambda = -\frac{\lambda_0^2}{2n_{\text{eff}}L}. \quad (\text{E2.12})$$

2.2.2 Effective Reflectivity

The dependence of the lasing characteristics of an ESEC LD on external-cavity length is described using various parameters: the LD facet reflectivity

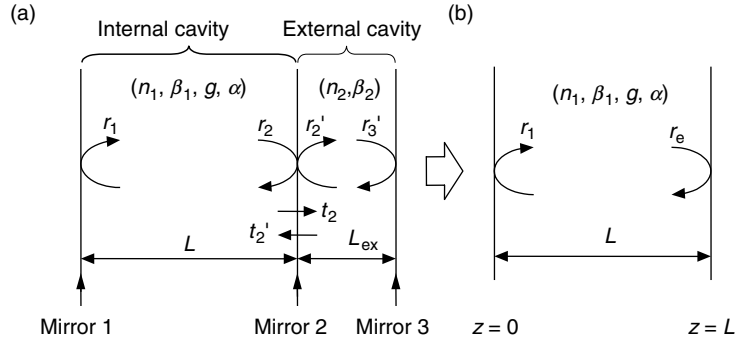


Fig. 2.2. Extremely short-external-cavity LD (ESEC LD) system which consists of the LD facet reflectivities R_1, R_2 , and the external mirror reflectivity R_3 (a), and introduced effective reflectivity R_2^{eff} instead of R_2 and R_3 (b). We can analyze the behavior of the ESEC LD by analyzing the solitary LD with a resonator composed of R_1 and R_2^{eff}

R_1 , the LD facet reflectivity R_2 facing the external mirror, the external mirror reflectivity R_3 , and the LD drive current. Figure 2.2a shows the ESEC LD system. The light emits from R_2 , reflects back at R_3 , and returns into the LD. The returned light changes the carrier density (refractive index) and the gain spectrum of the internal cavity medium of the LD, which leads to complicated behavior of the ESEC LD. To analyze this behavior more easily we introduce the effective reflectivity R_2^{eff} which has equivalent effect to the coupled R_2 and R_3 . Then we can analyze the behavior of the ESEC LD by analyzing the solitary LD composed of a resonator with R_1 and R_2^{eff} , as shown in Fig. 2.2b.

Effective reflectivity R_2^{eff} has been successfully introduced as expressed in (2.7) to assist the clarification of the lasing characteristics of the external-cavity LD

$$R_2^{\text{eff}} = r_2^{\text{eff}} r_2^{\text{eff}*} = \frac{r_2^2 + a^2 r_3^2 + 2ar_2 r_3 \cos(2\beta_2 L_{\text{ex}})}{1 + a^2 r_2^2 r_3^2 + 2ar_2 r_3 \cos(2\beta_2 L_{\text{ex}})}, \quad (2.7)$$

where n_1 is the refractive index of the internal cavity (LD medium), n_2 is that of the external cavity (air), $r_1 = \sqrt{R_1}$, $r_2 = \sqrt{R_2}$, $r'_2 = -r_2$ and $r_3 = -\sqrt{R_3}$ are the amplitude reflectivities, $\beta_i = 2\pi n_i / \lambda$ is the propagation constant, and $a (= \sqrt{\eta})$ is the amplitude coupling coefficient for the external-cavity-length L_{ex} .

Example 2.2. Derive the effective reflectivity R_2^{eff} in (2.7).

Solution 2.1. The light emits from R_2 , reflects back at R_3 , returns to R_2 , and then reflects at R_2 , which leads to multiple reflection in the external cavity. The returned light amplitude E_k after k time reflection is given,

$$E_k = E_0 t_2 t'_3 r_2^k r_3^{k-1} a^k \exp(-j2k\beta_2 L_{\text{ex}}), \quad (\text{E2.13})$$

where E_0 is the incident light amplitude and L_{ex} is the external cavity length. The total returned light E_{total} is the sum of (E2.13) and is given as

$$E_{\text{total}} = E_0 r_2 + \sum_{k=1}^{\infty} E_k = E_0 \left\{ r_2 + \frac{t_2 t'_2}{r'_2} \sum_{k=1}^{\infty} a^k (r_3 r'_2 \exp[-j2\beta_2 L_{\text{ex}}])^k \right\}. \quad (\text{E2.14})$$

As $t_2 t'_2 = 1 - r_2^2$, and $r'_2 = -r_2$ the effective amplitude reflectivity r_2^{eff} ($= E_{\text{total}}/E_0$) is given as

$$\begin{aligned} r_2^{\text{eff}} &= r_2 + \frac{t_2 t'_2 a r_3 \exp(-j2\beta_2 L_{\text{ex}})}{1 - a r_3 r'_2 \exp(-j2\beta_2 L_{\text{ex}})} \\ &= \frac{r_2 + a r_3 \exp(-j2\beta_2 L_{\text{ex}})}{1 + a r_2 r_3 \exp(-j2\beta_2 L_{\text{ex}})} \equiv \sqrt{R_2^{\text{eff}}} \exp(j\Delta_e). \end{aligned} \quad (\text{E2.15})$$

Then the effective intensity reflectivity R_2^{eff} and the phase Δ_e are given as the following equations:

$$R_2^{\text{eff}} = r_2^{\text{eff}} r_2^{\text{eff}*} = \frac{r_2^2 + a^2 r_3^2 + 2 a r_2 r_3 \cos(2\beta_2 L_{\text{ex}})}{1 + a^2 r_2^2 r_3^2 + 2 a r_2 r_3 \cos(2\beta_2 L_{\text{ex}})}, \quad (\text{E2.16})$$

$$\Delta_e = \tan^{-1} \left(\frac{\Im[r_e]}{\Re[r_e]} \right) = \tan^{-1} \left(\frac{a r_3 (r_2^2 - 1) \sin(2\beta_2 L_{\text{ex}})}{r_2 + a^2 r_2 r_3 + a r_3 (r_2^2 + 1) \cos(2\beta_2 L_{\text{ex}})} \right). \quad (\text{E2.17})$$

Example 2.3. Derive the coupling coefficient η which is defined by (2.8) as the ratio of the feedback light power E_z^2 to the original emitted light power E_0^2 , where the Gaussian beam waists ($1/e^2$) at the LD facet are w_{x0} and w_{y0} , and $z = 2L_{\text{ex}}$.

$$\begin{aligned} \eta &\equiv \frac{\left| \int \int_{-\infty}^{\infty} E_z E_0 dx dy \right|^2}{\int \int_{-\infty}^{\infty} |E_z|^2 dx dy \int \int_{-\infty}^{\infty} |E_0|^2 dx dy} \\ &= \frac{4 \sqrt{\left\{ 1 + \left(\frac{\lambda z}{\pi w_{x0}^2} \right)^2 \right\} \left\{ 1 + \left(\frac{\lambda z}{\pi w_{y0}^2} \right)^2 \right\}}}{\left\{ 2 + \left(\frac{\lambda z}{\pi w_{x0}^2} \right)^2 \right\} \left\{ 2 + \left(\frac{\lambda z}{\pi w_{y0}^2} \right)^2 \right\}}. \end{aligned} \quad (2.8)$$

Solution 2.2. The light in the Gaussian form of (E2.18) travels in the z direction in the form of (E2.19), where the beam waists at the LD facet are w_{x0} and w_{y0} , and C_0 and C_z are the constants, respectively.

$$E_0 = C_0 \exp \left[-\frac{x^2}{w_{x0}^2} \right] \exp \left[-\frac{y^2}{w_{y0}^2} \right], \quad (\text{E2.18})$$

$$E_z = C_z \exp \left[-\frac{x^2}{w_x^2(z)} \right] \exp \left[-\frac{y^2}{w_y^2(z)} \right]. \quad (\text{E2.19})$$

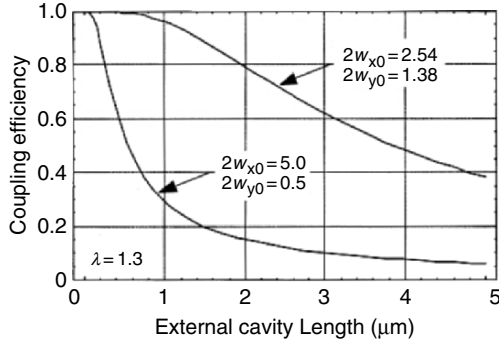


Fig. 2.3. Dependence of coupling efficiency η on external-cavity-length L_{ex}

The beam profile $w_x(z)$ and $w_y(z)$ are given as

$$w_x(z) = w_{x0} \sqrt{1 + \left(\frac{\lambda z}{\pi w_{x0}^2}\right)^2}, \quad w_y(z) = w_{y0} \sqrt{1 + \left(\frac{\lambda z}{\pi w_{y0}^2}\right)^2}. \quad (\text{E2.20})$$

Then the intensity coupling efficiency η becomes that expressed by (2.8).

2.2.3 Light Output

Figure 2.3 shows the dependence of coupling efficiency η on external-cavity-length L_{ex} . The beam waists are (1) $2w_{x0} = 2.54 \mu\text{m}$, $2w_{y0} = 1.38 \mu\text{m}$ and (2) $2w_{x0} = 5.0 \mu\text{m}$, $2w_{y0} = 0.5 \mu\text{m}$. Beam waist (1) corresponds to the light divergent angles of 10° in the x direction and 25° in the y direction which are typical for commercially available LDs. In the figure, we show the coupling efficiency of 50% at the external length of $3.5 \mu\text{m}$ for the LD with beam waist (1) which is used in the experiment presented in Sect. 2.2.4.

For a typical LD, the dependence of R_2^{eff} on L_{ex} is calculated using (2.7) and (2.8), and is shown in Fig. 2.4 for $R_1 = 0.32$ and $R_2 = 0.01$, with R_3 as a parameter. It is clear from the figure that R_2^{eff} changes every half-wavelength ($\lambda/2$) and decreases as L_{ex} increases. The light output and the wavelength of the ESEC LD vary as R_2^{eff} changes according to L_{ex} .

2.2.4 Wavelength

The wavelength of the ESEC LD can be determined by the lasing conditions of a solitary LD composed of two mirrors with the amplitude reflectivity r_1 and r_2^{eff} . A light emitted from the left mirror at $z = 0$ travels along the z -axis and is given by

$$E(z, t) = E_0 \exp [j(\omega t - \beta_1 z)] \quad (2.9)$$

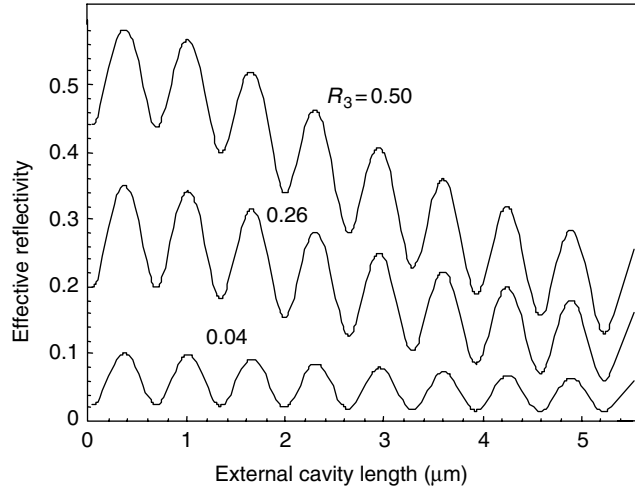


Fig. 2.4. Dependence of effective reflectivity R_2^{eff} on external-cavity-length L_{ex}

The light amplitude after a round trip is given as

$$E(2L, t) = r_1 r_2^{\text{eff}} E_0 \exp [j(\omega t - 2\beta_1 L)] \quad (2.10)$$

The lasing condition is that the amplitude corresponds to the original amplitude, $E(0, t) = E_0 \exp(j\omega t)$, namely

$$r_1 r_2^{\text{eff}} \exp(-j2\beta_1 L) = 1 \quad (2.11)$$

Equation (2.11) is rewritten using the effective intensity reflectivity and its phase using the composite propagation constant $\beta_1 = \beta_0 + jG/2$ (β_0 is the real part of Derive the couplingco efficient β_1 , G is the gain of the medium).

$$\sqrt{R_1 R_2^{\text{eff}}} \exp(GL) \exp[-j(2\beta_0 L - \Delta_e)] = 1. \quad (2.12)$$

Representing the real part and the imaginary part independently, the lasing conditions are given as follows:

$$\sqrt{R_1 R_2^{\text{eff}}} \exp(GL) = 1, \quad (2.13)$$

$$\cos[2\beta_0 L - \Delta_e] = 1, \quad (2.14)$$

$$\sin[2\beta_0 L - \Delta_e] = 0. \quad (2.15)$$

Substituting $G = \frac{1}{2L} \ln \frac{1}{R_1 R_2}$ (2.4), R_2^{eff} (E2.16) and Δ_e (E2.17), the ESEC LD lasing condition appears.

Mode Dependence

Figure 2.5 shows a model of the lasing frequency of the ESEC LD. Lasing occurs at frequency f when the internal mode frequency f_{m1} coincides with the external mode frequency f_{m2} in the gain spectrum curve, that is,

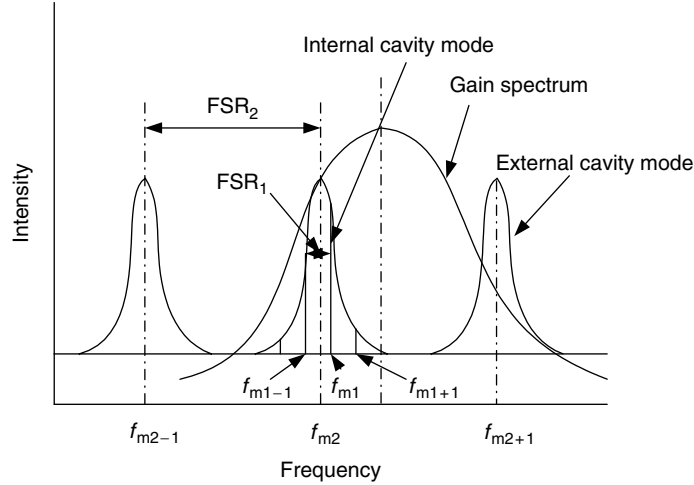


Fig. 2.5. Model of lasing frequency of the ESEC LD. Lasing occurs at the frequency f when the internal mode frequency f_{m1} coincides with the external mode frequency f_{m2} in the gain spectrum curve

$$f = f_{m1} = \frac{c}{2n_0 L} m_1 \quad (m_1 = 1, 2, \dots), \quad (2.16)$$

$$f = f_{m2} = \frac{c}{2L_{\text{ex}}} m_2, \quad (m_2 = 1, 2, \dots). \quad (2.17)$$

The free spectral ranges FSR (intervals between frequency modes) for the internal mode and the external mode are, respectively, given by (n_0 is the real part of n_1),

$$\text{FSR}_1 = f_{m1+1} - f_{m1} = \frac{c}{2n_0 L}, \quad (2.18)$$

$$\text{FSR}_2 = f_{m2+1} - f_{m2} = \frac{c}{2L_{\text{ex}}}. \quad (2.19)$$

In the case of the ESEC LD, the external FSR₂ expands due to the short L_{ex} , with the result that only one external mode exists in the gain spectrum curve. In terms of wavelength, they are expressed as

$$\lambda_{m1} = \frac{2n_0 L}{m}, \quad \Delta\lambda_1 = \frac{\lambda_{m1}^2}{2n_0 L}, \quad (2.20)$$

$$\lambda_{m2} = \frac{2L_{\text{ex}}}{m}, \quad \Delta\lambda_2 = \frac{\lambda_{m2}^2}{2L_{\text{ex}}}. \quad (2.21)$$

From (2.16) and (2.17),

$$m_1 = \frac{n_0 L}{L_{\text{ex}}} m_2 \quad (m_2 = 1, 2, \dots). \quad (2.22)$$

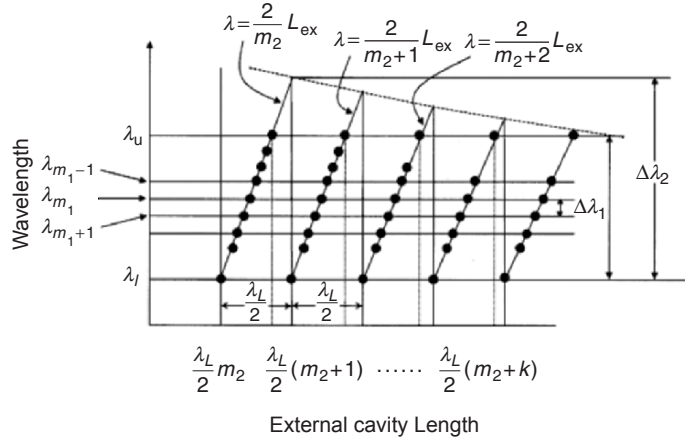


Fig. 2.6. Relationship between the wavelength and the external cavity length. The λ_u and λ_l on the vertical axis show the gain spectrum range and the $\lambda_L/2$ on the horizontal axis shows the half-wavelength interval

The wavelength variation ratio $\delta\lambda_{m2}$ due to L_{ex} for the mode number m_2 is expressed from (2.21) as

$$\delta\lambda_{m2} = \frac{2}{m_2} = \frac{\lambda_{m2}}{L_{\text{ex}}} \delta L_{\text{ex}}. \quad (2.23)$$

Figure 2.6 shows the relationship between the wavelength and the cavity length. Notations λ_u and λ_l on the vertical axis show the upper and lower gains (gain spectrum range) and $\lambda_L/2$ on the horizontal axis shows the half-wavelength interval. The internal cavity mode m_1 does not depend on L_{ex} . The external cavity mode m_2 is shown as the lines of the gradient $2/m_2$. The intersections between the two modes indicate the lasing wavelengths. As a result, the internal cavity mode wavelength in the gain spectrum (λ_u, λ_l) is lased discontinuously at the $\lambda_L/2$ period according to the L_{ex} change.

Carrier Density Dependence

The carrier density N in the semiconductor is changed due to the returned light, which leads to variation in the refractive index and the gain spectrum. As a result the wavelength changes with the variation of the external-cavity-length L_{ex} .

The peak wavelength λ_G giving the maximum gain spectrum decreases linearly as N increases and its variation ratio is given by [2.12]

$$\frac{\partial\lambda}{\partial N} \approx -6 \times 10^{-24} \text{ (cm}^4\text{)}. \quad (2.24)$$

The refractive index variation ratio $\partial n/\partial N$ as affected by the carrier density is given on the basis of a consideration of $\lambda = 2L/m$ and $L = nL_0$,

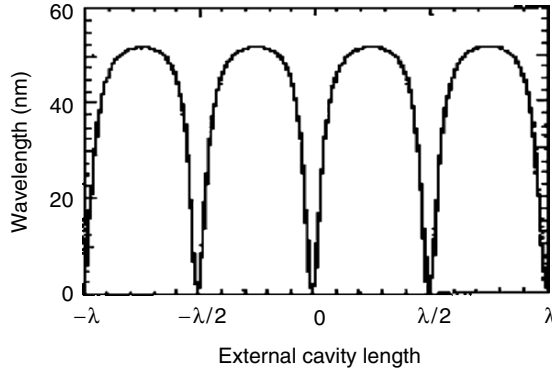


Fig. 2.7. Wavelength variation due to the external cavity length. Total wavelength tuning depends on effects of both mode change and carrier density change

$$\frac{\partial \lambda}{\partial N} = \frac{\partial \lambda}{\partial L} \frac{\partial L}{\partial n} \frac{\partial n}{\partial N} = \left(\frac{2}{m} \right) L_0 \left(\frac{\partial n}{\partial N} \right) = \frac{\lambda}{n} \left(\frac{\partial n}{\partial N} \right). \quad (2.25)$$

The value $\partial \lambda / \partial N$ of (2.25) based on the carrier density variation is about one to tenth to that of (2.24) based on the spectrum peak shift. The wavelength variation $\partial \lambda / \partial L_{\text{ex}}$ is given as follows:

$$\frac{\partial \lambda}{\partial L_{\text{ex}}} = \frac{\partial \lambda}{\partial N} \frac{\partial N}{\partial L_{\text{ex}}} = \frac{\partial \lambda}{\partial N} \frac{\partial N}{\partial R_2^{\text{eff}}} \frac{\partial R_2^{\text{eff}}}{\partial L_{\text{ex}}} \propto \frac{1}{R_2^{\text{eff}}} \frac{\partial R_2^{\text{eff}}}{\partial L_{\text{ex}}}. \quad (2.26)$$

Equation (2.26) shows that $\partial \lambda / \partial L_{\text{ex}}$ is inversely proportional to R_2^{eff} and is proportional to the effective reflectivity variation $\partial R_2^{\text{eff}} / \partial L_{\text{ex}}$. Figure 2.7 shows an example of the wavelength variation dependence on the external cavity length. Of course, the total wavelength change due to the external cavity length depends on the effects of both the mode change and the carrier density change.

In summary, to analyze the wavelength of the ESEC LD, it is necessary to know the effective reflectivity, carrier density variation, and the gain spectrum variation due to the light returned from the external mirror. Furthermore, the wavelength depends on the temperature and the drive current. These factors have not yet been fully analyzed theoretically. In the next section we will describe the experimental analysis of the ESEC LD.

2.3 Experimental Analysis

In this section a measurement method that uses an LD attached to a flying slider and a semitransparent rotating disk mirror for an ESEC configuration is presented. Not only the wavelength, but also the spectrum and the light output are measured at room temperature, with the external-cavity-length

L_{ex} , the reflectivities of the LD facets and external mirror, and the drive current as parameters. As a result, wavelength tuning as great as 30 nm by varying the external-cavity length is confirmed for a 1.3- μm wavelength LD with an antireflection coating on the LD facet facing the external mirror.

2.3.1 Experimental Setup

Some aspects of the feedback effect for an ESEC LD configuration are measured by the following method [2.13]. An extremely short external cavity was realized when an LD on a slider flew on a semitransparent optical disk. Figure 2.8 illustrates the experimental setup (upside down in reality) for monitoring the wavelength-related behavior of an LD by means of an integrated photodiode (PD) which is mounted on a flying slider. The InGaAsP/InP LD is isolated from the PD by reactive ion beam etching. The cavity length of the LD is 300 μm and the space between the LD and the PD is 5 μm . The monitor current sensitivity is 0.1 mA/mW.

Automatic and stable alignment is accomplished by the air bearing, which maintains a spacing ranging from submicrometers up to several micrometers depending on the disk velocity. The external-cavity-length L_{ex} ($= L_{\text{ex}}^0 + L_{\text{ex}}^1$) is 2–4.5 μm long in this experiment, where L_{ex}^0 is the flying height that varies according to the square root of the disk velocity and L_{ex}^1 is an LD–PD attachment error to the slider surface.

Light transmitted through the semitransparent optical disk is directed into an optical spectrum analyzer (Anritsu, MS96A) through an optical fiber placed opposite to the LD–PD. The corresponding laser power variation is monitored with the PD integrated on the LD.

The LD coupled with an optical disk forms a composite cavity LD as shown in Fig. 2.9a. Figure 2.9b shows a photograph of the monolithically integrated LD–PD chip on a slider. Optical feedback is varied by the external cavity length (disk rotation rate), the reflectivity of the LD facet facing the optical

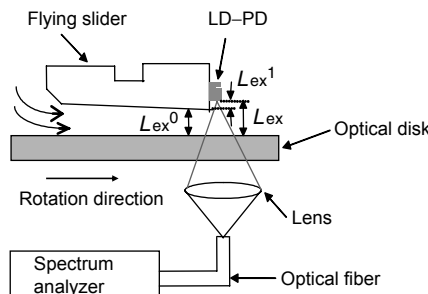


Fig. 2.8. Proposed set up for measurement of wavelength tuning based on ESEC length. An LD attached to an air-bearing slider flies by air resistance caused by disk rotation (upside down in reality)

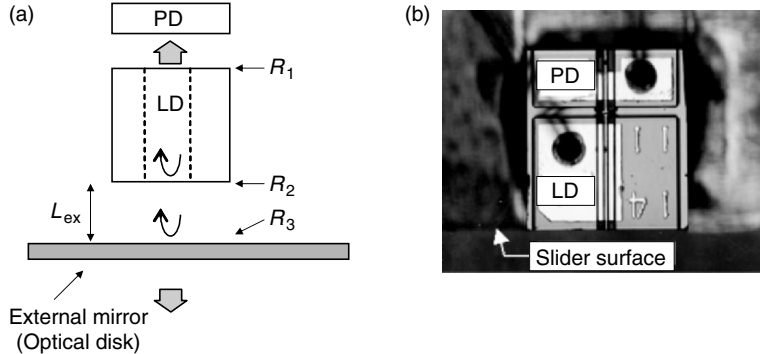


Fig. 2.9. Detailed representation of the ESEC LD system (a), and photograph of a monolithically integrated LD–PD chip on a slider (b)

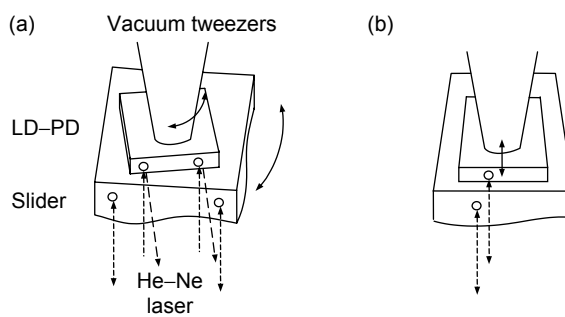


Fig. 2.10. Method of bonding an LD–PD chip on a slider. First, the LD–PD chip is pushed onto the electrode of the slider’s back end with vacuum tweezers and then rotated to align it parallel to the slider surface (a). Second, the moving stage on which the LD–PD chip is mounted is translated (b)

disk and the disk reflectivity itself. In the following, the LD facet reflectivity R_1 is 0.32 (cleaved facet), R_2 is 0.01 (antireflection coating) [2.14], and the disk reflectivities R_3 are 0.04, 0.26, and 0.50.

In order to reduce the attachment error L_{ex}^1 between the LD facet and the slider surface, an LD–PD was mounted on the slider surface by the following method. First, the LD–PD chip was pushed onto the electrode of the slider’s back end with vacuum tweezers and then rotated to align it parallel to the slider surface as shown in Fig. 2.10a. The parallelism was monitored using a He–Ne laser beam.

Second, the moving stage on which the LD–PD chip was mounted was translated, as shown in Fig. 2.10b, along the laser beam axis with an accuracy of $0.05 \mu\text{m}$ to minimize the following error signal. The attachment error was detected by a range sensor, called an optical lever, as shown in Fig. 2.11. The light output difference (focus error) between the LD–PD and the slider surface

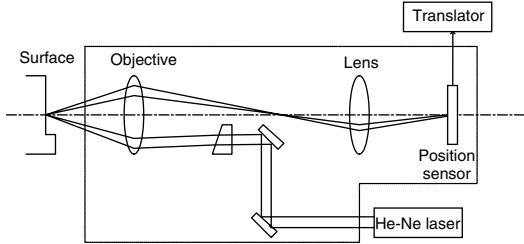


Fig. 2.11. Autofocusing geometry for investigating the attachment error L_{ex}^1 between an LD-PD facet and a slider surface

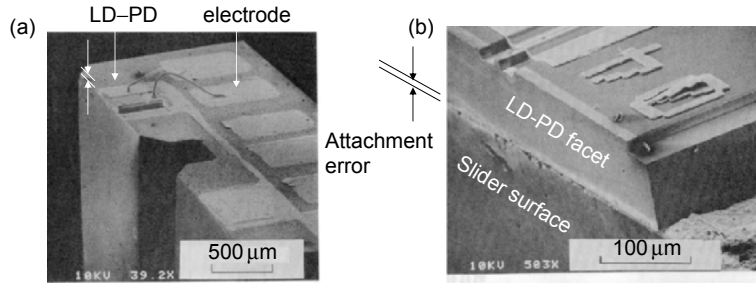


Fig. 2.12. Photograph of the back end of the slider on which an LD-PD chip is bonded to the electrode (a), and the LD-PD facet and the slider surface (b). The attachment error L_{ex}^1 is less than 1 μm . Courtesy of H. Nakata, NTT, Japan

corresponds to the attachment error, and in this experiment the attachment (displacement) error between the two surfaces was less than 1 μm .

Finally, the LD-PD chip was bonded precisely by melting a thin film solder in $\text{H}_2\text{-N}_2$ gas. Figure 2.12 shows photographs of an LD-PD bonded onto the electrode on the back end of the slider (a), and an enlarged view of the LD-PD facet and the slider surface (b).

2.3.2 Light Output

To analyze the feedback light effects specific to the ESEC LD configuration, we first measured the threshold current. The maximum light output versus drive current (I - L characteristics) with an external mirror is presented in Fig. 2.13, where $R_1 = 0.32$ and $R_2 = 0.01$. The light was detected by a PD placed at the opposite facet of the LD. The threshold current of the ESEC LD with feedback light is significantly reduced for the antireflection-coated LD ($R_2 = 0.01$). These coupled LD operations were calculated for the steady-state operation using the rate equations.

The light output versus external-cavity-length L_{ex} is shown in Fig. 2.14, with drive current I/I_{th} as a parameter. The light output coupled to the external mirror depends not only on L_{ex} , but also on the reflectivities of the

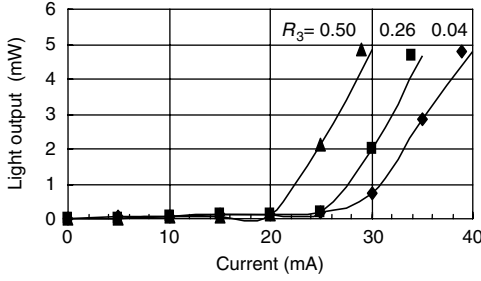


Fig. 2.13. I - L characteristics with an external mirror at the light-output maxima, with external mirror reflectivity R_3 as a parameter, where $R_1 = 0.32$ and $R_2 = 0.01$

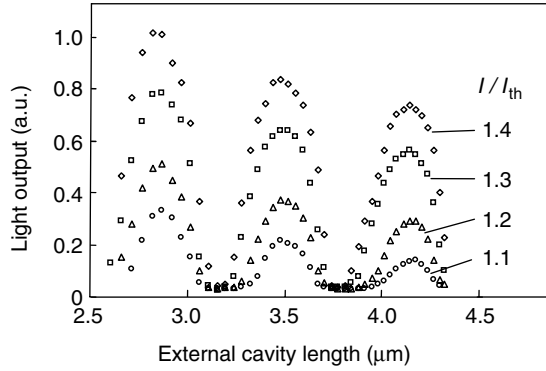


Fig. 2.14. Light output versus external-cavity-length $L_{\text{ex}} (= L_{\text{ex}}^0 + L_{\text{ex}}^1)$, drive current I/I_{th} normalized by threshold current as a parameter, where $R_1 = 0.32$, $R_2 = 0.01$, and $R_3 = 0.5$

LD facet R_1, R_2 , and that of the external mirror R_3 and varies with a period of a half-wavelength. The light output difference is defined as the difference between the successive light output maximum and the minimum in Fig. 2.14. Using the effective reflectivity R_2^{eff} , the relationship between the light output difference and R_2^{eff} , with the drive current I/I_{th} as a parameter, is shown in Fig. 2.15. The light output difference increases as R_2^{eff} increases.

2.3.3 Wavelength and Spectrum Characteristics

Wavelength tuning due to the strong light feedback is shown in Fig. 2.16 for the antireflection-coated LD where the drive current (normalized by the threshold current) $I/I_{\text{th}} = 1.8$, reflectivities $R_1 = 0.32$, $R_2 = 0.01$, and $R_3 = 0.5$. The wavelength variation exhibits an asymmetric but $\lambda/2$ periodic behavior with the external-cavity-length L_{ex} . As L_{ex} increases the wavelength increases linearly, similarly to the numbers (1)–(5), then remains similarly to the numbers (6)–(8) in every period as shown in Fig. 2.16.

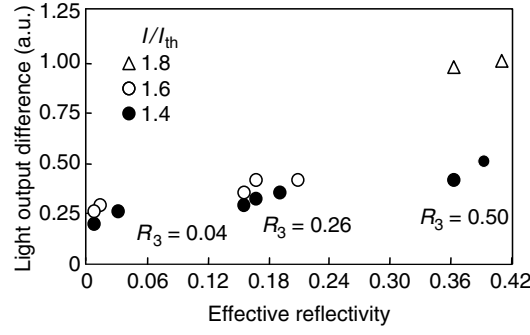


Fig. 2.15. Light output difference versus effective reflectivity, with I/I_{th} as parameters

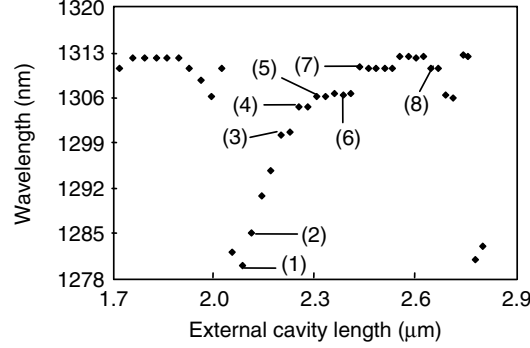


Fig. 2.16. Dependence of wavelength on external cavity length, where drive current $I/I_{\text{th}} = 1.6$, reflectivities $R_1 = 0.32$, $R_2 = 0.01$, and $R_3 = 0.5$

The spectral structure of the tuned light is shown in Fig. 2.17 corresponding to the numbers in Fig. 2.16. The former numbers (1)–(5) show that single longitudinal modes are tuned for the feedback light LD, while the latter numbers (6)–(8) show that multi modes are tuned for the feedback light LD. Considering these two types of experimental tuning results, we find that the spectrum varies from single mode to multi mode according to the external cavity length.

The separation between the longitudinal modes according to the LD's cavity length L is given by (2.6). The calculated mode interval of $\Delta\lambda$ equals 0.76 nm for $\lambda = 1,300 \text{ nm}$, $n_{\text{eff}} = 3.7$, and $L = 300 \mu\text{m}$ agrees well with the above experimentally obtained result. The span of the lasing mode shifts with the integral number times $\Delta\lambda$.

Dependence of Wavelength Variation on Effective Reflectivity

Dependence of wavelength tuning range on the effective reflectivity R_2^{eff} , with I/I_{th} as a parameter, is shown in Fig. 2.18. The wavelength tuning range is

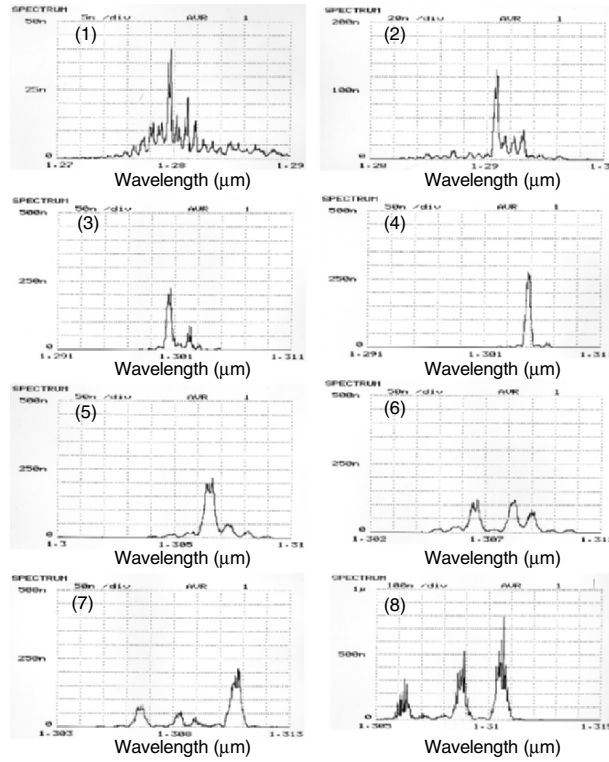


Fig. 2.17. Spectra at (1), (2), . . . , and (8) in Fig. 2.16

defined as the wavelength difference between the successive maximum and the minimum as shown in Fig. 2.16. Figure 2.18 shows that the wavelength tuning range increases as R_2^{eff} increases. The gradient of wavelength (the change of wavelength per external cavity length) also increases as R_2^{eff} increases, as shown in Fig. 2.19.

Figure 2.20 illustrates the typical spectrum structure and definitions of the side-mode suppression ratio $10 \log(a/b)$, spectrum line width (full width at half-maximum c) and mode interval (average of d, e, f, and g). Figure 2.21 shows that the tuning range increases linearly as R_2^{eff} increases. The side-mode suppression ratio increases as R_2^{eff} increases, but the spectrum line width becomes narrow as R_2^{eff} increases, as shown in Fig. 2.22.

In summary, an LD attached to a flying slider and a rotating optical disk mirror was used to measure the lasing characteristics for an ESEC LD. Not only the wavelength, but also the spectrum including the side-mode suppression ratio, the spectrum line width and the mode interval were measured precisely by controlling the slider flying height, with the reflectivities of the LD facets and external mirror, and the drive current as parameters. As a result,

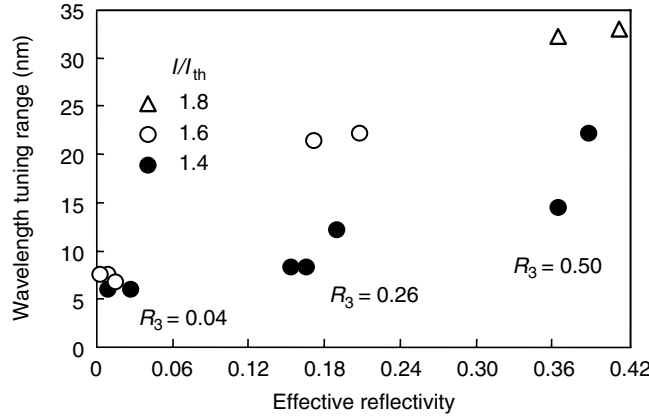


Fig. 2.18. Dependence of wavelength tuning range on the effective reflectivity R_2^{eff} , with I/I_{th} as a parameter

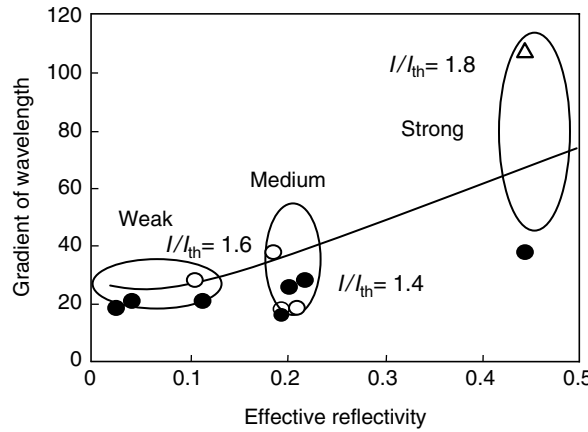


Fig. 2.19. Relationship between the gradient of wavelength variation and the effective reflectivity R_2^{eff}

we successfully measured all the parameters related to the light feedback and confirmed a wavelength tuning range as great as 30 nm for an LD with an antireflection coating on the facet facing the external mirror. Furthermore, we experimentally analyzed how the parameters of the coupling system affect the operation of the ESEC LD. A strongly coupled (low LD facet reflectivity facing an external mirror and high mirror reflectivity) short external-cavity length is the key to achieving a wide-range wavelength tuning.

2.4 Applications

An external-cavity LD has been demonstrated in monitoring the frequency-locked fringe pattern, which leads to the construction of a small interferometer

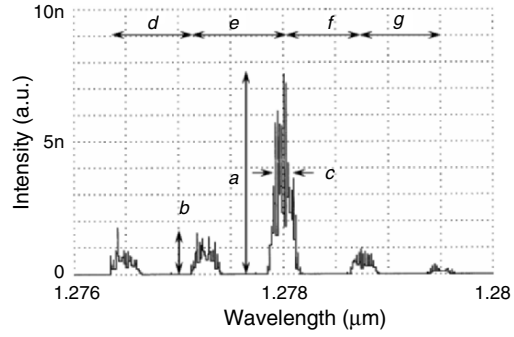


Fig. 2.20. Definitions of side-mode suppression ratio $10 \log(a/b)$, spectrum line width (full width half-maximum c) and mode interval (average of d, e, f, and g in this figure)

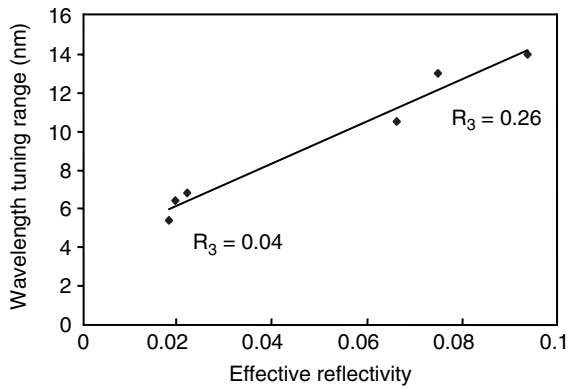


Fig. 2.21. Dependence of tuning range on R_2^{eff}

without an optical bench [2.15]. ESEC LDs have been demonstrated in monitoring the reflectivity and displacement. Optical disk bits are read out in the near field from the difference in medium reflectivity with an antireflection-coated LD and a PD [2.16]. Tunable LD can also be demonstrated in an ESEC configuration [2.4–2.6]. They include desirable properties for optical communication, optical data storage, spectroscopy, and a variety of sensing and measuring systems.

For micromechanical photonics applications using LDs, group III–V compounds are predominant for the monolithic integration of external microstructures. They include a tunable laser [2.5], a resonant sensor [2.17], and an optical head [2.18] which can provide super-small, cost effective microdevices. Such a small distance allows the use of a lensless system, which makes it easier to fabricate. The following micromechanical photonics devices employ a friction-less mechanism including a diaphragm, a cantilever and a slider in order to avoid microscale problems.

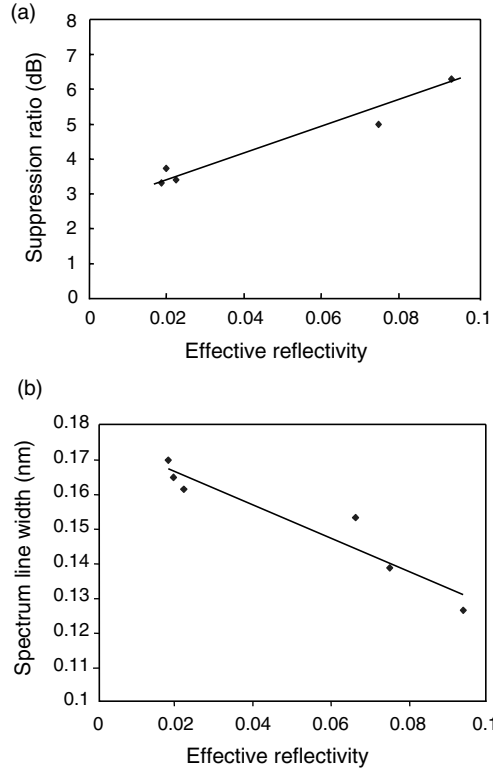


Fig. 2.22. Dependence of side-mode suppression ratio on R_2^{eff} (a), and dependence of spectrum line width on R_2^{eff} (b).

2.4.1 Tunable LD

A vertical cavity surface-emitting laser (VCSEL) diode or a light-emitting diode (LED) with a micromechanical reflector can be used in tuned devices [2.4, 2.5]. The structure is designed to have an air gap of approximately one wavelength. When a voltage is applied to the membrane reflector, the electrostatic force reduces the air gap, which in turn reduces the wavelength.

An edge-emitting LD is also applicable for micromechanically tunable LDs [2.7]. Recent micromachining technology has made it easy to eliminate the need for lens and fiber systems for guiding the light to a PD or a moving mechanism, leading to the integration of optics, mechanics, and electronics.

Structure

The edge-emitting tunable laser diode consists of a laser diode LD1, a microcantilever MC driven photothermally by an LD2 (Fig. 1.28). The light emitted from LD2 onto the side wall of the MC is partially absorbed, heating

the MC and producing the bending moment. At resonant frequency, the MC is excited easily due to the thermal stress caused by a pulsed laser beam from LD2. This sideways vibration varies the external-cavity-length L_{ex} between the MC wall and the LD1 facet, and there is so little incident light from the LD1 that it has no effect on the MC vibration. The variation of L_{ex} causes the wavelength shift of the LD1.

Manufacturing Method

An MC and the LDs were fabricated on a GaAs substrate. There are three micromachining processes involved in fabricating the MC (1) an etch-stop layer of AlGaAs is formed in the LD structure prepared by metalorganic vapor phase epitaxy (MOVPE). (2) The microstructure shape is precisely defined by a reactive dry-etching (RIBE) technique, which can simultaneously form the vertical etched mirror facets for LDs. (3) A wet-etch window is formed with photoresist and the MC is undercut by selective etching to leave the MC freely suspended (Fig. 1.11) [2.19].

These processes are compatible with laser fabrication, and thus an MC structure can be fabricated at the same time as an LD structure. Furthermore, because a single crystal epitaxial layer carries little residual stress, precise microstructures can be obtained without significant deformation. We fabricated an MC with an area of $400 \times 700 \mu\text{m}$. The MC was $3 \mu\text{m}$ wide, $5 \mu\text{m}$ high and $110 \mu\text{m}$ long. The shorter the MC-LD2 distance becomes, the higher the photothermal conversion efficiency. The threshold current of the LD was 46 mA. Figure 2.23 shows the main parts of the tunable LD. The hole for wet etching is visible under the MC between LD1 and LD2.

Monolithic integration of optics and micromechanics is possible not only on a gallium arsenide (GaAs) substrate [2.19], but also on an indium phosphide (InP) substrate [2.20, 2.21]. A smooth, etched surface and a deep vertical sidewall are necessary for good lasing characteristics of both types of semiconductor microstructures.

Basic Characteristics

In a micromechanically tunable LD, the moving part (MC) was integrated with an edge-emitting LD. By varying the external cavity length (MC deflection), the laser wavelength can be easily changed and the wavelength shift varied every half-wavelength ($\lambda/2$). Therefore, the MC must move more than $\lambda/2$ even at off-resonant frequencies. In Sect. 2.5.1, we present the design of the MC structure that satisfies photothermal deflection of greater than $\lambda/2$.

We have experimentally analyzed how the parameters of the coupling system affect the ESEC LD operation by using a rotating optical disk and an LD attached to a flying slider. The parameters included the reflectivities of the LD facets, the reflectivity of the external mirror, and the LD drive current. We confirmed a 30 nm tuning range around a wavelength of $1.3 \mu\text{m}$, as shown

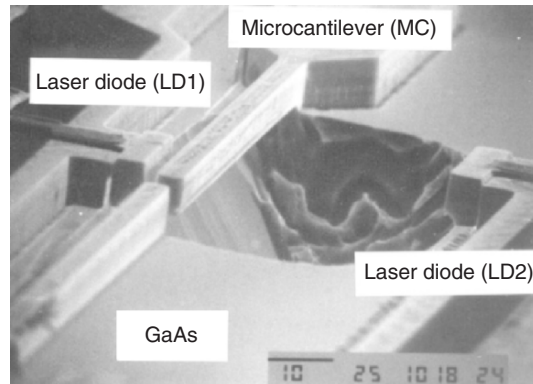


Fig. 2.23. Scanning electron microscope view of the main parts of the tunable LD. The released GaAs/AlGaAs microcantilever (MC) was fabricated by undercutting the sacrificial GaAs. The MC length, thickness and width are 110, 3, and 5 μm and the distances from the facet of LD1 to the side wall of the MC and LD2 to MC are 3 and 30 μm , respectively. Courtesy of O. Ohguchi, NTT, Japan

in Fig. 2.16, by changing the external-cavity length for the LD with an antireflection coating on the facet facing the external mirror. On the basis of these results, we consider that by employing the MC design and the fabrication method described earlier, a photothermally driven micromechanical tunable LD will be available in the future.

2.4.2 Resonant Sensor

A resonant sensor is a device that changes its mechanical resonant frequency as a function of a physical or chemical parameter, such as stress or mass-loading [2.22]. Electrostatic (capacitive) excitation and detection or piezoelectric excitation and detection have been used in conventional silicon-based resonant sensors. The former method requires comparatively large electrode areas to obtain good signals, which presents difficulties at the microscale. The latter requires a layer of a piezoelectric material, preferably zinc oxide (ZnO). However, unfortunately, ZnO is not compatible with integration technology.

Structure

A resonant MC, LDs, and a PD have been fabricated on the surface of a GaAs substrate, as shown in Fig. 2.24. The MC is excited photothermally by light from one laser diode (LD2). With a PD, the vibration is detected as the light output variation caused by the optical length difference between the MC and another LD (LD1).

The resonator was designed to optimize the efficiency of the photothermal excitation and the quality of the composite cavity signal with the structural

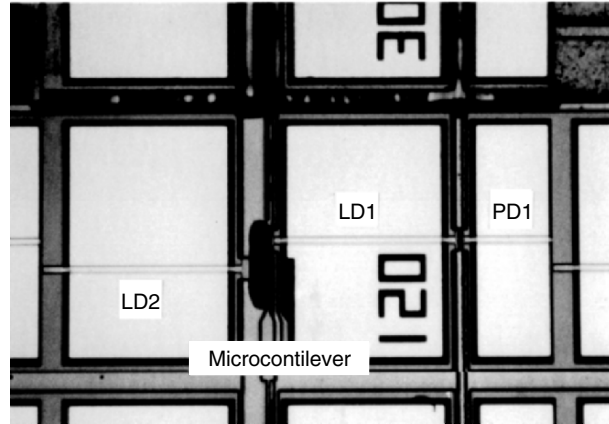


Fig. 2.24. Photograph of a resonant sensor with a MC driven photothermally from one side by LD2 and sensed optically from the other side by LD1 and photodiode PD1; LD2, MC, LD1, and PD1 are integrated on a GaAs substrate

configuration resulting from the fabrication process. The distance h_1 between the facet of LD1 and the wall of the MC was set to $3.0\text{ }\mu\text{m}$, on the basis of the composite cavity signal SNR and the aspect ratio h_1/w of the reactive dry-etching process. The distance h_2 between the facet of LD2 and the wall of the MC was set to be $30\text{ }\mu\text{m}$ considering the energizing light absorption on the MC, and the hole size for the wet process described later. The MC dimensions were set to a length $l = 50\text{ }\mu\text{m}$ and $110\text{ }\mu\text{m}$, a thickness $t = 3\text{ }\mu\text{m}$, and a width $w = 5\text{ }\mu\text{m}$, considering the resonant frequency of the MC. The positions of the excitation light (LD2) and the detection light (LD1) on the MC wall were chosen considering that the LD2 light strikes the MC closer to the support for better excitation, and that the LD1 light strikes further from the support for better detection as well as to prevent cross-talk between the two light beams.

The short distances in the LD2–MC–LD1–PD structure are useful for a vibration resonator because no lenses are required between LD1, MC, and LD2 to make the light beam converge, so it is easier to integrate the mechanical element with the optical elements. Furthermore, the integrated structure does not need any optical alignment like that required by conventional hybrid resonant sensors.

Basic Characteristics

The MC is excited by the resonant frequency due to the thermal stress caused by a pulsed laser beam from LD2. This sideways vibration is detected by the LD1 and the PD from the variation in the external cavity length between the MC wall and the facet of LD1 (phase difference). Light incident from LD1 is continuous illumination and is so small that it has no effect on the MC

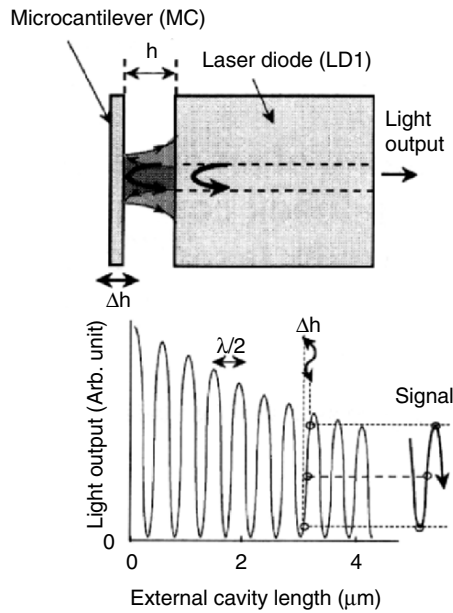


Fig. 2.25. Maximum peaks in the light output occur every $\lambda/2$ and their amplitude decays exponentially in proportion to the external cavity length

vibration. The variation in light output caused by this vibration is detected as a signal by the PD. Maximum peaks in the light output occur every $\lambda/2$ and their amplitude decays exponentially to the external cavity length as shown in Fig. 2.25. The variation in light output caused by this vibration is detected by the PD.

Figure 2.26 shows that the signal amplitude increases as the LD2 light power increases, but an inversion appears in the signal peak for the light power over 30 mW, because the vibration amplitude is larger than $\lambda/4$. We can determine the absolute amplitude on the basis of the fact that the peak signal amplitude corresponds to $\lambda/4$ (0.21 μm). As the incident light power rises, producing greater thermal expansion(stress) in the MC, the vibration amplitude increases.

Figure 2.27 shows a photograph with different excitation light positions. The MC deflections, Δh_1 (detecting side: LD1) and Δh_2 (excitation side: LD2), were measured independently by the method described earlier. Figure 2.28 shows the relationship between the deflection and the normalized excitation position with a laser power of 9.5 mW. It is confirmed that both deflections increase as the light strikes the MC closer to the support, and Δh_1 is greater than Δh_2 , probably due to the optical pressure exerted by the light from LD2.

To measure the resonant properties, LD2 was lased by the current with various frequencies. When the current frequency coincided with the MC

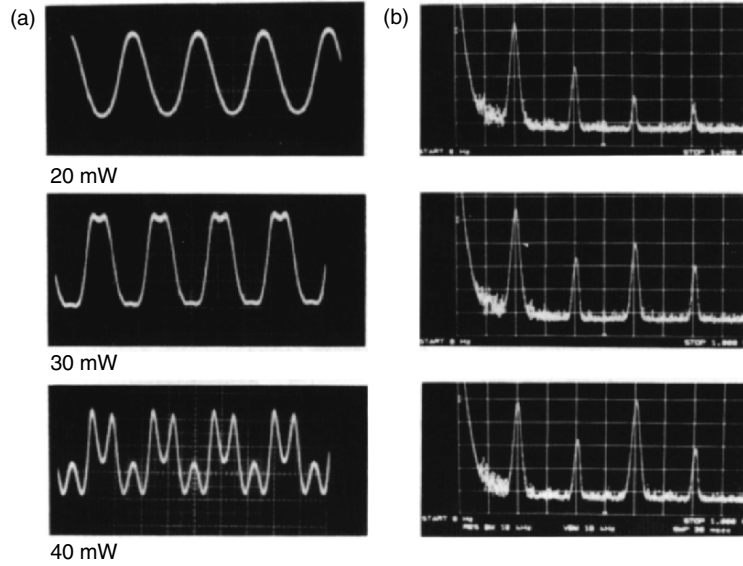


Fig. 2.26. Resonant signal amplitude and spectrum versus LD2 light power. The signal amplitude increases as the light power increases, but an inversion appears in the signal peak for the light power over 30 mW, because the vibration amplitude becomes larger than $\lambda/4$

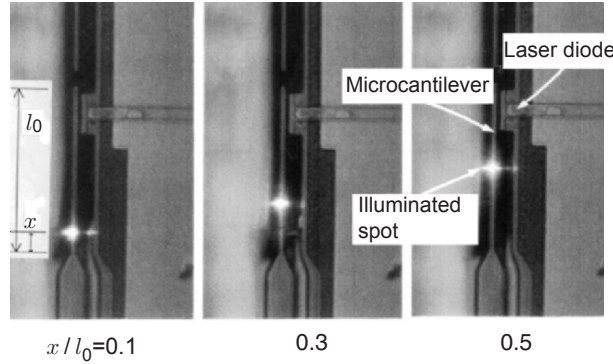


Fig. 2.27. Photograph of the illuminated spot on the MC, for investigating the excitation efficiency depending on the position of the MC

mechanical resonant frequency, the amplitude of the LD1 light output exhibited a maximum. The signal can be obtained from the interference between the LD1 output light and its reflected light from the MC sidewall. Figure 2.29 shows the resonant frequency and frequency spectra of the MC. The resonances of the MC for lengths of $110\text{ }\mu\text{m}$ and $50\text{ }\mu\text{m}$ were 200.6 kHz and 1.006 MHz , respectively. They are in good agreement with the theoretical

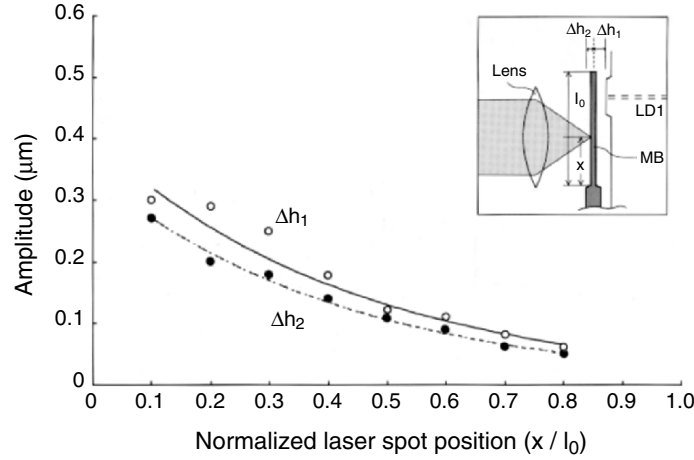


Fig. 2.28. Variation in MC vibration amplitude as a function of the illuminated spot position on the MC

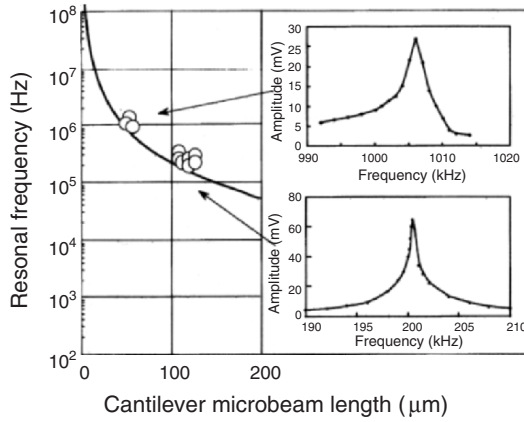


Fig. 2.29. Resonance frequency and frequency spectra as a function of MC length for GaAs

results calculated from (2.27) [2.23, 2.24]

$$f_0 = \lambda_0^2 \frac{t \sqrt{\frac{E}{12\rho}}}{2\pi l^2}, \quad (2.27)$$

where λ_0 is the eigen value of 1.875 determined by the vibration mode, E is Young's modulus, ρ the density, l the cantilever length, and t its thickness. The Q in air were approximately 250. In order to increase Q , damping mechanisms such as imbalance and radiation at the supporting rim require further studies. To increase the sensor sensitivity, the resonant frequency should be

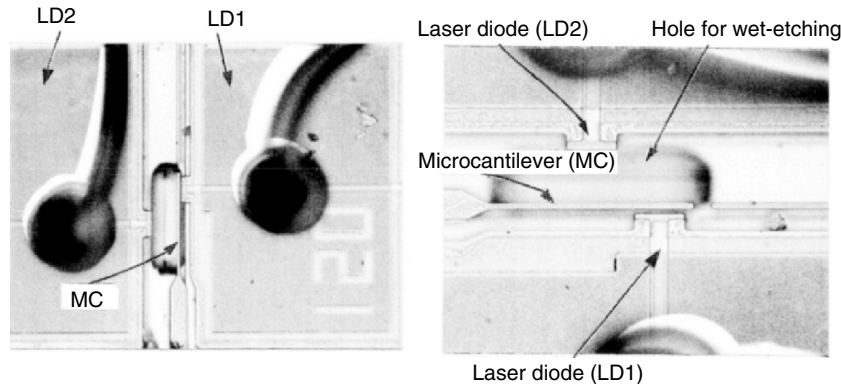


Fig. 2.30. Photograph of a resonant sensor deposited with chemically inductive material phthalocyanine of $1\text{ }\mu\text{m}$ thickness

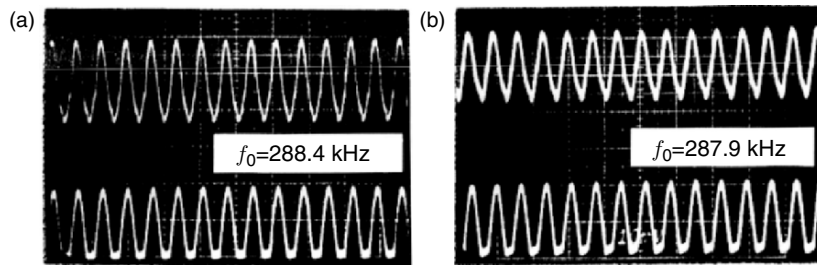


Fig. 2.31. Resonant frequency change of 500 Hz from 288.4 to 287.9 kHz, due to the mass increase of 54 ng for the 1- μm thick phthalocyanine deposition

increased by shortening the cantilever length. A resonant frequency of 10 MHz is applicable with a length of less than $20\text{ }\mu\text{m}$ ($3\text{ }\mu\text{m}$ thick).

Possible applications are resonant frequency change detection type accelerometers and gas sensors. Chemically inductive material phthalocyanine was deposited of $1\text{ }\mu\text{m}$ thickness on the resonator as shown in Fig. 2.30. Then the resonant frequency was changed by 500 Hz from 288.4 to 287.9 kHz due to the mass increase of 54 ng corresponding to the 1- μm thick phthalocyanine deposition. It was confirmed that the resonant sensitivity is very high (Fig. 2.31). Both figures show the possibility of detecting a gas.

The yield strength of single crystalline GaAs is less than that of Si, but it is five times greater than that of steel. Furthermore, micromachining can be used to fabricate microstructures of high purity with a low defect density and no residual stress. These mechanical properties mean that GaAs-based and InP-based microstructures are suitable for use in integrated micromechanical photonics systems.

2.4.3 Optically Switched Laser Head

In this section a small flying optical head and its high quality readout characteristics when used as an optically switched laser (OSL) head are described. The basic concept involved the use of light emitted and collected through a 1- μm diameter aperture of an LD placed less than 2 μm from a recording medium (ESEC LD configuration). For autofocus, the head operates like a magnetic head: air-bearing technology stabilizes the slider flying height approximately 1 μm as shown in Fig. 2.32. Controlled by a sampled servo track error signal, the arm used to seek from track to track is also used for track following as described later.

Drive Structure

A prototype drive consisting of a flying head and a phase change medium disk is constructed for experimental purposes. Figure 2.33 shows experimental optical disk drive using an OSL head and a phase change recording medium: linear actuator type (a) and rotary actuator type (b).

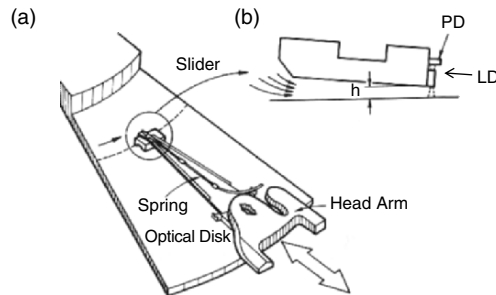


Fig. 2.32. Schematic representation of an optically switched laser (OSL) head flying on an optical disk (a), and detailed view of the flying slider on which an LD-PD is mounted (b)

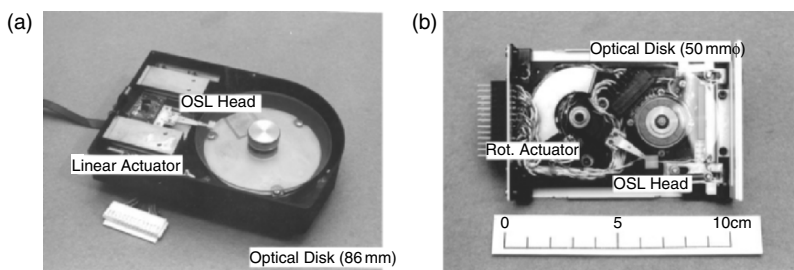


Fig. 2.33. Experimental optical disk drive using an OSL flying head and a phase change recording medium: linear actuator type (a), and rotary actuator type (b)

An LD monolithically integrated with a PD is mounted junction-up on a slider. Light reflects from the medium back into the active region of the LD. Head-medium spacing h (between the LD facet and the GeSbTe recording medium) is approximately $2\text{ }\mu\text{m}$: the sum of the slider flying height h_0 , LD-PD attachment error h_1 , and the protective layer thickness h_2 .

Head Structure

A monolithically integrated LD-PD chip with a wavelength of $1.3\text{ }\mu\text{m}$ was shown in Fig. 1.33. The LD is isolated from the PD by reactive ion beam etching (RIBE). The space between LD and PD is about $5\text{ }\mu\text{m}$ and the monitor current sensitivity is 0.1 mA/mW . The $1.2\text{-}\mu\text{m-wide}$ taper-ridged waveguide on the top of the LD cavity was also fabricated by RIBE. FWHM of its near field pattern are approximately $1\text{ }\mu\text{m}$ as shown in Fig. 2.34. This sharpened LD is useful for the flying optical head because it does not require an additional lens to converge the light beam, and hence does not lose power before reaching the recording medium.

A long-wavelength ($1.3\text{ }\mu\text{m}$) InGaAsP LD (LD#1), reliable in air, can be used in our flying head because its spot diameter is mainly constrained by the shape of the ridged waveguide [2.25]. A short-wavelength ($0.83\text{ }\mu\text{m}$) GaAlAs LD (LD#2) could be used if its facets were covered with dielectric protective films to prevent oxidation in air.

Medium Structure

The optical disk is made up of multiple layers: SiN/GeSbTe/SiN/Au/SiN/glass substrate as shown in Fig. 1.32. The first SiN layer operates as a protective film for a head-medium reliability. The GeSbTe layer serves as the phase change medium. The second SiN layer and the Au layer enhance the reflectivity change and the thermal diffusion speed of the recording medium.

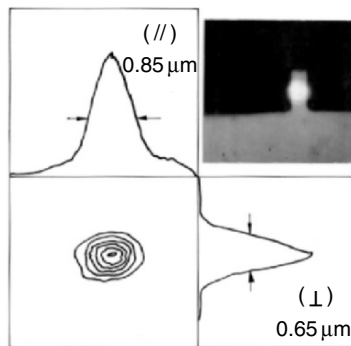


Fig. 2.34. Near field pattern of the emitted light from a $1.2\text{-}\mu\text{m-wide}$ taper-ridged waveguide

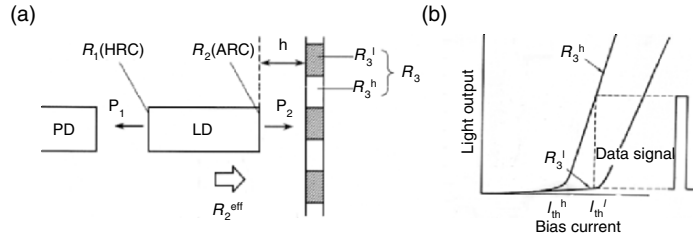


Fig. 2.35. LD used in an OSL flying head forms a complex cavity with the recording medium acting as an external mirror. (a) R_1 and R_2 are the power reflectivities of the LD facets, and R_3^h and R_3^l are those of the two states for the external recording medium. R_2^{eff} is the effective reflectivity coupled with the external recording medium. (b) Light output versus bias current in the two medium reflectivity states. There are two threshold currents: I_{th}^h for R_3^h and I_{th}^l for R_3^l . Data bits are read as the laser switches from R_3^l to R_3^h , biased between I_{th}^h and I_{th}^l , by the PD on the opposite side of the medium

The last SiN layer increases adhesion to the glass substrate. The reflectivity, transmittivity, and absorptivity of the as-deposited GeSbTe medium were 0.24, 0.22, and 0.54.

Basic Read/Write Operation

The LD used in an optically switched laser (OSL) head forms a complex cavity with the recording medium acting as an external mirror. In Fig. 2.35a, R_1 and R_2 are the power reflectivities of the LD facets, and R_3^h and R_3^l are those of the two states for the external recording medium. R_2^{eff} is the effective reflectivity coupled with the external recording medium. Figure 2.35b shows the light output versus bias current in the two medium reflectivity states. There are two threshold currents: I_{th}^h for the high reflectivity R_3^h and I_{th}^l for the low reflectivity R_3^l . Data bits are read as the light output difference between the two states.

Data bits are written, in this experiment, as the laser-induced phase change shifts the medium reflectivity from R_3^l (as depo. state) to R_3^h (crystal state). During the write operation, the light output changes from P_w to P'_w at a fixed write current of I_w according to the reflectivity change. The light output difference $P'_w - P_w$ (nearly equals to $P'_w - P_w$) is less than 1 mW, which does not destroy the information even if the medium stops. If the light output were 20 mW, the variation ratio in the write process would be only 5%. We, thereby achieve stable write operation. To increase the signal-to-noise ratio (SNR) and light output from the medium side laser facet, the medium side LD facet is coated with an antireflection film of $(\text{SiO})_x (\text{Si}_3\text{N}_4)_{1-x}$ [2.14].

Data Signal

Data signals are obtained by the light output difference due to the medium reflectivity. Varying the medium reflectivity R_3 as a parameter, Figs. 2.36a

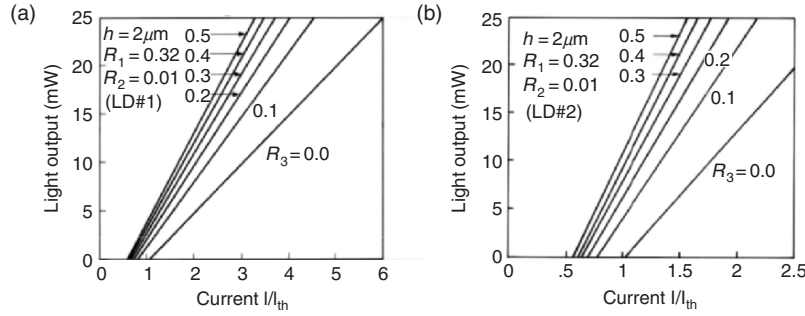


Fig. 2.36. OSL head light output characteristics with the medium reflectivity R_3 as a parameter for (a) an LD#1 ($\lambda = 1.3 \mu\text{m}$), (b) an LD#2 ($\lambda = 0.83 \mu\text{m}$)

and b plot the light output characteristics of the OSL head for LD#1 and LD#2, respectively. These values are calculated for the steady state single-mode operation by using the rate equations [2.26].

The external cavity can be described by replacing medium side laser facet reflectivity R_2 by effective reflectivity R_2^{eff} . The reflectivities R_2 , R_3 , and the coupling coefficient η are included in R_2^{eff} . We define η as (2.8). As for an LD#2, Gaussian half-power beam width 25^0 ($2w_{s0} = 1.38 \mu\text{m}$) and 10^0 ($2w_{p0} = 2.54 \mu\text{m}$), η is 0.5 for $h = 2 \mu\text{m}$ and 0.75 for $h = 1 \mu\text{m}$.

Since the LD facet reflectivity R_2 facing the medium is greatly reduced by an antireflection coating to improve the SNR, the light output P_1 (PD side) differs from P_2 (medium side). The light output ratio for a complex cavity laser is calculated using effective reflectivity R_2^{eff} instead of R_2 , as shown in Problem 2.3. For example, with $h = 2$, $P_2/P_1 = 1.5$ for $R_1 = 0.32$, $R_2 = 0.01$, and $R_3 = 0.3$; $P_2/P_1 = 5$ for $R_1 = 0.70$, $R_2 = 0.01$, and $R_3 = 0.3$ (see Fig. A.3). We used these ratios to estimate read/write power P_2 from the measured light output P_1 .

Track Error Signal

Since OSL head has only one PD, track error signals are obtained by the sampled servo method instead of the push–pull method for the continuous servo. Sampled servo method is expected to give good stability and compatibility.

Discrete block format (DBF) [2.27] marks with a $1.6-\mu\text{m}$ track-pitch are reproduced by the OSL flying head as shown in Fig. 2.37. They are preformatted on the glass substrate in phase pits. Figure 2.37a shows a DBF mark with two access codes and three patterns, different in phase, that correspond to the wobble A (WA), clock (CLK), and wobble B (WB). Figure 2.37b shows reproduced signals. Each pulse composed of five peaks, represents the servo signals (DBF mark) at the beginning of each 1,672 block per revolution. The third and the fifth peaks are wobbling signals, WA and WB, whose marks are displaced $+1/4$ and $-1/4$ pitches from the track center. Track error signals were

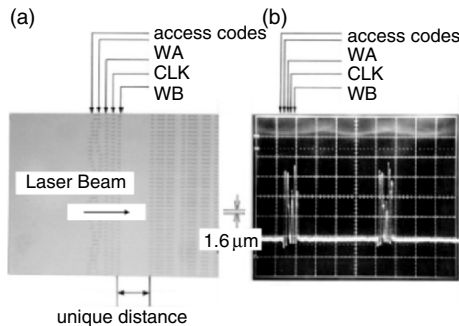


Fig. 2.37. Discrete block format (DBF) marks with a 1.6- μm track-pitch (a), and reproduced signals at 900 rpm. LD bias current is 40 mA (b)

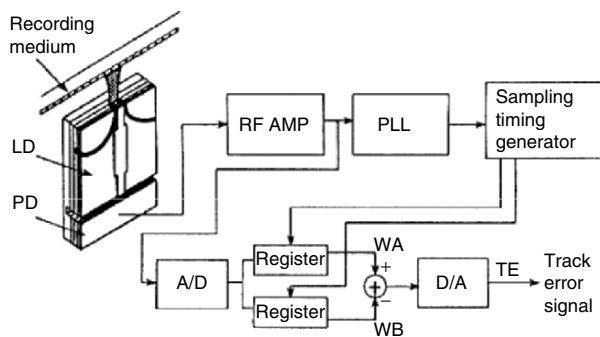


Fig. 2.38. Block diagram of track error signal detection. Track error signal is obtained by the signal amplitude difference between the two wobbling signals of the discrete block format (DBF)

derived from the difference in signal amplitudes between the two wobbling signals.

Figure 2.38 is a block diagram of the track error signal ($TE = WA - WB$) detection system. The reproduced track error signal confirms that the spot diameter of the lensless but taper-ridged waveguide LD is small enough to reproduce the DBF servo marks.

Reducing Laser Noise by Optimizing Bias Current

The SNR of the OSL flying head is high because of the large signal amplitude due to laser switching and the lack of feedback laser noise due to the external cavity being so much shorter ($2\mu\text{m}$) than the LD cavity ($300\mu\text{m}$). The SNR is degraded, however, by fluctuation of both high- and low-frequency light output. The former is caused by laser noise due to mode competition, while the latter is caused by variation of head-medium spacing (external cavity length) and of temperature.

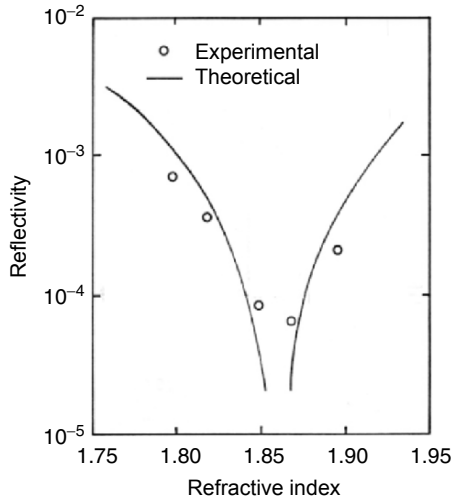


Fig. 2.39. Relationship between antireflection-coated (ARC) facet reflectivity and ARC-film refractive index. Circles show experimental results. Solid lines are fitting curves calculated using a plane wave approximation

The SNR degradation due to high-frequency laser noise can be reduced by increasing the difference between I_{th}^l and I_{th}^h , e.g., by reducing reflectivity of the medium side LD facet, and also by biasing the current between noise peaks located around threshold currents. This laser facet was therefore coated with an $(\text{SiO})_x(\text{Si}_3\text{N}_4)_{1-x}$ antireflection film by ion beam sputtering using a high purity silicon target and mixed O_2-N_2 discharges. Figure 2.39 shows the reflectivity of different films obtained by controlling gas flow rates to minimize reflectivity. Reflectivities less than 1×10^{-4} are reproducibly obtained.

To ascertain the optimum drive condition, the data signal amplitude and the SNR were measured with effective noise defined as the rms of the noise spectrum from 40 kHz to 20 MHz. An SNR peak, between the threshold currents corresponding to I_{th}^l and I_{th}^h , increases as facet reflectivity decreases. In a medium static condition, the SNR reaches 56 dB at a facet reflectivity of $R_2 = 7.0 \times 10^{-3}$. In a dynamic condition, it is 35 dB, which has been previously reported to be adequate for an optical disk drive. Reflectivity of the coated facet was estimated from the amplified spontaneous emission spectrum by the Fabry–Perot modulation depth method [2.28].

Reducing the Variation in Light Output

Degradation of the SNR due to variation of head-medium spacing can be compensated by reducing interference between the internal and the feedback lights. This can be done by reducing the laser facet reflectivity facing the recording medium.

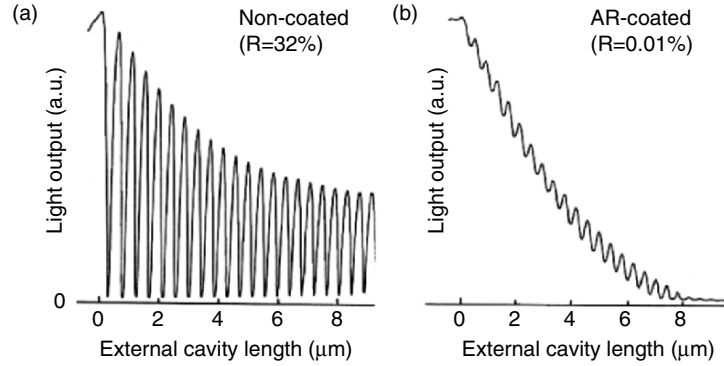


Fig. 2.40. Light output of a composite cavity LD as a function of external-cavity-length L_{ex} . Light output varies by a half-wavelength period as L_{ex} varies (a). Variation can be suppressed by an antireflection coating on the LD facet facing the recording medium (b)

Figure 2.40 shows a typical suppression of light output variation induced by reducing facet reflectivity (medium reflectivity $R_3 = 0.30$). The variation using an uncoated LD (left side) with a facet reflectivity of $R_2 = 0.32$ is extremely high due to strong interference between internal and feedback light, both of which have almost the same intensity. Using an antireflection-coated LD (right figure), on the other hand, with extremely low reflectivity of $R_2 = 1 \times 10^{-4}$ weakens interference and greatly reduces variation of light output.

Figure 2.41 shows the relationship between facet reflectivity R_2 and the variation ratio F , defined as the ratio of the amplitude change. The variation ratio decreases as R_2 decreases. At a facet reflectivity $R_2 = 1 \times 10^{-4}$, the variation ratio was reduced to the extremely small value of 1.6 compared to 9.2 for an uncoated LD.

Increasing Thermal Write Power

Laser power density on the medium is increased not only by the taper-ridged waveguide laser, but also by the highly thermally conductive slider and the reduction of LD-PD attachment error. Light output is higher for the slider with the higher thermal conductivity (AlN) than the lower thermal conductivity (sapphire). Not only the thermal property but also the electrical properties, precise fabrication, and head/medium reliability must be considered when choosing a slider material. We used an AlN slider for the following experiments.

As the head-medium spacing decreases the light output increases due to increased light feedback. The spacing h , set at 2 μm to keep the beam diameter below 1 μm , is the sum of the slider flying height h_0 , LD-PD attachment error h_1 (facet-to-slider surface error), and the protective-layer thickness h_2 . Since $h_0 = 0.9 \mu\text{m}$ and $h_2 = 0.24 \mu\text{m}$ in this experiment, h_1 must be $< 0.9 \mu\text{m}$. We

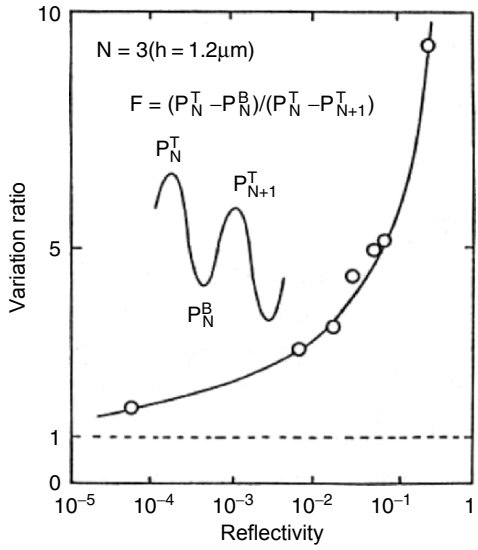


Fig. 2.41. Variation ratio versus facet reflectivity at the optimum bias current for OSL readout operation

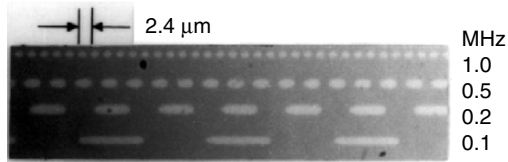


Fig. 2.42. Written bit patterns by 16 mW laser pulses at various frequencies

have developed a high-precision bonding machine to satisfy this requirement. Length measurement accuracy is $0.1\mu\text{m}$ with an autofocus mechanism, and moving resolution accuracy is $0.1\mu\text{m}$ with electrically controlled motion as described in Sect. 2.3.1.

Write Performance

Figure 2.42 shows the dependence of write frequency on written bit patterns for 16 mW light pulses with a duty cycle of 50%. These bits were written as spots crystallized from the as-deposited state in this experiment. The phase change was caused by the thermal energy of the light output with a fixed write current. This figure suggests that both the bit shapes and the levels of crystallization are uniform. Bit pitch was $2.4\mu\text{m}$ at a write frequency of 1 MHz. These bits are readout with a high SNR as the medium reflectivity changed between the two states (shown in the lower traces). The medium velocity here

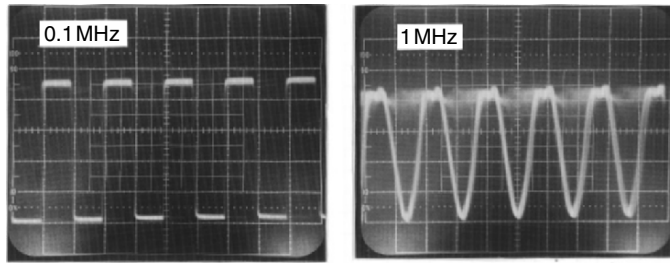


Fig. 2.43. Reproduced signals of the written bit at 0.1 and 1 MHz for a duty cycle of 50%

is 6.9 ms^{-1} . Figure 2.43 shows the reproduced signals for 0.1 and 1.0 MHz, both with high SNR.

Reliability Test

In an actual disk drive, contact between the slider and the disk is inevitable. We therefore identify a combination of slider and protective layer materials that reduces wear (scratching) during contact start/stop (CSS).

We have investigated experimentally the protective films such as silicon-dioxyside (SiO_2), zinc-sulfide (ZnS), and silicon-nitride (SiN). We also evaluated their thermal conductivity for writing sensitivity and thermal expansion difference between the multi layers described earlier. The SiN protective layer had smallest amount of scratch caused by repeated CSS with the AlN slider. Fabrication of the film was also studied with regard to internal stress and adhesion strength. The films, containing hydrogen atoms a- SiN:H (hydrogenated amorphous silicon nitride), showed good write sensitivity. Its mechanical property is also good because it has a high tensile force and resists scratching.

Figure 2.44 is an SEM photograph of the LD facet after 10,000 CSS cycles (900 rpm) in an office environment (class 350,000). The disk has a $\text{SiN}/\text{GeSbTe}/\text{SiN}/\text{Plastic}$ substrate structure. Protuberance dust (particles) adheres to the LD facet. The chemical composition of twelve randomly selected samples of protuberance dusts, analyzed by Äuger electron spectroscopy, is primarily C, O, Al, Si, and S, that is, the dust element included in the air. The elements from slider and protective layer are included only two of the 12 dusts (samples). These results indicate very small amount of slider/disk wear were produced even if scratch on the medium can not be seen with an optical microscope.

The LD-PD reliability and the dust in the air is evaluated by free-running test at 3,600 rpm, 4 mW light power, and with $h_0 = 1 \mu\text{m}$ in an experimental room environment (class 30,000). This test shows that the head has a lifetime (before bias current increases by 20%) of 2,040 h. This corresponds to 4.4×10^8 passes. Contact start/stop (CSS) test, bias current for constant signal amplitude versus the number of CSS cycles, shows that the head signal is

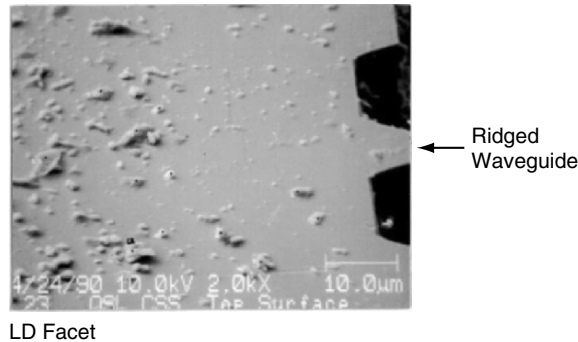


Fig. 2.44. SEM photograph of LD facet after 10,000 contact start/stop (CSS) cycles in an office environment (class 350,000). The disk has an SiN/SbTeGe/SiN/plastic substrate structure and is used at low rotation of 900 rpm

still good after more than 50,000 cycles in a class 30,000 environment (30,000 particles larger than $0.5 \mu\text{m}/\text{ft}^{-3}$).

The main factors contributing to the high reliability of the head/medium interface are the oxidation-free InGaAsP LD-PD, the high thermal conductivity of the slider, and the low residual stress and high adhesion strength of the SiN protective layer on the recording medium. Moreover, as the LD facet is about $1 \mu\text{m}$ behind the slider surface, it does not directly contact the medium.

The small optical head with only an LD-PD on a slider shows excellent read/write characteristics and reliability. An antireflection-coated LD combined with a taper-ridged waveguide has a high-SNR readout and high-resolution write-down performance. An oxidation-free InGaAsP LD ($\lambda = 1.3 \mu\text{m}$), a high thermal conductivity AlN slider, and a SiN protective layer ($0.24 \mu\text{m}$) on a phase change recording medium contribute to the high reliability of this flying optical head. Some kind of cartridge mechanism or dust-wiping method should be developed to allow removal and replacement of the recording medium. For high-performance use, a high-speed track following method and a multibeam head should be developed.

2.5 Designs for Related Problems of an ESEC LD

2.5.1 Enlargement of a Photothermal MC Deflection for a Tunable LD

A photothermally driven MC tunable LD that needs no electrode to apply voltage has been proposed. The advantages of the optical method in such integrated systems are that it is controlled remotely and not affected by electromagnetic interference; these factors are especially critical for highly integrated devices.

This section describes the increase in photothermal deflection of an MC by employing a bimorph and an antireflection structure. This deflection can be expected to exceed half a wavelength, which is required for a tunable LD, by the temperature increase of 100°C with an optical absorption rate above 98%. An antireflection coating of Au/Si₃N₄/Au on the Au and Si₃N₄ bimorph structure semiconductor MC provides enhanced deflection about 500 times greater than that of the solitary semiconductor MC at off-resonant frequencies. The designed MC monolithically integrated on InP ($\lambda = 1.3 \mu\text{m}$) or GaAs ($\lambda = 0.83 \mu\text{m}$) will be used for an external-cavity length-changing type edge-emitting tunable LD.

Design Considerations

An MC and LDs were fabricated on the surface of a GaAs substrate, as shown in Fig. 2.23. The light emitted from the LD2 onto the side wall of the MC is partially absorbed, heating the MC and producing the bending moment. When the MC is excited at the resonant frequency by the thermal stress caused by a modulated laser beam from LD2, the external cavity length between the MC wall and the LD1 facet varies sufficiently, but insufficiently at off-resonant frequencies. That variation of the external cavity length causes the wavelength change of the LD1.

By varying the external cavity length, the laser wavelength can be easily changed and the wavelength varies every $\lambda/2$. Therefore, an MC deflection of more than $\lambda/2$ is necessary for the tunable LD, even at an off-resonant frequency. Meanwhile, the light absorption should be increased to obtain a sufficient temperature rise for the large thermal strain. A bimorph structure and an antireflection coating are applied to satisfy these requirements. The following describes the enhanced MC photothermal deflection design for GaAs and InP materials.

Bimorph Design

Figure 2.45 shows the calculated relationship between photothermal deflection and thickness for a solitary GaAs MC. The tip deflection d at the free end of the MC is estimated by (2.28), where α is the thermal expansion coefficient, δT is the temperature difference between the surfaces of the MC illuminated by an LD, l and t are the length and thickness of the MC, respectively [2.29].

$$d = \frac{\alpha l^2}{2t} \delta T \quad (2.28)$$

Tip deflection d depends largely on the absorption coefficient (varies $\lambda/2$ due to the interference between the upper and lower surfaces) of the laser light and reaches 0.8 nm when illuminated with 1 mW of power.

We designed a metal-dielectric bimorph structure to increase the MC deflection by increasing in temperature resulting from absorption of light emitted

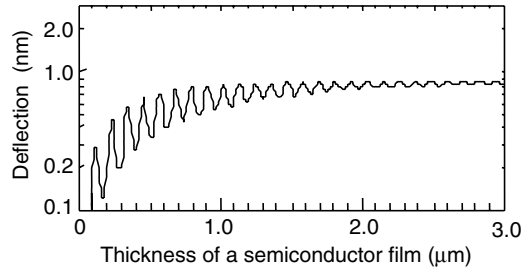


Fig. 2.45. Calculated relationship between photothermal tip deflection and thickness for a GaAs MC

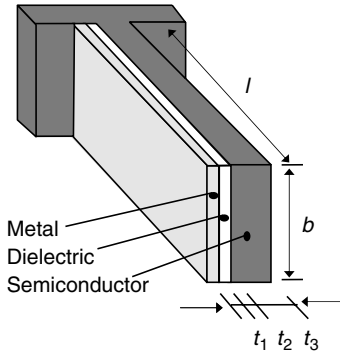


Fig. 2.46. Schematic drawing of a three-layer bimorph MC

by the LD2. Tip deflection is enhanced by the temperature rise from room temperature due to the thermal coefficient of expansion mismatch between two sandwiched components. The MC is made, for example, of a 0.1- μm gold (Au) layer, a 0.1- μm Si_3N_4 dielectric layer and a 2- μm thick semiconductor LD layer. Next, we developed a bimetallic MC deflection model [2.30] into a three-layer MC as follows.

The MC is composed of three layers of thickness t_1, t_2, t_3 , thermal expansion coefficients $\alpha_1, \alpha_2, \alpha_3$, the Young's moduli E_1, E_2, E_3 , a length of l and a width of b as shown in Fig. 2.46. Temperature distribution within the MC is assumed to be uniform and the temperature change from the room temperature to be ΔT .

Figure 2.47 shows the deflection of the MC and internal thermal stress due to temperature change. The internal stresses over the cross-section of material i can be reduced to a tensile force P_i and couple moment M_i . Since the internal forces and moments over any cross-section of the MC must be in equilibrium

$$P_1 + P_2 - P_3 = 0, \quad (2.29)$$

$$\frac{E_1 I_1}{r_1} + \frac{E_2 I_2}{r_2} + \frac{E_3 I_3}{r_3} - h_1 P_1 - h_2 P_2 - h_3 P_3 = 0, \quad (2.30)$$

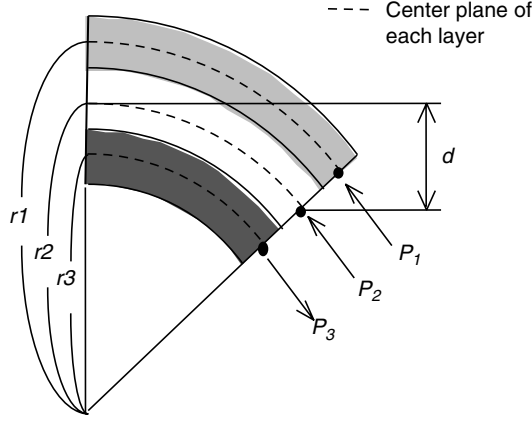


Fig. 2.47. Deflection of a bimorph MC and internal stress due to temperature change

where $M_i = E_i I_i / r_i$ ($I_i = bt_i^3/12$) is the moment of inertia of i th layer, h_i is the distance between the center plane of the MC and that of the i th layer and r_i is the radius of curvature of the i th layer of the MC, and $h_1 + h_2 = (t_1 + t_2)/2$, $-h_2 + h_3 = (t_2 + t_3)/2$, $h_1 + h_3 = (t_1 + 2t_2 + t_3)/2$.

At the interface between the two layers, the normal strain of the materials must be the same. Therefore

$$\alpha_1 \Delta T - \frac{P_1}{bE_1 t_1} - \frac{t_1}{2r_1} = \alpha_2 \Delta T - \frac{P_2}{bE_2 t_2} + \frac{t_2}{2r_2}, \quad (2.31)$$

$$\alpha_2 \Delta T - \frac{P_2}{bE_2 t_2} - \frac{t_2}{2r_2} = \alpha_3 \Delta T + \frac{P_3}{bE_3 t_3} + \frac{t_3}{2r_3}. \quad (2.32)$$

Here, $r_1 = r_2 = r_3 = r$ (very thin compared to length) and we derive the curvature $k = 1/r$ by eliminating P_1, P_2, P_3 from (2.29) to (2.32). Note that the deflection d at the free end of the MC from the curvature k is [2.30]

$$d = \frac{kl^2}{2} \quad (2.33)$$

for $l \gg r$.

Finally, the tip deflection of the MC by thermal strain due to the mismatch between the thermal coefficient of the expansion is:

$$d = \frac{A}{B}, \quad (2.34)$$

where

$$\begin{aligned} A &= 3\Delta T l^2 [E_1 E_2 t_1 t_2 (\alpha_1 - \alpha_2)(t_1 + t_2) + E_2 E_3 t_2 t_3 (\alpha_2 - \alpha_3)(t_2 + t_3) \\ &\quad + E_1 E_3 t_1 t_3 (\alpha_1 - \alpha_3)(t_1 + 2t_2 + t_3)] \\ B &= 2E_1 E_2 t_1 t_2 (2t_1^2 + 3t_1 t_2 + 2t_2^2) + 2E_2 E_3 t_2 t_3 (2t_2^2 + 3t_2 t_3 + 2t_3^2) \\ &\quad + 2E_1 E_3 t_1 t_3 (2t_1^2 + 6t_1 t_2 + 2t_2^2 + 6t_2 t_3 + 3t_1 t_3) + E_1^2 t_1^4 + E_2^2 t_2^4 + E_3^2 t_3^4. \end{aligned}$$

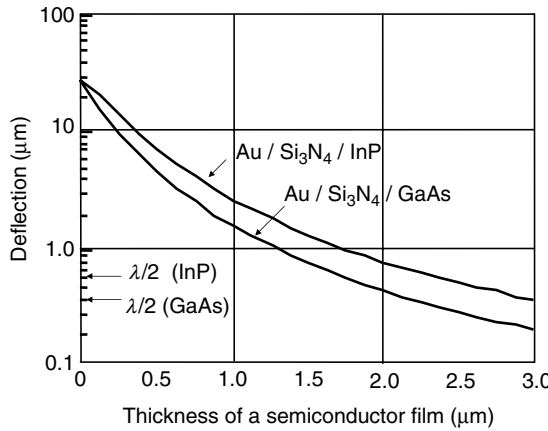


Fig. 2.48. Numerical simulation of the tip deflection versus semiconductor thickness by a temperature increase of 100°C for a metal-dielectric bimorph structure MC for two types of semiconductor materials

Table 2.1. Properties of materials used in photothermal MCs

material	thermal expansion coefficient 10^{-6} K^{-1}	young's modulus 10^{10} N m^{-2} (300 K)	refractive index (830 nm)	refractive index (1,300 nm)
Au	14.2	7.9	0.188 + i5.39	0.403 + i8.25
Si ₃ N ₄	0.8	0.52	1.5	1.5
InP	4.5	6.07	—	3.205
GaAs	6.86	8.53	3.67 + i0.08	—

Figure 2.48 shows the result of numerical simulation by the material parameters shown in Table 2.1. More than $\lambda/2$ deflection is possible for less than 2.2- μm thick semiconductor MC with 100°C temperature increases for both GaAs and InP LD. This provides enhanced deflection about 500 times greater than the solitary semiconductor MC deflection shown in Fig. 2.46.

Figure 2.49 shows a contour map of MC deflection for GaAs LDs, Young's modulus E and the thermal expansion coefficient α as parameters. In the figure, the dotted line corresponds to the displacement of $\lambda/2$; this displacement increases as the thermal expansion coefficient and Young's modulus increases.

Antireflection Coating Design

By increasing the MC displacement by the temperature rise resulting from the LD, the absorption of the light should be high. In this section we will describe our design for an antireflection coating for the MC.

Reflection and transmission of a plane wave in a two-layer film structure are shown in Fig. 2.50. The complex refractive index, thickness, and incident

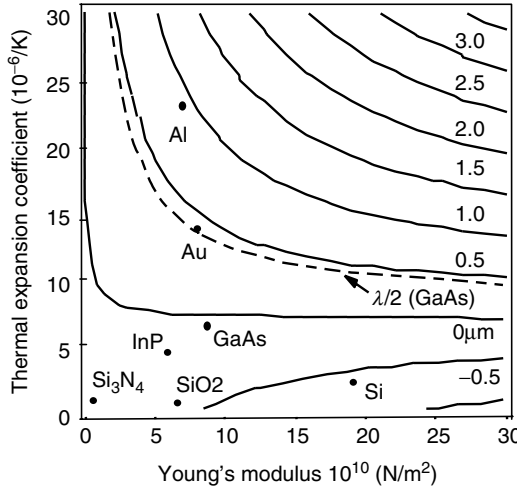


Fig. 2.49. Contour map of an MC deflection, with Young's modulus E and thermal expansion coefficient α as parameters

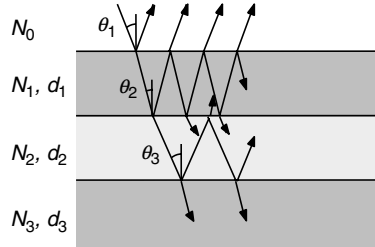


Fig. 2.50. Reflection and transmission of a plane wave in a two-layer film structure

angle for the j th layer film are denoted by N_j, d_j, θ_j , respectively. The phase shift in the j th film is

$$\beta_j = \frac{2\pi}{\lambda} d_j N_j \cos \theta_j. \quad (2.35)$$

The coefficients r_{ij} and t_{ij} associated with the reflection and transmission at the i and j interfaces are given by the Fresnel formula. The formula for r_{ijk} and t_{ijk} for the j th film sandwiched by the i th and k th films, are given as follows [2.31]:

$$r_{ijk} = \frac{r_{ij} + r_{jk} e^{-i2\beta_j}}{1 + r_{ij} r_{jk} e^{-i2\beta_j}}, \quad (2.36)$$

$$t_{ijk} = \frac{t_{ij} t_{jk} e^{-i2\beta_j}}{1 + r_{ij} r_{jk} e^{-i2\beta_j}}. \quad (2.37)$$

Therefore, the total r and t are given as

$$r = \frac{r_{012} + z_1 r_{23} e^{-i2\beta_2}}{1 - r_{210} r_{23} e^{-i2\beta_2}}, \quad (2.38)$$

$$t = \frac{t_{012} t_{23} e^{-i2\beta_2}}{1 - r_{210} r_{23} e^{-i2\beta_2}}. \quad (2.39)$$

$$\text{where } z_1 = t_{012} t_{210} - r_{012} r_{210}. \quad (2.40)$$

Consequently, the total energy reflectivity R and total energy transmission T are given as

$$R = rr^*, \quad (2.41)$$

$$T = \frac{N_3 \cos \theta_3}{N_2 \cos \theta_2} tt^*. \quad (2.42)$$

Figure 2.51 shows the energy reflectivity R of $\text{Au}^{(1)}/\text{Si}_3\text{N}_4/\text{Au}^{(2)}$ versus the Si_3N_4 thickness for the wavelengths $1.3\text{ }\mu\text{m}$ (a), and $0.83\text{ }\mu\text{m}$ (b), with the $\text{Au}^{(1)}$ thickness as a parameter. Both figures show that R reaches zero by changing the thickness of the $\text{Au}^{(1)}$ film. The smallest R will be achieved at the Si_3N_4 thickness of 366 nm at the wavelength $1.3\text{ }\mu\text{m}$ and 223 nm at $0.83\text{ }\mu\text{m}$. Figure 2.52 shows the total absorption A and the total reflectivity R of $\text{Au}^{(1)}/\text{Si}_3\text{N}_4/\text{Au}^{(2)}$ versus the $\text{Au}^{(1)}$ thickness at the above mentioned optimal Si_3N_4 thickness for the wavelength of $1.3\text{ }\mu\text{m}$ (a), and $0.83\text{ }\mu\text{m}$ (b). More than 98% absorption can be attained for both cases.

Figure 2.53 shows a schematic drawing of a five-layer MC that contains antireflection films and bimorph films. The five-layer MC deflection as shown in Fig. 2.54 by the thermal stress due to the absorption of the laser light is also derived numerically as follows:

$$d = \frac{C}{D}, \quad (2.43)$$

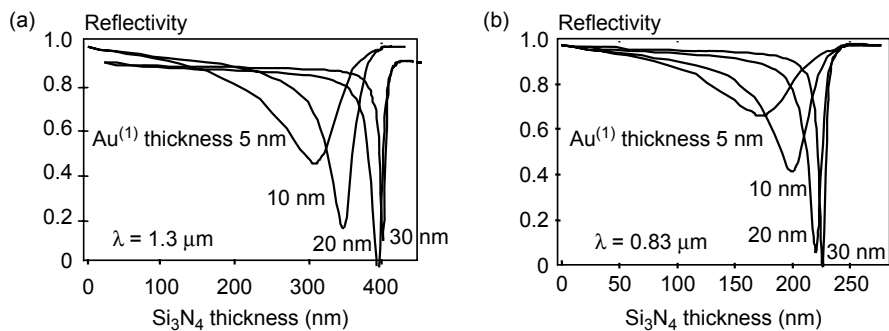


Fig. 2.51. Reflectivity of $\text{Au}/\text{Si}_3\text{N}_4/\text{Au}$ versus the Si_3N_4 thickness for the wavelength of $1.3\text{ }\mu\text{m}$ (a), and $0.83\text{ }\mu\text{m}$ (b)

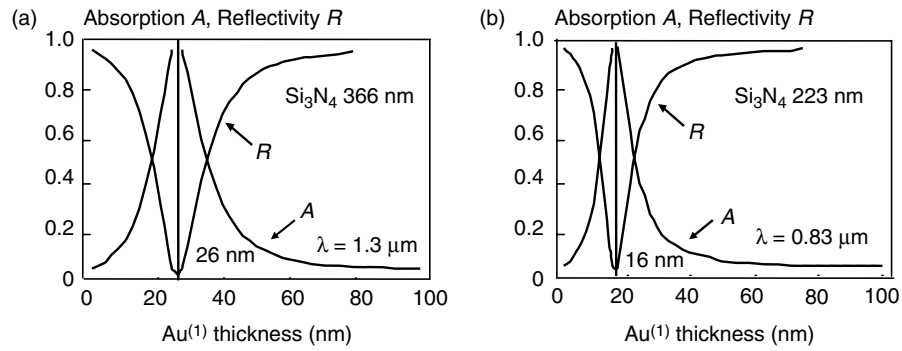


Fig. 2.52. Total absorption A and reflectivity R of Au/Si₃N₄/Au versus the Au thickness at the optimum Si₃N₄ thickness for wavelengths of $1.3 \mu\text{m}$ (a), and $0.83 \mu\text{m}$ (b)

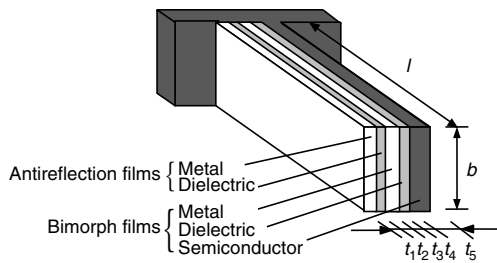


Fig. 2.53. Schematic drawing of a five-layer MC

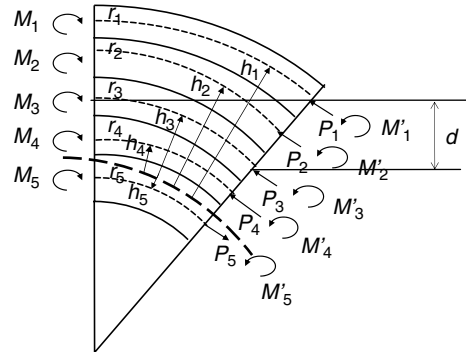


Fig. 2.54. Deflection of a five-layer MC and internal stress due to temperature change

where

$$\begin{aligned}
 & [E_1 E_2 t_1 t_2 (\alpha_1 - \alpha_2)(t_1 + t_2) + E_1 E_3 t_1 t_3 (\alpha_1 - \alpha_3)(t_1 + 2t_2 + t_3) \\
 & + E_1 E_4 t_1 t_4 (\alpha_1 - \alpha_4)(t_1 + 2t_2 + 2t_3 + t_4) \\
 C = 3\Delta T l^2 & + E_1 E_5 t_1 t_5 (\alpha_1 - \alpha_5)(t_1 + 2t_2 + 2t_3 + 2t_4 + t_5) \\
 & + E_2 E_3 t_2 t_3 (\alpha_2 - \alpha_3)(t_2 + t_3) \\
 & + E_2 E_4 t_2 t_4 (\alpha_2 - \alpha_4)(t_2 + 2t_3 + t_4) + E_2 E_5 t_2 t_5 (\alpha_2 - \alpha_5) \\
 & \times (t_2 + 2t_3 + 2t_4 + t_5) \\
 & + E_3 E_4 t_3 t_4 (\alpha_3 - \alpha_4)(t_3 + t_4) + E_3 E_5 t_3 t_5 (\alpha_3 - \alpha_5)(t_3 + 2t_4 + t_5) \\
 & + E_4 E_5 t_4 t_5 (\alpha_4 - \alpha_5)(t_4 + t_5)] \\
 & [E_1 E_2 t_1 t_2 (t_1 + t_2)^2 + E_1 E_3 t_1 t_3 (t_1 + 2t_2 + t_3)^2 \\
 & + E_1 E_4 t_1 t_4 (t_1 + 2t_2 + 2t_3 + t_4)^2 \\
 D = 3 & + E_1 E_5 t_1 t_5 (t_1 + 2t_2 + 2t_3 + 2t_4 + t_5)^2 + E_2 E_3 t_2 t_3 (t_2 + t_3)^2 \\
 & + E_2 E_4 t_2 t_4 (t_2 + 2t_3 + t_4)^2 \\
 & + E_2 E_5 t_2 t_5 (t_2 + 2t_3 + 2t_4 + t_5)^2 + E_3 E_4 t_3 t_4 (t_3 + t_4)^2 \\
 & + E_3 E_5 t_3 t_5 (t_3 + 2t_4 + t_5)^2 + E_4 E_5 t_4 t_5 (t_4 + t_5)^2] \\
 & +(E_1 t_1 + E_2 t_2 + E_3 t_3 + E_4 t_4 + E_5 t_5) \\
 & \times (E_1 t_1^3 + E_2 t_2^3 + E_3 t_3^3 + E_4 t_4^3 + E_5 t_5^3)
 \end{aligned}$$

Figure 2.55 shows the deflection of a bimorph MC with the antireflection coating, and $\text{Au}^{(2)}$ as a parameter. Deflection greater than $\lambda/2$ is possible when $\text{Au}^{(2)}$ is thicker than 78 nm for InP ($\lambda = 1.3 \mu\text{m}$), and thicker than 81 nm for GaAs ($\lambda = 0.83 \mu\text{m}$) LDs. As a result, the final five-layer MC design with antireflection and bimorph structures is shown in Table 2.2.

We derived an analytical model for a five-layer semiconductor MC to predict beam deflection that occurs due to temperature changes caused by a laser light. We confirmed that the tip deflection of a bimorph MC (0.1- μm gold layer and a 0.1- μm Si_3N_4 dielectric layer) with an antireflection coating is enhanced by more than a half-wavelength to widen the tunable LD wavelength variation.

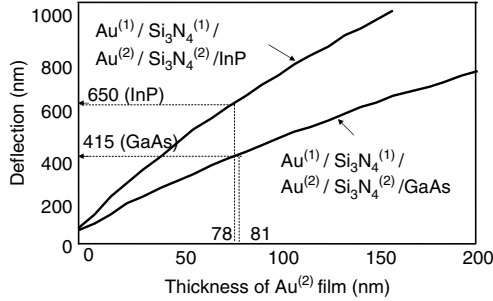


Fig. 2.55. Deflection of bimorph MCs with antireflection coating, $\text{Au}^{(2)}$ thickness as a parameter

Table 2.2. Final design of the MC with antireflection and bimorph structures

semiconductor	InP	GaAs
wavelength (nm)	1,300	830
thickness (nm)		
Au ⁽¹⁾	16	26
Si ₃ N ₄ ⁽¹⁾	366	223
Au ⁽²⁾	100	100
Si ₃ N ₄ ⁽²⁾	100	100
semiconductor	2,000	2,000
optical absorption (%)	98	99
deflection (nm) for the temperature rise of 100°C	767	486
$\lambda/2$ (nm) for reference	650	415

We produced a trial fabrication of the solitary semiconductor MC and LDs on the surface of a GaAs substrate. The MC was 3 μm thick, 5 μm width and 110 μm long, with a resonant frequency of 200.6 kHz, and the LD operated at the threshold current of 46 mA. We predict that with this MC design, a 30-nm wavelength variation will be possible for the photothermally driven micromechanical tunable LD.

2.5.2 Reflectivity Design of LD and Disk Medium for an OSL Head

An integrated optical head design is developed and its performance is assessed through the evaluation of LD efficiency, write-erase power margin, phase change medium sensitivity and permissible read power.

Design Method

The detailed parameter of the optically switched laser (OSL) head is shown in Fig. 2.35. Here, R_1 and R_2 are the reflectivities of the LD, and R_3^l and R_3^h are those of the two states of the recording medium. They confirm a complex cavity laser. The spacing h between the laser facet and the medium surface is 2 μm which is decided as that the FWHM beam width is less than 1 μm on the medium.

The reflectivity R_1 is improved by high reflectivity coating (HRC) to increase the light output P_2 for thermal recording, and the reflectivity R_2 is reduced to 0.01 by ARC to suppress the light output variation due to the spacing. Figure 2.56 shows a design guideline. Due to the relatively large number of free parameters, it is advantageous to first decide

$$h = 2 \mu\text{m}, \quad (2.44)$$

$$R_2 = 0.01 \quad (2.45)$$

on the basis of the experimental results described above, and then to design R_1 , R_3^h , and R_3^l taking design tradeoffs into consideration.

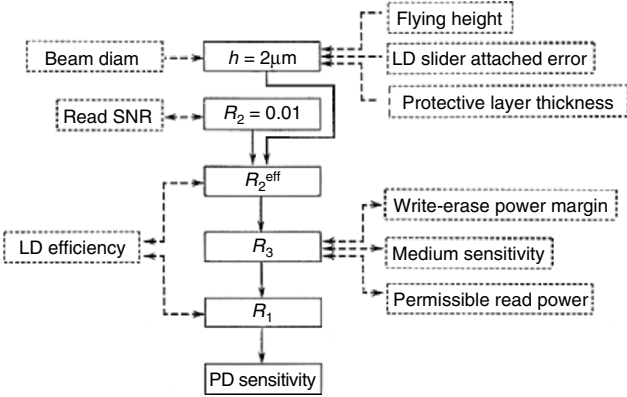


Fig. 2.56. Reflectivity design guideline for an optical disk using OSL head.

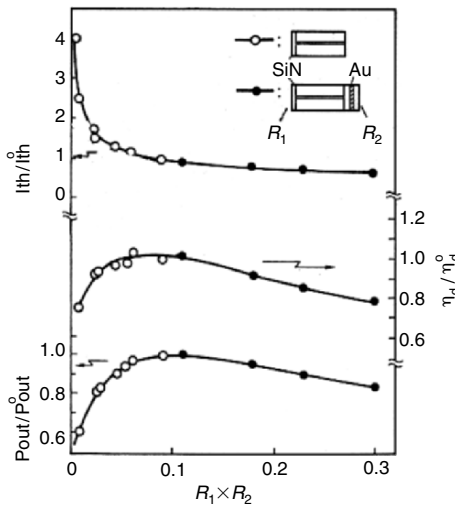


Fig. 2.57. Dependence of normalized I_{th} , η_d , and P_{out} on LD reflectivities product $R_1 \times R_2$ [2.32]

Evaluation Criteria of the Design

The light output for a complex cavity LD is calculated as shown in Fig. 2.36 using effective reflectivity R_2^{eff} instead of R_2 . Data signals are obtained by the light output difference due to the medium reflectivity of the two states. The relationship between the light output difference and a medium high reflectivity of R_3^{h} , with the medium reflectivity difference $R_3^{\text{h}} - R_3^{\text{l}}$ as a parameter can be calculated. Light output difference is an important parameter from the permissible read power and write-erase power margins [2.33].

LD efficiency, as shown in Fig. 2.57, such as the maximized total light output and medium sensitivity (absorption) also be considered. We proceed

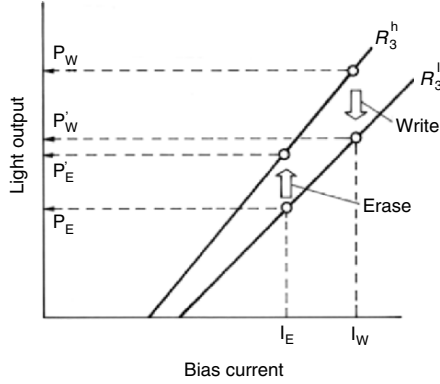


Fig. 2.58. Write-erase performance for a phase change medium. The write-erase power margin, $P_W - P'_E$ and $P'_W - P_E$, for a phase change medium is shown

with our analysis, considering the following design quantities [2.33]:

$$\text{LD efficiency} : 0.2 \geq R_1 \times R_2^{\text{eff}} \geq 0.05, \quad (2.46)$$

$$\text{Light output ratio} : P_2/P_1 \geq 8, \quad (2.47)$$

$$\text{Medium write sensitivity (absorption)} : A \geq 0.75. \quad (2.48)$$

Write-erase power margin for $P_W = 30 \text{ mW}$ and $P_E = 15 \text{ mW}$ for the phase change medium shown in Fig. 2.58

$$P_W - P'_E \geq 10 \text{ mW} \text{ and } P'_W - P_E \geq 10 \text{ mW}, \quad (2.49)$$

$$\text{Permissible read power} : P_R \leq 1.5 \text{ mW}, \quad (2.50)$$

which is 1/10 of the erasing power P_E . Both R_1 and $R_3^h - R_3^l$ are restricted to some appropriate values examined later.

Prefeared Reflectivity Design

Reflectivity design was performed for two kinds of LD; the wavelength of LD#1 is $1.3 \mu\text{m}$ and LD#2 is $0.83 \mu\text{m}$ (LD#2 has a higher quantum efficiency than LD#1). Appropriate choices are made for LDs and the phase change medium from the criteria of (2.46)–(2.50).

As the effective reflectivity R_2^{eff} (medium reflectivity) decreases, the light output ratio (P_2/P_1) increases, but the write-erase power margin ($P_W - P'_E$ and $P'_W - P_E$) decreases. The preferred medium reflectivities for LD#1 can be chosen as follows:

$$R_1 \geq 0.7, \quad (2.51)$$

$$R_2 \cong 0.01,$$

$$0.21 \geq R_3^h \geq 0.14,$$

$$0.10 \geq R_3^h - R_3^l \geq 0.02.$$

The preferred medium reflectivities for LD#2 can be chosen as follows:

$$\begin{aligned} R_1 &\geq 0.7, \\ R_2 &\cong 0.01, \\ 0.21 &\geq R_3^h \geq 0.14, \\ 0.05 &\geq R_3^h - R_3^l \geq 0.02. \end{aligned} \quad (2.52)$$

Compared with LD#2, LD#1 has advantages of a large permissible range medium reflectivity, but has the disadvantage of temperature rise due to low quantum efficiency.

In summary, the optimum design head consists of an LD facet with a reflectivity of $R_1 \cong 0.7$ and $R_2 = 0.01$, and a medium high reflectivity of $0.21 \geq R_3^h \geq 0.14$. The reflectivity difference between the two states $R_3^h - R_3^l \cong 0.05$ and the spacing between laser facet and medium is $2\text{ }\mu\text{m}$. This flying type optical head is now developing for the candidate of an ultra-high density optical near field storage (see Sect. 5.4.2).

Problems

2.1. Calculate (2.27) for Si and show the relationship between the cantilever resonant frequency f_0 and the length l in the range of $500\text{ }\mu\text{m} \geq l \geq 0$, thickness $t(5\text{ }\mu\text{m} \geq t \geq 0.5)$ as a parameter. Here, $\lambda_0 = 1.875$, $E = 1.9 \times 10^{12}$ dyne/cm², $\rho = 2.3$ g/cm³, l is the cantilever length, and t is the thickness.

2.2. Calculate spring constant $K = Et^3b/4l^3$ for Si and show the relationship between K and the length l in the same conditions described in Problem 2.1.

2.3. Calculate the light output ratio P_2/P_1 , with medium reflectivity R_3 as a parameter, versus the medium side laser facet reflectivity R_2 , where P_1 is the light from PD side and P_2 is from medium side, $R_1 = 0.7$, $h = 2\text{ }\mu\text{m}$.

2.4. What are the specific tracking issues that need to be addressed and solved for the higher disk rotation rate?

2.5. Are there any reasons to use a 1.3-μm wavelength LD?

2.6. Is contamination a serious issue, in practice, for the flying optical head?

3

Optical Tweezers

Solar radiation pressure causes manmade satellites to tilt in orbit and also to induce the rotational bursting of meteorites and tektites in space. The effect of optical pressure appears notable even in daily life when an object becomes smaller than several micrometers. Optical tweezers are tools that use optical pressure in trapping microobjects including living cells and microorganisms, and also in directionally rotating artificial microobjects fabricated by micromachining. Given their noninvasive nature, optical tweezers are useful particularly in biological processes. Nowadays, these optical tweezers are used to control and manipulate various types of micro/nanoobject in various research and industrial fields.

In this chapter, we first analyze the trapping efficiency of optical tweezers using geometrical optics and then compare the results with those obtained in experiments. Finally, we show the various applications of optical tweezers.

3.1 Background

Figure 3.1 shows a photograph of Halley's comet taken on March 21, 1986 at Nobeyama near Tokyo. The tail of the comet is said to be directed along the direction of solar radiation pressure. An optical pressure force is very weak but can be visualized as the tail of a comet in space. This force was measured on earth soon after the laser was invented. The measurement method is illustrated in Fig. 3.2 [3.1]. Small mirrors (vanes) were suspended by a gold wire in a vacuum chamber. Pulsed light emitted from a ruby laser hits the first vane, and light reflected from the vane hits the second vane and passes through an exit beam splitter. The reflection of the beam from both vanes generates sufficient optical pressure force to tilt the vanes and the scale mirror fixed to the lower end of the suspension wire, which changes light deflection on the scale. The experimental results were obtained in vacuum (10^{-5} Torr) under the conditions listed in Table 3.1 to eliminate the thermal effect of air molecules induced by light absorption.



Fig. 3.1. The tail of Halley's comet is directed along the direction of the solar light. This photograph was taken on March 21, 1986 at Nobeyama near Tokyo, Japan

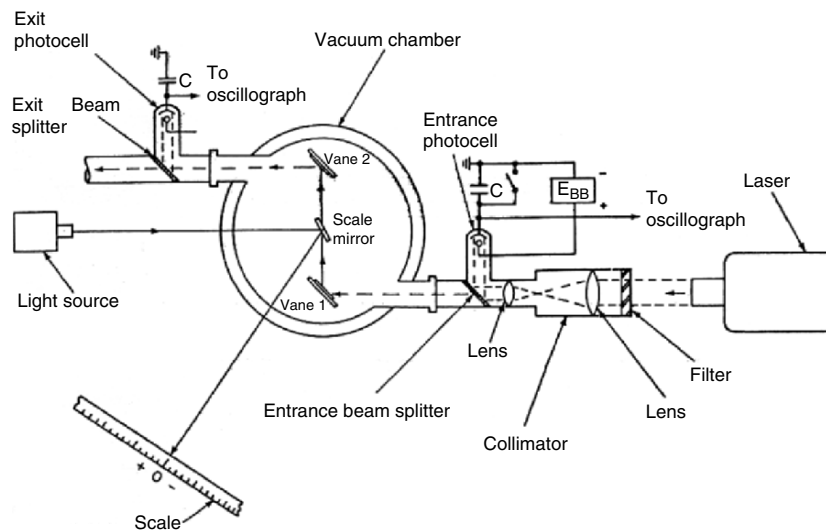


Fig. 3.2. Top view of two-vane torsion pendulum for measuring optical pressure force. Reprinted from [3.1] with permission by American Institute of Physics, Copyright Clearance Center License Number: 1273781240969

Table 3.1. Physical characteristics of optical pressure measurement [3.1]

item	value
moment of inertia, I	7.75 g cm^2
torque constant, k	$1.0 \times 10^{-2} \text{ dyne cm rad}^{-1}$
distance between vane centers, $2r$	7.40 cm
distance of scale from suspension, D	200 cm
transmissivity of window, T	0.92
reflectivity of vane, R	0.75
mass of suspension, M	0.98 g

Ashkin and his coworkers at ATT Bell Laboratory demonstrated a trapping phenomenon due to the optical pressure force generated by counterpropagating laser beams in the early 1970s [3.2]. There is a great deal of theoretical and experimental knowledge and technology in this field [3.3, 3.4]. Here, a single-beam gradient-force optical trap is applied in various scientific and engineering fields including biology [3.3, 3.5], microchemistry [3.6], physics [3.7], micromechanics [3.8]. It consists of a single beam that is strongly focused by a high-numerical-aperture (high-NA) objective lens of a microscope.

Table 3.2 shows typical conditions for the optical trap and Table 3.3 shows a list of the refractive indexes and densities of typical materials for trapping. Optical trapping is possible not only for solid particles but also for liquid particles and living cells, if they are transparent for the laser wavelength used and the refractive indexes are slightly higher than that of the surrounding medium. They include a droplet of paraffin wax (refractive index of 1.47) in ethanol liquid (refractive index of 1.36). The droplet becomes larger at the trapping position through successive droplet fusion. Another example is the living cell of a blade of grass (weed). We can manipulate a mitochondrion in the cell by illuminating and scanning it with a laser beam. Figure 3.3 shows that we can transfer an optically trapped particle from one beam to another.

Masuhara et al. [3.9] developed a laser scanning micromanipulation system and demonstrated the simultaneous trapping of multiple particles, micrometer-size particle pattern formation, and driving of particles along the patterns. Figure 3.4 shows that multiple particles are trapped by a single laser beam and aligned in the designed pattern (Japanese character “light”) formed by scanning the laser beam. This pattern can be moved or deformed in the space according to the scanning pattern. Figure 3.5 shows that we can trap particles so as to obtain a spatial light energy distribution pattern by interference fringe, which increases the efficiency of particle manipulation.

Table 3.2. Conditions for optical trapping

light source (wavelength)	YAG laser (1.06 μm), Ar ⁺ laser (0.515 μm), laser diode(0.4–1.3 μm)
lens	large NA, small NA, optical fiber
object	transparent for the light used, size (20 nm–50 μm), refractive index
circumstance	in air, in liquid, at the interface

Table 3.3. Microsphere materials for the analysis of the trapping efficiency with the wavelength of 1.06 μm

material	water	glass	polysterene	polyimide	SU-8
refractive index n	1.33	1.51	1.60	1.53	1.66 ($\lambda = 633 \text{ nm}$)
density $\rho(\text{g ml}^{-1})$	1.0	2.54	1.06	1.49	–

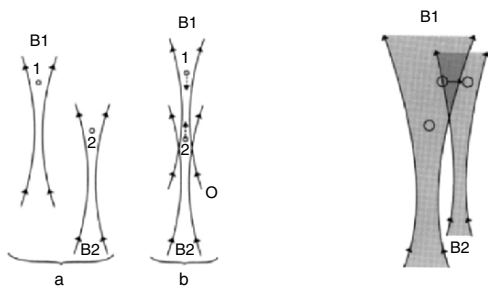


Fig. 3.3. Transfer of optically trapped particle from beam to beam

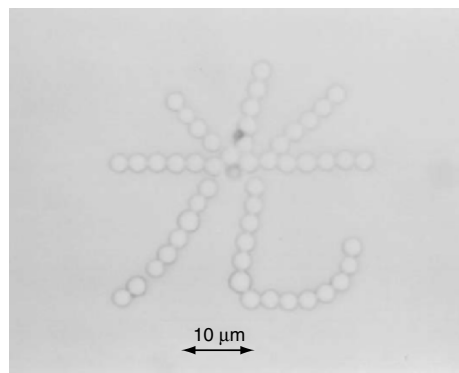


Fig. 3.4. Microsphere spatial pattern formation by scanning a focused laser beam [3.6]. Courtesy of H. Masuhara, Osaka University, Japan

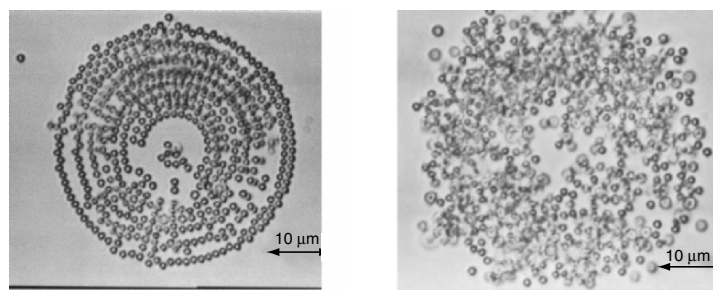


Fig. 3.5. Micrometer-size particle formation due to light intensity formed by interference fringe pattern [3.6]. Courtesy of H. Masuhara, Osaka University, Japan

Details of the analytical and experimental studies of the single-beam optical trap are presented in the following sections.

3.2 Theoretical Analysis

Trapping force/efficiency can be calculated with either a ray optics (RO) model [3.4] or an electromagnetic force (EM) model, as shown in Fig. 3.6 [3.10]. In the RO, a light beam is decomposed into individual rays with appropriate intensity and direction. The total force on the sphere is computed from the sum of the contributions of each ray entering the aperture. The RO model is applicable only to an object much larger than the wavelength (Mie regime). On the other hand, the EM model is applicable to an object much less than the wavelength (Rayleigh regime).

The RO model is used in Chaps. 3 and 4 to calculate the optical trapping force (on the piconewton order) exerted on a micrometer-size object. The Brownian movement is also considered for the small sphere [3.11]. The EM model is used in Chap. 5 for the nanometer-size object.

3.2.1 Optical Pressure

When a ray in a medium of refractive index n_1 is incident to boundary with a medium of index n_2 , what happens? Figure 3.7 shows reflected and refracted rays, the angle of incidence θ_1 , reflection θ_r , and refraction θ_t and the momentum of incidence M_i , reflection M_r , and refraction M_t . Optical pressure force, that is, momentum change per second, acts as to conserve the momentum of light at the interface. The direction of optical pressure is normal to the surface because the momentum in the transverse direction is continuous (Example 3.1).

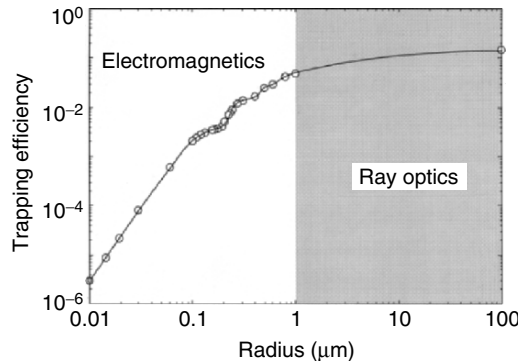


Fig. 3.6. Trapping efficiencies calculated with a ray optics model and an electromagnetic force model. Reprinted from [3.10] with permission by Michael W. Berns

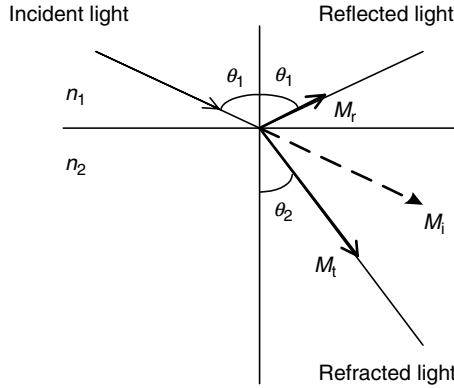


Fig. 3.7. Relationship between incident, reflected, and refracted rays at interface

The optical pressure force F exerted due to the reflection and refraction at the interface is given by (3.1) considering the momentum change in the vertical direction (Example 3.2).

$$F = \left\{ (1 + R) \cos \theta_1 - \frac{n_2}{n_1} T \cos \theta_2 \right\} \frac{n_1 P}{c}, \quad (3.1)$$

where c is the speed of light in vacuum, T and R are the Fresnel transmission and reflection coefficient, respectively. In the case of circularly polarized light, R is given as the average of R_s for s-polarization and R_p for p-polarization leading to (3.2)

$$R = \frac{1}{2}(R_s + R_p) = \frac{1}{2} \left\{ \frac{\tan^2(\theta_2 - \theta_1)}{\tan^2(\theta_2 + \theta_1)} + \frac{\sin^2(\theta_2 - \theta_1)}{\sin^2(\theta_2 + \theta_1)} \right\}. \quad (3.2)$$

Since no absorption is assumed

$$T = 1 - R. \quad (3.3)$$

The total optical pressure acting on a microobject is the vector sum of the force over the entire cross-section.

Example 3.1. Show that optical pressure is perpendicular to the surface.

Solution. When a ray with a momentum of M_i is incident to the interface between index of n_1 and n_2 with an angle of θ_1 , the momentums of reflection M_r and refraction M_t are expressed as $M_r = RM_i$ and $M_t = (n_2/n_1)TM_i$ which comes from the speed of light c/n and the light energy Mc/n . The transverse components of the momentum of incidence, reflection, and refraction rays are

$$\begin{aligned} &M_i \sin \theta_1 \\ &M_r \sin \theta_1 = RM_i \sin \theta_1, \\ &M_t \sin \theta_2 = (n_2/n_1)TM_i \sin \theta_2 = TM_i \sin \theta_1. \end{aligned}$$

As a consequence, the momentum change along the transverse direction before and after the ray incidence is expressed as

$$M_i \sin \theta_1 - (M_r \sin \theta_1 + M_t \sin \theta_2) = M_i \sin \theta_1 (1 - R - T) = 0.$$

Example 3.2. Show that the optical pressure force exerted by a ray incidence at the interface is given by (3.1).

Solution. The vertical components of the momentum of incidence, reflection, and refraction rays are

$$\begin{aligned} M_i \cos \theta_1, \\ M_r \cos \theta_1 = RM_i \cos \theta_1, \\ M_t \cos \theta_2 = (n_2/n_1)TM_i \cos \theta_2. \end{aligned}$$

The momentum change along the vertical direction before and after the ray incidence is

$$M_i \cos \theta_1 - (-M_r \cos \theta_1 + M_t \cos \theta_2) = M_i[(1 + R) \cos \theta_1 - (n_2/n_1)T \cos \theta_2].$$

Since $M_i = n_1 P/c$, the optical pressure F is given as (3.1).

In summary, a light momentum change ΔM per second through reflection, refraction, scattering and absorption causes the optical pressure F . F increases as the incident angle increases, leading to the lifting of the microobject if laser light is strongly focused by an objective lens with a high NA.

The principal relationship between F and the power P is

$$F = Q(n_1/c)P, \quad (3.4)$$

where Q is a nondimensional efficiency parameter (called trapping efficiency) and $n_1 P/c$ is the incident momentum per second of a ray of the power P in a medium of the refractive index of n_1 . The trapping efficiency Q depends on not only the object shape and refractive index but also the optical parameters of the trapping laser beam. It has the maximum value of 2 when all incident rays are reflected from a totally reflecting mirror.

3.2.2 Optical Trapping Efficiency

Qualitative optical trapping description is possible for a small transparent particle whose refractive index is slightly higher than that of the surrounding medium. Figure 3.8a shows that the focused laser beam illuminates the upper part in a microsphere. Consider a typical pair of rays a and b of the focused beam under the assumption of zero surface reflection. When an incident ray refracts at the top surface, the momentum changes and the upward optical pressure force (perpendicular to the sphere surface) F_{at} is exerted. The optical pressure force F_{ao} is also exerted when ray a is emitted from the bottom surface. The sum of the both pressure force leads to force F_a owing to ray a. Similarly, ray b produces the pressure force F_b . The sum of F_a

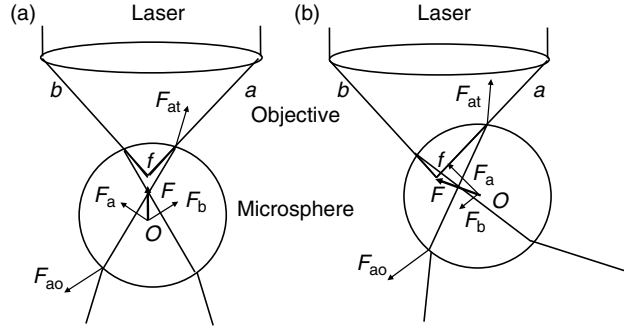


Fig. 3.8. Qualitative description of optical trap. The microsphere is transparent and its refractive index is slightly higher than that of the surrounding medium [3.4]

and F_b is shown pointing in the direction of the laser focus f from the center of the sphere. As a result, the sphere is trapped stably at the point where the optical pressure force F balances the difference between the gravity force and the buoyant force.

We can see, for the arbitrary displacement of the sphere center O from the focus f , that the vector sum of F_a and F_b gives a net optical pressure force F directs to the focus as shown in Fig. 3.8b. Since the optical pressure F is expressed as (3.4), the axial and transverse trapping force analysis results the simulation of the nondimensional Q of the object, beam convergence angle, sphere size, shape and relative refractive index with respect to the surrounding medium, polarization state, and beam profile as parameters.

First, consider a ray of the power P incident to a microsphere at the angle θ_1 . Figure 3.9 shows the geometry for this model and trapping force is calculated according to Ashkin [3.4]. The expressions of the net optical pressure by the emerging rays in the direction parallel (F_s : scattering force) and perpendicular (F_g : gradient force) to the incident ray can be expressed (Example 3.3) as

$$F_s = \left[1 + R \cos 2\theta_1 - \frac{T^2 \{ \cos 2(\theta_1 - \theta_2) + R \cos 2\theta_1 \}}{1 + R^2 + 2R \cos 2\theta_2} \right] \frac{n_1 P}{c} = Q_s \frac{n_1 P}{c}, \quad (3.5)$$

$$F_g = \left[R \sin 2\theta_1 - \frac{T^2 \{ \sin 2(\theta_1 - \theta_2) + R \sin 2\theta_1 \}}{1 + R^2 + 2R \cos 2\theta_2} \right] \frac{n_1 P}{c} = Q_g \frac{n_1 P}{c}, \quad (3.6)$$

where θ_1 is the incident angle, θ_2 is the refracted angle, T and R are the Fresnel transmission and reflection coefficients, and Q_s and Q_g are the scattering and gradient trapping efficiency, respectively. As a result, total Q and total F are

$$Q_t = \sqrt{Q_s^2 + Q_g^2}, \quad (3.7)$$

$$F_t = \sqrt{F_s^2 + F_g^2} = Q_t \frac{n_1 P}{c}. \quad (3.8)$$

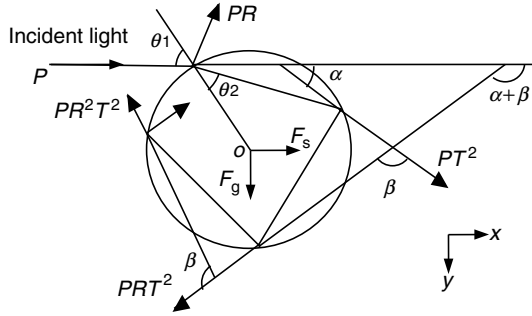


Fig. 3.9. Optical pressure force on microsphere exerted by single incident ray [3.4]

Example 3.3. Show that the optical pressure forces exerted by a ray of the power P incident to a dielectric microsphere of the refractive index n_2 at the angle θ_1 surrounding the medium of n_1 are given by (3.5) and (3.6).

Solution. When the ray strikes the sphere, a fraction of the light PR is reflected and the remainder is transmitted into the sphere, as shown in Fig. 3.9. No absorption is assumed for the sphere. The transmitted fraction produces an infinite number of internal reflections within the sphere and infinite numbers of scattered rays escape the sphere. A series of scattered ray powers are expressed as

$$PR, PT^2, PRT^2, \dots, PR^nT^2, \dots \quad (n = 0, 1, 2, 3, \dots)$$

where T and R are the Fresnel transmission and reflection coefficients on the surface at θ_1 , respectively. The angles of the scattered rays with the incident ray are expressed as

$$\pi + 2\theta_1, \alpha, \alpha + \beta, \alpha + 2\beta, \dots, \alpha + n\beta, \dots \quad (n = 0, 1, 2, 3, \dots),$$

where $\alpha = 2(\theta_1 - \theta_2)$ and $\beta = \pi - 2\theta_2$.

Since the optical pressure force in the x -direction is defined as the momentum change per second due to the scattered rays

$$Fs = \frac{n_1 P}{c} - \left\{ \frac{n_1 PR}{c} \cos(\pi + 2\theta_1) + \sum_{n=0}^{\infty} \frac{n_1 P}{c} R^n T^2 \cos(\alpha + n\beta) \right\},$$

where $n_1 P/c$ is the incident light momentum per second in the x -direction. Similarly, for the y -direction,

$$Fg = 0 - \left\{ \frac{n_1 PR}{c} \sin(\pi + 2\theta_1) + \sum_{n=0}^{\infty} \frac{n_1 P}{c} R^n T^2 \sin(\alpha + n\beta) \right\}.$$

Here introducing the following equations to the sum over n in the above equations lead to (3.5) and (3.6).

$$\sum_{n=0}^{\infty} R^n \cos(\alpha + n\beta) = \frac{\cos \alpha - R \cos(\alpha - \beta)}{1 - 2R \cos \beta + R^2},$$

$$\sum_{n=0}^{\infty} R^n \sin(\alpha + n\beta) = \frac{\sin \alpha - R \sin(\alpha - \beta)}{1 - 2R \cos \beta + R^2}.$$

Since $\theta_2 = \arcsin\{(n_1/n_2) \sin \theta_1\}$, R is from (3.2), and T is from (3.3), we can express (3.5) and (3.6) using a ray incident angle θ_1 .

Figure 3.10 shows the dependence of the trapping efficiencies Q_s , Q_g and Q_t on θ_1 . The microsphere index of refraction is $n_2 = 1.5$ (glass) and the surrounding medium index of refraction is $n_1 = 1.33$ (water). The maximum Q_g is obtained at an incident angle of 71.8° . Therefore, the numerical aperture of the objective lens corresponding to the angle $\arcsin(\text{NA}/n_1)$ is greater than 1.2, which leads to the tight convergence of the laser beam.

For the calculations presented earlier, a trapping force is obtained by the vector sum of the contributions of all rays within the convergence angle. This trapping force varies according to the focus of the laser beam. Axial trapping efficiency is defined when the focus is on the center line of the microsphere parallel to the optical axis, as shown in Fig. 3.11. Transverse trapping efficiency is defined when the focus is on the center line of the microsphere perpendicular to the optical axis, as shown in Fig. 3.12.

Figure 3.13 shows the total trapping efficiency Q_t exerted on a polystyrene sphere suspended in water by a trap with a uniformly filled input aperture of $\text{NA} = 1.25$ which is focused along the optical axis at positions $+s$ and $-s$ below the center of the sphere. In the figure, (a) shows the trapping efficiency for the axial trap (Example 3.4) and (b) that for the transverse trap (Problem 3.4). Both show the maximum when the focus is near the surface of the sphere and decrease as the focus comes to the center of the sphere. The positions for the maximum trapping efficiency are $f = -1.02$ and $f = 1.05$ for the axial trap, and $f = \pm 1.05$ for the transverse trap. At these positions the laser power for trapping become minimum. We can also find that

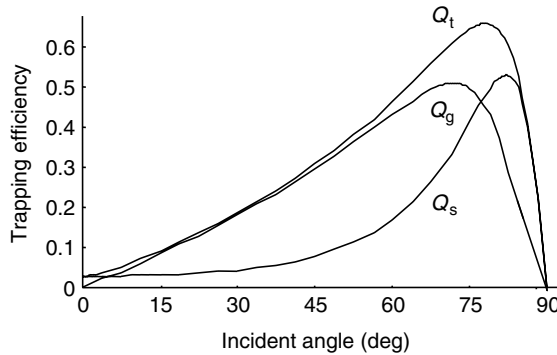


Fig. 3.10. Predicted trapping efficiency dependence on incidence angle θ_1 for Q_s , Q_g and Q_t .

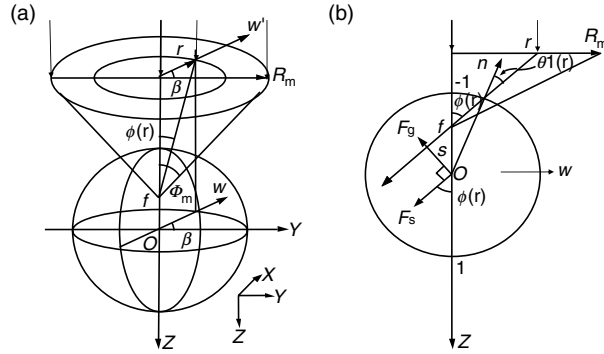


Fig. 3.11. Geometry for calculating axial trapping efficiency of polystyrene microsphere. The laser focus is on the optical axis which is parallel to the center line of the microsphere [3.4]

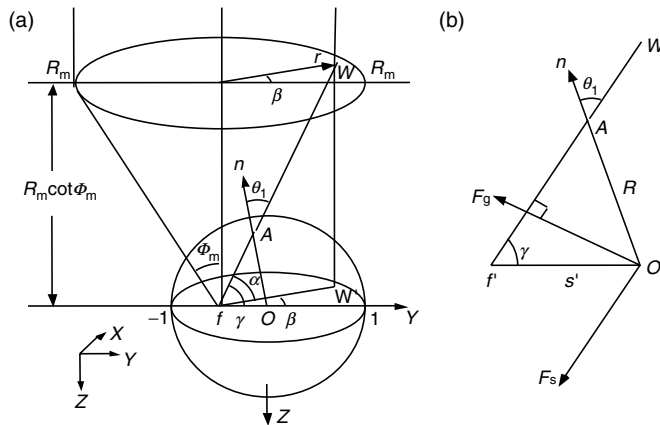


Fig. 3.12. Geometry for calculating the transverse trapping efficiency of polystyrene microsphere. The laser focus is located along the transverse center line of the sphere [3.4]

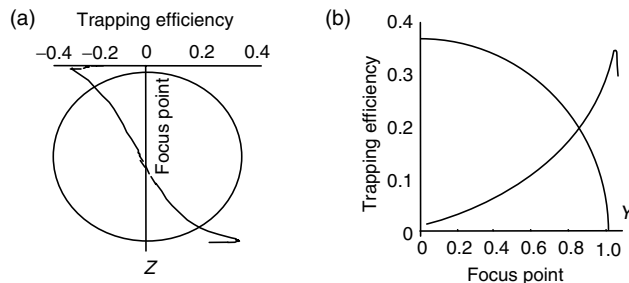


Fig. 3.13. Total trapping efficiency Q_t exerted on a polystyrene microsphere suspended in water by trap with a uniformly filled input aperture of NA = 1.25 for axial (a), and for transversal (b) directions

Table 3.4. Maximum trapping efficiency for axial trap with various laser beam profiles

beam profile	downward directed	upward directed
Gaussian (TEM_{00})	0.21	0.33
uniform	0.25	0.39
donut (TEM_{01}^*)	0.26	0.41

the upward directed beam is more effective in trapping the microsphere than the downward-directed beam. Table 3.3 shows microsphere materials for the analysis in this book.

The trapping efficiency dependence on the incident angle of a ray means that trapping efficiency is related to the profile of the laser beam. Table 3.4 shows the maximum trapping efficiency calculated for input beams with various mode intensity profiles: Gaussian, uniformly filled, and donut. The maximum Q increases as the outer part intensity increases. Good trapping is possible when the outer part of the aperture is filled by a high intensity to give a laser beam with a high convergence angle.

Example 3.4. Calculate the axial trapping efficiency for a microsphere when the focus of the uniformly input laser beam is along the optical axis in the center line of the sphere.

Solution. First, we find the incident angle $\theta_1(r, \beta)$ of a ray entering the input aperture of the objective lens at the arbitrary point (r, β) , as shown in Fig. 3.11a [3.4]. Since axial trapping efficiency is independent on β due to axial symmetry, we consider r -dependence for the $\theta_1(r, \beta)$. The angle $\phi(r)$ between the incidence ray and z -axis is $r_0 \sin \theta_1(r) = s \sin \phi(r)$ where r_0 is the radius of the microsphere (we take $r_0 = 1$ since the results in the ray optics model are independent on r), s is the distance between the center of the microsphere and the laser focus. From Fig. 3.11b,

$$\phi(r) = \tan^{-1} \left(\frac{r}{R_m} \tan \Phi_m \right),$$

where R_m is the lens radius and Φ_m is the maximum convergence angle. Then the incident angle $\theta_1(r)$ becomes

$$\theta_1(r) = \sin^{-1} \left[\frac{s r \tan \Phi_m}{R_m} \middle/ \sqrt{1 + \left(\frac{r \tan \Phi_m}{R_m} \right)^2} \right].$$

Next, the trapping efficiencies $Q_s(r)$ and $Q_g(r)$ are computed by the vector sum of the contributions of all rays within the convergence angle using (3.5) and (3.6). Here, the y -component is cancelled out due to the symmetry, only the z -component is calculated as

$$\begin{aligned} Q_{sz}(r) &= Q_s(r) \cos \phi(r), \\ Q_{gz}(r) &= Q_g(r) \sin \phi(r). \end{aligned}$$

Finally, Q_s and Q_g are obtained by integrating all the rays using

$$Q_s = \frac{1}{\pi R_m^2} \int_0^{2\pi} \int_0^{R_m} r Q_{sz}(r) dr d\beta = \frac{2}{R_m^2} \int_0^{R_m} r Q_{sz}(r) dr,$$

$$Q_g = \frac{1}{\pi R_m^2} \int_0^{2\pi} \int_0^{R_m} r Q_{gz}(r) dr d\beta = \frac{2}{R_m^2} \int_0^{R_m} r Q_{gz}(r) dr.$$

The total trapping efficiency is given by $Q_t = \sqrt{Q_s^2 + Q_g^2}$.

3.2.3 Effect of Beam Waist

In the ray optics, a laser beam is decomposed into individual rays with appropriate intensity, direction and polarization, which propagate in straight lines. In actual conditions, the focused light beam has a beam waist, which means that each ray varies its direction near the focus. Therefore, the incident angle θ_1 varies from that of the straight line, leading to the recalculation of the exact optical pressure force.

We introduce a Gaussian beam profile (3.9) of a beam waist ω_0 and the depth of focus Z_0 instead of straight line ray optics as

$$\omega_0 = \frac{\lambda}{2NA}, Z_0 = k\omega_0^2, \quad (3.9)$$

where k is the wave number $2\pi/\lambda$, λ is the wavelength, and NA is the numerical aperture of the objective.

To determine the incident angle $\theta_1(r)$ of a Gaussian ray passing at $r = r$ in the aperture of the objective enters at the point (α, β) on the sphere surface as shown in Fig. 3.14. The coordinates (α, β) are expressed

$$\alpha = \frac{2sZ_0^2 - \sqrt{4s^2Z_0^2 - 4Z_0^2 \left(s^2 - r_0^2 + \left(\frac{r}{R_m} \right)^2 \omega_0^2 \right) \left(Z_0^2 + \left(\frac{r}{R_m} \right)^2 \omega_0^2 \right)}}{2 \left(Z_0^2 + \left(\frac{r}{R_m} \right)^2 \omega_0^2 \right)}, \quad (3.10)$$

$$\beta = \sqrt{r_0^2 - (s - \alpha)^2}. \quad (3.11)$$

Then the incident angle $\theta_1(r)$ is calculated as the angle between the tangent vector \mathbf{a} of the Gaussian ray at (α, β) and the direction vector \mathbf{b} pointing to the center of the sphere. After the incident angle $\theta_1(r)$ is defined, the trapping efficiency along the optical axis can be computed. Figure 3.15 show the result for a polystyrene sphere suspended in water. Considering the beam

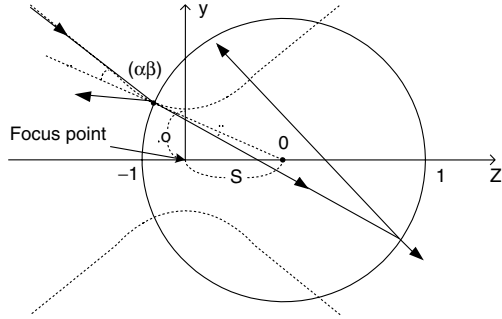


Fig. 3.14. Geometry for calculating exact axial trapping efficiency for microsphere considering beam waist

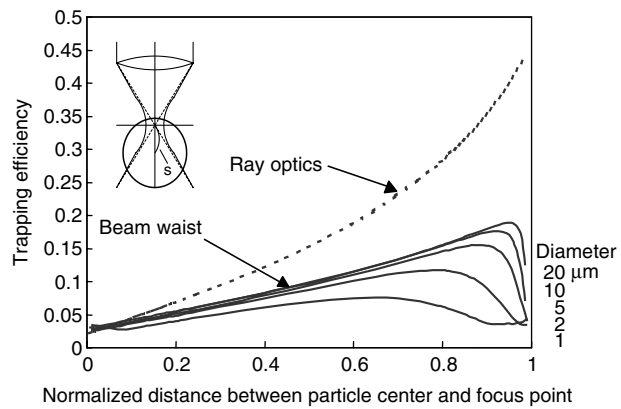


Fig. 3.15. Axial trapping efficiency of polystyrene microsphere suspended in water by converging ray approximations of straight line (ray optics) and parabolic line (beam waist) with beam waist ω_0

waist, it is seen from the figure that the axial trapping efficiency decreases to 50% that of the straight lines. This is caused by the fact that focused rays are almost parallel to the optical axis near the focus, as shown in the upper left sketch in the figure.

Figure 3.16 shows the transverse trapping efficiency along the axis perpendicular to the optical axis. It is seen from the figure that both straight and parabolic Gaussian beam rays have almost the same numerical results. This is based on the fact that the incident angles at the surface of the sphere are almost the same for both approximations because the laser focus is located near the surface edge, maximum trapping efficiency, on the center line of the sphere (see the upper left sketch in the figure).

Example 3.5. Compute the trapping efficiency of a microsphere suspended in water along the propagation axis by the laser beam emitted from the tapered

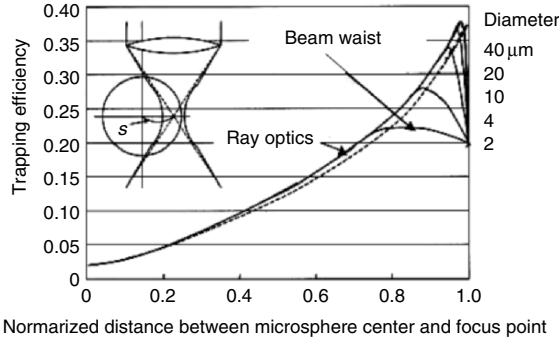


Fig. 3.16. Transverse trapping efficiency of polystyrene microsphere by two converging ray approximations

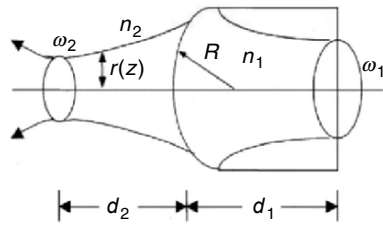


Fig. 3.17. Geometry for calculating trapping efficiency for microsphere along propagation axis by laser beam emitted from tapered lensed optical fiber

lensed optical fiber of curvature $R = 10 \mu\text{m}$, beam waist radius $\omega_1 = 5.0 \mu\text{m}$, core refractive index $n_1 = 1.462$, as shown in Fig. 3.17. The focus distance from the tapered lensed fiber end d_2 and the beam radius $r(z)$ with the beam waist ω_2 are given as

$$d_2 = -\frac{n_2 R(n_2 - n_1)}{(n_2 - n_1)^2 + R^2 \left(\frac{\lambda}{\pi \omega_1^2}\right)^2}, \quad r(z) = \omega_2 \sqrt{1 + \left(\frac{z}{k \omega_2^2}\right)^2}.$$

Solution. An equation of a ray going along the z -direction is expressed by the variable parameter t ($0 \leq t \leq 1$) as

$$y = t \omega_2 \sqrt{1 + \left(\frac{z}{Z_0}\right)^2}, \quad Z_0 = k \omega_2^2,$$

where $t = r/R_m$ and

$$\omega_2 = \frac{\omega_1}{\sqrt{\left(\frac{\pi \omega_1^2}{\lambda}\right)^2 \left(\frac{n_2 - n_1}{n_1 R}\right)^2 + 1}}.$$

The equation of the microsphere located on the z -axis is $(z - s)^2 + y^2 = r_0^2$ where r_0 is the radius of the microsphere and s is the distance between the center of the microsphere and the beam waist. From the two equations given earlier, the intersection point α between the ray and the sphere surface is

$$\alpha = \frac{2sZ_0^2 - \sqrt{4s^2Z_0^2 - 4Z_0^2(s^2 - r_0^2 + t^2\omega_2^2)(Z_0^2 + t^2\omega_2^2)}}{2(Z_0^2 + t^2\omega_2^2)}.$$

According to the Pythagoras theorem

$$\beta = \sqrt{r_0^2 - (s - \alpha)^2}.$$

The incident angle θ_1 of a Gaussian ray entering the sphere at the intersection point (α, β) is the angle between the tangential vector \mathbf{a} of the ray and the vector \mathbf{b} pointing from the point (α, β) to the center of the sphere is

$$\theta_1 = \arccos \frac{\mathbf{a}\mathbf{b}}{|\mathbf{a}| \cdot |\mathbf{b}|},$$

where $\mathbf{a} = (1, f(t, \alpha))$, f is the derivative function of y , that is

$$f(t, \alpha) = \frac{t\omega_2\alpha}{Z_0^2\sqrt{1 + \frac{\alpha^2}{Z_0^2}}},$$

$$\mathbf{b} = (s - \alpha, -\beta).$$

Here

$$\theta_2 = \arcsin\{(n_1/n_2)\sin\theta_1\},$$

$$R(t, s) = \frac{1}{2} \left[\left\{ \frac{\tan(\theta_2 - \theta_1)}{\tan(\theta_2 + \theta_1)} \right\}^2 + \left\{ \frac{\sin(\theta_2 - \theta_1)}{\sin(\theta_2 + \theta_1)} \right\}^2 \right],$$

and $T = 1 - R$.

The trapping efficiencies Q_s and Q_g are given from (3.5) and (3.6) as

$$Q_s = 1 + R(t, s)\cos(2\theta_1) - \frac{T^2 \{ \cos(2\theta_1 - 2\theta_2) + R(t, s)\cos(2\theta_1) \}}{1 + R(t, s)^2 + 2R(t, s)\cos(2\theta_2)},$$

$$Q_g = R(t, s)\sin(2\theta_1) - \frac{T^2 \{ \sin(2\theta_1 - 2\theta_2) + R(t, s)\sin(2\theta_1) \}}{1 + R(t, s)^2 + 2R(t, s)\cos(2\theta_2)}.$$

Considering the z -component,

$$Q'_s = Q_s \cos \phi, \quad \cos \phi = \frac{1}{\sqrt{1 + f(t, s)^2}},$$

$$Q'_g = Q_g \sin \tau, \quad \sin \tau = \frac{f(t, s)}{\sqrt{1 + f(t, s)^2}}.$$

The trapping efficiency along the z -axis due to a ray is given as $Q_z = Q'_s + Q'_g$.

Next, the trapping efficiency due to a circular element of radius β is given as

$$Q_c = 2\pi\beta Q_z.$$

Finally, this trapping efficiency is integrated over the entire cross-section of the sphere for all individual rays using the Shimpson formula under the conditions in Table 3.5.

Figure 3.18 shows the axial trapping efficiency dependence on the distance from the optical fiber end for a polystyrene sphere of radii 2.0 and 2.5 μm . The laser beam profile is Gaussian and the wavelength is 1.3 μm . It is seen from the figure that trapping force increases as axial distance increases from zero to a beam waist of 40 μm , i.e., it increases over the region in which the fiber lens is focusing, and then begins to decrease monotonically as the beam diverges beyond the focus. Therefore, we can expect that the optimum dual fiber lens spacing will exists at a point where axial trapping efficiency is changing rapidly (see Sect. 3.3.4).

3.2.4 Off-axial Trapping by Solitary Optical Fiber

In recent years, studies of optical tweezers have been conducted on optical-fiber tweezers [3.12] to improve their operation in the fields of life science and

Table 3.5. Conditions for analysis of tapered lensed optical fiber trapping efficiency

refractive index	
water	1.33
particle	1.59
fiber core	1.446
beam waist in the core (μm)	5.0
beam waist distance (μm)	49.24
radius of curvature (μm)	10
wavelength (μm)	1.31
particle radius (μm)	2–10

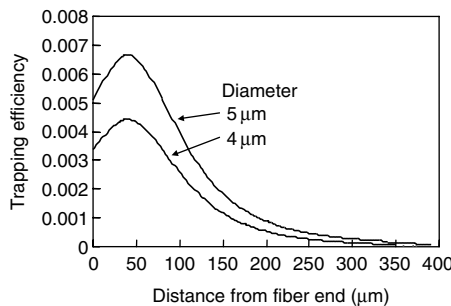


Fig. 3.18. Axial trapping efficiency dependence on distance from optical fiber end of polystyrene sphere

micromachines. The optical fiber implementation of such tweezers is simple and inexpensive. The apparatus that uses a laser diode and an optical fiber is particularly simple since no external optics such as a dichromatic mirror, a beam splitter, and filters are required.

Trapping forces can be resolved into two components: the gradient force F_g , which pulls microspheres in the direction of the strong light intensity, and the scattering force F_s , which pushes microspheres in the direction of light propagation. If a microsphere is located on the light propagation axis, the gradient forces cancel out, thereby resulting in pushing the sphere. Therefore, two counterpropagating coaxially aligned optical fibers are used to trap the sphere suspended in water [3.13]. Although the sphere is stabilized axially at a location where the scattering forces of the two beams balance each other, the trapping in the transverse direction is weak. The freedom of operation for the counterpropagating coaxially aligned optical fibers is poor. In this section, we theoretically analyze an off-axial microsphere trapping force [3.14] in three dimensions in order to trap it with a solitary optical fiber.

Analysis of Off-axial Trapping

Trapping efficiency for a microsphere on an optical axis can be calculated, from axial symmetry, as shown in Fig. 3.19a, by integrating the optical pressure force due to an individual ray in two dimensions. On the other hand, calculation in three dimensions is necessary for the off-axial trapping efficiency because of axial dissymmetry. Figure 3.19b shows that a ray enters at

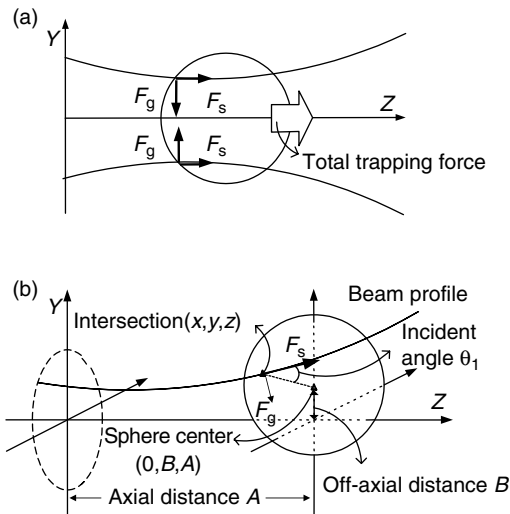


Fig. 3.19. Geometry for calculating trapping efficiency for a microsphere when focus is located on optical axis (a), and at off-axis (b)

the incident angle θ_1 on the arbitrary intersection (x, y, z) of the surface of a sphere, whose center is located at $(0, B, A)$. The y -coordinate is expressed as

$$y_{(x,z)} = B + \sqrt{r^2 - x^2 - (z - A)^2} \quad (3.12)$$

The beam profiles for the x - and y -directions are given as

$$\omega_y = t\omega_0 \sqrt{1 + \left(\frac{z}{Z_0}\right)^2}, \quad \omega_x = u\omega_0 \sqrt{1 + \left(\frac{z}{Z_0}\right)^2}, \quad (3.13)$$

where ω_0 is the radius at the beam waist, Z_0 is the depth of focus, and $t(0 \leq t \leq 1)$ and $u(0 \leq u \leq 1)$ are variable parameters.

Next, the incident angle θ_1 of a ray entering the sphere at the intersection point (x, y, z) is defined as the angle between the tangential vector $\mathbf{a} = (\omega'_x, \omega'_y, 1)$ of the ray and the vector $\mathbf{b} = (x, B - y_{(x,z)}, A - z)$ pointing from the intersection (x, y, z) to the center $(0, B, A)$ of the sphere

$$\theta_1 = \arccos \frac{\mathbf{a} \cdot \mathbf{b}}{|\mathbf{a}| \cdot |\mathbf{b}|}. \quad (3.14)$$

As a result, the trapping efficiencies $Q_{s(x,z)}$ and $Q_{g(x,z)}$ owing to a ray hits the intersection (x, y, z) can be obtained using (3.5) and (3.6). The entire trapping efficiency due to the entire surface of the microsphere is given later.

Figure 3.20 shows the sectional view of the off-axial trapping (a), indicating how to integrate $Q_{s(x,z)}$ and $Q_{g(x,z)}$ along the z -axis (b). Calculate the incident angle at the arbitrary point z in the circle in the yz plane and compute the optical trapping efficiency for the ray. Then integrate $Q_{s(x,z)}$ and $Q_{g(x,z)}$ along the z -direction leading to $Q_{s(x)}^z$ and $Q_{g(x)}^z$ in the yz plane. The integration is carried out for the upper and lower hemispheres individually because of the dissymmetry due to off-axial trapping. The integration starts from the

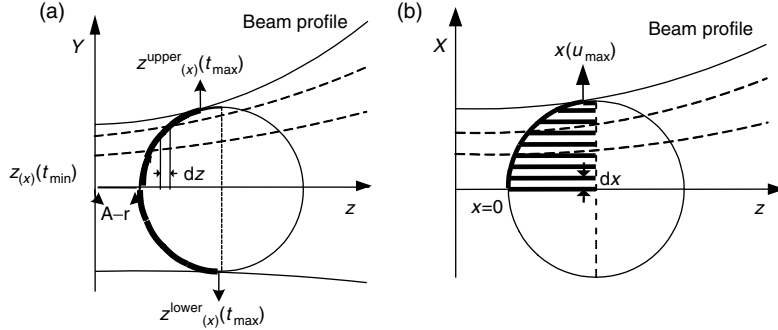


Fig. 3.20. Method of optical pressure integration when a sphere is located at an off-axis, side view (a), and top view (b)

left side $z_{(x)}(t_{\min}) = A - \sqrt{r^2 - x^2}$ in Fig. 3.20a for both the upper and lower hemispheres. The integration ends at the tangential point between the ray and the surface profiles of the upper and the lower hemispheres. The integration end points $z_{(x)}^{\text{upper}}(t_{\max})$ for the upper hemisphere and $z_{(x)}^{\text{lower}}(t_{\max})$ for the lower hemisphere are given by the solution between two equations shown as

$$\left. \begin{aligned} r^2 - x^2 &= (y_{(x,z)} - B)^2 + (z - A)^2 \\ \omega_y &= t\omega_0 \sqrt{1 + \left(\frac{z}{Z_0}\right)^2} \end{aligned} \right\}. \quad (3.15)$$

Then, $Q_{s(x)}^z$ and $Q_{g(x)}^z$ are given as

$$Q_{s(x)}^z = \int_{z_{(x)}(t_{\min})}^{z_{(x)}^{\text{upper}}(t_{\max})} Q_{s(x,z)} dz + \int_{z_{(x)}(t_{\min})}^{z_{(x)}^{\text{lower}}(t_{\max})} Q_{s(x,z)} dz, \quad (3.16)$$

$$Q_{g(x)}^z = \int_{z_{(x)}(t_{\min})}^{z_{(x)}^{\text{upper}}(t_{\max})} Q_{g(x,z)} dz + \int_{z_{(x)}(t_{\min})}^{z_{(x)}^{\text{lower}}(t_{\max})} Q_{g(x,z)} dz. \quad (3.17)$$

Next, our integration goes along the x -axis. Figure 3.20b shows the top view, indicating how to integrate along the x -axis. The trapping efficiencies $Q_{s(x)}^z$ and $Q_{g(x)}^z$ in the yz plane are summed along the x -axis in the xz plane. In this case, the integration starts from $x = 0$ and ends at $x = x(u_{\max})$, which is the tangential point between the ray profile (3.13) and the sphere circle (3.18) in the xz plane

$$\left. \begin{aligned} x^2 + (z - A)^2 &= r^2 \\ \omega_x &= u\omega_0 \sqrt{1 + \left(\frac{z}{Z_0}\right)^2} \end{aligned} \right\}. \quad (3.18)$$

Then, Q_s^{all} and Q_g^{all} are given as

$$Q_s^{\text{all}} = 2 \int_0^{x(u_{\max})} Q_{s(x)}^z dx, \quad (3.19)$$

$$Q_g^{\text{all}} = 2 \int_0^{x(u_{\max})} Q_{g(x)}^z dx. \quad (3.20)$$

As a result, the total trapping efficiency comes from (3.7). Followings are the numerical results for the off-axial trapping in three dimensions.

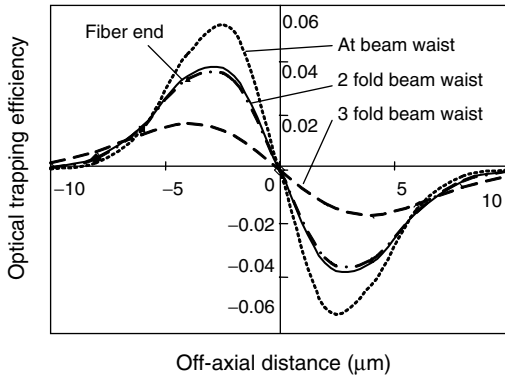
Off-axial Distance and Microsphere Radius Dependence

In the analysis a circularly polarized laser beam by a laser diode with a $1.3\text{ }\mu\text{m}$ wavelength, a tapered lensed optical fiber with a curvature of $10\text{ }\mu\text{m}$, and microspheres $2\text{--}10\text{ }\mu\text{m}$ in radius are used under the conditions listed in Table 3.6.

First, transverse trapping efficiency on the off-axial distance (transverse offset) is analyzed for a polystyrene sphere of $2.5\text{ }\mu\text{m}$ radius located at different

Table 3.6. Microspheres for analysis of solitary fiber trapping

material	refractive index	density (g cm^{-3})	radius (μm)
polystyrene	1.6	1.06	2–10
glass	1.51	2.54	2–10

**Fig. 3.21.** Variation in transverse trapping efficiency for a 2.5- μm -radius microsphere as function of off-axial distance, with beam axial distance as a parameter

axial distances of zero (fiber end), beam waist, two-fold beam waist, and three-fold beam waist. The axial distance of the sphere is measured along the symmetry axis of the laser beam and the off-axial distance of the sphere is measured as a relative distance to the symmetry axis (transverse offset) of the laser beam. It is seen from the numerical results in Fig. 3.21 that the optical pressure force towards the beam axis (transverse force) is exerted by off-axial trapping and becomes maximum at an axial distance of 3 μm .

Second, transverse trapping efficiency at the off-axial distance is analyzed for polystyrene spheres of 2–10 μm radius at an axial distance from the beam waist location. It is seen from Fig. 3.22 that the transverse trapping efficiency increases as the sphere radius increases and the location where the trapping efficiency becomes maximum is far away from the beam axis. When the radius increases, more power illuminates the sphere; thus the maximum transverse efficiency is realized.

Optical Trapping by Solitary Fiber

In off-axial trapping, the optical pressure force towards the beam axis (transverse force) F_g is exerted as described earlier. Finally, we realize solitary optical fiber trap by balancing the horizontal components of the gradient force F_g , which always pulls a sphere to the beam axis and the scattering force F_s , which always pushes a sphere along the beam axis. Figure 3.23 shows the concept of the horizontal component balanced between the optical pressures F_s and F_g owing to the oblique incident θ for an optical fiber [3.15].

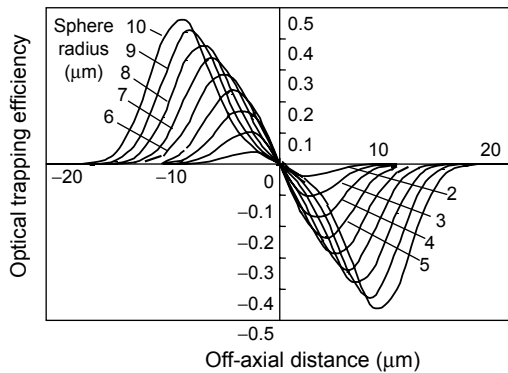


Fig. 3.22. Variation in transverse trapping efficiency at beam waist as function of off-axial distance, with microspore radius as a parameter

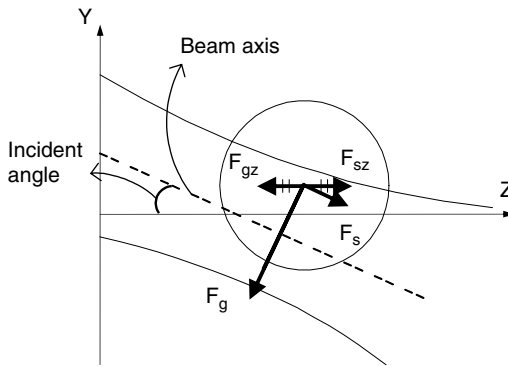


Fig. 3.23. Balancing between scattering force F_s and gradient force F_g at fiber incident angle of θ [3.15]

Following are the analyses for the incident angle of θ that satisfies $F_{gz} = F_{sz}$ for polystyrene radii ranging from 2 to 10 μm . Figure 3.24 shows the fiber incident angle for different sphere radii at the maximum gradient force on off-axial position. It is seen from the figure that as axial distance increases the fiber incident angle illuminating the sphere first decreases, then increases a little and becomes constant (about 40°) at the axial distance of 10 μm .

Figure 3.25 also shows the numerical results, showing that incident angle decreases at radius intervals of 0–3 μm ; after that it remains almost constant at 35°. From the results stated earlier, we may trap a microsphere two dimensionally by a solitary fiber illuminating at an angle of about 40°. By the way, the experimental results for glass and polystyrene microspheres of 5 μm diameter show that the minimum trapping power linearly increases with stage velocity (Fig. 3.37).

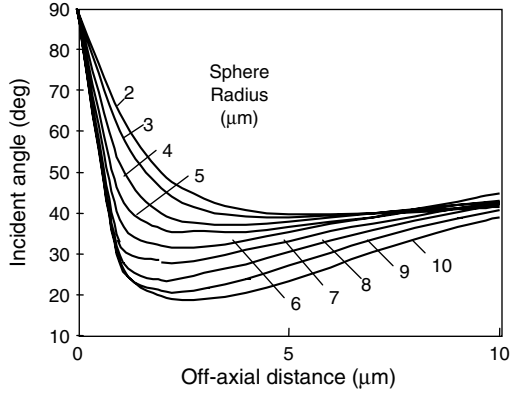


Fig. 3.24. Relationship between optimum fiber incident angle and radius of microsphere for $F_{sz} = F_{gz}$ at maximum F_g on off-axial position

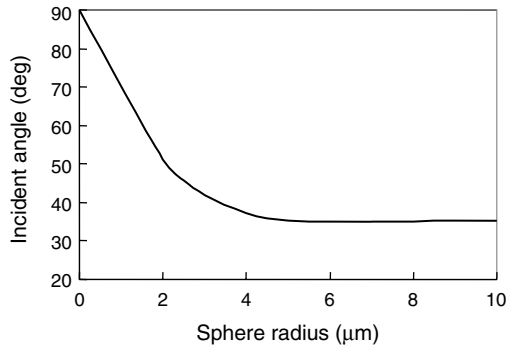


Fig. 3.25. Variation in fiber incident angle as function of off-axial distance at $F_s = F_g$, with microsphere radius as a parameter

3.3 Experimental Measurement and Comparison of Experimental and Theoretical Predictions

The use of optical tweezers is seen as a method of manipulating [3.16], aligning [3.17], fabricating and rotating [3.8] microobjects mainly in aqueous solutions. The optical trapping characteristics of spherical particles for these types of application were analyzed theoretically in Sec. 3.2 and are analyzed experimentally in this section. We not only describe the results of the experiments required to determine the characteristics of the optical trap but also compare the results with that of theoretical ones.

3.3.1 Experimental Setup

An experimental setup for trapping and manipulating particles using upward-directed and downward-directed YAG laser beams at a wavelength of 1.06 μm

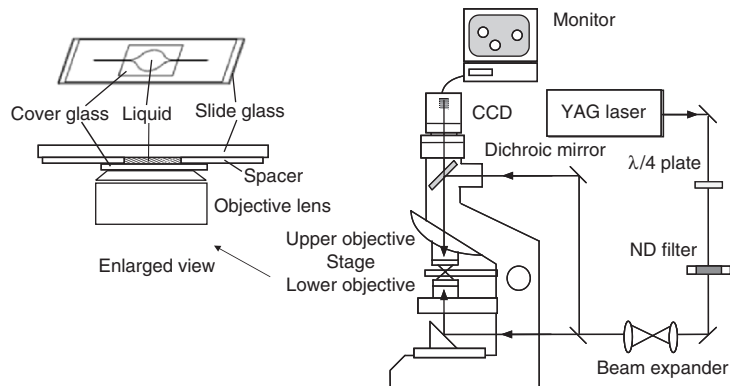


Fig. 3.26. Experimental setup for trapping and manipulating microobjects using upward-directed and downward-directed YAG laser beams with wavelength of $1.06 \mu\text{m}$

having a TEM_{00} mode structure is shown in Fig. 3.26. The laser beam diameter is increased from 0.7 to 8.2 mm by a beam expander to fill the entire aperture of the objective uniformly. A quarter-wave plate is placed to generate a circularly polarized beam. The intensity of the laser beam is varied using a ND filter. The beam is divided by a beam splitter to enter two objective lenses for focusing the downward-directed and upward-directed laser beams. A dichroic mirror is used to separate the transmitted image from the trapping beam. The total transmittance efficiency from YAG laser to the objective is about 35%. The transmittance efficiency of the immersion oil objective lens ($\text{NA} = 1.25$) is 21% at a wavelength of $1.06 \mu\text{m}$.

Figure 3.27 shows photographs of the experimental setup. Microobjects are suspended in an aqueous medium in a chamber. The chamber is made similar to a hole of a spacer (50–150 μm in depth) inserted between a coverslip (150 μm in depth) and a glass slide. The particle is trapped so as to be pulled to the focus of a strongly converging laser beam transmitted through the coverslip. When the objective lens moves, the particle follows the objective motion. The trapping behavior of the microobjects is monitored using a CCD camera. We have measured the minimum laser power for both axially trapped and transversely trapped particles by balancing the gravitational force and the viscous drag force, respectively.

The particles have also been manipulated successfully using the upward-directed and downward-directed laser beams. Two beams do not interfere each other, which leads to the appropriate manipulation of microobjects such as in the assembly of particles in the fabrication of a 3-D microobject.

3.3.2 Axial Trapping Power

To measure the minimum axial trapping power P_{\min}^{ax} , first, polystyrene/glass spheres are dispersed in water and trapped by a circularly polarized laser beam converged with a 1.25-NA objective lens. Second, the power of the trapping

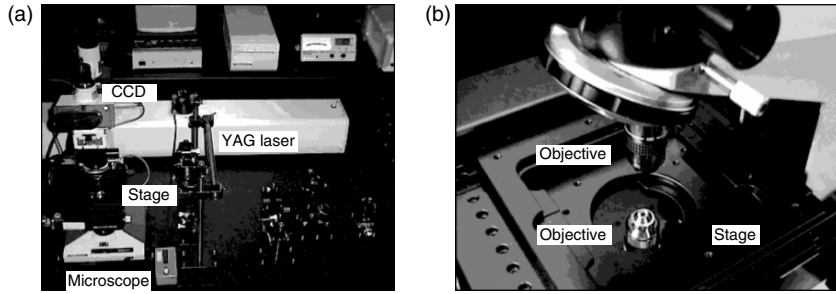


Fig. 3.27. Photograph of optical trapping apparatus. Upper and lower objective lenses are seen around the microscope stage lower left in (a). Two objective lenses used in trapping particles in water with downward-directed and upward-directed laser beams (b)

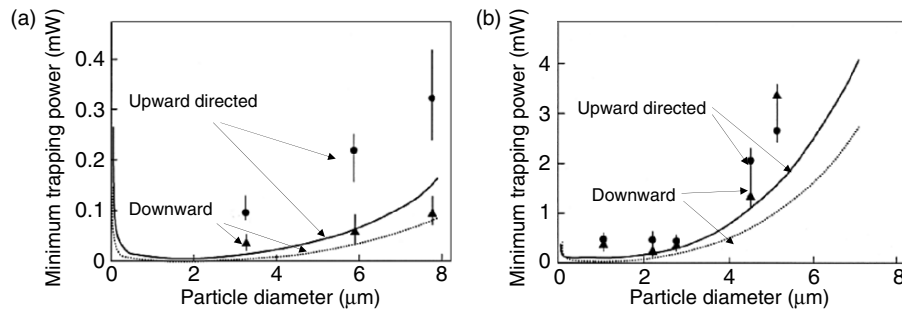


Fig. 3.28. Dependence of minimum axial trapping power on diameter for polystyrene spheres (a), and glass spheres (b)

beam decreased until the microsphere is observed to fall out of the trap. This P_{\min}^{ax} is taken to be the difference between the gravitational and buoyant forces. The spheres used for experiments are polystyrene ($\rho = 1.06 \text{ g cm}^{-3}$, $n = 1.60$) of 3.23, 5.85, 7.73, 10, 20, 30, 40 and 50 μm in diameter and glass ($\rho = 2.54 \text{ g cm}^{-3}$, $n = 1.51$) of 1.0, 2.5, 3.1, 5.1 and 5.8 μm in diameter.

Figure 3.28 shows the dependence of the measured P_{\min}^{ax} on sphere diameter at $T = 10 \mu\text{m}$ for the polystyrene (light) spheres (a), and glass (heavy) spheres (b), where T is the distance of the laser focus from the coverslip. P_{\min}^{ax} with an upward-directed (lower) laser beam is less than that with the downward-directed (upper) laser beam because the scattering force is added to the gradient force to trap the particle with an upward-directed beam. The discrepancy between the predicted and the measured forces is found to be smaller for a heavy particle (glass) than that for a light particle (polystyrene). This may be because the glass has smaller effects in both Brownian motion and electrostatic force than polystyrene.

The theoretical axial trapping power $P_{\text{pre}}^{\text{ax}}$ is shown by the solid line (upward directed) and the broken line (downward directed) from (3.21) [3.11]

that considers gravity, buoyancy and Brownian movement (theoretical trapping power is calculated using the expression $P_{\text{pre}}^{\text{ax}} = F_{\text{pre}}^{\text{ax}} c / n_1 Q_{\max}$).

$$F_{\text{pre}}^{\text{ax}} = \frac{\pi}{6} (\rho_s - \rho_m) d^3 g + 2kT/d, \quad (3.21)$$

where ρ_s and ρ_m are the densities of the sample spheres and suspending medium, respectively; d is the diameter of the spheres, g is the gravitational acceleration, and kT is the thermal energy.

Results of comparison of traps between experimental and theoretical methods are summarized in Table 3.7 as the ratio of P_{\min}^{ax} to $P_{\text{pre}}^{\text{ax}}$. The measured P_{\min}^{ax} for glass beads matches the theoretical $P_{\text{pre}}^{\text{ax}}$ at large diameters (only about 1.5 times difference for the diameter of 5.8 μm) because the ray optics model is appropriate and the Brownian effect is relatively small for large diameters. In parentheses, the experimental value with the upward-directed beam for the 5.8 μm diameter becomes large because the wall force (between the bead and the cover slip) strongly pulls the bead downward at a small distance of about 4.2 (= 10 – 5.8) μm .

A comparison is also given for the axial trapping power in both straight ray and parabolic ray approximations. Figure 3.29 shows the minimum axial trapping power for polystyrene microspheres comparing the experimental measurements to the predicted results for a straight ray model (broken line) and a parabolic ray model (solid line). It is seen from the figure that the minimum axial trapping power largely increases for the parabolic ray model and is close to the experimental results. This is because the actual focused trapping laser beam has a beam waist (parabolic ray model) and the individual ray enters almost vertically to the sphere surface leading to a reduced trapping efficiency.

3.3.3 Transverse Trapping Power

Next, the transverse trapping power P_{\min}^{trans} was measured as the minimum power for trapping a particle moving at the constant velocity v in water, as

Table 3.7. Ratio of experimental and theoretical minimum axial trapping powers of polystyrene sphere (**a**), and those of glass sphere (**b**)

diameter (μm)	downward directed	upward directed
<i>(a) Polystyrene</i>		
3.25	7.6	4.0
5.85	3.5	1.7
7.73	2.4	1.5
<i>(b) Glass</i>		
1.0	40	50
2.5	2.5	2.2
3.1	1.9	2.0
5.1	1.8	1.7
5.8	1.5	-

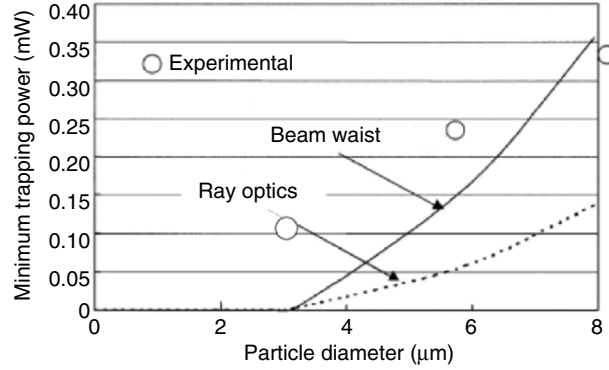


Fig. 3.29. Minimum axial trapping power for polystyrene sphere comparing the experimental measurement with the predicted results for straight ray (ray optics) and parabolic ray (beam waist) optics

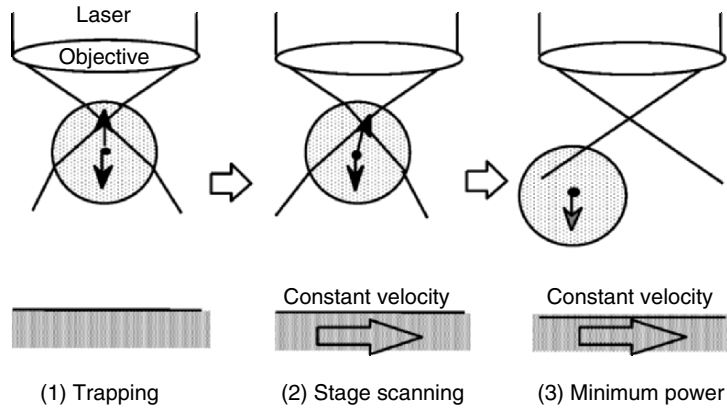


Fig. 3.30. Meathod of measuring transverse trapping power as minimum power for trapping a particle moving at the constant velocity of v in water

shown in Fig. 3.30. The theoretical transverse trapping power $P_{\text{pre}}^{\text{trans}}$ can be expressed as (3.22) [3.11] by considering viscous drag force, trapping depth and the maximum trapping efficiency Q_{\max} ($= 0.406$) [3.4].

$$P_{\text{pre}}^{\text{trans}} = \frac{3\pi\mu dvc}{n_1 Q_{\max}} \left\{ 1 + \frac{9d}{32} \left(\frac{1}{T} - \frac{1}{H-T} \right) \right\}. \quad (3.22)$$

Here, μ and n_1 are the viscosity and the index of refraction of the suspending medium (water), respectively; c is the speed of light, and H is the height of the specimen chamber ($150\mu\text{m}$). A transversely moving sphere should stably remain near the sphere surface (Q_{\max}) on the transverse axis for the light bead.

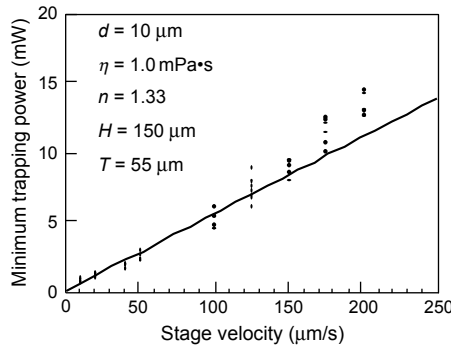


Fig. 3.31. Dependence of minimum transverse trapping power on the velocity for $d = 10 \mu\text{m}$ polystyrene particle

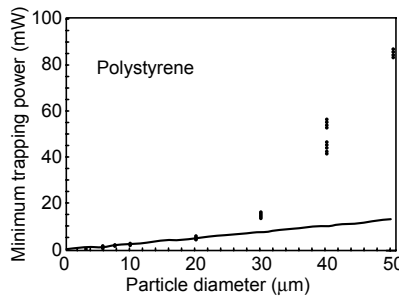


Fig. 3.32. Dependence of minimum transverse trapping power on diameter of polystyrene microspheres

Figure 3.31 shows the dependence of P_{\min}^{trans} on sphere velocity for $d = 10 \mu\text{m}$ polystyrene particles (small gravity). P_{\min}^{trans} increases as bead velocity increases and the experimental values are fairly in good agreement with the theoretical ones.

Figure 3.32 shows the dependence of P_{\min}^{trans} on sphere size (diameter) for polystyrene particles with a downward-directed beam. P_{\min}^{trans} substantially increases as d increases due to the Stokes drag force increase. The discrepancies between the theory and experiment for the trapping forces at $d > 30 \mu\text{m}$ is due to the fact that the trapping position moves to upward from the transverse center line in the sphere, and that Q becomes smaller, since the gravitational force increases for such large spheres [3.18] (Q3.7).

3.3.4 Optical Fiber Trapping

To realize a simple and inexpensive implementation of an optical trap, 3-D trapping using the counterpropagating light beams from two optical fibers and 2-D trapping using a solitary fiber were demonstrated. Figure 3.33 shows

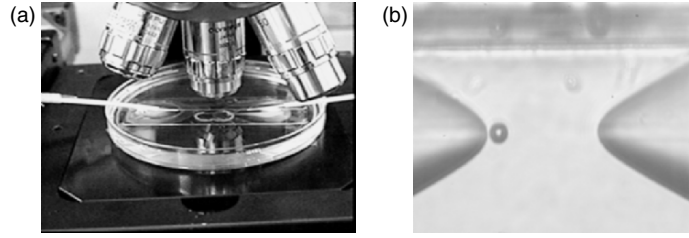


Fig. 3.33. Photographs of setup around fiber ends (a), and dual tapered fiber trap (b)

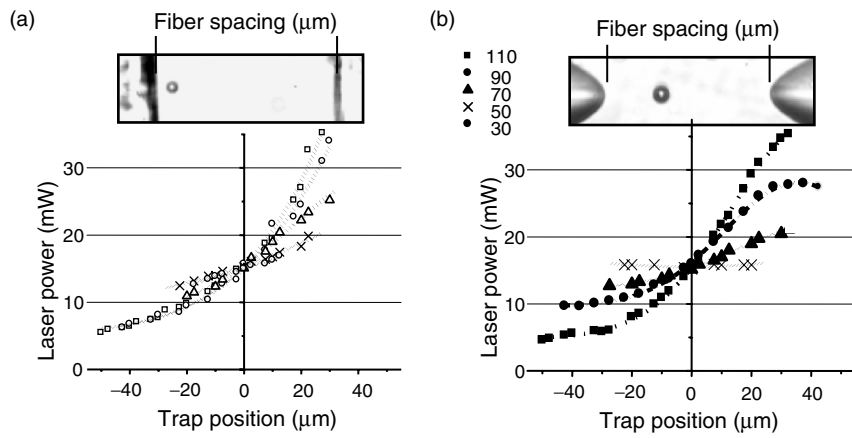


Fig. 3.34. Relationship between trap equilibrium position and output power from left side fiber ranging from 0 to 40 mW when output power is 15 mW from right side fiber for different spacings between fiber lens

photographs of the setup around fiber ends (a), and the dual tapered fiber trap (b). The trap equilibrium position of a 5- μm -diameter glass bead varies depending on the laser power ratio between the dual fibers. Laser diodes of 1.3 μm wavelength and cleaved/tapered (hemispherically machined lensed end) optical fibers are used for the experiment (Tables 3.5, Example 3.6).

Figure 3.34 shows the relationship between the trap equilibrium position and the output power from the left side fiber ranging from 0 to 40 mW when the output power from right-side fiber is 15 mW for different fiber lens spacings, which leads to enables the trapping of the particle at any positions in the dual fiber spacing by changing power ratio. The performance of a lensed fiber trap (b) is less sensitive in position than that of a cleaved fiber trap (a) due to its focus depth characteristics.

Figure 3.35 shows that the particle moves to the right continuously as the left power increases for small spacing of the fiber lens, but jumps for large spacing of the fiber lens. When the spacing becomes large, axial trapping becomes

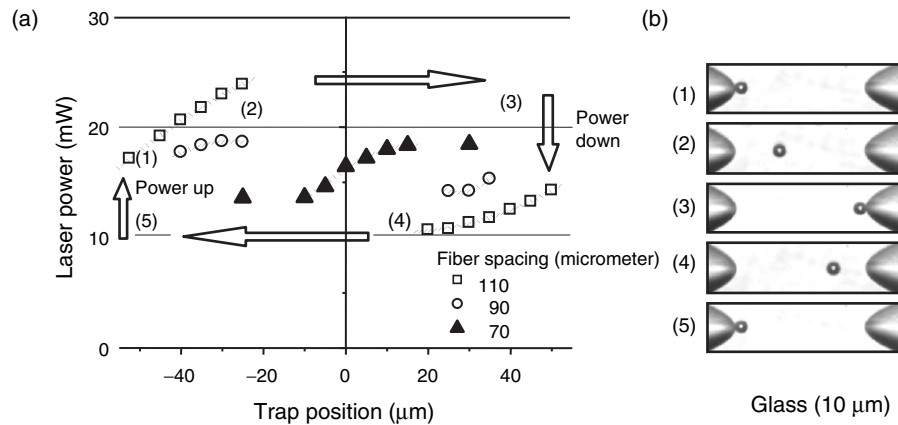


Fig. 3.35. Particle behavior when left power increases for different spacings between fiber lens

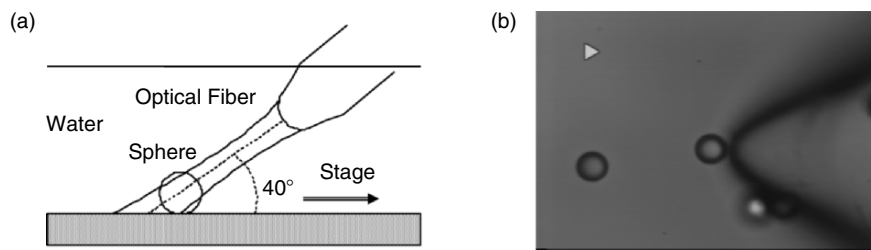


Fig. 3.36. Trapping performance by solitary optical fiber inserted at angle of 40°

unstable. Anyway, adjusting the relative powers of the optical fibers allow us to trap and position a bead over axial distances using the counterpropagating coaxially aligned optical fibers.

Figure 3.36 shows the trapping performance of a solitary fiber. The fiber, with an illuminating angle of 40°, traps a microsphere of 10 μm diameter. The minimum trapping power is linearly proportional to the velocity of the stage as shown in Fig. 3.37. The power is smaller for polystyrene than that for glass because the polystyrene refractive index (trapping efficiency) is larger and its density (friction force at the surface due to the 2-D trapping) is smaller than that of the glass.

In summary, we measured the optical-trapping force on polystyrene and glass microspheres of different diameters in two orthogonal directions with upward-directed and downward-directed laser beams and optical fibers. Following are our experimental results:

1. We confirmed that the upward-directed beam has a higher trapping efficiency than the downward beam for both polystyrene and glass

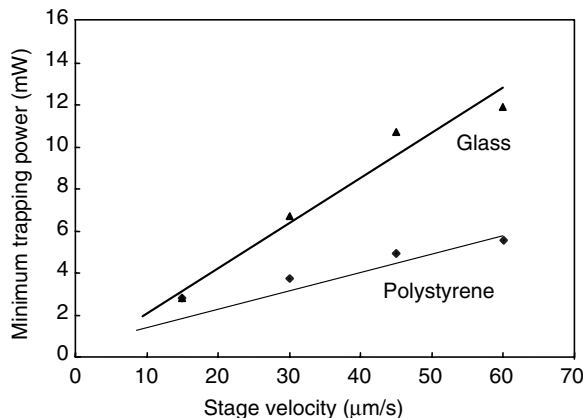


Fig. 3.37. Relationship between minimum trapping power obtained using solitary optical fiber and stage velocity for microspheres of 10 micrometer in diameter

microspheres. This is because the trapping force is equivalent to $F_g - F_s$ for downward illumination, but to $F_g + F_s$ for upward illumination. Theoretically, the minimum trapping power ratios between the upward- and downward-directed beams are 1.8 for polystyrene sphere and 1.6 for glass sphere.

2. The experimental minimum trapping powers are in fairly good agreement with the theoretical ones for axial trapping, but not in good agreement for transverse trapping. This is because the trapping position for transverse trapping changes due to the large gravitational force, particularly for high-density and/or large particles.
3. The minimum axial trapping power increases as the trapping position increases from the chamber surface. This is because the spherical aberration due to the refractive index difference between the immersion oil of the objective and the aqueous medium in which a microsphere is suspended.
4. Brownian motion is active for microspheres less than about $1\text{ }\mu\text{m}$ in diameter, which increases trapping power.
5. Optical fiber trapping is expected to improve both the operation and implementation.

Example 3.6. Show that the force due to Brownian motion of a microsphere suspended in water is equivalent to $F = 2kT/d$ where k is the Boltzman constant, T is the absolute temperature and d is the diameter of a microsphere.

Solution. Microspheres smaller than about $1\text{ }\mu\text{m}$ in diameter seem to fall out of the optical trap when laser power is reduced below a certain level. This is due to the thermal energy driving the particle in the weakest direction of the optical trap, i.e., parallel to the beam axis. To express the thermal effect in force units we assume that the harmonic trap potential $Kz^2/2$ (K is the

optical spring constant) equals the thermal energy $kT/2$ (Brownian motion energy) [3.11], Therefore, $K = kT/z^2$.

At the moment of escape, $z = d/2$ because the maximum trapping efficiency is close to the surface of the sphere. In this case, the equivalent force of the Brownian motion is

$$F = Kz = \frac{kT}{z^2}z = \frac{2kT}{d}.$$

3.4 Applications of Optical Tweezers

Ashkin et al. [3.19] demonstrated the optical trapping of a transparent microsphere by a strongly focused laser beam. A single-beam gradient-force optical trapping technique has been proved to be useful in the study of biological processes because of its noninvasive nature [3.20]. Recently, optical tweezers have been applied in various scientific and engineering fields listed in Table 3.8. Inexpensive fiber manipulation is expected for easy implementation.

Not only a solid laser but also an LD can be used as a light source for trapping. The optical pressure force is very weak, nearly pN/mW, but can manipulate particles on the micrometer scale. Since the gravitational force increases proportional to the third power of the particle radius and the Brownian effect increases inversely proportional to the radius, there exists an adequate objective size in trapping. It corresponds to several micrometers, facilitating the manipulation of living cells in its early developing stage. 3-D trapping is possible for various particles ranging from 20 nm to tens of micrometers including biological, dielectric and polymer particles which are transparent for the laser beam, as shown in Fig. 3.38.

Recently, materials have been widening for further applications. For example, the 3-D trapping of metallic objects is possible due to a gradient force of the light intensity in the Rayleigh regime where the size is much less than the wavelength, and also due to the diffractive effect of the light at the surface of the object with a size of several wavelengths [3.21]. Gahagam et al. of Worcester Polytechnic Institute demonstrated the 3-D trapping of low-index particles in the size range of 2–50 μm using a donut-shaped intensity profile beam [3.22]. Higurashi et al. of NTT trapped ringlike (hollow), low-index microobjects in a high-index liquid using upward bottom-surface radiation pressure [3.17]. The ringlike microobject was made of fluorinated polyimide, with a refractive index of 1.53 and a surrounding liquid refractive index of 1.61. Following are the actual applications of the optical tweezers classified in the field of basic research and industry.

3.4.1 Basic Research

Biology

Living cells of several micrometers in size, which are easy to trap, leads to optical tweezers were first used in biology [3.23]. For example, results of the

Table 3.8. Applications of optical tweezers

technology fields	applications
basic research	<ol style="list-style-type: none"> 1. Physics: Measurement of optical pressure (1964) [3.1] 2. Biology: Measurement of swimming velocity of bacteria (1987) [3.23] 3. Biology: Measurement of compliance of bacterial flagella (1989) [3.24] 4. Chemistry: Microchemical conversion system (1994) [3.6] 5. Optics: Microsphere laser oscillation (1993) [3.29] 6. Biology: Kinesin stepping with 8 nm (1993) [3.25] 7. Mechanics: Measurement of particle rotation rate (1995) [3.34] 8. Mechanics: Measurement of the drag force on a bead (1995) [3.33] 9. Physics: Optically trapped gold particle near-field probe (1997) [3.31] 10. Biology: Single molecule observation (1998) [3.26]
industry	<ol style="list-style-type: none"> 1. Space engineering: Solar sail flight [http://planetary.org] 2. Applied optics: Particle transport (1986) [3.19, 3.35] 3. Biological engineering: Living cell fusion (1991) [3.20] 4. Mechanical engineering: 3-D microfabrication (1992) [3.9] 5. Mechanical engineering: Shuttlecock type optical rotor (1994) [3.8, 1.62] 6. Applied optics: Optical fiber trapping (1995) [3.13], (1999) [3.15] 7. Mechanical engineering: Optical rotor with slopes(2003) [1.63] 8. Applied optics: Optically induced angular alignment (1999) [3.17] 9. Mechanical engineering: Gear type optical rotor (2001) [1.65] 10. Applied optics: Optical mixer (2002) [1.50], (2004) [1.66] 11. Applied chemistry: Patterning surfaces with nanoparticles (2002) [3.40, 3.41] 12. Applied optics: Microstructure formation and control (2004) [3.39]

manipulation of bacteria and the measurement of the swimming speed of mitochondria are shown in Fig. 3.39. Furthermore, living cell fusion [3.20] by violet light exposure in the contact area of two cells trapped independently is shown in Fig. 3.40.

Another example is the compliance measurement of bacterial flagella. The torque generated by the flagella motor of a bacterium tethered to a glass surface by a flagella filament was measured by balancing that generated by the optical pressure force. The balance was realized by calibrating optical power [3.24].

The direct observation of kinesin stepping was performed by optical trapping interferometry with a special and temporal sensitivity for resolving movement on the molecular scale, as shown in Fig. 3.41 [3.25]. Silica spheres carrying single molecules of the motor protein kinesin were deposited on microtubules using optical tweezers and their motion was analyzed to determine whether kinesin moves in 8 nm steps.

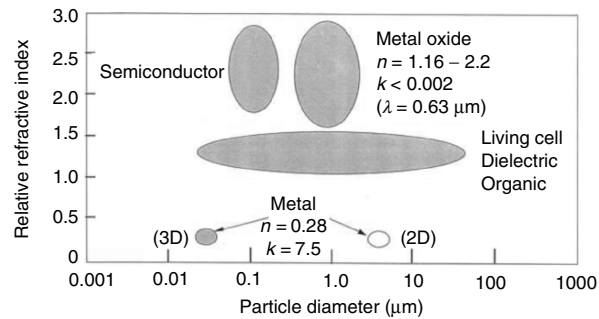


Fig. 3.38. Reported materials and sizes possible for optical trapping by YAG laser beam. Various particles ranging from 20 nm to tens micrometer in size including biological, dielectric, polymer and metal particles are included

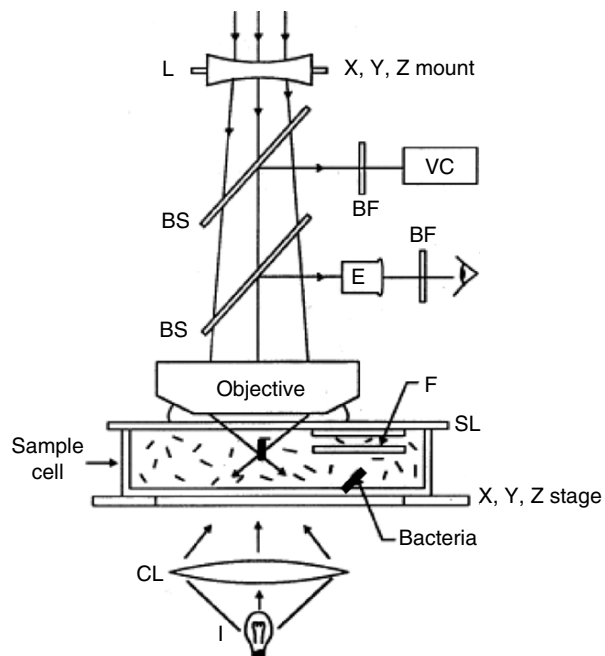


Fig. 3.39. Example of bacterial manipulation and measurement of swimming speed of mitochondria by optical tweezers [3.23]

Figure 3.42 shows the simultaneous measurement of individual ATPase and mechanical reactions of single one-headed myosin molecules [3.26]. A single actin filament with beads attached to both ends was suspended in a solution by YAG laser trapping. The fluorescence was excited by the evanescent wave generated by the total reflection of the green laser shown in the figure. The local illumination by the evanescent light greatly reduced the background luminescence.

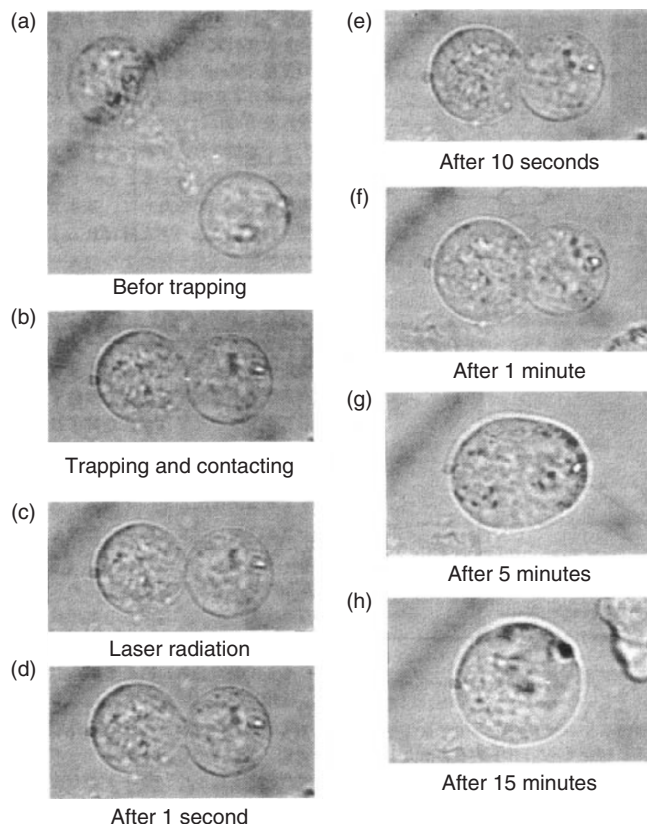


Fig. 3.40. Living cell fusion by violet light exposure at contact area between two cells trapped independently [3.20]. Courtesy of S. Sato, Tohoku University, Japan

Displacement and force due to actin–myosin interactions were determined by measuring bead displacement with nanometer accuracy by a quadrant photodiode. Individual ATPase reactions were monitored by an SIT camera as changes in fluorescence intensity due to association–(hydrolysis)–dissociation events of a fluorescent ATP (analog labeled with Cy3-ATP) with the myosin head. As a result, it was found that the myosin head produces several hundred of milliseconds after a bound nucleotide is released. This suggests that myosin has hysteresis or memory state, and stores chemical energy from ATP hydrolysis [3.26].

Chemistry

Optical tweezers are used in the field of chemistry. Figure 3.43 shows a microchemical conversion system [3.6] for the studies of reaction kinetics that allows the selective excitation of optically manipulated particles in reaction environments, which was prepared by micromachining. Continuous wave YAG

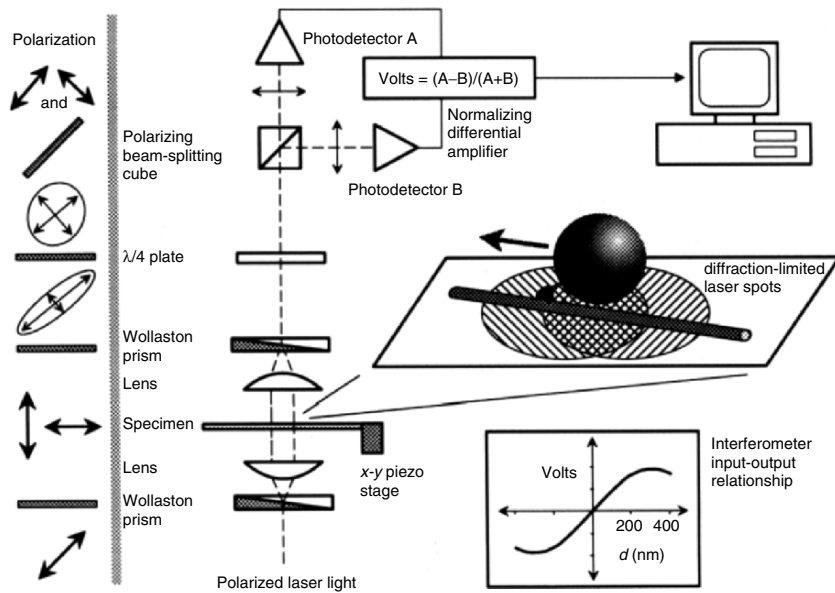


Fig. 3.41. Direct observation of kinesin stepping by optical trapping interferometry [3.25]

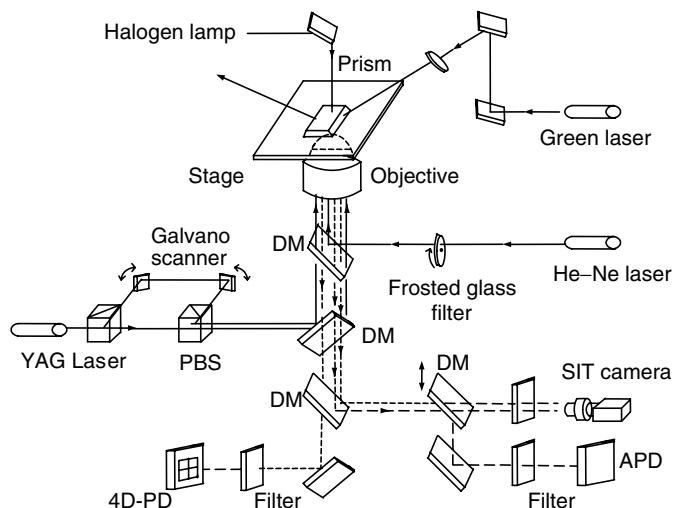


Fig. 3.42. Simultaneous measurement of individual ATPase and mechanical reactions of single myosin molecules. Reprinted from [3.26] with permission by T. Yanagida, Osaka University, Japan

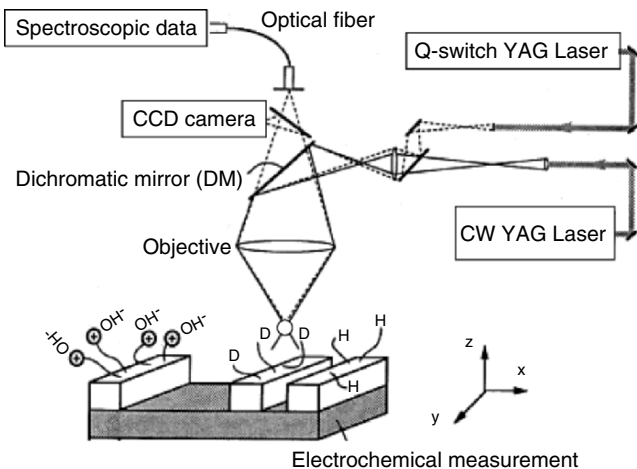


Fig. 3.43. Microchemical conversion system for studies of chemical reaction process. Reprinted from [3.6] with permission by H. Masuhara, Osaka University, Japan

lasers ($\lambda = 1,064 \text{ nm}$) trap and close particles in contact with each other. Q-switched YAG laser ($\lambda = 350 \text{ nm}$) stimulates the photochemical reaction between such particles. Such a chemical reaction was studied by a picosecond time-resolved laser spectroscopy. They expect that such approaches will make it possible to study the chemical and physical properties of a single fine particle as a function of its size, shape, surface morphology and to promote highly selective/efficient material conversion [3.27].

Optics

Micrometer-sized spherical particles can act as optical cavities in air or liquid [3.28]. Resonant field is formed inside the surface of particles doped with laser dye such that the light propagates in a circumferential manner due to the total internal deflection at the interface [3.29]. The optical characteristics of the microsphere laser oscillation, such as polarization of resonant modes and interaction between close particles, were studied. Photon tunneling from the lasing microsphere to an object was demonstrated as a marked change of an emission spectrum depending on microsphere-to-object distance. Lasing microspheres have the advantage of high sensitivity due to the intracavity enhancement of tunneling loss, i.e., a probe of a scanning near-field optical microscopy (SNOM) [3.30]. In addition, an optically trapped gold particle was demonstrated to be a useful near-field probe for the study of the surface characteristics beyond the diffraction limit resolution [3.31, 3.32].

Micromechanics

Laser scanning manipulation was applied to measure the drag force [3.33] acting on a glass bead moving in mineral oil between two glass plates. The rotation rate of a small particle induced by optical pressure was measured by the cycle of the scattered light from optically trapped particles [3.34].

3.4.2 Industry

Particle Transport

The spatial patterning and directional transport of plural particles in water were shown to be possible by single-beam laser trapping. For radioactive substance or nucleus materials, the optical trapping of metallic oxide particles with various optical constants were performed to confine, position and transport without physical contact in water by Omori et al. 3-D trapping was possible for a ThO₂ particle but only 2-D trapping was observed for a UO₂ particle in water using an He–Ne laser light at 633 nm. This is because a UO₂ particle has a relatively large refractive index and a large extinction coefficient in the visible region [3.35].

Figure 3.44 shows the relationship between optical constant (refractive index n and extinction coefficient k) and the maximum trapping efficiency Q_{\max} for microspheres with a wavelength of 633 nm. The objective's NA is 1.3 and the microsphere diameters are 2 μm (a) and 10 μm (b). In this calculation, absorption was considered, therefore decreasing Q_{\max} with increasing the diameter. It is also seen from the figure that 3-D trapping was possible for the metallic oxide having a refractive index less than 2.4 by an He–Ne laser light ($Q_{\max} < 0$). They also demonstrated that laser trapping was also possible in air [3.36].

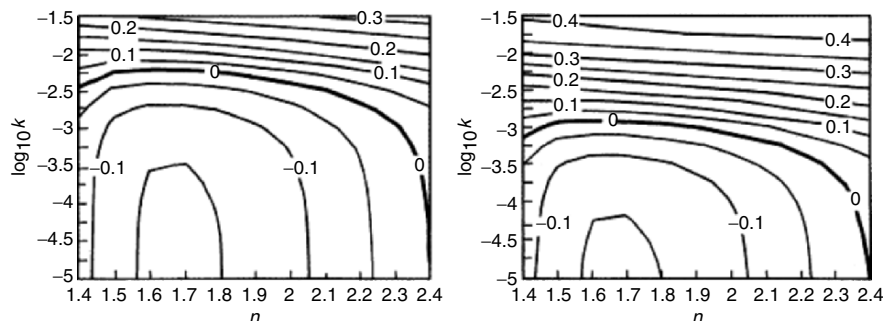


Fig. 3.44. Relationship between optical constant and maximum trapping efficiency Q_{\max} for microsphere with wavelength of 633 nm [3.35]

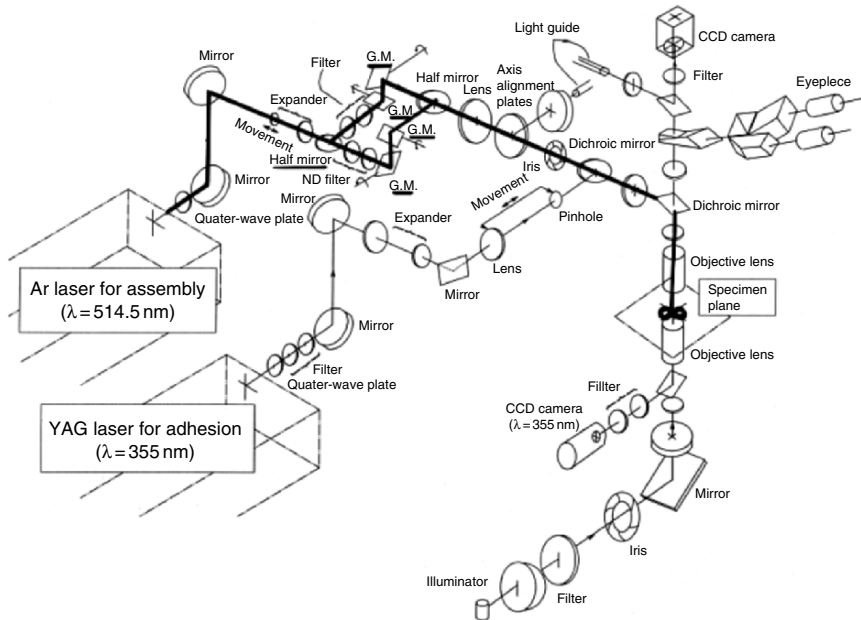


Fig. 3.45. Micro assembly system using two laser beams, one is for trapping (assembly) and the other is for ablation (adhesion).

Fabrication of 3-D Microstructures

The simultaneous manipulation and microfabrication of spatially arranged fine particles are attained using optical tweezers by introducing pulsed violet laser illumination [3.9]. Figure 3.45 shows a microassembly system. The trapping and ablation (adhesion) laser sources used are a 515-nm CW Ar⁺ laser and a 355-nm pulsed YAG laser, respectively.

Such systems mentioned earlier were limited to a small number of objects trapped in a single plane. Recently, components can be designed to split a laser beam into many separate beams. Holographic optical tweezers can trap objects in different focal planes allowing many objects to be simultaneously trapped [3.37]. Crystal-like structures over a scale of tens micrometers were constructed using holographic optical tweezers [3.38]. Eight 2-μm-diameter silica spheres were trapped through the multiple trapping function of the hologram at the corner of a cube [3.39]. The real-time calculation of the required holographic pattern allows us to rotate the structure about an arbitrary axis.

Patterning Surfaces with Nanoparticles

The 2-D arrangement of colloids on a substrate is of interest for photonics, electronics, magnetic, and sensor applications. Optical tweezers are used to

bring particles from a reservoir and pattern nanoparticles on the substrate. Fixing was carried out using opposite charges [3.40] or local photopolymerization [3.41] around the nanoparticle assembly.

Optical Rotor

Optical pressure can also rotate dissymmetrical microobjects. Many types of optical rotor have been proposed for future applications, which will be described in Chap. 4.

Problems

- 3.1.** Explain the method of measuring an optical pressure force.
- 3.2.** Explain the procedure how to simulate the trapping force exerted on a microsphere illuminated by a converging laser beam.
- 3.3.** Compare the axial trapping efficiencies for a microsphere predicted by a straight ray with a parabolic ray.
- 3.4.** Calculate the transverse trapping efficiency for a microsphere when the focus of the uniformly input laser beam is located along the transverse center line (perpendicular to the optical axis) of the sphere.
- 3.5.** Compare the transverse trapping efficiency for a microsphere predicted by a straight ray with a parabolic ray.
- 3.6.** Calculate the total trapping efficiency for a microsphere when the focus of the input laser beam is located at arbitral positions in the sphere.
- 3.7.** Consider the reasons for the transverse trapping power discrepancy between the theoretical prediction and the experimental result. Show the trajectory of the trapping (focus) position in the sphere.

Optical Rotor

Optical tweezers have been successfully utilized in various scientific and engineering fields such as biology, microchemistry, physics, optics and micro-mechanics. Their ability to rotate microobjects remotely without the use of bearings presents important opportunities in optical microelectromechanical systems (optical MEMS) and biotechnology. This chapter describes the principle, design, fabrication, and evaluation of an optical rotor to increase the mixing performance of microliquids to enable future fluidic applications. The optical rotor will be used as a mixer in micrototal analysis systems (μ -TAS).

4.1 Background

In space, small particles are blown away rotationally by the radiation pressure of the sun, the so-called windmill effect. In micromechanics the following methods are known for rotating a microobject using a single laser beam: one in which a circularly polarized laser beam is used [4.1] and another in which the rotating nonuniform intensity profile of a higher-order-mode laser beam is used [4.2]. However, the rotation speeds of both methods are very slow, about $6.7 \times 10^{-1} - 6.7 \times 10^{-2}$ rpm [4.1] and 6 rpm [4.2].

Trapping and manipulation of micrometer-sized particles were demonstrated firstly by Ashkin using a laser beam through a microscope objective [3.2]. Presently, optical tweezers have been successfully applied in various fields. The optical pressure can also be used to rotate the dissymmetrical microobjects shown in Fig. 4.1, which are a polystyrene particle (refractive index $n = 1.6$, density $\rho = 1.07 \text{ g cm}^{-3}$), a broken glass ($n = 1.5$, $\rho = 2.2 \text{ g cm}^{-3}$), a glass rod having concave end on the top and elongated cylindrical body, a broken ZnO ($n = 2.0$, $\rho = 5.67 \text{ g cm}^{-3}$), a broken Si ($n = 3.5$, $\rho = 2.33 \text{ g cm}^{-3}$), and a broken GaP ($n = 2.12$, $\rho = 4.13 \text{ g cm}^{-3}$) for example. However, we cannot control the rotational direction for arbitrarily shaped broken micro-objects.

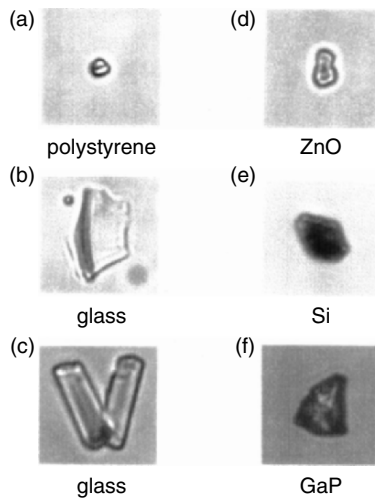


Fig. 4.1. Dissymmetrical/arbitrarily shaped broken microobjects which can be rotated but not controlled the rotational direction by optical pressure. They are a polystyrene (a), a broken glass (b), a glass rod (c), a ZnO (d), an Si (e), and a broken GaP (f)

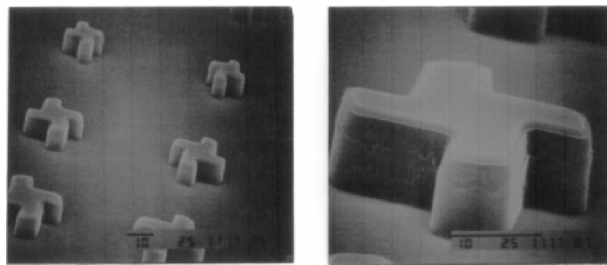


Fig. 4.2. Fabricated shuttlecock optical rotors with shape dissymmetry on their sides

Higurashi et al. reported in 1994 that they could experimentally cause a directional high-speed rotation, for example, 22 rpm of artificial rotors in water [4.3]. Yamamoto et al. measured the rotation rate of anisotropically shaped particles using the temporal variation of light scattered from the rotation particle [4.4]. Gauthier showed an example of a numerical computation of the torque exerted on a rotor under restricted conditions [4.5].

Figure 4.2 shows a rotor with shape dissymmetry on its side [4.3]. The rotor was made by reactive ion-beam etching of a 10- μm -thick silicon dioxide (SiO_2) layer. When incident laser light refracts at the top surface of the rotor, the momentum of the light changes and an upward optical pressure force for trapping is exerted as shown in Fig 4.3a. Optical pressure force is also exerted when the light emits from the side surfaces. Fig. 4.3b shows the optical pressure exerted on side surfaces I and II but not on side surface III. This is

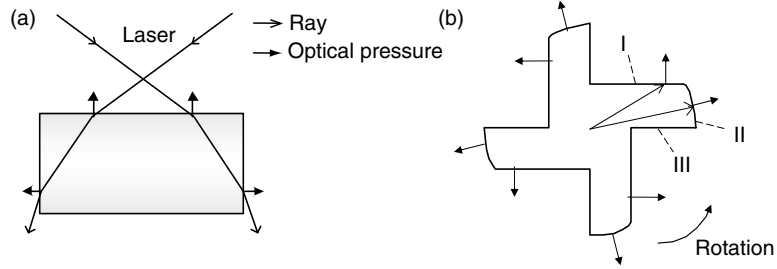


Fig. 4.3. Optical pressure force exerted on the light-incident upper surface lifts the rotor (a), and that exerted on the light-emission side surfaces rotates it (b)

because surface III is parallel to the radial direction and does not refract the laser beam. The optical pressure on side surface II does not contribute to the optical torque because its direction is radial. The optical pressure on side surface I, however, rotates the microobject counterclockwise, and we can see that the direction of rotation can be controlled by appropriately designing the dissymmetric geometry. Nevertheless, this type of optical rotor has the following drawbacks.

1. a strongly focused laser beam is required
2. only a fraction of the incident light is effective for rotation
3. the viscous drag force is very large due to the complicated side shape.

To solve these problems, Ukita et al. extended their work and invented a new rotor remotely driven by not only a focused laser beam but also an unfocused (parallel) laser beam [4.6]. Fig. 4.4 shows the designed optical rotor that has a sloped top, a cylindrical body and a flat plane on the bottom. This rotor has shape dissymmetry on the top, which generates an optical trapping force and optical torque at the same time. The optical force F , perpendicular to the rotor slope, is torsionally exerted along the beam axis. F is separated into two components, scattering force F_s , and gradient force F_g . The gradient force F_g is further separated into the torque force F_t , and radial force F_r . On the lower surface, only the scattering force is exerted, and no z -axis torque is exerted because the surface is perpendicular to the optical axis. On the side surface, optical pressure does not contribute to the z -axis torque because of its radial direction.

The total z -axis torque and the rotation speed have been evaluated using the ray-tracing method taking into consideration the beam waist with various optical parameters such as the numerical aperture (NA) of the lens and the laser beam profile, as well as rotor shape parameters including oblique angle, height and diameter. As a result, the cylindrical rotor driven by forces exerted on its top surface is expected to rotate much faster than the previous rotors [4.3] driven by forces exerted on their side surfaces. This is because all incident light that hits the upper surface generates torque and also because the viscous drag force is small due to the cylindrical structure.

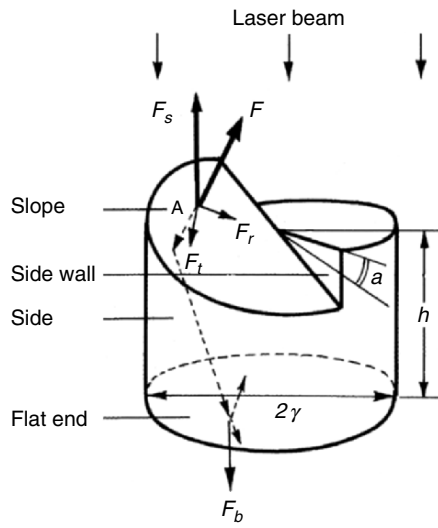


Fig. 4.4. Rotation principle by the optical pressure exerted on the slopes of the light-incident surface and the cylindrical body

Applications include optical motors for micromachines and optical mixers for μ -TAS. These technologies related to the optical rotor could have a significant effect on developments in optical MEMS and micromechanical photonic systems; recently, a micromotor [4.7], a microgear [4.8], a micromachine element [4.9], and a micromachine with complicated shape [4.10] have been presented.

4.2 Theoretical Analysis I – Optical Torque

Two kinds of optical rotors are presented: a rotational but not bilaterally symmetrically structured rotor to which optical torque is applied on its side surfaces and a cylindrical optical rotor which has slopes for rotation on its top. Their rotation mechanisms have been clarified both experimentally and theoretically. The optical rotor is expected to solve the problems of an MEMS motor, i.e., short lifetime due to friction and requirement of electrical wires for the power supply.

4.2.1 Optical Rotor Having a Dissymmetrical Shape (Shuttlecock) on its Side

The optical rotation principle of a shuttlecock optical rotor that has no bilateral symmetry in the horizontal cross-section is shown in Fig. 4.3. In order to simulate the optical torque, the laser beam was divided into 100×100 elements on the objective lens aperture, as shown in Fig. 4.5. We considered

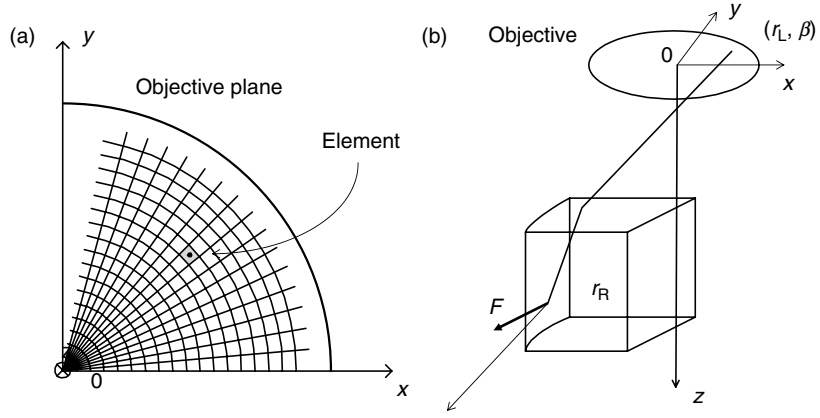


Fig. 4.5. Ray optics to simulate the optical torque of the shuttlecock rotor, where ray incidence (r_L, β) on the lens aperture is considered and the torque is estimated at the point r_R on side surface I

the ray incidence (r_L, β) on the lens and estimated the torque at point r_R on side surface I in Fig. 4.3. Radius r_R is expressed as

$$r_R = \frac{w}{\cos \beta}, \quad (4.1)$$

where w is the wing width. Optical pressure F at the incident light angle of θ . is derived in Example 3.2 and expressed as

$$F = \frac{n_1}{c} P \left\{ (1 + R) \cos \theta_1 - \frac{n_2}{n_1} T \cos \theta_2 \right\}, \quad (4.2)$$

where n_1 and n_2 are the refractive indexes of the surrounding medium and the rotor, respectively. P is the laser power, c_0 is the speed of light in vacuum, and θ_2 is the refractive angle calculated from Snell's law. R and T are the reflectivity and transmittivity, and they are derived from the Fresnel formula. As a consequence, optical pressure F can be calculated if the incident light angle θ_1 is defined.

The optical torque T at r_R is given as

$$T = r_R F \sin \beta. \quad (4.3)$$

The total optical torque M exerted on the four-wing surfaces is

$$M = 4 \int_{\beta=0}^{\beta=\cos^{-1} \frac{2w}{d}} \int_{r_{L \min}}^{r_{L \max}} F \sin \alpha r^2 dr d\beta \quad (4.4)$$

where d is the rotor diameter and $r_{L \min}$ and $r_{L \max}$ are the minimum and maximum distances from the optical axis, respectively. They are given as

$r_{L\min} = 0$ and $r_{L\max} = \tan\{\arcsin(\text{NA}/n_1)\}$, where NA is the numerical aperture of the objective lens.

Figure 4.6a shows the optical torque dependence on the focal point where the refractive indexes are $n_1 = 1.33$ and $n_2 = 1.6$. The diameter is $d = 20\text{ }\mu\text{m}$, and the thickness is $t = 10\text{ }\mu\text{m}$, and the wing width is $w = 3.3\text{ }\mu\text{m}$. The optical torque reaches a maximum when the focal point is $4\text{ }\mu\text{m}$ above the top surface. Fig. 4.6b shows the simulated results at the focal point located $5\text{ }\mu\text{m}$ above the upper surface of the rotor under the same conditions as above. The optical torque increases as the NA increases and reaches a maximum at NA = 1.2 because the large divergent angle increases the amount of light emitted from the side surface, as shown in Fig. 4.3a, but it decreases due to the increase in reflectivity at the top surface when NA becomes greater than 1.2. Table 4.1 lists the conditions of torque simulation for the optical rotor.

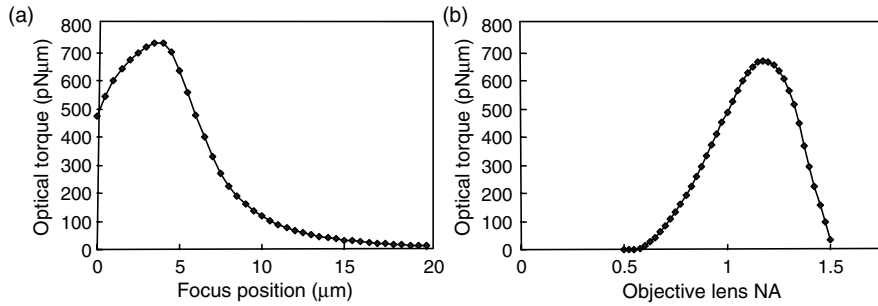


Fig. 4.6. Simulated optical torque dependence on focal position with objective lens NA=1.2 (a), and dependence on objective lens NA (b) with focus above $5\text{ }\mu\text{m}$, for shuttlecock rotor with uniform light beam profile

Table 4.1. Conditions of torque simulation for an optical rotor

optical conditions	
laser intensity profile	uniformly filled
laser power	0–200 (typical 100) mW
objective NA	1.25
refractive index of the medium	1.33 (water)
refractive index of the rotor	1.6
focus above a rotor upper surface	0–20 (typical 5) μm
speed of light in vacuum	$3 \times 10^8\text{ m/s}$
rotor size	
diameter	10–50 (typical 20) μm
thickness	1–20 (typical 10) μm
wing width	2.7–5 (typical 3.3) μm

4.2.2 Optical Rotor with Slopes on the Light-Incident Surface

The characteristics of the optical trapping force and optical torque for a cylindrical optical rotor with slopes on the light-incident surface are analyzed using a ray optics model for both parallel and focused laser beam illuminations. The rotor is expected to be aligned with the light beam propagation axis. Since the total illuminated light beam contributes to the rotation and the cylindrical shape is effective in decreasing the viscous drag force, this new rotor is expected to rotate much faster than the conventional one.

First, light-driven cylindrical rotors with various slope angles and height-to-radius ratios are analyzed. Figure 4.4 shows that the optical pressure force F perpendicular to the surface, at an arbitrary point on the top surface is torsionally directed along the beam axis. Force F is decomposed into two components: scattering force F_s pointing in the direction of the beam axis and gradient force F_g pointing in the direction perpendicular to the beam axis. Gradient force F_g (not shown) is decomposed further into torque force F_t and radial force F_r . On the lower surface, only scattering force F_b is exerted, and no z -axis torque exists because the surface is perpendicular to the optical axis.

Parallel Beam Illumination

We assume that a circularly polarized Gaussian Nd:YAG laser beam (wavelength $\lambda = 1.064\text{ }\mu\text{m}$, power $P = 100\text{ mW}$) illuminates the rotor (refractive index $n_2 = 1.5$, density $\rho = 2.2\text{ g cm}^{-3}$, diameter $2r = 3\text{ }\mu\text{m}$ and height $h = 10\text{ }\mu\text{m}$) in water ($n_1 = 1.33$). When vertically illuminated on the top surface by a parallel beam, the incident angle a_1 is equal to a (the slope angle of the rotor) and the optical pressure F at arbitrary point A is given by (4.2). Quantities R and T are derived from the Fresnel reflection and transmission coefficients using (3.2) and (3.3). Scattering force F_s and torque force F_t at point A are given by

$$F_s = F \cos(a) \quad (4.5)$$

$$F_t = F_g \sin(\theta) = F \sin(a) \sin(\theta) \quad (4.6)$$

Therefore, torque T_q at point A is

$$T_q = rF_t = Q_{\text{torque}}(n_1 P/c), \quad (4.7)$$

where Q_t is the torque efficiency in unit of m.

When vertically illuminated by a parallel beam, all the refracted light is reflected by the side surface, which leads to the incident angle to the bottom surface being $(a_1 - a_2)$. Therefore, optical pressure F_b at the bottom surface is given by

$$F_b = \{(n_2/n_1)(1 + R') \cos(a - a_2) - T' \cos(a_3)\}(n_2 P'/c), \quad (4.8)$$

where a_3 is the refraction angle for the incident angle of $(a - a_2)$, P' is the incident light power at the bottom, R' is the reflectivity and T' is the transmittance at the bottom. The total trapping force is given as the total sum

$$F_{\text{trap}} = \int \int (F_s + F_b) dS, \quad (4.9)$$

and total torque M_{opt} acting on the rotor is given as the sum

$$M_{\text{opt}} = \frac{n_1}{c} P \int \int Q_{\text{torque}} dS. \quad (4.10)$$

Figure 4.7 shows the dependence of trapping force F_{trap} on slope angle a . We have defined the positive axial trapping force to be in the $+z$ direction. The curves show F_{trap} on the top (upper), bottom (lower), and both surfaces (total). Since all the rays refracted at the top surface are reflected from the side surface, scattering force F_b on the flat bottom is always greater than scattering force F_s on the top. Thus the net trapping force ($F_b - F_s$), always positive, pushes the rotor away, which leads to two-dimensional (2-D) trapping.

Figure 4.8 shows the dependence of the rotation rate on the slope angle. Assuming that the rotor is cylindrical, we can approximate the rotation rate by $M_{\text{opt}} = M_{\text{drag}} (= 4\pi\mu r^2 h\omega)$, where M_{opt} is the optical torque of (4.10), μ is the medium viscosity ($\mu = 1 \text{ mPas}$), r is the radius, h is the height of the rotor and ω is the angular velocity.

Focused Beam Illumination

A ray tracing method considering the beam waist is employed to analyze the optical forces exerted by a focused laser beam. Figure 4.9 shows ray tracing for the rotor illuminated with a focused beam. An incident ray repeats reflection

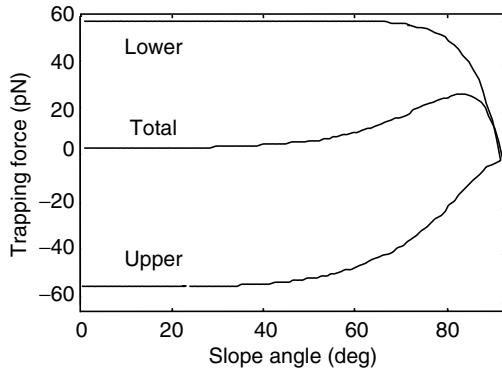


Fig. 4.7. Dependence of trapping forces on slope angle

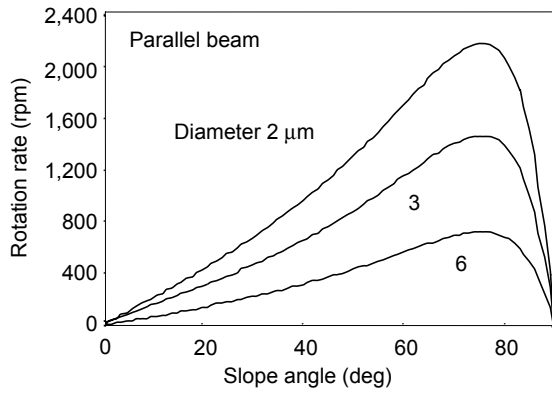


Fig. 4.8. Dependence of rotation rate on slope angle, with rotor diameter as a parameter ($P = 100 \text{ mW}$)

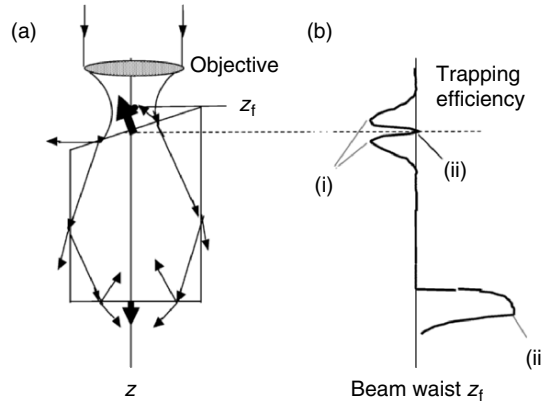


Fig. 4.9. Ray tracing for the rotor illuminated with a focused beam (a), and trapping efficiency along the light beam axis (b)

and refraction on each surface of the rotor. Since optical torque, that is, optical pressure times radius, is exerted on the light-incident surface, the minimum radius of the waist should be considered in the numerical analysis, particularly for the cylindrical rotor with slopes.

When the rotor is illuminated by a focused laser beam, the individual rays propagate parabolically near the waist, as shown in Fig. 4.10. The Gaussian beam radius along the z -directed propagation axis is given by

$$W(z) = W_0 \sqrt{1 + \left(\frac{z - z_f}{Z_0} \right)^2}, \quad (4.11)$$

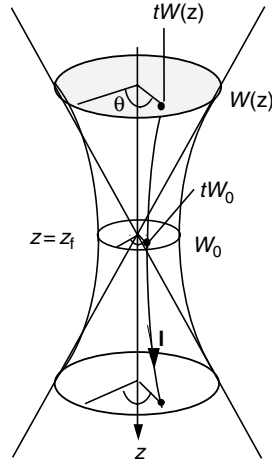


Fig. 4.10. Ray optics model for a focused laser beam considering beam waist. The ray of $tW(z)$ passes tW_0 at the beam waist ($z = z_f$) where $0 \leq t \leq 1$

where W_0 is the minimum waist radius, z_f is the minimum waist position and $2Z_0$ corresponds to the depth of focus. An arbitrary point on the ray, angle θ in the xy plane, can be described as

$$\{W(z) \cos \theta, W(z) \sin \theta, z\}. \quad (4.12)$$

Ray vector \mathbf{I} of $tW(z)$ that passes through tW_0 ($0 \leq t \leq 1$) on the beam waist ($z = z_f$) plane can be expressed as

$$\mathbf{I} = \{tW'(z) \cos \theta, tW'(z) \sin \theta, z\}, \quad (4.13)$$

where $W'(z)$ is the z derivative of $W(z)$. Reflected ray vector \mathbf{l}_r and refracted ray vector \mathbf{l}_t on the incident plane can be written, using vector \mathbf{I} of the incident $tW(z)$ ray as

$$\mathbf{I}_r = \mathbf{I} - 2(\mathbf{I} \bullet \mathbf{n}) \mathbf{n}, \quad (4.14)$$

$$\mathbf{I}_t = \mathbf{I} + (\mathbf{I} \bullet \mathbf{n}) \left(\frac{\tan(\theta_2)}{\tan(\theta_1)} - 1 \right) \mathbf{n}, \quad (4.15)$$

where \mathbf{n} defines the vector normal to the interface, θ_1 is the angle of incidence and θ_2 is the angle of refraction. The optical forces at each point are calculated using these ray vectors as follows.

We traced the rays until they hit the bottom surface and computed the optical pressure on each surface. The light reflected from the bottom causes an error in the optical pressure. The ratios of such light power to the input

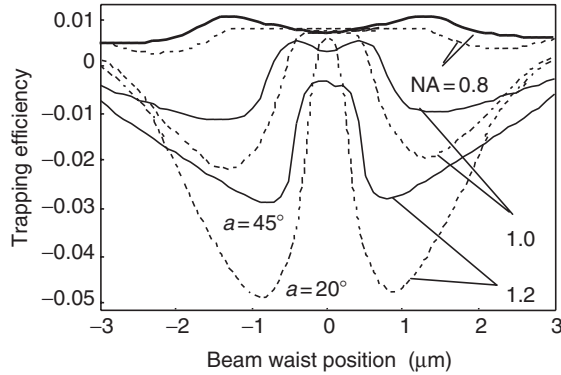


Fig. 4.11. Trapping efficiency Q vs beam waist position for the slope angles of $a = 20^\circ$ (dotted lines) and 45° (solid lines) with numerical aperture NA as a parameter

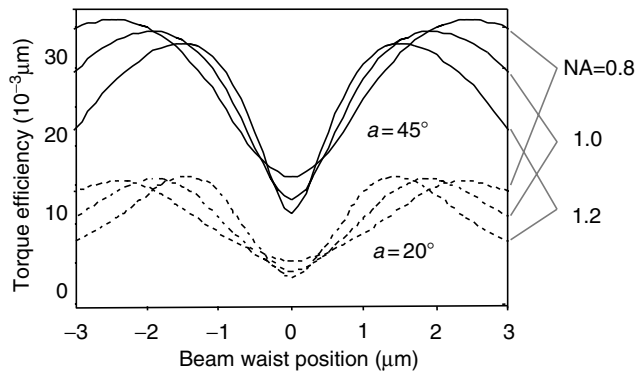


Fig. 4.12. Torque efficiency Q_{torque} vs beam waist position for the slope angle of $a = 20^\circ$ and 45° with numerical aperture NA as a parameter

power are below 0.3% and the computation error may be negligible. In the computation, the beam was divided into 100×100 area segments on the aperture.

Figure 4.11 shows examples of trapping efficiency Q and Fig. 4.12 shows torque efficiency Q_{torque} vs beam waist position for the slope angles of 20° and 45° with numerical aperture NA as a parameter. A negative value of Q is observed in Fig. 4.11. It indicates that the trapping force pulls the rotor toward the focused point of the incident beam, which leads to 3-D trapping. Torque efficiency Q_{torque} increases as NA decreases. Fast rotation is possible when NA decreases to produce a laser beam with a large radius on the top surface.

Figure 4.13 shows the illuminated region on the upper surface of $a = 20^\circ$ for several NAs where $P = 100$ mW. The radius of the illuminated region

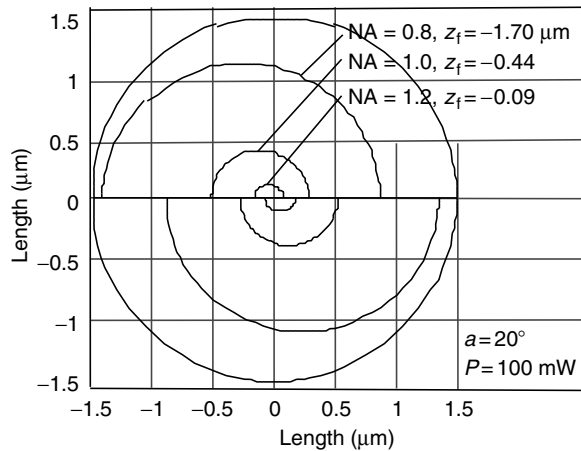


Fig. 4.13. Illuminated region on the upper surface of an $a = 20^\circ$ slope for several NAs. The radius of the illuminated region decreases as NA increases

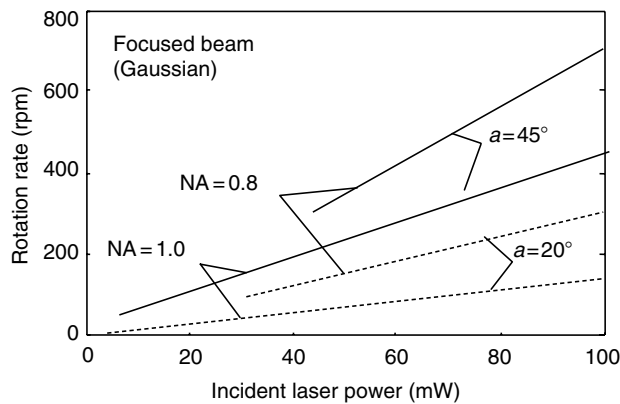


Fig. 4.14. Relationship between rotation rate and laser power for two NAs assuming $M_{\text{opt}} = M_{\text{drag}} (= 4\pi\mu r^2 h\omega)$

decreases as NA increases. Therefore, the optical torque also decreases as NA increases.

Figure 4.14 shows the relationship between the rotation rate and beam power for two NAs, assuming $M_{\text{opt}} = M_{\text{drag}} (= 4\pi\mu r^2 h\omega)$. The rotation rate is linearly proportional to the beam power and it increases as NA decreases. A rotation rate as high as 700 rpm is predicted using a 100 mW laser beam with a focused beam illumination of NA = 0.8. A cylindrical optical rotor is expected to rotate at a high speed due to its highly efficient optical torque generation and small viscous drag force under parallel beam illumination.

Effect of Light Beam Profiles

The trapping force and rotation rate are calculated for various beam intensity profiles of the form

$$\text{TEM}_{00}(\text{Gaussian}) \text{ mode : } I(r) = I_0 \exp(-2r^2/w_0^2), \quad (4.16)$$

$$\text{uniformly filled aperture mode : } I(r) = I_0, \quad (4.17)$$

$$\text{TEM}_{01}(\text{donut}) \text{ mode : } I(r) = I_0(r/w_0)^2 \exp(-2r^2/w_0^2). \quad (4.18)$$

The fractions of the total beam power that enters the lens aperture are 87% (a), 100% (b), and 59% (c). Below, all the light powers are normalized after the lens aperture.

Example 4.1. Analyze the relationship between the rotation rate and the slope angle with illuminated by beams with Gaussian (a), uniformly filled (b), and donut (c) intensity profiles.

Solution. Figure 4.15 shows the numerical results for the rotor of $d = 3\text{ }\mu\text{m}$, $h = 10\text{ }\mu\text{m}$, and $n_2 = 1.53$ in water of $\mu = 1\text{ mPa s}$ at the laser power of $P = 100\text{ mW}$. Since the torque at an arbitrary point is defined as the product of force F_t and distance r from the rotation axis, a high rotation rate (torque efficiency) can be obtained with beam profile (c) which has high intensity at the outer part of the aperture. Optical torque increases in linear proportion to the radius of the rotor, and the drag force increases as twice the radius, therefore, rotation rate decreases inversely proportional to the radius. Rotation rate increases as the slope angle a increases and reaches a maximum at $a = 75^\circ$. As a result, a laser beam with a strong profile at the outer part and a rotor with small radius are effective for increasing the rotation rate.

Example 4.2. Analyze the relationship between torque efficiency Q_{torque} and beam waist position z_f for the rotor illuminated by converging laser beams of the intensity profiles with (a)–(c).

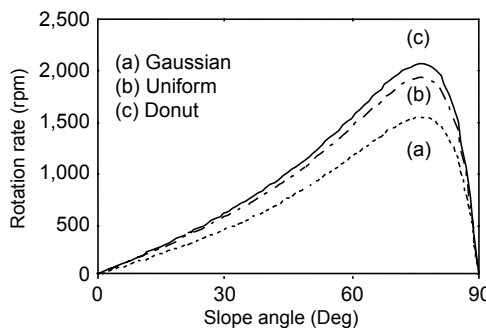


Fig. 4.15. Relationship between rotation rate and slope angle of the rotor of $d = 3\text{ }\mu\text{m}$, $h = 10\text{ }\mu\text{m}$, and $n_2 = 1.53$ in water at $P = 100\text{ mW}$ for the Gaussian (a), uniformly filled (b), and donut (c) beam intensity profiles

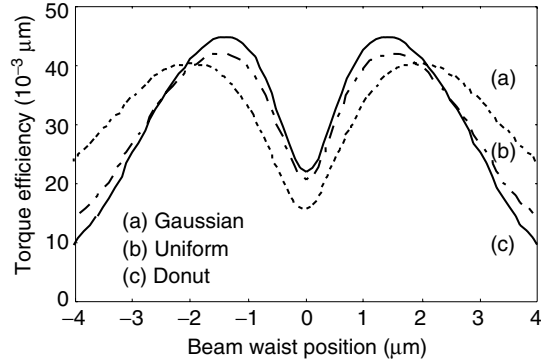


Fig. 4.16. Relationship between torque efficiency Q_{torque} and beam waist position z_f for different beam profiles

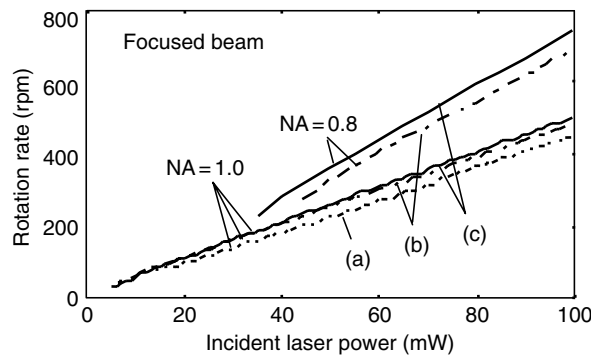


Fig. 4.17. Relationship between rotation rate and incident laser power for different beam profiles

Solution. Figure 4.16 shows the relationship between Q_{torque} and z_f for the different beam profiles. Good trapping and fast rotation are possible when the outer part of the input aperture is filled by a high intensity beam. In addition, the dependence of the rotation rate on the incident power for two NAs is shown in Fig. 4.17. The rotation rate increases as the intensity of the outer part becomes high. We can improve the rotation rate by adjusting the incident beam profiles.

In summary, it is confirmed that a high rotation rate can be obtained under the following conditions:

1. high NA of the objective lens
2. large slope angle of the microobject
3. high refractive index of the microobject (Problem 4.3)
4. large number of slopes on the microobject (Problem 4.4)
5. beam profile of high intensity at the outer part of the aperture.

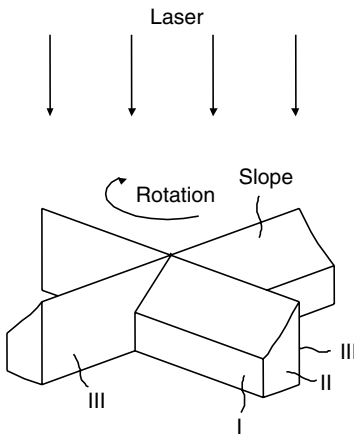


Fig. 4.18. Shuttlecock rotor with slopes on the top surfaces

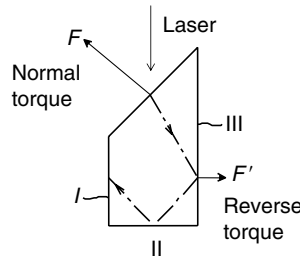


Fig. 4.19. Optical torque exerted for the shuttlecock rotor with slopes

4.2.3 Enhanced Shuttlecock Rotors with Slopes

In order to obtain high torque efficiency, a shuttlecock optical rotor with slopes, as shown in Fig. 4.18, is proposed. The enhanced rotor has the ability to generate optical torque upon parallel beam illumination at not only the side of the wing but also on the wing slope.

In order to simulate the optical torque, we considered a ray incidence on the slope. The ray refracts at the slope, exerting optical pressure F (generates torque in normal direction), and reflects back side surface III, exerting F' (generates torque in the reverse direction) as shown in Fig. 4.19. The optical pressure exerted at bottom surface II and at side surface I are very low owing to low reflectivities.

Figure 4.20 shows the simulated results for the enhanced shuttlecock rotor for parallel beam illumination with the refractive index of $n_2 = 1.6$. The diameter is $d = 20 \mu\text{m}$, and the thickness is $t = 10 \mu\text{m}$, and the wing width is $w = 3.3 \mu\text{m}$. The simulation conditions are listed in Table 4.2 (optical conditions are the same as listed in Table 4.1). Fig. 4.20 shows that the total optical

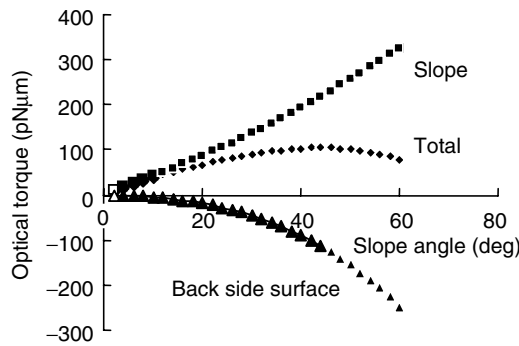


Fig. 4.20. Simulated optical torque dependence on the slope angle of the shuttlecock rotor

Table 4.2. Conditions of optical trapping efficiency simulation for the shuttlecock rotor with 45° slopes

rotor size	
slope angle a	45°
diameter d	$20\text{ }\mu\text{m}$
thickness t	$10\text{ }\mu\text{m}$
wing width w	$5\text{ }\mu\text{m}$
number of element on the aperture	
radial direction	100
circular direction	100

torque increases as the slope angle increases and reaches a maximum at 45° because the large divergent angle increases the reverse torque at back side surface III.

Figure 4.21a shows that the total optical torque increases as the wing width increases and Fig. 4.20b shows that total optical torque decreases as the thickness increases owing to the increase of reverse torque, which indicates that the optimum thickness equals that of the slope.

4.3 Theoretical Analysis II – Fluid Dynamics

Microflow around the rotor is analyzed through the process shown in Fig. 4.22. The simulation was performed in a 3-D geometry with a commercial computational fluid dynamics tool (CFX-4, AEA Corp.) [4.11].

First, the rotor shape is input and the cube grid is formed. The initial conditions of the medium, water at 283 K, density, and viscosity are defined. The control volume is a cube, in which each domain has a set of discretized equations that are formulated by evaluating and integrating the fluxes across

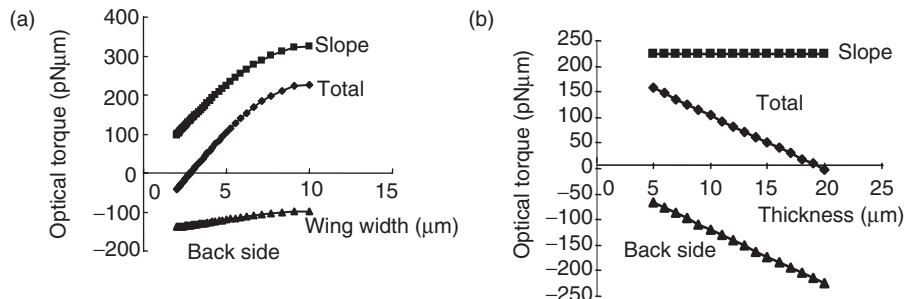


Fig. 4.21. Simulated optical torque dependence on the wing width (a), and on the thickness (b) of the shuttlecock rotor with slopes

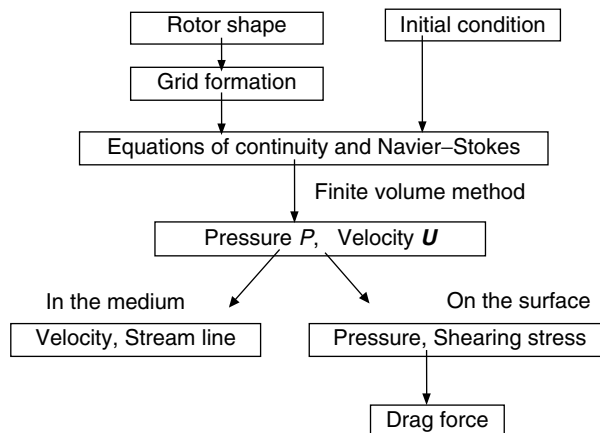


Fig. 4.22. Process for flow field and drag force analyses of optical rotor in water at room temperature by computational fluid dynamics (CFD)

the faces of the volume to satisfy the continuity equation (4.19) and Navier–Stokes equation (4.20), where \mathbf{U} is the fluid velocity, \mathbf{u} is the velocity of the sliding mesh, t is the time, P is the pressure and ν is the kinematic viscosity [4.12].

$$\nabla \cdot (\mathbf{U} - \mathbf{u}) = 0, \quad (4.19)$$

$$\frac{\partial \mathbf{U}}{\partial t} + ((\mathbf{U} - \mathbf{u}) \cdot \nabla) \mathbf{U} = -\nabla P + \nu \nabla^2 \mathbf{U}. \quad (4.20)$$

Second, to discretize (4.19) and (4.20), the finite volume method is used. The solver performs a number of iterations to minimize the overall change in selected parameters from one iteration to another. We obtained pressure P and velocity \mathbf{U} for each volume. On the rotor surface, pressure P and

shearing stress S are obtained. On the other hand, in the medium, velocity \mathbf{U} and streamlines are obtained.

Lastly, from the above computational results, the drag force is calculated as the sum of the torque components of both the pressure (normal component) and the shearing stress (tangential component) on all surfaces of the rotor as

$$M_{\text{drag}} = \int \int (P_t + S_t) r^2 dr d\theta, \quad (4.21)$$

where P_t is the torque component of pressure P , S_t is that of the shearing stress and r is the radius at that point.

4.3.1 Optical Rotor Having a Dissymmetrical Shape on its Side

Velocity Vectors and Streamlines

To evaluate the performance of the optical rotor in water, the streamlines around the rotor and the viscous drag force acting on the surface of the rotor were investigated using a fluid flow solver. The fluid is water ($n_1 = 1.33$) at 283 K (incompressible viscous flow, density $\rho = 1.0 \text{ g cm}^{-3}$, viscosity $\mu = 1.0 \text{ mPa s}$). The corresponding Reynolds number ($Re = r\omega d^2/4\pi$) nearly equals 10^{-4} .

Velocity vectors $\mathbf{U} = (u, v, w)$ in the proximity of the rotor at the speed of 200 rpm were analyzed, and the results are shown in Fig. 4.23. We found that the velocity vector has a component in the z direction even with horizontal rotation. Contour lines around the mixer for the 1- $\mu\text{m s}^{-1}$ pitch horizontal component (a), and for the 0.1- $\mu\text{m s}^{-1}$ pitch vertical component (b) are shown in Fig. 4.24. The flow goes not only outward but also up and down, which leads to circulation.

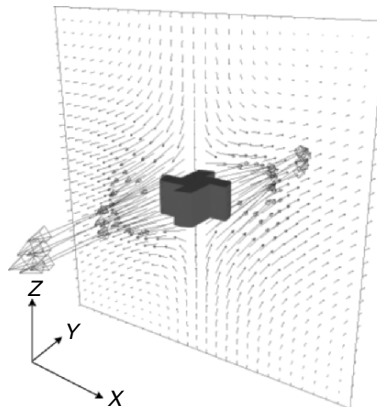


Fig. 4.23. Squint view of velocity vectors in the proximity of optical rotor for 200 rpm

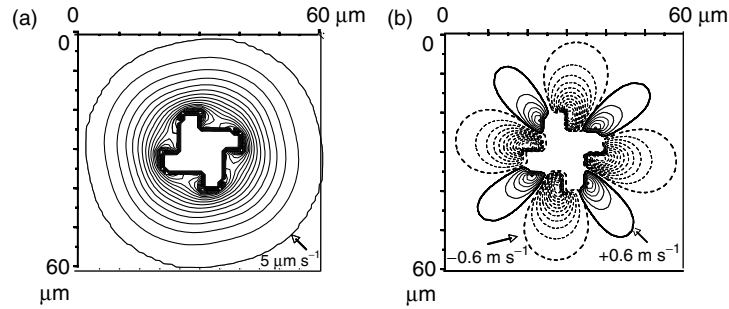


Fig. 4.24. Contour lines around optical rotor for horizontal component (a), and vertical component (b)

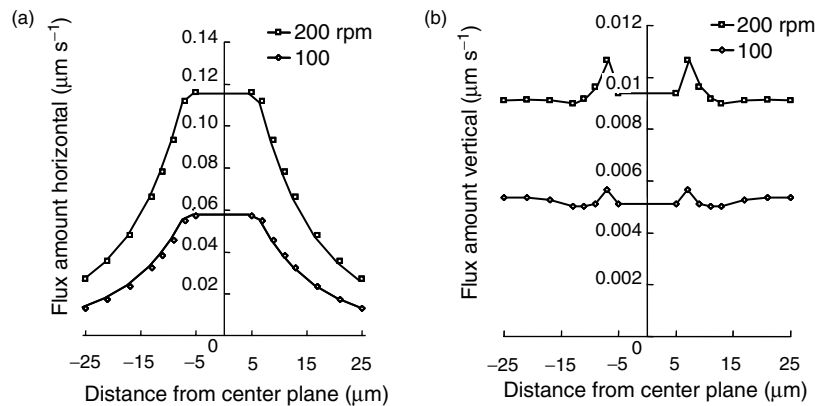


Fig. 4.25. Horizontal component (a), and vertical component (b) of fluid in the proximity of optical rotor

Figure 4.25 shows the flux amount in the proximity of the rotor for horizontal component $\sqrt{u^2 + v^2}$ (a), and for vertical component w (b). Here, flux amount is defined as the sum of absolute \mathbf{U} in the observation plane of $54\text{ }\mu\text{m} \times 40\text{ }\mu\text{m}$. From the figures, we can see that horizontal component $\sqrt{u^2 + v^2}$ decreases exponentially as the depth increases and that vertical component w reaches a maximum near the upper and lower surfaces of the rotor. From these theoretical analyses, we conclude that the velocity increases near the rotor and that the flow goes outward and up and down, which promotes fluid mixing.

Figure 4.26 shows the effect of the enhanced shuttlecock rotor with slopes (angle of 45°) on the flux amount. We find that the flux amount vertical with slopes becomes much larger than that without slopes.

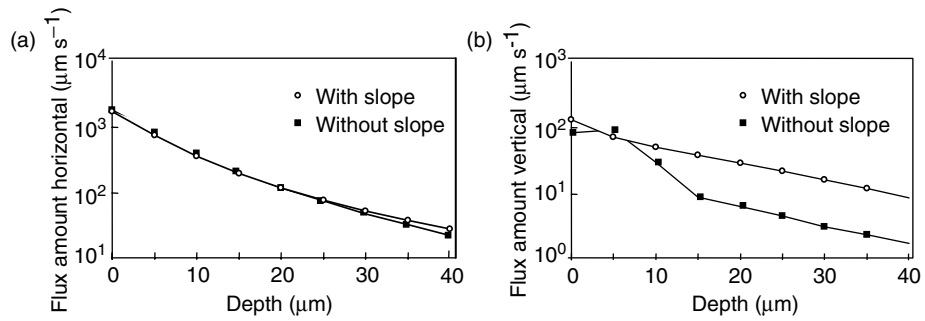


Fig. 4.26. Effect of the slope (angle of 45°) of the shuttlecock rotor on the flux amount. Horizontal (a), and vertical (b)

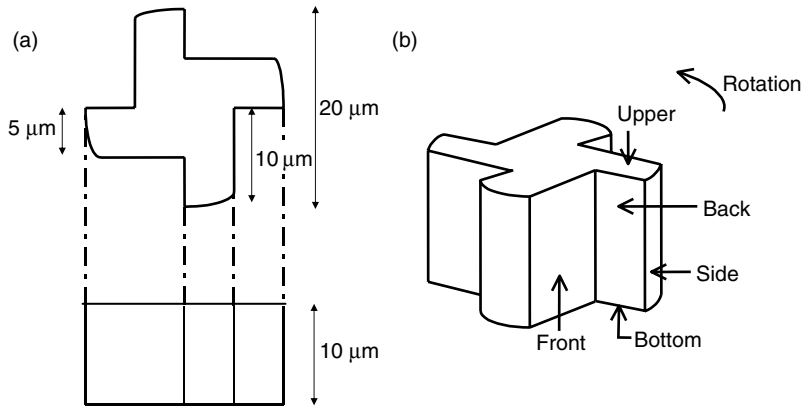


Fig. 4.27. Side view indicating the size of the rotor (a), and sectional view indicating the name of its side parts (b)

Pressure, Shearing Stress and Viscous Drag Force

Figure 4.27 shows the side view indicating the size of the rotor (a), and the sectional view indicating the names of parts (b). Pressure P (a), and shearing stress $S (= dU/dx)$ (b), exerted on the surfaces of the rotor at the rotation rate of 500 rpm are analyzed and shown in Fig. 4.28. We find that high pressure appears on the outer part of the front surface where the fluid velocity is high. Flow-in occurs near the back surface due to the negative pressure. The pressure on the flat ends is very small due to the tangential direction of the rotation axis. On the other hand, the shearing stresses are high on the side surface and the outer corner. As a result, the drag force is large at the side surface and the outer parts of the back surface.

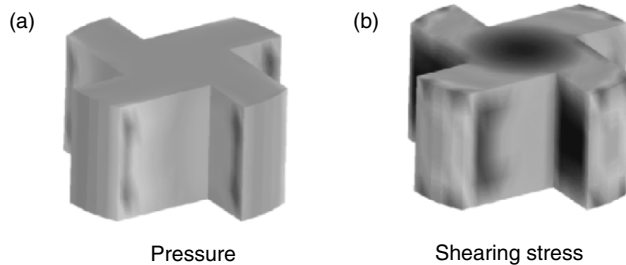


Fig. 4.28. 3-D images of the pressure distribution (a), and the shearing stress distribution (b)

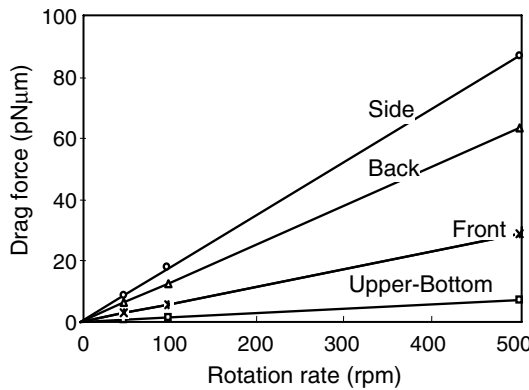


Fig. 4.29. Drag force at different parts of the shuttlecock rotor

Figure 4.29 shows the drag forces of different parts of the rotor. By balancing the optical torque with the drag force, the rotation rate of the shuttlecock rotor can be computed, as shown in Fig. 4.30; we obtain 600 rpm at the incident laser power of 100 mW under the conditions listed in Table 4.1.

4.3.2 Optical Rotor with Slopes on the Light Incident Surface

Velocity Vectors and Streamlines

The velocity vectors and the streamlines in the proximity of the cylindrical rotor rotating at the speed of 3,000 rpm are analyzed for the refractive index $n_2 = 1.5$, slope angle $a = 45^\circ$, diameter $2r = 3 \mu\text{m}$, and height $h = 10 \mu\text{m}$. The results are shown in Fig. 4.31a and b. Figure 4.31a shows that the velocity increases close to the rotor and the flow goes upward near top A but downward near the opposite top B, according to the counterclockwise rotation. The streamlines in Fig. 4.31b show that the flow goes outward and upward in the proximity of the slope ($h = 10 \mu\text{m}$) but slightly outward in the middle

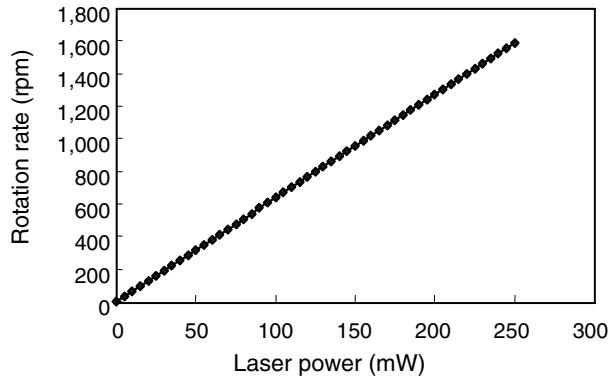


Fig. 4.30. Shuttlecock rotor rotation rate dependence on a laser power

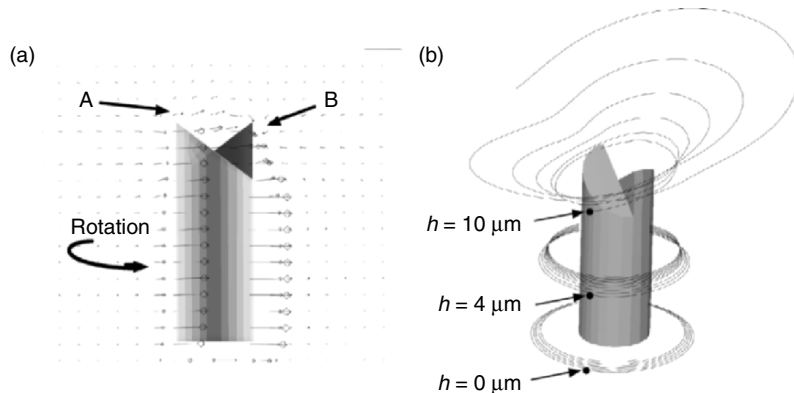


Fig. 4.31. Velocity vectors in the plane 0.5 μm before the center plane for the rotor of $a = 45^\circ$, $2r = 3 \mu\text{m}$ and $h = 10 \mu\text{m}$ (a), and streamlines around the rotor (b)

($h = 4 \mu\text{m}$), and slightly inward at the bottom ($h = 0 \mu\text{m}$). Arrows show the starting point of the flow.

Pressure and Shearing Stress

Figure 4.32 shows pressure P (a), and shearing stress S (b), on the surface of the rotor. A high pressure ($1.24 \text{ pN} \mu\text{m}^{-2}$) arises on the upper edge of the slope where the fluid velocity is high.

Flow-in occurs near the side wall due to the negative pressure. The pressure on the flat end is very low due to the tangential direction of the rotation axis. On the other hand, the shearing stresses are large at the top of the edge ($2.24 \text{ pN} \mu\text{m}^{-2}$). The shearing stress on the side surface is small, which leads to a low fluid flow along the side surface.

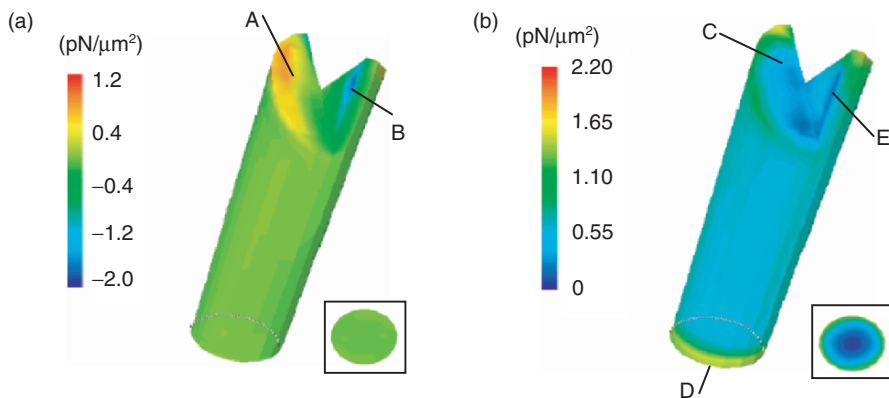


Fig. 4.32. 3-D images of the pressure distribution (a), and the shearing stress distribution (b), for cylindrical rotor of $a = 45^\circ$, $2r = 3\text{ }\mu\text{m}$ and $h = 10\text{ }\mu\text{m}$ at $P = 100\text{ mW}$

Table 4.3. Comparison of the drag force between CFD and the approximation method for the 3,000 rpm optical rotors with $a = 45^\circ$, $2r = 3\text{ }\mu\text{m}$, and $h = 3\text{ }\mu\text{m}$

method	CFD ($\text{pN }\mu\text{m}^{-2}$)	approximation ($\text{pN }\mu\text{m}^{-2}$)
slopes	6.37	0
side walls	4.99	0
side	39.3	35.4
flat end	3.56	0
total	54.2	35.4

CFD: computational fluid dynamics, approximation: $4\pi\mu r^2 h\omega$

Viscous Drag Force and Rotation Rate

Viscous drag force M_{drag} acting on the surface of the rotor is evaluated as described earlier. Table 4.3 shows a comparison of the drag force between computational fluid dynamics (CFD) and the approximation method for the 3,000 rpm optical rotors. The sum of the drag force on the slope ($6.37\text{ pN }\mu\text{m}^{-2}$) and the side wall ($4.99\text{ pN }\mu\text{m}^{-2}$) is three times that on the flat end ($3.56\text{ pN }\mu\text{m}^{-2}$).

Table 4.4 shows the drag force of each part of the rotor simulated by CFD for $2r = 3\text{ }\mu\text{m}$, and $h = 3\text{ }\mu\text{m}$ at the rotation rate of 3,000 rpm. Figure 4.33 shows the drag force dependence on the rotor height calculated by CFD and by the approximation method. It is clear that as the rotor height decreases, the difference between drag forces calculated by CFD and by the approximation method increases, as expected.

Assuming that the rotor is cylindrical, we can calculate rotation rate ω by $M_{\text{opt}} = M_{\text{drag}} (= 4\pi\mu r^2 h\omega)$ where μ is the viscosity of the medium ($\mu = 1\text{ mPa s}$). The correct rotation rate ω is adjusted by balancing optical torque

Table 4.4. Simulated drag forces of each part of the optical rotor with $a = 45^\circ$, $2r = 3\mu\text{m}$, and $h = 3\mu\text{m}$ at the rotation rate of 3,000 rpm

slope angle ($^\circ$)	0	30	60
slopes ($\text{pN }\mu\text{m}^{-2}$)	3.60	5.07	8.10
side walls ($\text{pN }\mu\text{m}^{-2}$)	0	3.07	9.27
side ($\text{pN }\mu\text{m}^{-2}$)	43.7	38.2	41.5
flat end ($\text{pN }\mu\text{m}^{-2}$)	3.60	3.56	3.61
total ($\text{pN }\mu\text{m}^{-2}$)	48.1	49.9	62.5

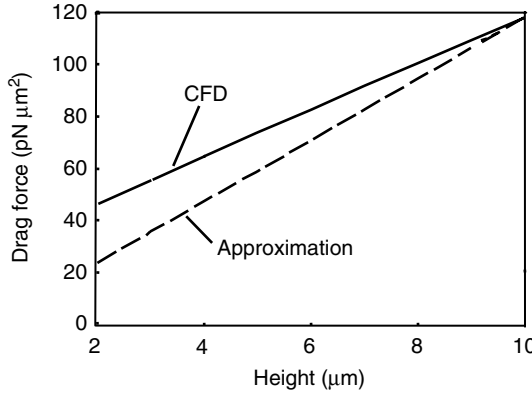


Fig. 4.33. Drag force obtained by CFD and the approximation method with rotor height as a variable

M_{opt} of (4.10) with drag force M_{drag} of (4.21). Figure 4.34 shows the rotation rates calculated by the approximation and by CFD for an $a = 45^\circ$ rotor, with the rotor height as a parameter. Figure 4.35 shows the rotation rates obtained by the approximation method and by CFD, with slope angle as a parameter. A laser power of 100 mW is directed onto the rotor with parallel beam illumination.

From these figures, we confirm that the slope effect on the drag force becomes strong for heights less than $10\mu\text{m}$ or for slope angles greater than 30° . The rotation rates calculated by CFD for a rotor with a $3\mu\text{m}$ diameter and $3\mu\text{m}$ height are 0.67 ($a = 45^\circ$) and 0.56 ($a = 60^\circ$) times the approximated values when the cylindrical-body drag force is $4\pi\mu r^2 h\omega$.

4.3.3 Mixing Performance in a Microchannel

Mixing efficiency of an optical rotor designed to be used in micrototal analysis systems (μ -TAS) has been studied by CFD [4.13]. The finite volume method is used to discretize (4.19) and (4.20), in which the third-order upwind scheme is used for the advection terms of the Navier–Stokes equation (4.20), and the

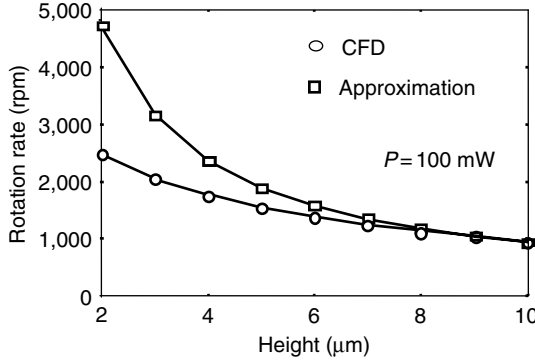


Fig. 4.34. Rotation rate obtained by CFD and approximation with parallel beam illumination at $P = 100 \text{ mW}$, $a = 45^\circ$, $2r = 3 \mu\text{m}$ with rotor height as a parameter

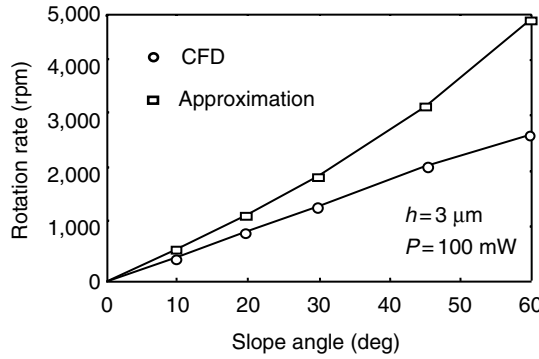


Fig. 4.35. Rotation rate obtained by approximation and CDF with slope angle as a parameter

second-order central differencing scheme is used both for the viscosity terms and the pressure terms of the Navier–Stokes equation (4.20) and for all the terms of the continuity equation (4.19). For time marching, the implicit backward Euler differencing scheme is used. The algorithm of the numerical solution is based on the SIMPLEC algorithm [4.12].

The shuttlecock optical rotor ($d = 20 \mu\text{m}$, $w = 4 \mu\text{m}$, $t = 10 \mu\text{m}$) is placed at the center of a Y-shaped microchannel ($30 \mu\text{m}$ width and $20 \mu\text{m}$ depth) and rotates at speeds of 100–2,000 (typical 500) rpm. The corresponding Reynolds number ($Re = rwd^2/4\pi$) is 10^{-2} to 10^{-4} . The fluid used is water at room temperature and its inlet fluid speed is in the range of 0 to $100 \mu\text{m s}^{-1}$. Figure 4.36 shows the grid system of the Y-shaped microchannel and the rotor. The mesh

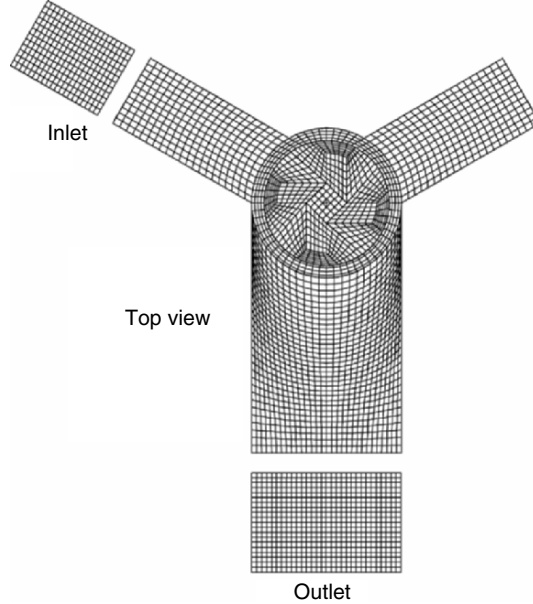


Fig. 4.36. Grid system of Y-shaped microchannel (inlet: 15 μm width and 20 μm depth, outlet: 30 μm width and 20 μm depth) and optical rotor ($d = 20 \mu\text{m}$, $w = 4 \mu\text{m}$, $t = 10 \mu\text{m}$) [4.13]. Courtesy of Y. Ogami, Ritsumeikan University, Japan

numbers are 12×20 for the inlet and 30×20 for the outlet. The total mesh becomes about 70,000.

Mixing rate M is defined on the outlet plane as

$$M = 1 - \frac{1}{C} \sqrt{\frac{\sum(C_i - 0.5)^2}{N}}, C = \frac{\sum C_i}{N} \quad (4.22)$$

where C_i is the mixing volume ratio of the i th mesh, N is the total mesh (600), and C is the average of the volume ratio, which leads to 0 in the state of no mixing and 1 in the state of complete mixing.

Figure 4.37a shows the relationship between mixing rate and rotation rate with diffusion coefficient $D = 0$, inlet fluid velocity as a parameter. The mixing rate increases as the rotation rate increases and it becomes high for slow fluid velocity. Figure 4.37b shows the relationship between the mixing rate and diffusion coefficient with rotation rate $\omega = 0$, inlet velocity as a parameter. The mixing rate increases as the diffusion coefficient increases and it becomes high for low fluid velocity.

Figure 4.38 shows the mixing rate dependence on the ratio of the wing top speed (circumferential speed corresponding to ω) to inlet fluid speed u . It is found that the mixing rate depends on ω/u . Figure 4.39 shows the mixing rate

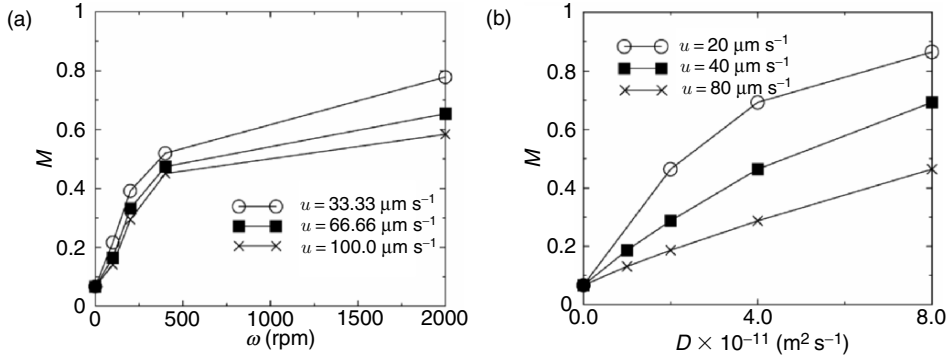


Fig. 4.37. Mixing rate M at various rotation rates ω and fluid velocities u with $D = 0$ (a), and M at various diffusion coefficients D and fluid velocities u with $\omega = 0$ (b) [4.13]

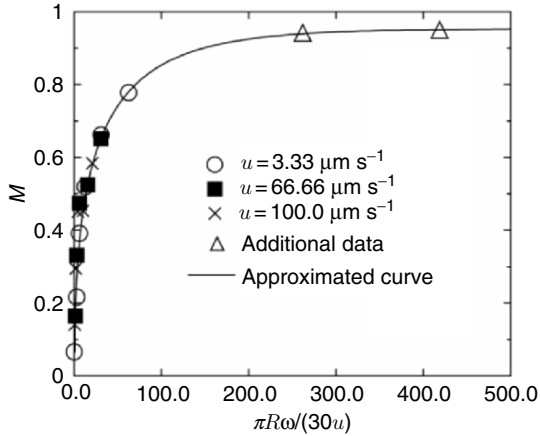


Fig. 4.38. Similarity of mixing rate M at $D = 0$, where R is the radius of the rotor [4.13]. Courtesy of Y. Ogami, Ritsumeikan University, Japan

dependence on the ratio of the diffusion coefficient to u . It is found that the mixing rate depends on D/u . From these results, an enhancement effect of convection generated by the rotor and the diffusion of fluids on the mixing performance is confirmed.

In microscale systems, the flow is considered to be laminar and convective mixing was considered to be negligible. Nevertheless, from the results obtained earlier, it is confirmed that the mixing efficiency increases due to convection generated by the rotor, through the effective increase of the diffusion coefficient.

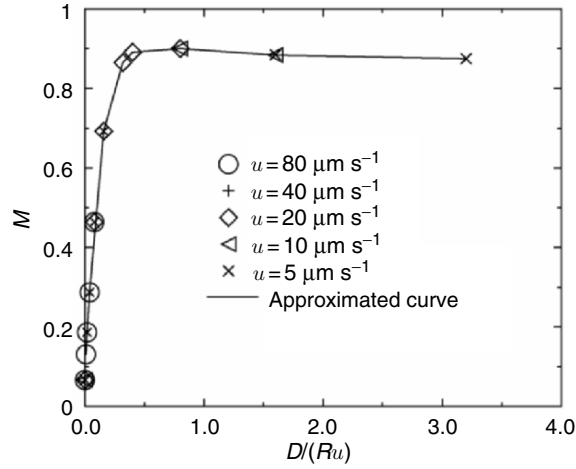


Fig. 4.39. Similarity of mixing rate M at $\omega = 0$ [4.13] Courtesy of Y. Ogami, Ritsumeikan University, Japan

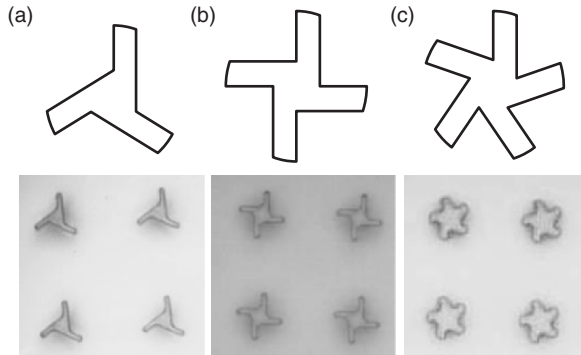


Fig. 4.40. Variation of the shuttlecock wing number for considering the stability, rotation rate and agitation in the medium

4.4 Fabrication

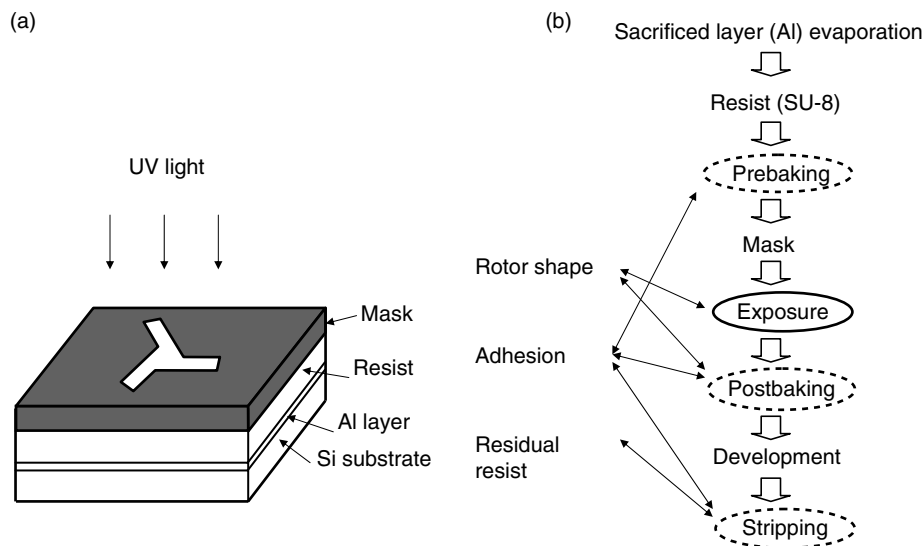
4.4.1 Potolithography

We can choose the wing number according to the desired characteristics, i.e., stable rotation, high rotation rate, and high agitation in the medium, under the conditions that the direction of surface III is parallel to the radial direction and the shape of surface II is circular. These are illustrated in Fig. 4.40 for 3, 4, and 5 wings. Such rotors can be fabricated by micromachining [1.1] such as dry etching [1.62], wet etching (photolithography) [1.23], and microphotoforming [1.27]. In the figure, photographs of the SU-8 photoresist rotors of

Table 4.5. Fabrication conditions of photolithography

photo resist	SU-8-25
spinner condition	1st: 1,000 rpm, 10 s 2nd: 5,000 rpm, 40 s
prebaking ^a	100°C, 20 min
postbaking ^a	140°C, 20 min
development	4.1 min
thickness	10 µm

^a Hot plate

**Fig. 4.41.** Optical rotor fabrication by photolithography

20 µm diameter fabricated by photolithography are shown. The fabrication conditions of photolithography are listed in Table 4.5.

Figure 4.41 shows the photolithography process. Not only the exposure and development conditions [4.14] but also the baking methods and conditions are important, particularly for achieving the correct rotor shape and avoiding adhesion between rotors [4.15]. An example of the fabricated three-wing rotor is shown in Fig. 4.42 along with the mask. Roundness at the wing top and swelling at the wing root are seen in the figure. To fabricate the correct shape, parallelism between the resist and the mask is important. We used a hotplate instead of an oven to prevent resist deformation during prebakeing and postbaking. We adjusted the baking temperature of 140°C to polymerize the resist firmly.

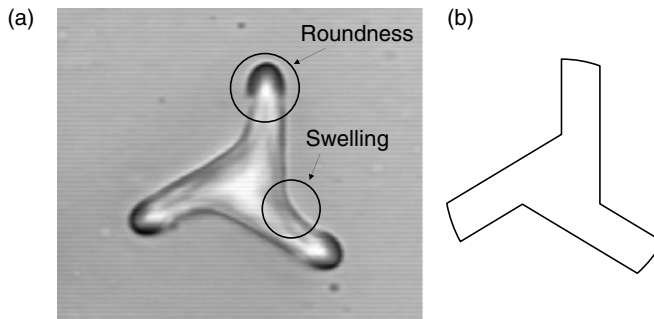


Fig. 4.42. Example of fabricated three-wing rotor shape (a) compared with the mask shape (b)

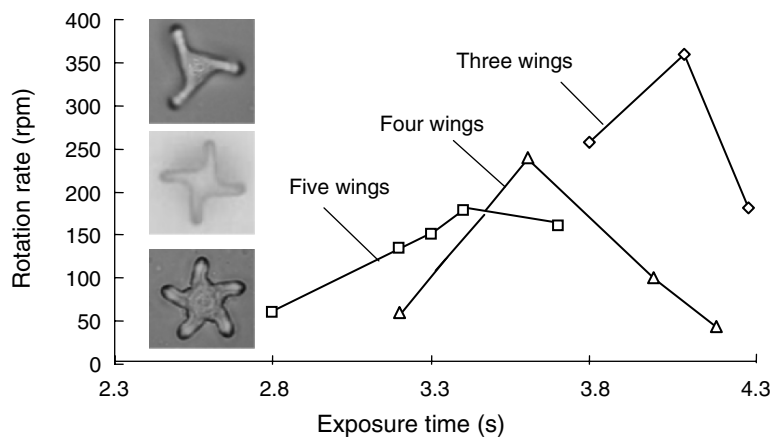


Fig. 4.43. Measured rotation rates for three kinds of rotors

We released the rotor into the laser trap environment by etching away the aluminum under the resist. The measured rotation rates for three kinds of rotors are shown in Fig. 4.43. Rotation rate varies according to the exposure time (varies the rotor shape), but the maximum speed (corresponds to the correct shape) is fast for small number of wings. Three wings provide the fastest rotation in this experiment.

Fluorinated polyimide is also suitable for the microrotor because it is highly transparent in the near-infrared region and it is easy to etch into a particular shape using oxygen plasma. The fabrication process of the polyimide rotor is as follows [4.16]:

1. a polyimide solution is spin-coated onto an Si substrate, which is then heated to 370°C

2. a Si-based negative resist with high resistance to oxygen reactive ion-beam etching (O_2 RIE) is spin-coated onto the polyimide layer and exposed to an electron beam
3. the polyimide layer is etched down to the Si substrate by O_2 RIE
4. after removal of the resist, the microrotor are freed from the substrate by ultrasonic vibration.

Fluorinated polyimide has a density of 1.49 and a refractive index of 1.53 at a wavelength of $1.064\text{ }\mu\text{m}$ as listed in Table 3.3.

4.4.2 Microphotoforming

In order to increase the optical torque of the rotor, it is effective to adopt a 3-D structure with slopes on its upper surface. To fabricate such 3-D microstructures, photoforming is applied. However, the presently proposed photoforming apparatus is large and requires a special laser beam (ultra-short-pulsed near-infrared Ti:sapphire) or special resin (two-photon-absorbed urethane material) [1.29, 4.17].

We developed a desktop microphotoforming apparatus using a DVD optical head and a visible light-curable resin (DF-200N, Nippon Kayaku Corp.), both of which are commercially available [4.18]. Since the microstructure is generated by scanning a focused laser beam to solidify the contour of a liquid photopolymer, the resolution is determined by the laser beam intensity distribution and the absorption of light within the polymer. To decrease the solidified depth, a thin resin film was made using a spinner, as shown in Fig. 4.44

Figure 4.45 shows the shuttlecock optical rotor with a $30\text{ }\mu\text{m}$ diameter and $15\text{ }\mu\text{m}$ thickness. The fabrication conditions were a scan speed of $25\text{ }\mu\text{m s}^{-1}$, scan pitch of $0.3\text{ }\mu\text{m}$, single scan and a laser power of 0.35 mW . The overall time was 12 min to fabricate 16 rotors.

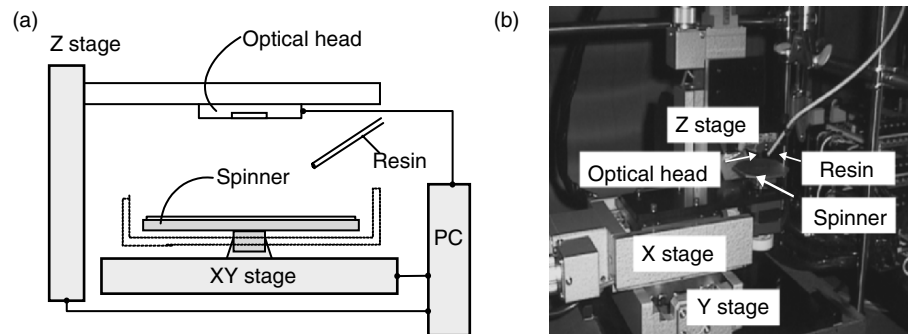


Fig. 4.44. Schematic diagram (a), and photograph (b) of the spinner-type microphotoforming apparatus

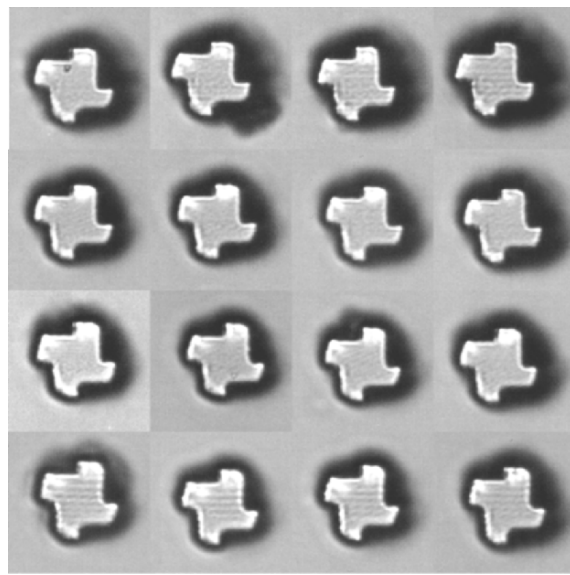


Fig. 4.45. Shuttlecock optical rotors, 30 μm diameter and 15 μm thick, fabricated by photoforming

Table 4.6. Photoforming conditions for the slope of the rotor

optical power	0.35 mW
scanning velocity	25–70 $\mu\text{m s}^{-1}$
scanning pitch	0.3 μm
scanning method	single scan
layer thickness	5 μm
resin	visible light-curable resin ^a
resin amount	360 μl

^a DF-200N, Nippon Kayaku Corp.

Complicated 3-D microstructures were fabricated by stacking thin resin layers that had been solidified into the cross-sectional shape using a DVD LD with the wavelength of 650 nm. Table 4.6 shows the photoforming conditions for the slope of the rotor. Figure 4.46 shows the 3-D design (upper), cross-sections (middle) and fabricated layers (lower) of 5 μm thick each. It is found that the fabricated layer shapes are similar to those of the corresponding cross sections.

4.5 Evaluation

In this section, evaluation methods of the microflow field generated by the optical rotor are discussed, considering the future application as a mixer in

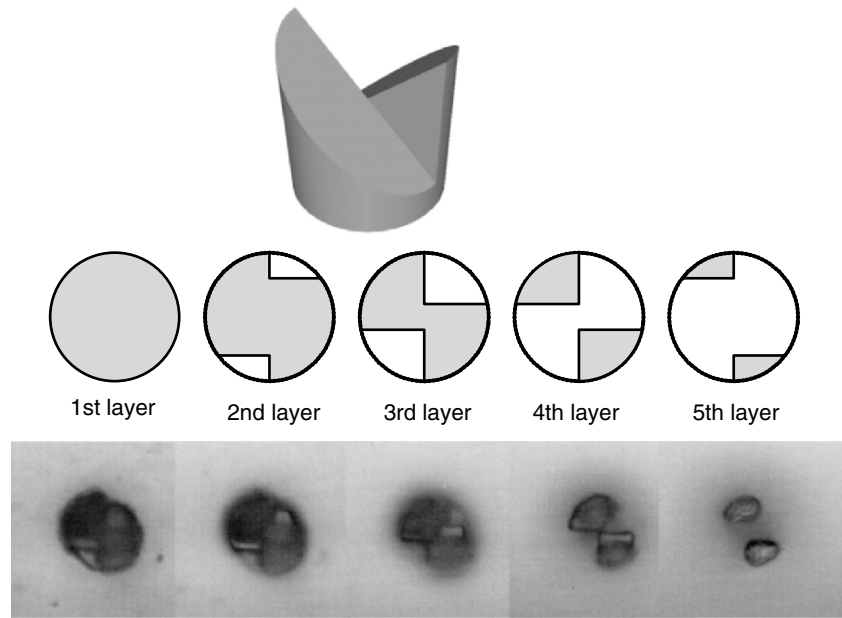


Fig. 4.46. Microstructures with slopes are fabricated by stacking of thin resin layers having the 2-D cross-sectional shape, *upper*: 3-D designed shape, *middle*: 2-D cross-sections designed, and *lower*: fabricated 2-D cross-sectional-shape layers of $5\text{ }\mu\text{m}$ thick each

μ -TAS [4.18, 4.19]. In addition, the rotation rate of the rotor was measured by two techniques using the video frame time and the period of scattered light variation [4.4].

4.5.1 Visualization of Microflow (Agitation)

In the actual evaluation, the microflow fields generated by the optical rotor are analyzed using images obtained with a newly constructed evaluation system. To obtain the images, we use two methods. One is the tracer method in which we trace many particles suspended in the medium. The other is an optical method in which we observe the medium density variation [4.20]. By comparing the results of the two methods, we confirm that the optical method is appropriate for visualizing the overall microflow behavior.

Figure 4.47 shows the experimental setup for trapping and rotating the rotor with an upward-directed YAG laser beam and for visualizing the microflow using a high-speed camera. Figure 4.48 shows a photograph of the experimental apparatus. The rotor in the medium inside the chamber is secured at the focal point of the $\text{NA} = 1.4$ objective lens.

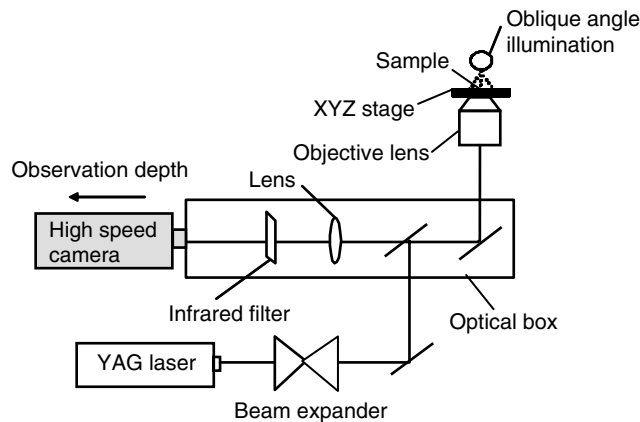


Fig. 4.47. Experimental setup to visualize microflow around mixer. The upward-directed YAG laser traps the rotor. Generated microflows are visualized with oblique angle illumination

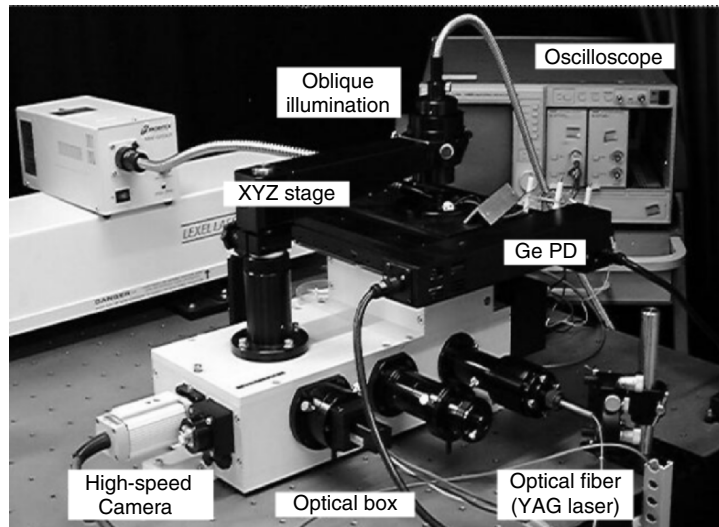


Fig. 4.48. Photograph of experimental apparatus to visualize the microflow around rotor

To visualize the flow field in the proximity of the rotor, the light scattered due to the medium density variation upon illumination at a grazing angle is observed. The oblique illumination increases the image contrast, because only the scattered light is observed. The sample chamber, in which optical rotors and milk fat colloid are suspended in water, as shown in Fig. 4.49, is sealed with a cover glass.

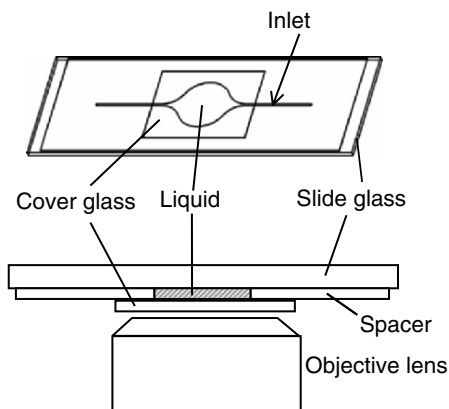


Fig. 4.49. Fabricated sample chamber sealed with cover glass. When liquid is dropped at the edge of the inlet it moves toward the center by surface tension

Tracer Method

Arbitrarily-shaped glass particles ($n = 1.51, \rho = 2.54 \text{ g cm}^{-3}$) ranging from 5 to $15 \mu\text{m}$ in size and the photoresist shuttlecock rotors ($n = 1.6, \rho = 1.16 \text{ g cm}^{-3}$) of 10 to $30 \mu\text{m}$ in diameter were used in the experiment. They are transparent to the YAG laser wavelength of $1.06 \mu\text{m}$, which prevents optical damage.

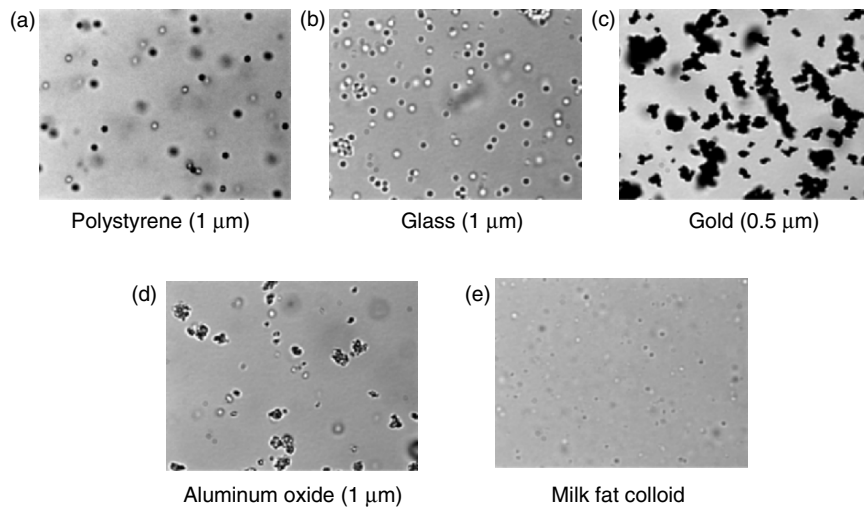
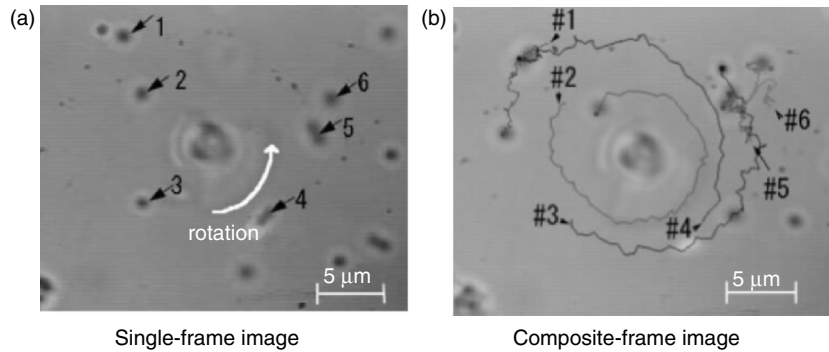
Tracers added to mark the flow included polystyrene, glass, gold, aluminum oxide, diamond, tooth powder, pigment, a shampoo colloid and a milk fat colloid. Some of them are shown in Fig. 4.50. Polystyrene and glass are spherical, but gold and aluminum have no definitive shape. The particles were dispersed in water with a surface active agent, but the gold and aluminum were condensed due to electrostatic force.

Figure 4.51 shows the results for microflow analyzed by the tracer method for the $1.0 \mu\text{m}$ glass beads in 30% glycerol solution. We recorded a 2.3-second motion (71 frames) with a high-speed camera. The resolution was $640 \times 240 \times 8$ bits per frame.

The velocity and the direction of each of beads #1 through #6 were traced as the pathlines. In the figure, the following interesting characteristics of microflow are recognized.

1. The flows are strong for tracers #2, #3, and #4, which were very close at the rotor, but weak for #1, #5, and #6, which were at very distant locations.
2. The flows expand to two to three times the rotor diameter.

Figure 4.52 show the variation in the tracer velocity due to the rotor and the Brownian motion. Microflow and the diffusion effect will promote stirring or mixing in microscale systems.

**Fig. 4.50.** Various particles used to visualize microflow**Fig. 4.51.** Visualization and pathlines using glass tracers. Single-frame image (a), and analized pathlines (b)

The following are the requirements for the tracers used with an optical rotor. (1) They must be small (less than 1 μm in this case) and sufficiently dense, (2) The tracers should be prevented from undergoing Brownian motion, and (3) The tracers should not be affected by optical pressure. Condition (1) is satisfied with an optical rotor of about 10 μm , and condition (2) is satisfied by using glycerol to increase the medium viscosity. Since high density glycerol affects the rotor motion, heavy beads are suitable for the tracer. Concerning condition (3), particles such as polystyrene, glass, and milk fat colloid were not significantly affected by the optical pressure, but metallic particles such as gold and aluminum oxide were expelled from the laser focal point, as shown in Fig. 4.53.

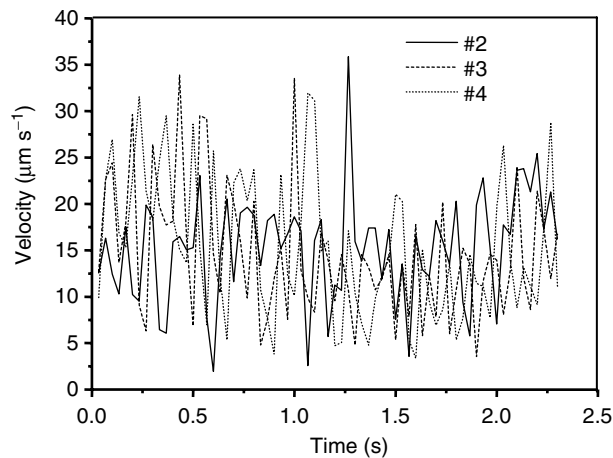


Fig. 4.52. Variation in tracer velocity due to the flow generated by the rotor and the Brownian motion. Notation # corresponds to that of Fig. 4.51

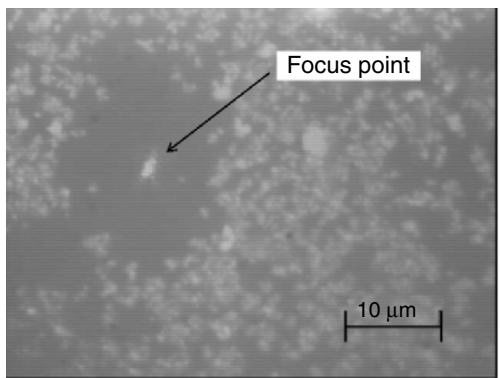


Fig. 4.53. Effect of optical pressure. Gold particles around the laser spot are expelled by the optical pressure

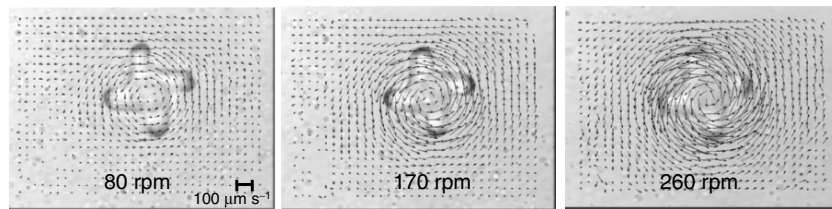
Table 4.7 lists the evaluation results of the visualized images for a number of different kinds of tracer and medium combinations. The symbol \bigcirc indicates excellent, Δ good, and \times poor results, which suggests that 1- μm -diameter glass beads and milk fat colloid are suitable for microflow visualization.

Optical Method

In the optical method, we observe the medium density variation. The microflows generated by the optical rotor are analyzed through visualized images of medium density variation. We can see microflow around the rotors. Compared to the tracer method, this optical method can easily yield the total image of

Table 4.7. Effect of the tracer on the images of the visualized microflow

tracer (size)	glycerol (%)	visualization	
		tracer	optical
polystyrene (0.5 μm)	50	×	×
polystyrene (1.0 μm)	30	△	×
glass (0.5 μm)	50	×	×
glass (1.0 μm)	30	○	×
aluminum (1.0 μm)	30	×	×
gold (0.5 μm)	50	×	×
milk fat colloid	30	○	○

**Fig. 4.54.** Velocity vector analysis by tracking the density pattern of the medium, with rotation rate as a parameter

the microflow. We analyze the microflow using the visualized images obtained by the optical method. Velocity vectors and the flux amount around the mixer are derived to evaluate the degree of agitation of the liquid. Through the analysis, we confirmed that both the rotor shape and the rotation velocity affect on microflow.

Optical rotors were trapped near the upper surface of the chamber, and the rotation rate was varied to 80, 170, and 260 rpm by changing the laser power. The velocity vectors due to the medium density variation caused by the optical rotor was observed for different rotation rates, as shown in Fig. 4.54 at the frame rate of 1/120 s.

4.5.2 Medium Density Pattern Tracking

These flow-field analyses can be carried out using a fast pattern tracking algorithm based on the correlation between the density variation patterns (Flow-vec 32, Library Corp.), as shown in Fig. 4.55. The measuring points are located at 0.5 μm intervals in the observation plane. The correlation between the medium density pattern in an element with size of $3.5 \times 3.5 \mu\text{m}^2$ and that in the search size are calculated to obtain the reliability, which is defined as the pattern tracking accuracy for the medium density variation. The velocity of flow at the measuring point can be calculated from the distance between the measuring point in the current frame and the maximum correlation point in the next frame, divided by the frame time (1/120 s).

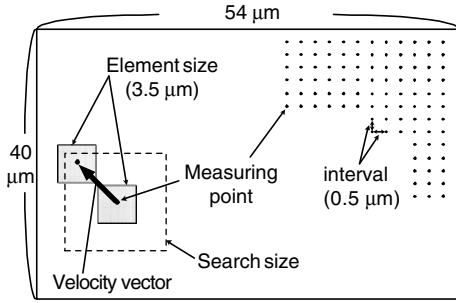


Fig. 4.55. Analytical model used to obtain velocity vectors and measuring points in horizontal plane

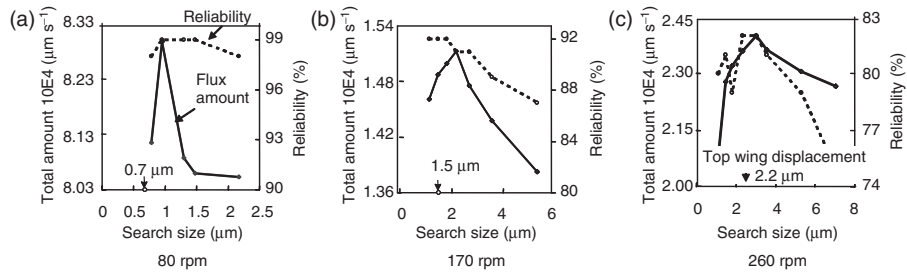


Fig. 4.56. Determination of optimum search size for rotation rates of 80, 170, and 260 rpm; arrow shows displacement of wing top per frame (1/120 s). The optimum search size is that at which flux amount reaches a maximum

The flux amount is defined here as the total sum of the absolute velocity vectors \mathbf{U} at all the measuring points in the observation plane. They are averaged over the frame time. Average flux amount is also defined as total flux amount divided by the number of measuring points in the observation plane.

Figure 4.56 shows the relationship between the total flux amount/reliability and the search size for the rotation rates of 80, 170, and 260 rpm. The optimum search size is determined by the maximum flux amount. Arrows in the figure show the calculated displacement of the mixer wing top per frame. We can see that the optimum search size nearly equals 1.4 times the wing top displacement per frame [4.19].

4.5.3 Velocity Vector and Flux Amount Analyses

Microflow at different depths was observed by placing a high-speed camera along the optical axis. An optical mixer, 12 μm in thickness, was trapped and horizontally rotated at 170 rpm in contact with the upper surface of the chamber. Figure 4.57 shows the analyzed velocity vectors around the rotor at

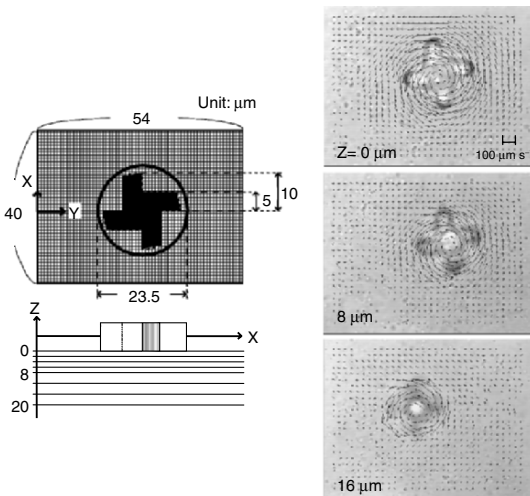


Fig. 4.57. Velocity vectors around optical mixer at different depths for horizontal rotation

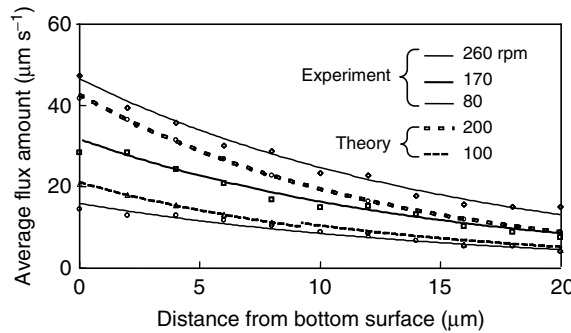


Fig. 4.58. Average flux amount at different depths

different depths measured from the bottom surface of the rotor. The velocity vectors at the bottom surface $z = 0 \mu\text{m}$ are directed along the rotation in the circle but expand outward outside the circle. The fluid expands to more than twice the thickness of the rotor.

The average flux amount outside the rotor decreases exponentially as the depth increases, as shown in Fig. 4.58 for the rotation rates of 80, 170, and 260 rpm. In the figure, theoretical results for 100 and 200 rpm are also shown for reference. Both results are in fairly good agreement, even in the microscale.

When an optical mixer, $9 \mu\text{m}$ in thickness, is 3-D trapped in an off-axis position in the medium, it rotates vertically around the axis perpendicular to the laser beam axis. The flows are visualized with a frame rate of 120 at speeds of 115, 155, and 215 rpm, as partly shown in Fig. 4.59. The velocity vectors at the focal plane originate from the left wing, flow into the right

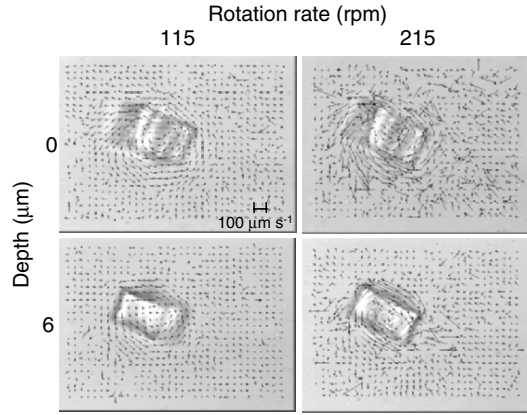


Fig. 4.59. Velocity vectors around optical mixer for vertical rotation, with observation depth and rotation rate as parameters

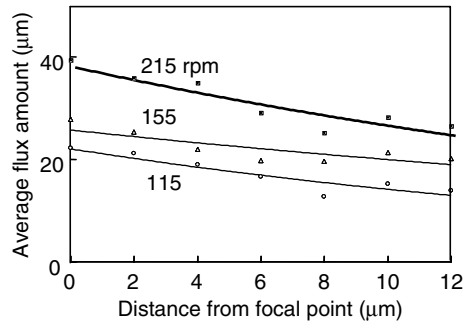


Fig. 4.60. Average flux amount at different depths for vertical rotation, rotation rate as a parameter

wing, expand outward, and gradually decrease as the depth increases. The flux amount decreases gradually from focal point, as shown in Fig. 4.60

To improve the agitation efficiency, we fabricated three kinds of optical rotors. Figure 4.61 shows the effect of the number of wings of the rotor on the rotation rate and flux amount. Figure 4.62 shows the relationship between the average flux amount and rotation rate, with the number of wings as a parameter. The rotation rate of a three-wing rotor reaches 600 rpm with a laser power of 200 mW. The average flux amount of a five-wing rotor is 1.15 times greater than that of the three-wing rotor because the five-wing rotor is in contact with the liquid more frequently, even at the same rotation rate. We also observed that the higher the rotation rate, the greater the flux amount. These results show that both the wing number and the rotation rate affect the flux amount.

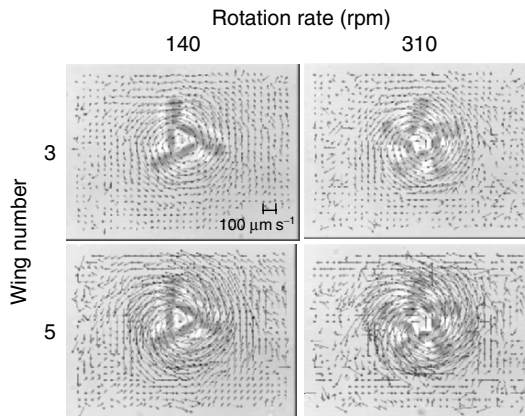


Fig. 4.61. Velocity vectors for rotors with different numbers of wings, with rotation rate as a parameter

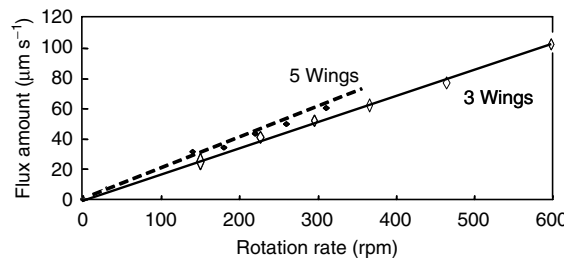


Fig. 4.62. Flux amount generated by shuttlecock optical rotors with different wing numbers

In summary, three kinds of optical rotors are proposed stirring the liquid around them, and the characteristics that promote mixing are confirmed. The fluidic velocity vectors around the 20-μm-diameter SU-8 rotors are visualized, and the flux amounts are derived at different depths both theoretically and experimentally.

The microflow arises within two to three times the rotor diameter and thickness for the horizontal rotation, and the flow goes not only outward but also up and down. The average flux amount gradually decreases as the depth increases. The flux amount of the five-wing rotor is 1.15 times greater than that of the three-wing rotor at the same rotation rate. The velocity vectors of the vertical rotation originate from the left wing and flow into the right wing and expand outward partly along the optical axis, which promotes convective mixing.

4.6 Mixer Application for μ -TAS

Because the Reynolds number in a microchannel in future μ -TAS will be small, mixing devices that increase two liquid contact areas are proposed to promote the diffusion effect. Interweaving of two liquids has been achieved by adopting various structure geometries in a channel, such as micronozzle arrays and intersecting channels which induce chaotic flow, as shown in Fig. 4.63 [4.21]. These mixers have been characterized as static devices. On the other hand, active micromixers with pressure perturbations that are applied transversally to the main stream, as shown in Fig. 4.64 have been presented [4.22]. They are called cross-channel mixers [4.23], fabricated by using MEMS technology, in which chaotic-like mixing is achieved in an efficient way. The optical mixer proposed in this book is another type of active mixer to stir a liquid in a microchannel [4.19].

μ -TAS is also called a Labs-on-a-chip. The chip will have components such as inlets for loading the sample and reagent, microfabricated fluidic channels

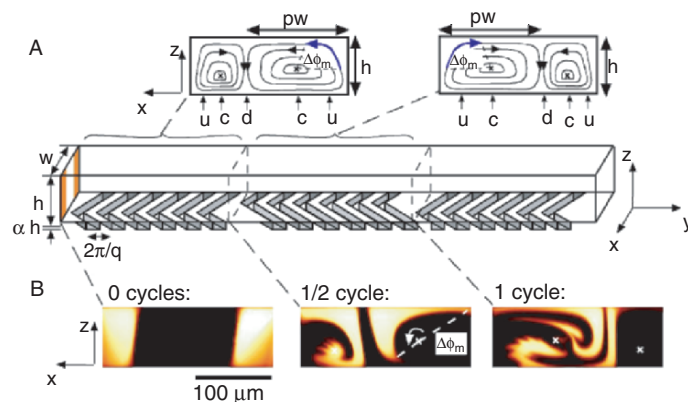


Fig. 4.63. Mixing by intersecting microchannels, which induces chaotic behavior of microflow [4.21]. Courtesy of A. Stroock, Cornell University, USA

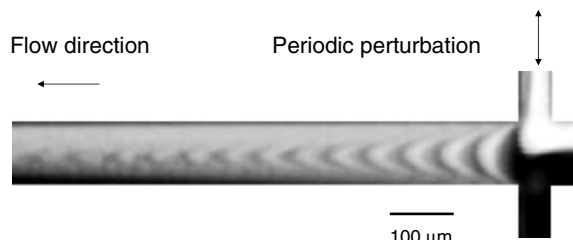


Fig. 4.64. Chaotic mixing by using the mechanical micromixer [4.22]. Courtesy of Y.K. Lee, University of California, USA

with a mixing chamber and an analyzing chamber, a detector of the reaction products, and outlets for exhausting sample waste. The analyte specimen and the reagents will be actuated by pressure force using syringe pumps.

Figure 4.65 shows the mixing part of the microchannel and the optical rotor. The microchannel width and depth are both $50\text{ }\mu\text{m}$. Such an optically driven rotor is expected to be used as the mixer in future chemical Labs-on-a-chip and have the advantage of remote control without the use of bearings. Reaction results in the mixing part are analyzed by, for example, optical (fluorescence), thermal [4.24], electrochemical, and mass spectrographic methods.

Figure 4.66a shows the merging of flows of NaOH solution (4 mmol L^{-1}) and BTB solution (BromoThymol Blue, 4 mmol L^{-1}), both having the inlet fluid velocity of $3.3 \times 10^3\text{ }\mu\text{m s}^{-1}$ with surfactants, and Fig. 4.66b shows the optical mixer ($d = 20\text{ }\mu\text{m}$) having the rotation rate of 1,000 rpm at the laser power of 200 mW. The mixer is held stable using optical tweezers even in such

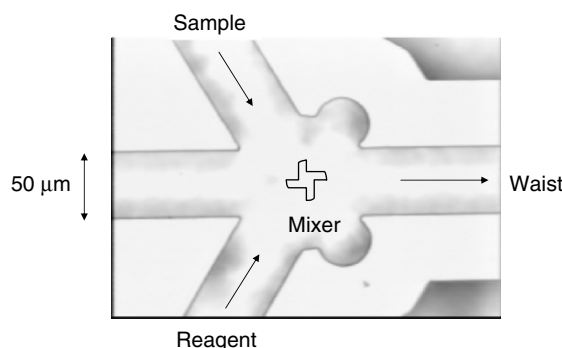


Fig. 4.65. Concept of an optical mixer for use in future μ -TAS. The integrated system will have components such as inlets, fluidic channels with a mixing chamber, a detector (not shown) and outlets

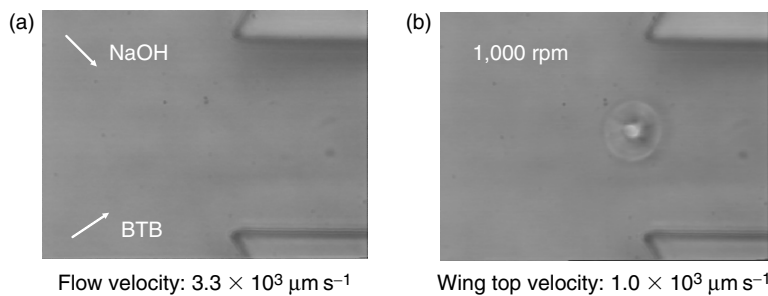


Fig. 4.66. Merging of the flows of NaOH solution (4 mmol/L) and BTB solution (a), and optical mixer ($d = 20\text{ }\mu\text{m}$) with the rotation rate of 1,000 rpm at the power of 200 mW (b)

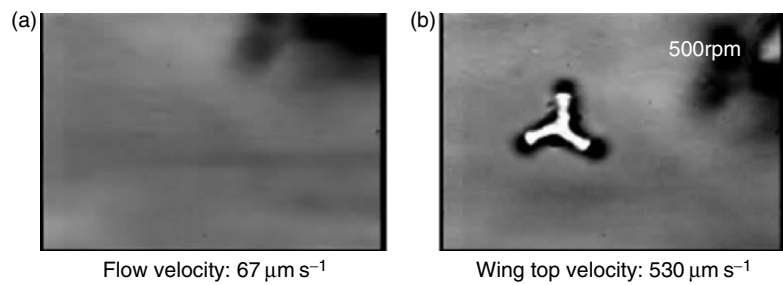


Fig. 4.67. Visualization of two-liquid mixing: without mixer (a), with mixer (b); 20% milk fat colloid for visualization was included only in the NaOH solution

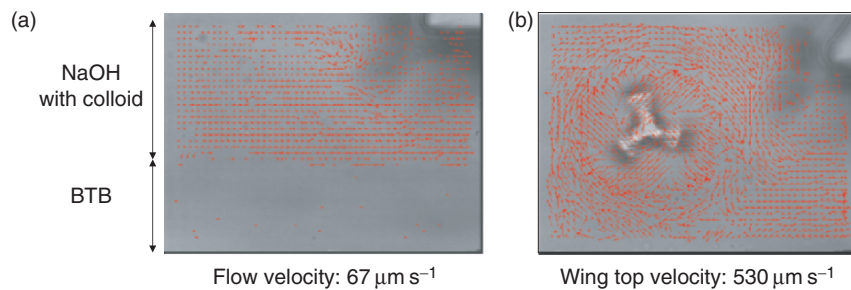


Fig. 4.68. Two-liquid mixing. Velocity vectors appear only in NaOH solution without mixer (a), but they appear in both liquids upon mixing using the optical mixer (b).

a high-speed flow. The wing top speed (circumferential speed) corresponds to $1 \times 10^3 \mu\text{m s}^{-1}$.

To visualize the mixing of two liquids, 20% milk fat colloid is included only in the NaOH solution. Figure 4.67a shows the flows without mixer and b shows the flows with mixer. We can recognize stirred flow of the milk fat colloid in the NaOH solution. To confirm the mixing of the two liquids, the velocity vectors are analyzed for the two liquids, as shown in Fig. 4.68. Velocity vectors appear only in the NaOH solution without mixer (a), but they appear in both liquids due to the mixing by the optical rotor (b).

μ -TAS is expected to reduce inspection time or the amount of reagent needed [4.25, 4.26]. In order to promote convective mixing, a shuttlecock optical mixer, which rotates in fluids and is capable of stirring the fluid around it, is proposed and the following basic technologies are confirmed:

1. mixer shape design by analyzing the optical torque by a ray optics model
2. microflow analysis around the mixer by CFD
3. mixer fabrication both by photolithography using an SU-8 and microphotoforming with a visible light-curable resin

4. flow visualization using milk fat colloid in glycerol solution with grazing angle illumination
5. pathline and velocity vector analyses around the mixer
6. flow amount analysis around the mixer
7. two-liquid mixing performance in a microchannel is confirmed using the optically trapped mixer both by theoretically and experimentally.

Problems

- 4.1.** How can the optical torque for a three-wing shuttlecock rotor be increased?
- 4.2.** How is the optical torque dependence on the rotor diameter simulated for a four-wing shuttlecock under the conditions listed in Table 4.1?
- 4.3.** How is the rotation rate dependence on the refractive index for the cylindrical optical rotor with a slope angle of 45° simulated under the conditions listed in Table 4.2?
- 4.4.** What is the relationship between the rotation rate and the number of slopes of the cylindrical rotor with 45° slope angle under the conditions listed in Table 4.2?
- 4.5.** What is a suitable optical mixer structure for used in the microchannel of future μ -TAS?

Near Field

The near field represents an electromagnetic evanescent field that has its intensity maximum at the surface and an exponentially decaying field perpendicular to it. It is localized within a hundred nanometers. The near field cannot be probed by conventional light detectors because it does not propagate. However, if we could access and control it, we would be able to observe or read/write or fabricate beyond the wavelength resolution. These science and technology fields, which include near-field scanning microscopy, optical data storage, and the processing industry, are also concerned with micromechanical photonics.

In this chapter we describe the near field's features, theoretical analyses, experimental analyses, and applications mainly related to optical storage.

5.1 Background

The evanescent field is widely known as a solution to Maxwell's equations [5.1–5.4]. It is localized near the surface and decays exponentially within a hundred nanometers. To excite the near field, it is necessary to have the following nonpropagating conditions, as shown in Fig. 5.1:

1. Attenuated total reflection (ATR): the use of a highly refractive prism is the simplest method of producing a near field. When a light is incident at the interface from a high-refraction medium to a low-refraction medium at an angle greater than that of total reflection, the light is reflected totally to the high-refraction medium and a near field is produced at the low-refraction medium surface, as shown in Fig. 5.2.
2. An aperture smaller than the wavelength of light: if the aperture size is smaller than the wavelength, the light does not propagate through the aperture but produces evanescent light. An optical fiber with a sharpened end is often used for this purpose.

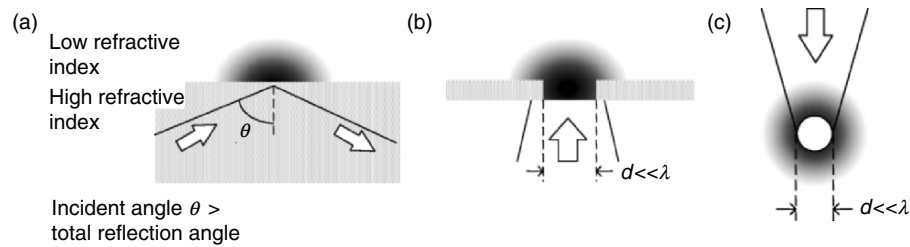


Fig. 5.1. Methods how to produce near field at object surface

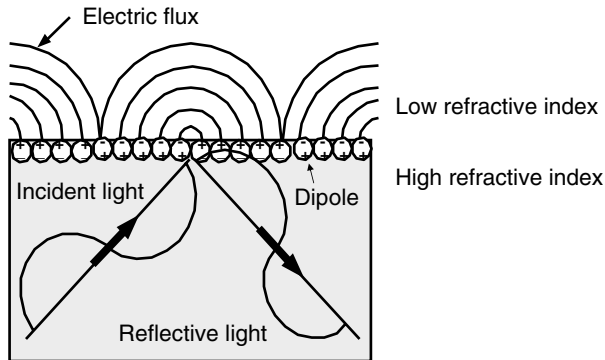


Fig. 5.2. Sketch of the near field produced at the low-refraction medium surface as the electric flux generated by dipoles due to the attenuated total reflection of light

3. An apertureless scattering probe: a metallic needle [5.5, 5.6] and a nanometer-size metallic sphere [5.7, 5.8] are used for strong enhancement of the near field.

The idea of using a small aperture for high-resolution microscopy was reported a long time ago. Pohl et al. [5.9] showed a high-resolution capability (20 nm) by line scanning with a transparent probe coated with metal and having a small aperture at the apex in 1884. Imaging in reflection by a scanning near-field microscopy (SNOM) was demonstrated with an aperture probe by Fischer et al. in 1888 [5.10]. In the 1990s, Betzig at Bell Labs. invented a pulled-fiber probe with a metal coating. He and his coworkers demonstrated various applications in superresolution microscopy [5.11]. Ohtsu et al. fabricated many sophisticated sharpened structured fiber probes and they are also developing atom-manipulation techniques using near-field light [5.3]. Kawata et al. developed a new concept of physics and instrumentation by combining near-field and surface plasmon polaritons [5.4].

Driven by great expectations, various studies of microscopy were carried out. However, success in practical use was delayed by problems of probe

fabrication reproducibility and an artifact caused by the vertical tip displacement [5.12]. Using the near field we can observe [5.11], read/write [5.13], and fabricate [5.14] beyond the diffraction limit of the conventional optics.

5.2 Theoretical Analysis

The quantitative description of the near field is given by vector theory. We can obtain analytical solutions for only limited structures, resulting in a computational solution approach to Maxwell's equations. The finite difference time domain (FDTD) method [5.15] is often used for such an approach because a new structure of interest can be modeled easily by systematic mesh generation.

5.2.1 FDTD Method

FDTD is a direct solution method for Maxwell's equations by space-grid time-domain techniques employing no potentials. It is based on volumetric sampling of an unknown electric field E and a magnetic field H within and surrounding the structure of interest, and over a period of time. The sampling in space is, typically, more than 10 per wavelength. The sampling in time is selected to ensure numerical stability of the algorithm. At present, the best choices for the computational algorithm and mesh remain unclear.

Since this technique requires no special knowledge, FDTD is emerging in a variety of fields of science and engineering. Optics-related fields are concerned with near fields, microdisk resonators, photonic band-gap devices, and colliding spatial solitons. FDTD is becoming a standard method in these fields. We consider the foundation of FDTD electromagnetic field analysis using the algorithm introduced by Yee in 1996 [5.16]. The main steps of the FDTD algorithm are as follows:

1. Define the space domain to be computed
2. divide the domain into cells
3. rewrite Maxell's equation (5.1) using the time and space derivatives
4. calculate E and H at each location under initial conditions and continue the process cycle for the time step

$$\begin{aligned}\nabla \times \mathbf{E} &= -\mu \frac{\partial \mathbf{H}}{\partial t}, \\ \nabla \times \mathbf{H} &= \sigma \mathbf{E} + \varepsilon \frac{\partial \mathbf{E}}{\partial t}.\end{aligned}\quad (5.1)$$

We introduce the following notation (in one spatial dimension), denoting a space point in a uniform, rectangular lattice as:

$$(x, y, z, t) = (i\Delta x, j\Delta y, k\Delta z, n\Delta t), \quad (5.2)$$

where Δx , Δy , and Δz are the lattice space increment in the x -, y -, and z - axis, respectively, and Δt is the time increment, and i, j, k and n are integrals. Abbreviating Δx , Δy , Δz , and Δt , the expression can be rewritten more simply as

$$F(x, y, z, t) = F^n(i, j, k), \quad (5.3)$$

where (i, j, k) are the coordinates of the lattice. The finite-difference expressions for the space derivatives used in the curl operators are central difference in nature and second-order accurate.

Figure 5.3 shows the space-time chart of the Yee algorithm in one dimension showing the use of central differences for space derivatives and leapfrog for time derivatives. E is positioned at $t = (n - 1)\Delta t, n\Delta t, (n + 1)\Delta t$, and H is positioned at $t = (n - 1/2)\Delta t, (n + 1/2)\Delta t$. In actual case, E^n is derived from E^{n-1} at $t = (n - 1)\Delta t$ and $H^{n-1/2}$ at $t = (n - 1/2)\Delta t$ and $H^{n+1/2}$ is derived from $H^{n-1/2}$ and E^n . Figure 5.4 shows the position of the electric- and magnetic-field vector components in two dimension. E and H components are positioned alternately, i.e., H is on every cell edge and E is between cells.

In three-dimensional (3-D) space, E and H components are positioned so that every E component is surrounded by four circulating H components, and

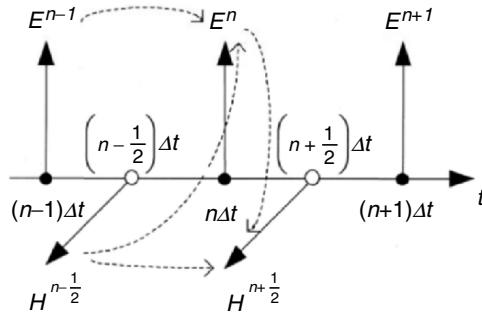


Fig. 5.3. Space-time chart of Yee algorithm in one dimension showing the use of central differences for space derivatives and leapfrog for time derivatives [5.15]

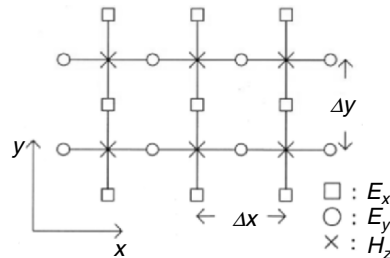


Fig. 5.4. Positions of electric- and magnetic-field vector components in two dimension. E and H components are positioned alternately, i.e., H is on every cell edge and E is between cells [5.15]

every H component is surrounded by four circulating E components. The position of the electric- and magnetic-field vector components is approximately a cubic unit of the Yee space lattice.

We now rewrite the vector components of (5.1), yielding the following system of six coupled scalar (5.4)–(5.9) [5.15].

$$\frac{\partial H_x}{\partial t} = \frac{1}{\mu} \left(\frac{\partial E_y}{\partial z} - \frac{\partial E_z}{\partial y} \right), \quad (5.4)$$

$$\frac{\partial H_y}{\partial t} = \frac{1}{\mu} \left(\frac{\partial E_z}{\partial x} - \frac{\partial E_x}{\partial z} \right), \quad (5.5)$$

$$\frac{\partial H_z}{\partial t} = \frac{1}{\mu} \left(\frac{\partial E_x}{\partial y} - \frac{\partial E_y}{\partial x} \right), \quad (5.6)$$

$$\frac{\partial E_x}{\partial t} = \frac{1}{\epsilon} \left(\frac{\partial H_z}{\partial y} - \frac{\partial H_y}{\partial z} - \sigma E_x \right), \quad (5.7)$$

$$\frac{\partial E_y}{\partial t} = \frac{1}{\epsilon} \left(\frac{\partial H_x}{\partial z} - \frac{\partial H_z}{\partial y} - \sigma E_y \right), \quad (5.8)$$

$$\frac{\partial E_z}{\partial t} = \frac{1}{\epsilon} \left(\frac{\partial H_y}{\partial x} - \frac{\partial H_x}{\partial y} - \sigma E_z \right). \quad (5.9)$$

Here, from (5.3) we define the function F on (i, j, k) at the time increment n as

$$F^n(i, j, k) = F(i\Delta x, j\Delta y, k\Delta z, n\Delta t). \quad (5.10)$$

The space and time derivatives are given as

$$\frac{\partial F^n(i, j, k)}{\partial x} = \frac{F^n(i + \frac{1}{2}, j, k) - F^n(i - \frac{1}{2}, j, k)}{\Delta x}, \quad (5.11)$$

$$\frac{\partial F^n(i, j, k)}{\partial t} = \frac{F^{n+\frac{1}{2}}(i, j, k) - F^{n-\frac{1}{2}}(i, j, k)}{\Delta t}. \quad (5.12)$$

The space derivative (5.11) has the same form for y, z and the time derivative (5.12) is given between half an increment and half a decrement. Considering F as E or H , (5.4)–(5.9) are expressed as the time-stepping expressions (5.13)–(5.18).

$$\begin{aligned} H_x^{n+\frac{1}{2}} \left(i, j + \frac{1}{2}, k + \frac{1}{2} \right) &= H_x^{n-\frac{1}{2}} \left(i, j + \frac{1}{2}, k + \frac{1}{2} \right) + \frac{\Delta t}{\mu(i, j + \frac{1}{2}, k + \frac{1}{2})} \\ &\times \left[\frac{E_y^n(i, j + \frac{1}{2}, k + 1) - E_y^n(i, j + \frac{1}{2}, k)}{\Delta z} \right. \\ &\quad \left. + \frac{E_z^n(i, j, k + \frac{1}{2}) - E_z^n(i, j + 1, k + \frac{1}{2})}{\Delta y} \right], \end{aligned} \quad (5.13)$$

$$\begin{aligned}
H_y^{n+\frac{1}{2}} \left(i + \frac{1}{2}, j, k + \frac{1}{2} \right) &= H_y^{n-\frac{1}{2}} \left(i + \frac{1}{2}, j, k + \frac{1}{2} \right) + \frac{\Delta t}{\mu(i + \frac{1}{2}, j, k + \frac{1}{2})} \\
&\times \left[\frac{E_z^n(i + 1, j, k + \frac{1}{2}) - E_z^n(i, j, k + \frac{1}{2})}{\Delta x} \right. \\
&\quad \left. + \frac{E_x^n(i + \frac{1}{2}, j, k) - E_x^n(i + \frac{1}{2}, j, k + 1)}{\Delta z} \right],
\end{aligned} \tag{5.14}$$

$$\begin{aligned}
H_z^{n+\frac{1}{2}} \left(i + \frac{1}{2}, j + \frac{1}{2}, k \right) &= H_z^{n-\frac{1}{2}} \left(i + \frac{1}{2}, j + \frac{1}{2}, k \right) + \frac{\Delta t}{\mu(i + \frac{1}{2}, j + \frac{1}{2}, k)} \\
&\times \left[\frac{E_x^n(i + \frac{1}{2}, j + 1, k) - E_x^n(i + \frac{1}{2}, j, k)}{\Delta y} \right. \\
&\quad \left. + \frac{E_y^n(i, j + \frac{1}{2}, k) - E_y^n(i + 1, j + \frac{1}{2}, k)}{\Delta x} \right],
\end{aligned} \tag{5.15}$$

$$\begin{aligned}
E_x^{n+1} \left(i + \frac{1}{2}, j, k \right) &= \frac{1 - \frac{\sigma(i + \frac{1}{2}, j, k)\Delta t}{2\varepsilon(i + \frac{1}{2}, j, k)}}{1 + \frac{\sigma(i + \frac{1}{2}, j, k)\Delta t}{2\varepsilon(i + \frac{1}{2}, j, k)}} E_x^n \left(i + \frac{1}{2}, j, k \right) + \frac{\frac{\Delta t}{\varepsilon(i + \frac{1}{2}, j, k)}}{1 + \frac{\sigma(i + \frac{1}{2}, j, k)\Delta t}{2\varepsilon(i + \frac{1}{2}, j, k)}} \\
&\times \left[\frac{H_z^{n+\frac{1}{2}}(i + \frac{1}{2}, j + \frac{1}{2}, k) - H_z^{n+\frac{1}{2}}(i + \frac{1}{2}, j - \frac{1}{2}, k)}{\Delta y} \right. \\
&\quad \left. + \frac{H_y^{n+\frac{1}{2}}(i + \frac{1}{2}, j, k - \frac{1}{2}) - H_y^{n+\frac{1}{2}}(i + \frac{1}{2}, j, k + \frac{1}{2})}{\Delta z} \right],
\end{aligned} \tag{5.16}$$

$$\begin{aligned}
E_y^{n+1} \left(i, j + \frac{1}{2}, k \right) &= \frac{1 - \frac{\sigma(i + \frac{1}{2}, j, k)\Delta t}{2\varepsilon(i + \frac{1}{2}, j, k)}}{1 + \frac{\sigma(i + \frac{1}{2}, j, k)\Delta t}{2\varepsilon(i + \frac{1}{2}, j, k)}} E_y^n \left(i, j + \frac{1}{2}, k \right) + \frac{\frac{\Delta t}{\varepsilon(i + \frac{1}{2}, j, k)}}{1 + \frac{\sigma(i + \frac{1}{2}, j, k)\Delta t}{2\varepsilon(i + \frac{1}{2}, j, k)}} \\
&\times \left[\frac{H_x^{n+\frac{1}{2}}(i, j + \frac{1}{2}, k + \frac{1}{2}) - H_x^{n+\frac{1}{2}}(i, j + \frac{1}{2}, k - \frac{1}{2})}{\Delta z} \right. \\
&\quad \left. + \frac{H_z^{n+\frac{1}{2}}(i - \frac{1}{2}, j + \frac{1}{2}, k) - H_z^{n+\frac{1}{2}}(i + \frac{1}{2}, j + \frac{1}{2}, k)}{\Delta x} \right],
\end{aligned} \tag{5.17}$$

$$\begin{aligned}
E_z^{n+1} \left(i, j, k + \frac{1}{2} \right) = & \frac{1 - \frac{\sigma(i+\frac{1}{2},j,k)\Delta t}{2\varepsilon(i+\frac{1}{2},j,k)}}{1 + \frac{\sigma(i+\frac{1}{2},j,k)\Delta t}{2\varepsilon(i+\frac{1}{2},j,k)}} E_z^n \left(i, j, k + \frac{1}{2} \right) + \frac{\frac{\Delta t}{\varepsilon(i+\frac{1}{2},j,k)}}{1 + \frac{\sigma(i+\frac{1}{2},j,k)\Delta t}{2\varepsilon(i+\frac{1}{2},j,k)}} \\
& \times \left[\frac{H_y^{n+\frac{1}{2}}(i+\frac{1}{2},j,k+\frac{1}{2}) - H_y^{n+\frac{1}{2}}(i-\frac{1}{2},j,k+\frac{1}{2})}{\Delta x} \right. \\
& \quad \left. + \frac{H_x^{n+\frac{1}{2}}(i,j-\frac{1}{2},k+\frac{1}{2}) - H_x^{n+\frac{1}{2}}(i,j+\frac{1}{2},k+\frac{1}{2})}{\Delta y} \right].
\end{aligned} \tag{5.18}$$

From (5.13)–(5.18), it is found that H at the time step $n+1/2$ can be obtained by E at n and H at $n-1/2$, E at $n+1$ is obtained by H at $n+1/2$ and E at n (see Fig. 5.3). The cycle begins again with the computation of E components based on the newly obtained H . This process continues until the solutions remain constant. To avoid numerical instability, the time increment must satisfy the following Courant condition:

$$v_{\max}\Delta t \leq \left(\frac{1}{\Delta x^2} + \frac{1}{\Delta y^2} + \frac{1}{\Delta z^2} \right)^{-\frac{1}{2}}. \tag{5.19}$$

Here, v_{\max} is the maximum phase velocity of the electromagnetic wave. Moreover, to prevent the reflection at the outermost space-lattice planes of the computational domain, absorbing boundary conditions (ABCs) must be introduced. Since first-order Mur ABCs are effective only for normally incident plane wave, second-order Mur ABCs are often used [5.17]. On the other hand, Berenger's perfectly matched layer (PML) ABCs are effective for the plane waves of arbitrary incidence, polarization, and frequency [5.18]. In the case of a perfect conductor, the electric field equals zero on the surface.

5.2.2 Numerical Examples of Near Field Analysis

The following are examples of the application of FDTD to problems including the interaction between a plane wave and typical subwavelength structures.

Example 5.1. Compute the electromagnetic field around a small aperture on the perfect conductor plane when a TM (p-polarized) plane wave is normally incident, and show the intensity profile in two dimensions.

Solution. Figure 5.5 shows (a) a process for analysis, and (b) a 2-D Cartesian computational domain ($1500 \text{ nm} \times 500 \text{ nm}$). We consider a TM (p-polarized) plane wave normally incident on a 100-nm-diameter aperture with the parameters $\Delta x = \Delta y = 1 \text{ nm}$, $\Delta t = 2.3586769 \times 10^{-19} \text{ s}$ and $n = 3,000$. Figure 5.6 shows a numerical result in the domain of $75 \text{ nm} \times 500 \text{ nm}$ by FDTD, indicating that the electric field is enhanced at the edge and decays rapidly [5.19].

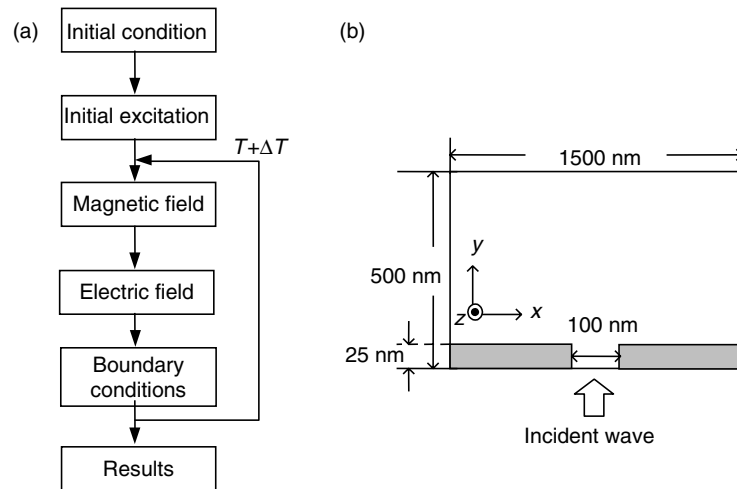


Fig. 5.5. Calculation process for FDTD (a), and computational domain for calculation (b)

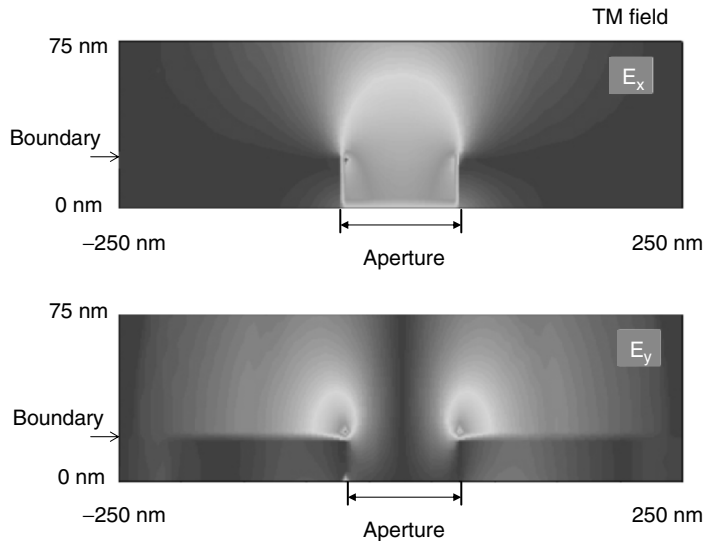


Fig. 5.6. Numerical result indicating that the electric evanescent field is enhanced at the edge and decays rapidly

- Example 5.2.* (1) Show the time-step dependence on the electric field intensity E_x for Example 5.1.
 (2) Show the round-trip number dependence on the electric field E_x at 20 nm above the aperture for Example 5.1.

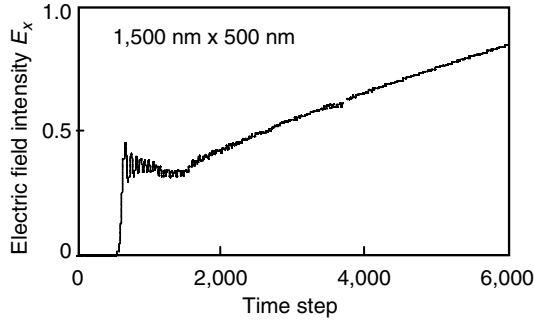


Fig. 5.7. Relationship between electric field E_x and time steps of FDTD

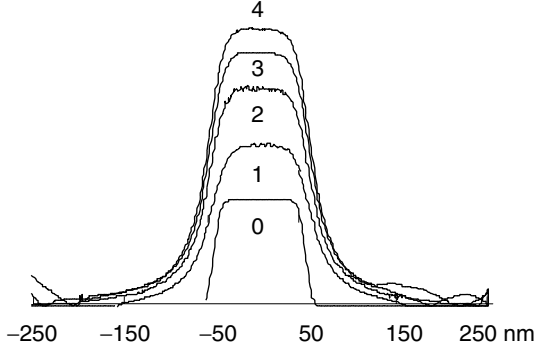


Fig. 5.8. Numerical results for the calculation of E_x , round-trip number as a parameter

Solution. Figure 5.7 shows the relationship between E_x and n for a computational domain of $1,500 \text{ nm} \times 500 \text{ nm}$. Figure 5.8 shows the numerical results of E_x , round-trip number as a parameter. The electromagnetic wave propagates from the aperture and reflects at the upper boundary of the computational domain leading to a round trip. The round-trip numbers 0, 1, 2, 3, and 4 correspond to the time steps 636, 1,908, 3,180, 4,452 and 5,724, respectively. It is seen from the figure that the solution converges stably without the wave reflection effect.

Example 5.3. Compute E_x around the tapered optical fiber end with a silica core and a perfect conductor clad shown in Fig. 5.9. Compare the obtained three E_x s for the diameters of (a) 34 nm, (b) 68 nm, and (c) 136 nm in two dimensions.

Solution. Figure 5.10 shows numerical results of E_x for the TM (p-polarized) plane wave. The evanescent light becomes sharp as the diameter of the aperture becomes small. To obtain a high resolution it is necessary to make the probe-sample distance short.

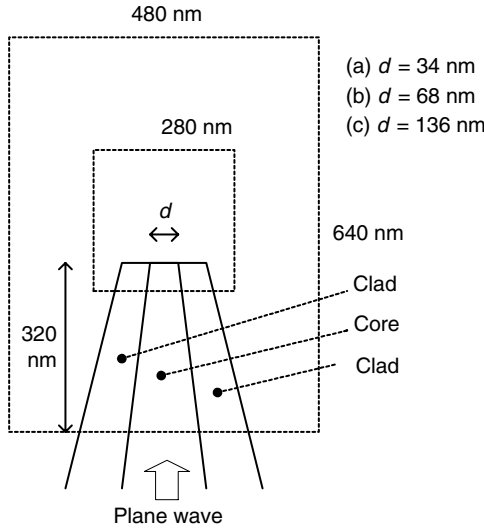


Fig. 5.9. 2-D Cartesian computational domain of $480 \text{ nm} \times 640 \text{ nm}$ for calculation of E_x around tapered fiber end with silica core and perfect conductor clad. Here, the refractive index and electrical permittivity of silica are 1.46 and $2.25\epsilon_r$, (ϵ_r : free-space permittivity), respectively

Example 5.4. Compute the scattered light field from an optically trapped gold particle in the evanescent light, which is produced by a total reflection on a prism-air interface.

Solution. First, we produce an evanescent light by the incident s-polarized plane wave expressed by the following equations at an angle of $\theta = 45^\circ$ with a wavelength of $\lambda = 488 \text{ nm}$:

$$\begin{aligned} E_z(i, j) &= \sin \left[2\pi f \left\{ n\Delta t - \frac{\sqrt{\epsilon_r}}{c} (i-1)\Delta x \sin \theta \right\} \right], \\ H_y(i, j) &= -\sin \left[2\pi f \left\{ \left(n - \frac{1}{2}\right) \Delta t - \frac{\sqrt{\epsilon_r}}{c} \left\{ (i-1)\Delta x \sin \theta + \frac{\Delta y}{2} \cos \theta \right\} \right\} \right] \\ &\quad \times \frac{\sqrt{\epsilon_r}}{Z} \cos \theta, \\ H_x(i, j) &= \sin \left[2\pi f \left\{ \left(n - \frac{1}{2}\right) \Delta t - \frac{\sqrt{\epsilon_r}}{c} (i-1)\Delta x \sin \theta \right\} \right] \times \frac{\sqrt{\epsilon_r}}{Z} \sin \theta. \end{aligned}$$

Here, $f = c/\lambda$, c is the speed of light in vacuum, ϵ_r is the free-space permittivity and Z is the intrinsic impedance.

Next, a 100-nm-diameter perfect conductor sphere is located 10 nm above the surface of the prism and the electromagnetic field near the surface is

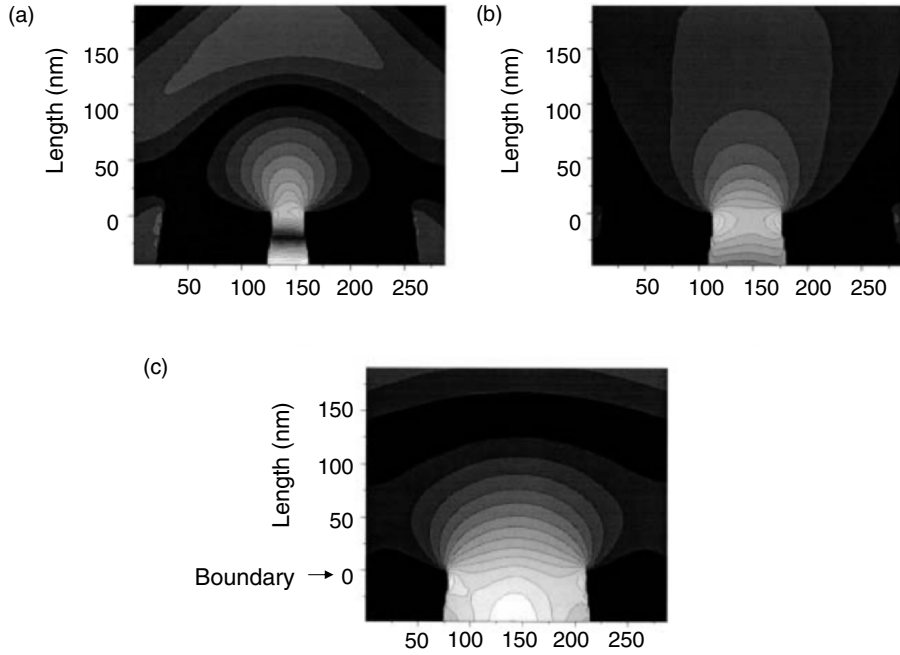


Fig. 5.10. Calculated electric field E_x around aperture for TM plane wave. The evanescent light becomes sharp as the diameter of the aperture becomes small

Table 5.1. Conditions for calculation of scattered light by an optically trapped gold particle in evanescent field

incident plane wave	s-polarized
wavelength	488 nm
space increment $\Delta x, \Delta y$	10 nm
space domain to be computed	$4,000 \text{ nm} \times 2,000 \text{ nm}$
time increment Δt	$2.0 \times 10^{-17} \text{ s}$
time step n	10,000
substrate	
refractive index	1.6
conductivity	1.1×10^{-12}
electrical permittivity	$2.56 \times \epsilon_r$
incident angle θ	45°
diameter of the trapped metal particle	100 nm

ϵ_r : free-space permittivity ($8.854 \times 10^{-12} \text{ F m}^{-1}$)

calculated by FDTD with parameters $\Delta x = \Delta y = 10 \text{ nm}$, $\Delta t = 2.0 \times 10^{-17} \text{ s}$, $n = 10,000$, the refractive index of the prism 1.6, and electrical permittivity of $2.56 \epsilon_r$ ($\epsilon_r = 8.854 \times 10^{-12} \text{ F m}^{-1}$). The computational domain is $4,000 \text{ nm} \times 2,000 \text{ nm}$ (twice the output domain). See Table 5.1.

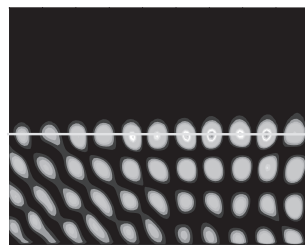


Fig. 5.11. Input plane wave and evanescent field produced at interface (*white line*) by total reflection

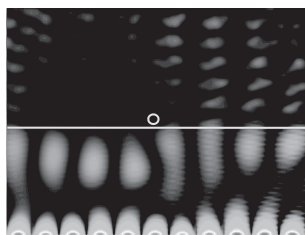


Fig. 5.12. Scattered light field of evanescent field by perfect conductor particle of 100 nm diameter (*white circle*) located 10 nm above the interface (*white line*)

Figure 5.11 shows the input plane wave and evanescent field produced. In the figure, an incident light and a reflected light interfere in the prism and the evanescent light is produced near the interface (white line) mentioned earlier. Figure 5.12 shows the scattering field produced by a perfect 100-nm diameter conductor particle (white circle). In the figure, the evanescent field is scattered in space by the particle and the field in the prism becomes weakened.

Developing these basic computations described earlier, FDTD is applied usefully to the following contemporary and emerging fields related to micro-mechanical photonics:

- Electromagnetic field near a small aperture^{1,2}
- Field enhancement by a metallic probe³
- Electromagnetic interaction with nanoparticles⁴

¹ Kann JL, Milster TD, Froehlich FF (1995) Near-field detection of asperities in dielectric surfaces. *J Opt Soc Am* 12:501–511

² Christensen DA (1995) Analysis of near field tip patterns including object interaction using finite-difference-time-domain calculations. *Ultramicroscopy* 57:189–195

³ Furukawa H, Kawata S (1998) Local field enhancement with an apertureless near-field-microscope probe. *Opt Commun* 148:221–224

⁴ Shinya A, Fukui M (1999) Finite-difference-time-domain analysis of the interaction of Gaussian evanescent light with a single dielectric sphere or ordered dielectric spheres. 6:215–223

- Electromagnetic field around a near-field optical head^{5,6,7}
- Readout performance for ultrahigh density near-field recording^{8,9,10}

5.3 Experimental Analysis

In order to observe the near field, the evanescent light scattering characteristics of a tip probe should be understood. In this section, we first compare the characteristics of different tip probes. Next we measure the evanescent field intensity by detecting the scattered light by a photocantilever, vibrating at its mechanical resonant frequency, placed near the interface. Then we observe the profile of a topological grating by scanning the photocantilever. At last we observe the distribution of the refractive index grating and topological grating, by detecting the scattered light of an Ar⁺ laser, by scanning a nanogold particle optically trapped by a YAG laser, two-dimensionally on the surface.

5.3.1 Comparison of Near-Field Probes

When a sample is illuminated by a light the evanescent field is locally excited near the surface according to its surface property and structure. This evanescent field is scattered by a tip probe and then can be detected by a photodiode (PD) or a photomultiplier tube (PMT). We can observe the surface by scanning the probe two-dimensionally on the surface. The imaging mechanism of the SNOM is different from that of conventional optical microscopy; the scattered light intensity is detected as a result of the interaction between the tip probe and the sample surface. With growing understanding of the underlying probe-sample interaction mechanism, SNOM has found applications in many scientific and industrial fields.

As a typical near-field probe, a small aperture [5.3], a metallic needle [5.5, 5.6], and a small metallic sphere [5.7, 5.8] are well known. The most popular probe is a metal-coated sharpened optical fiber with a subwavelength aperture at the end. We use this aperture to illuminate the surface and collect

⁵ Tanaka K, Ohkubo T, Oumi M, Mitsuoka Y, Nakajima K, Hosaka H, Itao K (2001) Numerical simulation on read-out characteristics of the planar aperture-mounted head with a minute scatterer. *Jpn J Appl Phys* 40:1542–1547

⁶ Mansuripur M, Zakharian AR, Moloney JV (2003) Interaction of light with subwavelength structures. *Opt Photon News*:56–61

⁷ Kataja K, Olkkonen J, Aikio J, Howe D (2004) Readout modeling of superresolution disks. *Jpn J Appl Phys* 43:4718–4723

⁸ Liu J, Xu B, Chong TC (2000) Three-dimensional finite-difference-time-domain analysis of optical disk storage system. *Jpn J Appl Phys* 39:687–692

⁹ Nakano T, Yamakawa Y, Tominaga J, Atoda N (2001) Near-field optical simulation of super-RENS disks. *Jpn J Appl Phys* 40:1531–1535

¹⁰ Chiu KP, Lin WC, Fu YH, Tsai DP (2004) Calculation of surface plasmon effect on optical disks. *Jpn J Appl Phys* 43:4730–4735

the scattered light to propagate it to the PMT placed at the other end, leading to the prevention of background light noise. The metal-coated fiber has a cutoff frequency for light transmission, i.e., an aperture minimum of 48 nm due to skin depth for aluminum coating.

We use a cantilever or a metallic needle as an apertureless probe. The probe is ideal in terms of resolution and field intensity. Its spatial resolution is higher than that of the aperture probe because of the smaller radius of the apex. The near-field intensity is much stronger than that of the aperture probe because of the field enhancement effect [5.7, 5.20]. The probe is easy to fabricate and has a wide spectrum range owing to no waveguide, but the surrounding stray light must be fully removed. There are two scanning methods, the constant height mode and the constant distance mode. We need the same control technology as that used for scanning tunnel microscopy (STM) and atomic force microscopy (AFM).

As a small metallic probe, we use an optically trapped gold particle [5.8, 5.21]. The metal particle scatters the surface plasmon excited depending on the sample surface property and the scattered light is gathered by an objective lens guiding it to a PMT. The scattered light includes information not only on the optical, physical, chemical, mechanical properties but also the profile. We need to discriminate between these effects [5.12]. Trapping force strength is very weak (on the pN order), thereby not destroying the sample. So we need not control the distance (gap) between the probe particle and the sample. The metal particle probe is considered to have the following advantages (1) It has a high experimental reproducibility depending on the shape and size of the particles being made, (2) It does not require control of above mentioned gap, (3) It not only has the ability to obtain a surface property but also obtains the spectroscopic data of the sample. Table 5.2 shows the performance comparison between the three.

5.3.2 Photocantilever Probe

To increase SNR for an apertureless SNOM, it is necessary to distinguish the scattered light (signal) produced by the probe from the background light (noise). One method is to place the detector close to the probe apex. A photocantilever is a photosensitive Si-based microfabricated cantilever with a PD

Table 5.2. Comparison of probes for detection of near field. The symbol \circ indicates excellent, Δ good, and \times poor

probe	optical fiber	metallic needle	metal particle
reproducibility	Δ	Δ	\circ
space resolution	Δ	\circ	\circ
SNR	Δ	\circ	\circ
gap control	Δ	Δ	\circ
optical recording	\circ	Δ	\times

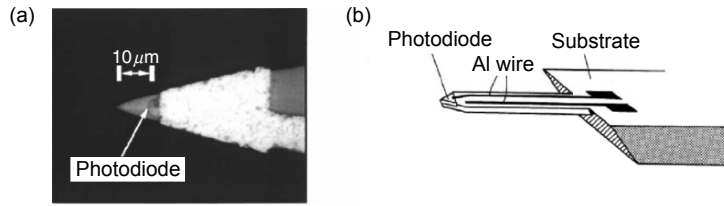


Fig. 5.13. Photograph of photocantilever, in which top photodiode (PD) is fabricated (a), and sketch of that (b)

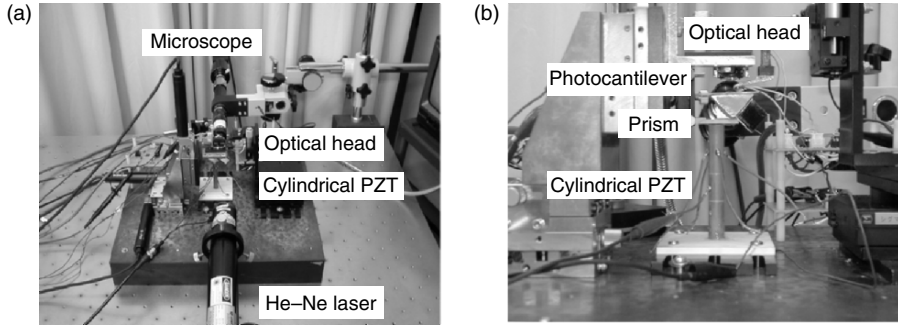


Fig. 5.14. Photograph of AFM/SNOM setup mounted on a vibration-damped table

placed very close to the probe tip [5.22]. Figure 5.13 shows a photograph of a photocantilever (a), and a sketch of that (b). The photocantilever is attached to a piezoelectric transducer (PZT) allowing z distance regulation. The photocantilever is moved close to the sample surface and the distance between the cantilever and the surface is detected from the focus error signal of the optical head placed above the cantilever.

Experimental Setup

Figure 5.14 shows a photograph of an AFM/SNOM setup mounted on a vibration-damped table. An He-Ne laser (this side) incident to a prism and a microscope (other side) are used to observe the sample and the cantilever tip, which is helpful in aligning the setup. An evanescent light is produced at the prism surface by the total internal reflection arrangement. The prism is mounted on a cylindrical PZT, allowing xyz movement. The z movement is used for the gap (distance) control and xy for 2-D scanning. Since the piezoelectric transducer has characteristics of creep and hysteresis, it is driven by a small voltage or with feedback control. Figure 5.15 shows a sketch of the main part of the setup using the photocantilever.

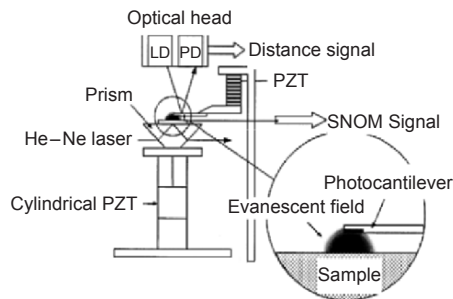


Fig. 5.15. Sketch of experimental setup. Distance signal is used for measuring surface profile and SNOM signal is used for observing surface property by detecting the scattered light from the evanescent field

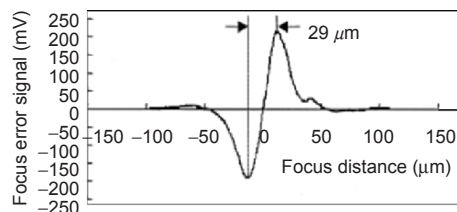


Fig. 5.16. Focus error signal representing typical S-shape curve of optical head

The photocantilever tip scatters the localized evanescent light changing to a propagating light to be detected by the PD. Since the PD is integrated very close to the tip, the SNR is markedly increased compared with the conventional arrangement used in the PMT method.

A small gap between the cantilever and the sample surface (displacement of the tip) is detected as the focus error signal of the optical head. Figure 5.16 shows a focus error signal representing a typical S-shape curve. From this S-shape curve, it is found that the dynamic range becomes approximately $29\text{ }\mu\text{m}$. This optical head's focus error detection makes the setup simpler resulting in better manipulability than that of the combined laser source and quadrant PD arrangement.

Measurement of Evanescent Light Distribution

First, a 7-mW He-Ne laser incident to a prism at an angle of 45° , refracts and goes through the prism and reflects at the upper surface creating an evanescent light by the total internal reflection. Figure 5.17 shows the actual prism configuration: three corner prisms at 45° are attached together by an optical bond (refractive index of 1.55) and black paper sheets are inserted between the prism boundaries to prevent random reflection of light.

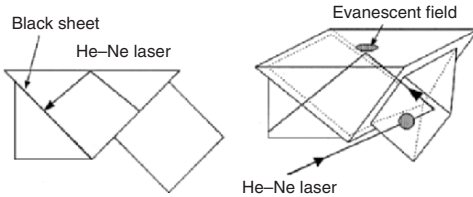


Fig. 5.17. Prism configuration consists of three corner prisms at 45°

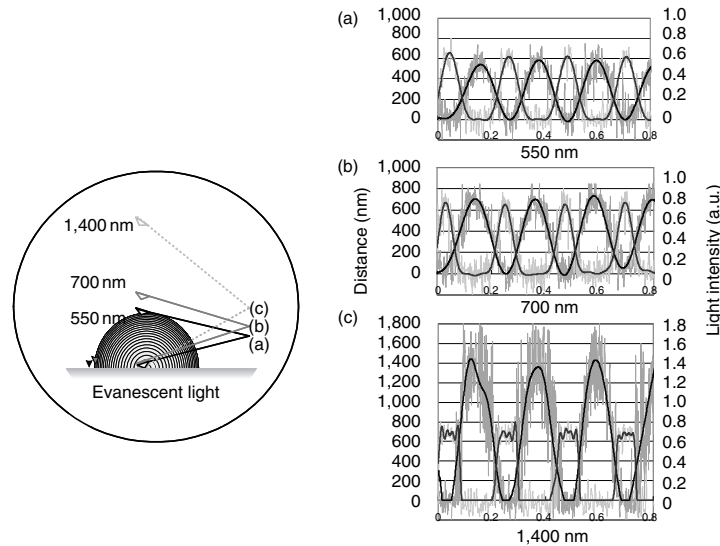


Fig. 5.18. Measured evanescent light intensity with cantilever amplitudes of 550 nm (a), 700 nm (b), and 1,400 nm (c)

Second, the photocantilever is moved close to the prism surface with the vibration of its resonance frequency (4.2 kHz) at an amplitude of approximately 500 nm. The cantilever tip scatters the evanescent light and the PD close to the tip detects the scattered light. To approach the tip to the surface in the nanometer range, both manual control (rough positioning) and piezoelectric control (fine positioning) are required. The distance between the tip and the sample surface is obtained by the focus error signal of the optical head.

Figure 5.18 shows the evanescent light intensity with the cantilever amplitude of 550 nm (a), 700 nm (b), and 1,400 nm (c). An FFT low-pass filter is used to remove noises resulting in solid lines in the figure. In the cases of (b) and (c), a flat signal region appears during the period when the cantilever tip reaches the prism surface owing to a large vibration amplitude.

Simultaneous light and gap (distance) observations lead to the evanescent field intensity distribution as shown ‘experimental’ in Fig. 5.19. It is found

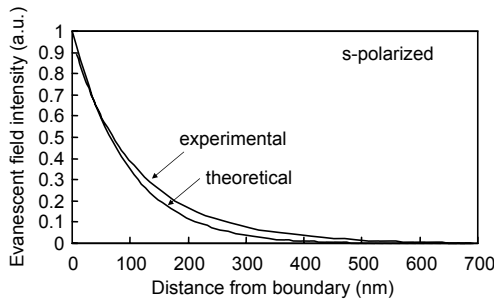


Fig. 5.19. Dependence of measured evanescent field intensity on distance from boundary. Theoretical result is also shown for reference

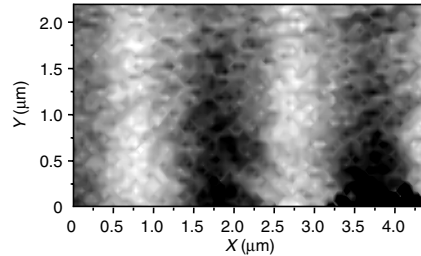


Fig. 5.20. Gray-scale image of optical disk tracking groove; intensity is proportional to profile

from the figure that the evanescent intensity increases rapidly when the gap reaches approximately 100 nm.

Surface Profile Observation

An optical disk tracking groove ($1.6\text{ }\mu\text{m}$ pitch, $0.1\text{ }\mu\text{m}$ in depth) is line-scanned at a pitch of 50 nm in the constant height mode, and the scattered light from the evanescent field at the groove surface is detected by the photocantilever. Figure 5.20 shows a gray-scale image of the groove. Since the intensity of the image is proportional to the scattered light due to the evanescent field, the image represents the profile of the sample.

In summary, an apertureless near-field optical-imaging method is presented by exploiting a photocantilever with a PD integrated very close to the tip. This apertureless SNOM can offer substantially improved spatial resolution, as well as combined operation with AFM.

5.3.3 Gold Particle Probe

It is well known that surface plasmon existing on a metal surface and a metal/dielectric interface causes strong field enhancement at the interface

[5.20]. According to the theoretical analysis, surface refractive index distribution mapping with a high contrast is predicted to be possible [5.7]. A metal particle probe is considered to have the advantages of high experimental reproducibility, not requiring gap control, and not only the ability to obtain the surface image, but also to obtain the spectroscopic data of the sample. The scattering efficiency of a silver particle is higher than that of a gold particle, but the latter is more chemically stable. Therefore a gold particle is frequently used as an SNOM probe.

Sugiura et al. [5.8] observed a dip on a cover glass and a gold colloidal particle adhering to the cover glass. However, these images were thought to have been an artifact problem due to the vertical displacement of the gold probe [5.12]. On the other hand, the following are observed for a refractive index grating on a flat surface, which was made on a planar light waveguide circuit (PLC) [5.24], by scanning an optically trapped 100-nm-diameter gold particle. The scattered Ar⁺ laser light from the gold particle has a high intensity due to the high refractive index of the grating with periods of 1.06 and 0.53 μm, both by s- and p-polarized illuminations.

Moreover, the surface profile of an optical disk tracking groove is also observed with and without the gold particle and the results compared to discuss the artificial effect due to the vertical displacement of the particle caused by the surface topology.

Experimental Setup

Figure 5.21 shows an experimental setup to trap a gold particle with an upward-directed Nd:YAG laser beam ($\lambda = 1.06 \mu\text{m}$) and to scan it on the sample surface two-dimensionally using an XY stage. The upward-directed

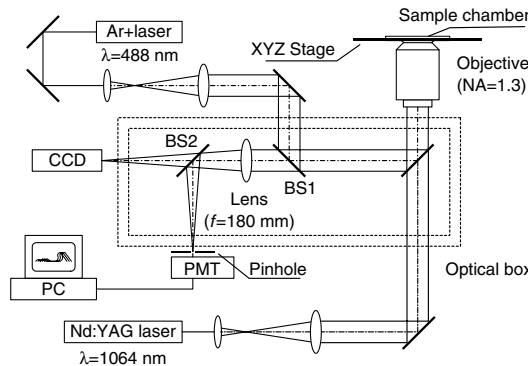


Fig. 5.21. Experimental setup of SNOM using an optically trapped gold particle. An Nd:YAG laser is used for trapping, and an Ar⁺ laser is used illuminating the gold particle. All the optical elements except mirrors to guide the lasers are installed inside the small optical box (*white box* in Fig. 5.22a) for easy operation

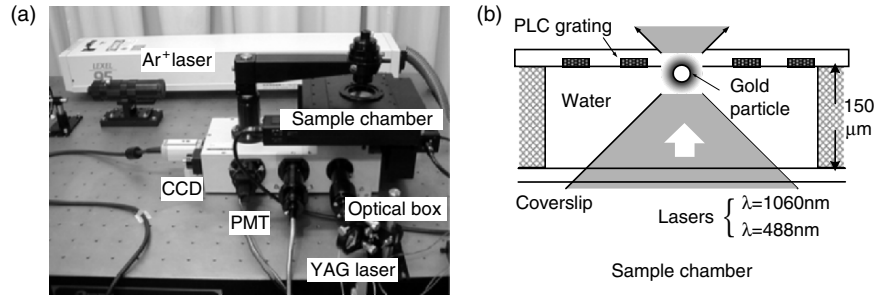


Fig. 5.22. Photograph of experimental setup of SNOM (a), and enlarged view of sample chamber (b)

laser beam has a higher trapping efficiency than the downward one [5.25]. Figure 5.22a shows a photograph of the setup. The gold particle at the focal point of the objective lens is in the medium of a coverslip-shield chamber and is pushed onto the sample surface and scanned as shown in Fig. 5.22b.

An Ar⁺ laser ($\lambda = 488 \text{ nm}$) is focused through the same objective to illuminate the particle. The scattered light from the gold particle is collected through the objective and imaged on the pinhole (5 μm in diameter) in front of a PMT. The scattered light variation due to the interaction between the gold particle and the sample surface is recorded on a personal computer (PC). A CCD camera observes the operation of the gold particle in the medium. All the optical elements, except the mirrors to guide the Nd:YAG laser and Ar⁺ laser, are installed inside the optical box for easy operation.

Trapping Principle

A metallic Rayleigh particle (much smaller than the wavelength) can be optically trapped at the focal point by the gradient force. The particle in such a tightly focused beam is polarized by the electric field and drawn into the beam focus by the large intensity gradients created in both the axial and transverse directions. The gradient force F_{grad} for the Rayleigh particle is given by [5.4, 5.8]

$$F_{\text{grad}} = \frac{1}{4} n_1 \alpha \text{ grad} (|E|^2), \quad (5.20)$$

where n_1 is the refractive index of the medium, α is the polarizability of the gold particle and E is the electric field. The polarizability is given as

$$\alpha = 4\pi\epsilon\epsilon_r \frac{m^2 - 1}{m^2 + 2} r^3, \quad (5.21)$$

where m is the relative refractive index of the particle to the medium, r is the radius and ϵ is the electric permitivity of the particle, and ϵ_r is the free-space permitivity.

Table 5.3. Parameters for calculation of gradient force of Rayleigh particles

refractive index of medium n_1	1.33
refractive index of particle n_2	$0.272 + i7.07$
objective NA	1.3
laser power	20 mW
laser wavelength	1,064 nm
beam profile	Gaussian

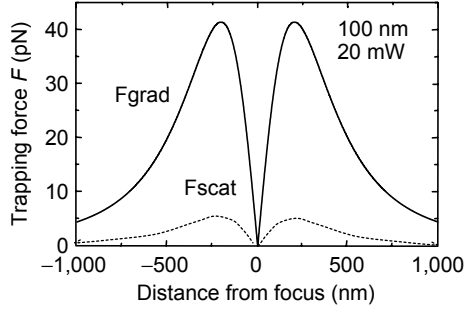


Fig. 5.23. Calculated gradient force F_{grad} in transverse direction and in axial direction for gold particle with refractive index $n_2 = 0.272 + i7.07$, diameter 100 nm, medium refractive index $n_1 = 1.33$, objective lens NA = 1.3, and Gaussian laser power 20 mW

F_{grad} in the transverse direction and in the axial direction were calculated for the gold particle refractive index $n_2 = 0.272 + i7.07$, the gold particle diameter $2r = 100$ nm, the medium refractive index $n_1 = 1.33$, the objective lens NA = 1.3, and the Gaussian laser power is 20 mW as listed in Table 5.3. We found from Fig. 5.23 that the gradient force along the transverse direction is eight times greater than that along the axial direction. This result shows that the trapped particle is very stable along the transverse direction but unstable along the optical axis, which leads to the particle being trapped and pushed onto the sample surface by the upward-directed beam.

Here, we estimate the forces [5.26] between the optically trapped particle and the sample surface for reference. See the problems at the end of this chapter.

Dependence on Scanning Velocity

The theoretical transverse trapping power $P_{\text{pre}}^{\text{trans}}$ can be expressed in (5.22) by taking into consideration the maximum trapping efficiency Q_{\max}

$$P_{\text{pre}}^{\text{trans}} = \frac{3\pi\mu dvc \left\{ 1 + \frac{9d}{32} \left(\frac{1}{T} - \frac{1}{H-T} \right) \right\}}{n_1 Q_{\max}}, \quad (5.22)$$

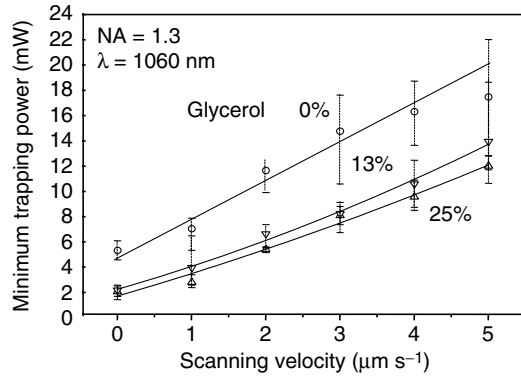


Fig. 5.24. Dependence of minimum trapping power on scanning velocity of optically trapped gold particle at different viscosities

where μ and n_1 are the viscosity and refractive index of the suspending medium, respectively; c is the speed of light, and H is the height of the sample chamber ($150\text{ }\mu\text{m}$) [5.27]. Q_{\max} is found from the maximum gradient force at $1.49/(2\pi/\lambda)\text{NA} = 193\text{ nm}$ along the transverse direction.

Although the calculated result is based on an aberration-free optical system, the actual trapping characteristics are affected by the color aberration of the objective lens (for near infrared $\lambda = 1.06\text{ }\mu\text{m}$) and the spherical aberration due to the refractive index difference between the immersion oil (1.52) and the medium (1.33).

Figure 5.24 shows the dependence of the minimum trapping power P_{\min}^{trans} on the scanning velocity of an optically trapped gold particle for different viscosities, which were controlled by altering the glycerol density. P_{\min}^{trans} was measured as the minimum power needed to trap the bead moving at the velocity v in water. P_{\min}^{trans} increases as scanning velocity increases, but decreases as viscosity increases. However, if we increase the laser power to hold the gold particle in position, the trapping becomes rather unstable because Brownian motion hastens due to the temperature increase resulting from the light absorption. The addition of glycerol is effective in slowing down Brownian motion by increasing viscosity.

Observation of PLC Refractive Index Grating

The sample for the trapped-particle probe is a refractive index grating fabricated by UV exposure through a phase mask under the conditions outlined in Table 5.4 [5.28]. The grating is formed in a cladding layer ($30\text{ }\mu\text{m}$ thick) on a planar light waveguide circuit (PLC) as shown in Fig. 5.25. Figure 5.26a shows the top view of the grating obtained by optical microscopy. The grating period of $1.06\text{ }\mu\text{m}$ (zeroth order) is clearly observed but the grating period of $0.53\text{ }\mu\text{m}$ (first order) is only partially visible. Figure 5.26b shows a sketch of

Table 5.4. Conditions to fabricate refractive index grating in PLC

core ($\text{SiO}_2 + \text{GeO}_2$) index	1.46
clad (SiO_2) index	1.45
refractive index difference (grating)	0.001–0.002 (estimated)
phase mask method	source: ArF laser ($\lambda = 193 \text{ nm}$) phase mask pitch: $1.06 \mu\text{m}$ energy density per pulse: $1.0 \text{ J cm}^{-2} \text{ pulse}^{-1}$ pulse repetition rate: 50 Hz grating pitch (zero-order): $1.06 \mu\text{m}$

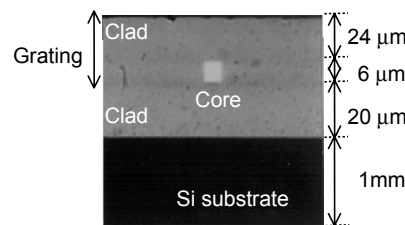


Fig. 5.25. Sectional view of refractive index grating fabricated by UV exposure through phase mask. The grating is formed in a clad layer on a PLC. Courtesy of T. Maruno and Y. Hibino, NTT, Japan

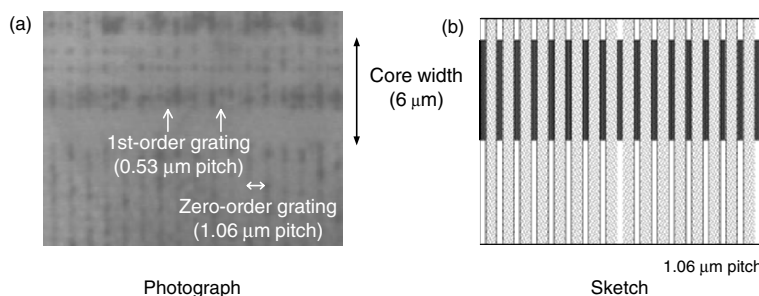


Fig. 5.26. Top view of grating fabricated on PLC (a), and sketch of the grating (b)

Fig. 5.26a. The relative refractive index difference between the gratings in the cladding layer is estimated to be 0.001–0.002, where the cladding layer index is 1.45.

We observed the scattered Ar^+ laser light ($P = 0.13 \text{ mW}$) by the 100 nm gold particle optically trapped by a Nd:YAG ($P = 25 \text{ mW}$) laser, which was scanned over the refractive index grating at the PLC surface. The scanning velocity and pitch were $1.6 \mu\text{m s}^{-1}$ and 50 nm , respectively. Observation time for the square $5 \mu\text{m} \times 5 \mu\text{m}$ was 5 min. These conditions are outlined in Table 5.5.

Table 5.5. Conditions for observation of refractive index grating using optically trapped gold particle

gold particle diameter	100 nm
medium	water
YAG laser intensity	25 mW ($\lambda = 1,064 \text{ nm}$)
Ar ⁺ laser intensity	130 μW ($\lambda = 488 \text{ nm}$)
scan velocity	1.6 $\mu\text{m s}^{-1}$
scan pitch	50 nm
scan area	$5 \times 5 \mu\text{m}^2$
measurement time	5 min

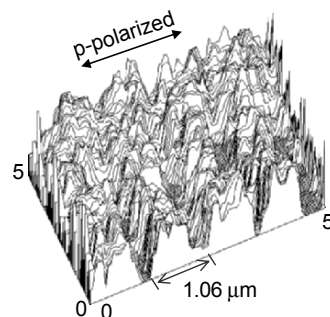


Fig. 5.27. SNOM images (scattered light intensity) of refractive index grating obtained by gold particle probe with p-polarized illumination

Figure 5.27 shows the SNOM image (scattered light intensity) of the refractive index grating produced by a gold particle probe with p-polarized illumination (electric field is perpendicular to the gratings as shown). Figure 5.28 shows the SNOM image (scattered light intensity) with s-polarized illumination (electric field is parallel to the gratings as shown). We can clearly recognize the grating pitch of $1.06 \mu\text{m}$ in both images.

Figure 5.29 shows the relationship between scattered light intensity and the refractive index grating distribution. The scattered lights are averaged for ten data lines. The scattered averaged light corresponds to the grating distribution of the periods of 1.06 and $0.53 \mu\text{m}$ for both p- and s-polarized illuminations. The higher-order-grating of $0.53 \mu\text{m}$ can also be seen for the 100 nm gold particle. By collecting the scattered light under a scanning gold particle that induces a local electric field, we have resolved two individual refractive index periods on the sample surface. We confirm that the optical near field is effective for observing the sample surface beyond the diffraction limit of optical microscopy [5.29].

Next, we investigated the possibility of profiling the topography of the sample surface. Figure 5.30 shows a sectional view of the optical disk tracking groove, which is observed via scanning electron microscopy (SEM). The period is $1.6 \mu\text{m}$, $0.1 \mu\text{m}$ deep, and the groove edge width is 200 nm .

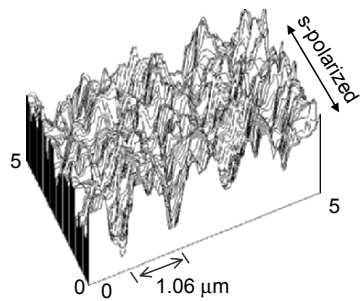


Fig. 5.28. SNOM images (scattered light intensity) of refractive index grating by gold particle probe with s-polarized illumination

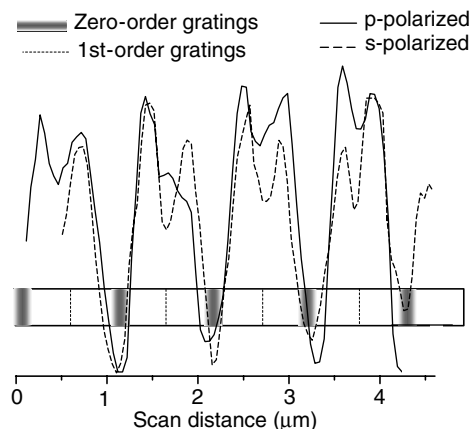


Fig. 5.29. Relationship between scattered light intensity and refractive index grating distribution

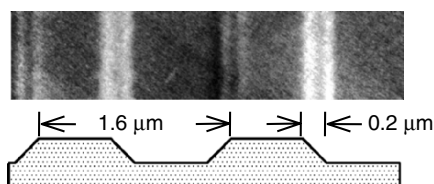


Fig. 5.30. SEM photograph of optical disk groove and its profile

Figure 5.31 shows the SNOM topography profile obtained with and without a gold particle probe under p-polarized illumination with the addition of glycerol (13%) to suppress the particle's Brownian motion. We can clearly see the groove pitch of $1.6\text{ }\mu\text{m}$ with the gold probe. Figure 5.32 shows the relationship between the averaged scattered light intensity and the groove profile. The scattered light with the gold particle (solid line) has a high intensity at the groove edge and has split peaks, which correspond to the gradient of the

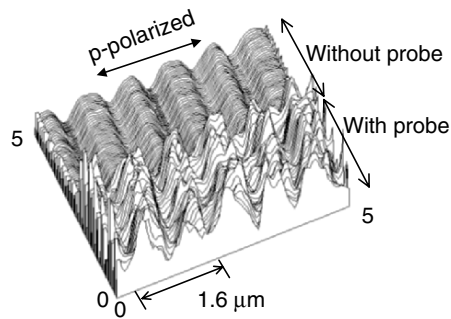


Fig. 5.31. SNOM topography of optical disk tracking groove with/without gold particle probe under p-polarized illumination

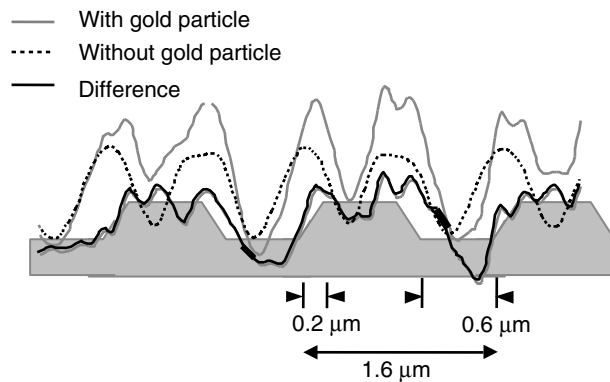


Fig. 5.32. Relationship between scattered light intensity and disk groove profile with and without gold particle

surface profile. On the other hand, the scattered light without the gold particle (broken line) has a single peak at the groove edge. The difference between the two (bold solid line) seems to correspond to the surface topology because the effect of the laser light reflection is removed and the vertical displacement of the gold particle appears due to the scanning on the groove.

In summary, the near field for a refractive index grating fabricated on a PLC is observed by scanning an optically trapped 100-nm-diameter gold particle. The amplitude for the refractive index modulation of the cladding layer (index 1.45) is estimated to be between 0.001 and 0.002. Stable trapping and scanning occur with a Gaussian laser beam at a scan velocity of $1.6 \mu\text{m s}^{-1}$ and a Nd:YAG laser power of 25 mW. The scattered Ar^+ laser light from the gold particle is strong at high refractive indexes of the grating with periods of 1.06 and 0.53 μm, both by s- and p-polarized illuminations.

In addition, an observation under p-polarization was also carried out for the topographical optical disk tracking groove. The scattered light from the gold particle was strong at the groove edge and had split peaks corresponding

to the gradient of the surface profile, whereas the scattered light without a gold particle had no split peaks.

From the result mentioned earlier, we confirm that an optically trapped gold particle is effective in observing both the physical and topological properties of a sample. Further investigation will be required to clarify the exact effect of the vertical displacement of the particle, i.e., to distinguish the probe vertical displacement effects from the SNOM signal [5.12].

On the other hand, to improve the spatial resolution further, the robustness of the optically trapped particle must be increased by an increase in medium viscosity or by a follow up control of the particle position [5.30].

5.4 Future Applications

For future ultrahigh density optical storage, the so-called fourth generation optical disk, many types of methods are being proposed. These methods are holography [5.31, 5.32], superresolution near-field structure (super-RENS) recording [5.33], near field recording [5.34], and a 3-D recording [5.35]. Holographic storage is expected to have the possibility of storing over 1 terabyte of data on a 120 mm diameter disk for data archiving [5.32]. In this section, near-field methods, particularly super-RENS, are introduced in detail. Super-RENS has the merit that a recording apparatus the same as that of a conventional optical storage system can be used and is considered to have the highest potential for on-line storage.

5.4.1 Conventional Superresolution

I would like to start to explain beyond the diffraction limit readout principle (superresolution) [5.36], which is used actually for today's digital versatile disk (DVD). Fig. 5.33 shows the pit size comparison between a CD, a DVD, a next-generation DVD and a near-future optical disk. The pit size decreases owing to not only the short wavelength [5.37] and high objective NA but also the superresolution scheme.

We can make a write mark infinitesimally small by choosing the critical thermal conditions so that only the peak area of the temperature distribution corresponds to the writable temperature. This is called "brush tip recording". However, information bits cannot be detected when two marks are included in a diffraction-limited spot (λ/NA) in conventional readout as shown in Fig. 5.34a.

Nevertheless, bits can be detected by superresolution because its effective aperture is restricted within a crescent-shaped region, as shown in Fig. 5.34b. Fig. 5.34c shows a spot intensity profile and the temperature distribution in a mask layer. The material is melted in the rear area of the light spot because the absorbed heat dissipated in the moving disk direction. The reflectance is designed to be very low for the melted region so that it works as a mask.

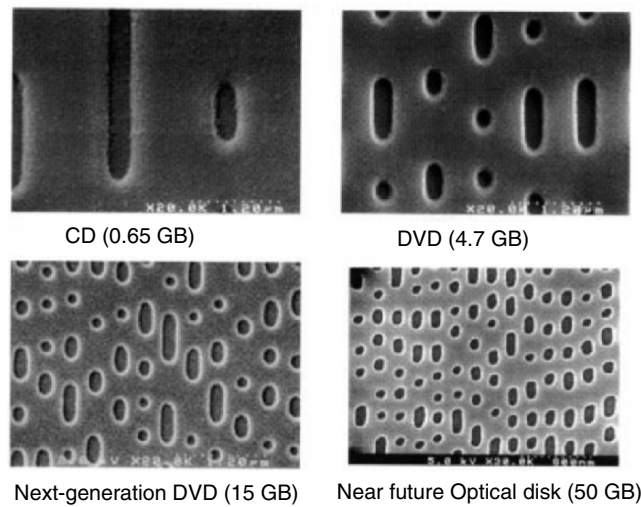


Fig. 5.33. Optical disk pit size comparison between CD, DVD, next-generation DVD and near-future optical disk. Courtesy of S. Sugiura, Pioneer Co., Japan

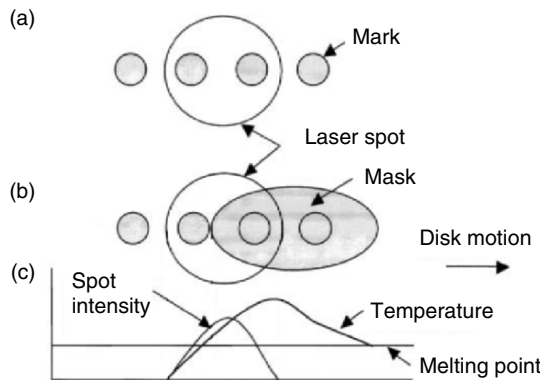


Fig. 5.34. Principle of superresolution readout through crescent-shaped aperture thermally formed in mask layer. Conventional readout (a), superresolution readout (b), and spot intensity profile and temperature distribution in a mask layer (c). Reprinted from [5.36] with permission by A. Fukumoto

As a result, the superresolution readout is possible through a crescent-shaped aperture thermally formed in a mask layer [5.36].

In actual case, a medium with a mask layer/protective layer/recording layer is formed as shown in Fig. 5.35a. Some type of dye or phase change medium is employed as a mask layer. We can evaluate the effect of a thermally induced mask on the performance of an optical disk for a model shown in Fig. 5.35b. We assume that the thermally induced mask can be represented

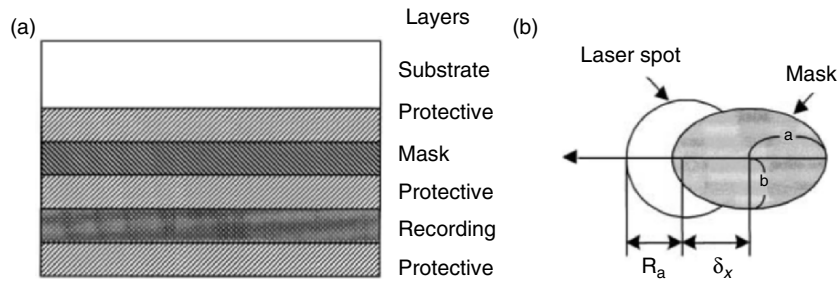


Fig. 5.35. Medium composition with mask layer/protective layer/recording layer (a), and schematic illustration of partial readout principle of superresolution optical disk (b)

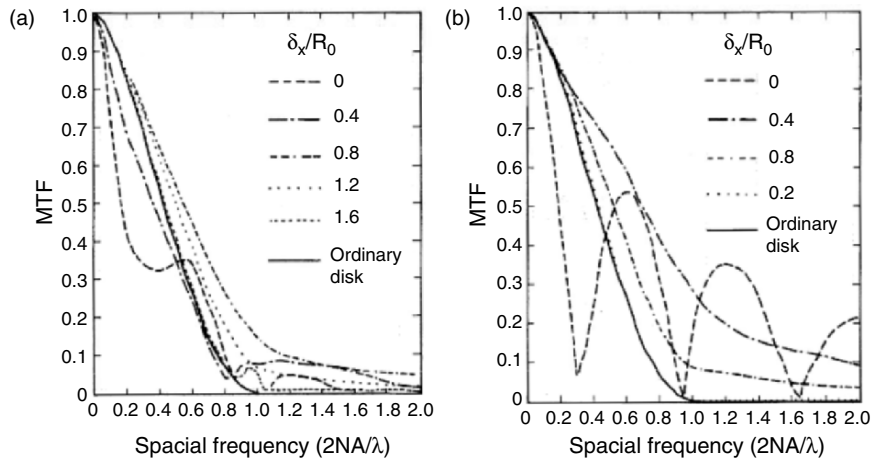


Fig. 5.36. Calculated MTF of system with ideal mask, relative shift δ_x as parameter (a), and with 90° rotation different mask shape (b). Reprinted from [5.38] with permission by Yi hong Wu

by an ellipse with a variable shape and a relative position with respect to the center of the laser spot.

Simulation has been performed to evaluate the modulation transfer function (MTF) of this system. First, the point-spread function $h(u, v)$ of the disk system is calculated and then multiplied by the mask function $f(u, v)$ on the disk plane. Here, the mask function is represented as an ellipse with radii a and b , and with the relative shift of δ_x with respect to the center of the readout laser spot. For simplicity, we assume that the reflectivity of the mask is 0% and that of the aperture 100%.

Figure 5.36a shows the calculated MTF for $R_0 = 1.1 \mu\text{m}$, $a = R_0$, $b = R_0/2$ where $\text{NA} = 0.45$, $\lambda = 0.78 \mu\text{m}$ and $R_0 = 1.22/2\text{NA}$ [5.38]. It is found that the MTF depends on the relative position of the mask and the superresolution

effect reaches a maximum with $\delta x = 0.8$. Figure 5.36b shows the same results for $a = R_0/2$ and $b = R_0$ by changing the mask shape elongated perpendicular to the track by the mask rotation of 90° . This perpendicularly elongated mask enables us to cover more of the read spot, resulting in a higher MTF compared with that of (a). As a result, it is confirmed that the MTF depends strongly on both the shape and relative position of the mask.

5.4.2 Near-field Recording

Ultrahigh-density optical storage is performed by switching a material phase or a magnetization point by point using the light energy from an aperture fiber probe. Heat-assist recording is particularly useful for magnetic recording on flux-detectable media because of the high sensitivity of giant magnetoresistive (GMR) devices [5.39]. There are mainly three read/write schemes for an ultrahigh-density optical near-field storage; a scanning probe microscope (SPM), an optically switched laser (OSL) head, and a solid immersion lens (SIL).

Scanning Probe Microscopy

There are various types of SPM storage; STM-based, AFM-based, MFM-based and SNOM-based storages. Figure 5.37 shows an SNOM-based storage [5.40] using an Al-coated fiber probe and a phase change medium (GeSbTe). An aperture probe induces an evanescent light, heating the nanometer area, changing the medium phase from crystal to amorphous such that the reflectivity of the illuminated area decreases. The smallest mark size obtained is 60 nm in diameter, which corresponds to 170 Gb in.^{-2} .

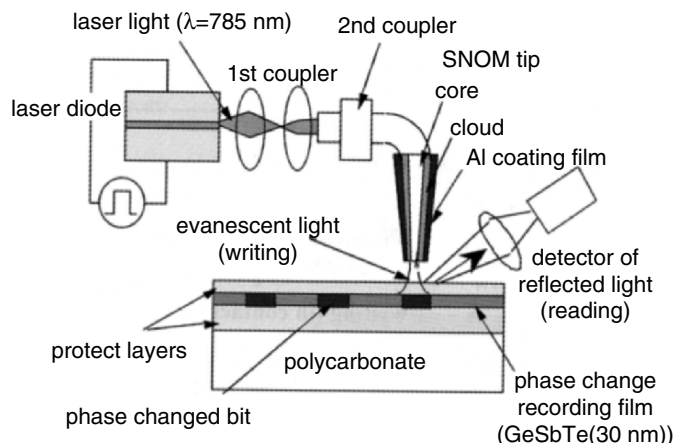


Fig. 5.37. SNOM-based storage using Al-coated fiber probe and phase change medium (GeSbTe). Reprinted from [5.40] with permission by S. Hosaka, Gunma University, Japan

To achieve a high-speed readout, the gap control between the probe and the medium sample is realized using an SNOM slider head, which consists of a flying slider and an air-bearing spindle motor. However, readout speed is basically restricted with the resonant frequency of the gap control system. A schematic diagram of proto-type SNOM slider head is shown in [5.40].

The experimental results indicate the possibility of achieving a density over 100 Gb in.^{-2} and a readout speed over 2 Mb s^{-1} . However, some technical problems such as nanometer size aperture probe productivity, precise gap and tracking control for each track independently remain unsolved.

Optically Switched Laser Head

A lensless flying optical head suitable for near-field recording arrangements was firstly proposed by Ukita et al. in 1987 [5.33, 5.41, 5.69]. A tapered laser diode attached on a slider forms an extremely short-external-cavity (ESEC) with a phase change optical disk as described in Chap. 2. This is called an OSL head due to its working mechanism.

After ten years, Partovi et al. [5.42] fabricated a very small aperture laser (VSAL) for near-field recording and Chen et al. [5.43] reported a method for producing a VSAL from a low-cost, commercial index guided edge diode laser. Recently, Kataja et al. [5.44] presented a numerical study of near-field writing on a phase change optical disk.

This direct read/write scheme by a laser diode is thought to be a promising approach for near-field storage because of its structure simplicity, smallness, and low cost.

Solid Immersion Lens/Solid Immersion Mirror (SIM)

To overcome the fragility and yield of fiber probes of an SPM storage, the use of an SIL [5.45] or an SIM [5.46] on a flying head has been proposed and studied. An SIL has a higher numerical aperture (NA) and is easier to fabricate than an SIM, however, its lens center is more difficult to align. The flying height of this head is 20 nm at present [5.47]. Use of an SIL/SLM is not restricted by readout speed but restricted by area recording density due to NA. However, these devices are also suitable for heat-assisted magnetic recording (HAMR), avoiding the superparamagnetic limit of the HDD as shown in Fig. 5.38.

HAMR schemes combining a bow-tie antenna attached on a flying slider are under development to achieve storage densities greater than 1 Tb in.^{-2} (corresponding to a mark size of 25 nm) in many institutes. Moreover, to achieve recording data rates of 500 MHz, the thermal response time of the medium must be less than 1 ns and a temperature rise of at least a 200°C is required. From thermal modeling calculation, approximately 1 mW of optical power will cause 200°C temperature rise in a 25 nm spot of a recording film stack [5.48]. Techniques based on apertures, antennas, waveguides, SILs and

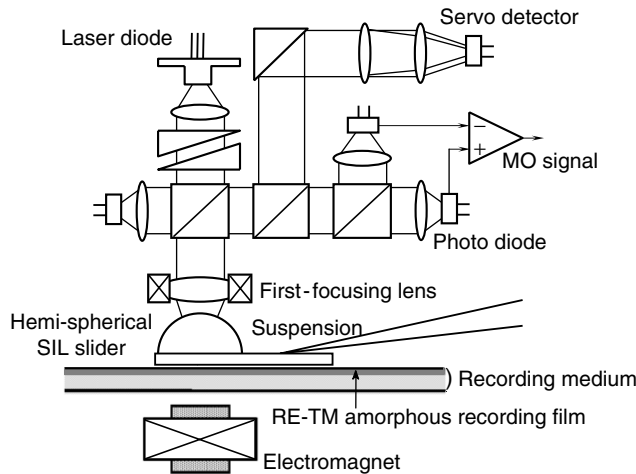


Fig. 5.38. Heat-assisted magnetic recording (HAMR), avoiding superparamagnetic limit of HDD. A SIL has a higher NA [5.39]. Courtesy of H. Sukeda, Hitachi, Japan

SIMs have been suggested for delivering a substantial amount of optical power. However, many practical technologies for HAMR have remained unsolved to date.

5.4.3 Super-RENS Optical Disk

The near-field recording schemes described earlier have difficulties in fabricating a nanometer-size probe with reproducibility and distance control between a probe and a recording medium. Why is not the conventional superresolution scheme using a mask layer employed? Tominaga et al. [5.33] proposed beyond the diffraction limit optical readout in the near field using superresolution structure in 1998. Transmission efficiency of very small apertures is thought to decay as d^{-4} , where d is the aperture size, but it can be markedly enhanced with the aid of surface plasmons and localized surface plasmons [5.49, 5.50].

There are three types of beyond the diffraction limit optical readout using super-RENS. The first is by a transparent aperture formed in an Sb mask layer [5.33]. The mask layer is uniformly crystallized but the high temperature region of the super-RENS readout power opens a small aperture similar to the superresolution technique [5.38]. This type optical disk consists of PC-substrate (0.6 mm)/SiN (170 nm)/Sb (15 nm)/SiN (30 nm)/GeSbTe (15 nm)/SiN (20 nm). The success of 90 nm mark length readout and direct observation of the near-field aperture [5.51] formed on the super-RENS, the phase change mechanism for two layers (mask and recording layers) [5.52] and thermal lens model of the Sb thin film [5.53] have been reported, but the carrier to noise ratio (CNR) has been poor (approximately 15 dB for 100 nm marks).

The second is by the aperture formed with the Ag nanoparticle ring in the mask layer (AgO_x) and the CNR is increased by 20 dB as that of the transparent-aperture type described earlier [5.54]. The CNR increase is thought due to the plasmon scattering by Ag particles. This type optical disk consists of PC-substrate (0.6 mm)/ ZnSiO_2 (170 nm)/ AgO_x (15 nm)/ ZnSiO_2 (15 nm)/ GeSbTe (15 nm)/ ZnSiO_2 (20 nm). The functional structures of AgO_x thin film for near-field recording has reported [5.55]. The aggregated Ag cluster produced by a lower input energy, high reflectivity, scatters near field efficiently and the Ag ring produced by a higher input energy, low reflectivity, not only confines the input light energy for writing but also enhances the scattering fields for reading.

Kataja et al. [5.56] studied the AgO_x super-RENS phenomena numerically using a 2-D FDTD method. They indicated that a super-RENS structure having an AgO_x active layer can produce beyond the diffraction limit resolution when the aperture surrounded by small Ag particles formed and filled with a low index material such as O_2 . Recently, read/write characteristics have been studied through systematic experiments and the detailed mechanism to explain the Ag type super-RENS has been proposed more clearly [5.57].

This mechanism by a deformed gas bubble associated with metallic nanoparticles was also elucidated for a platinum oxide super-RENS disk. The CNR of over 47 dB for 100 nm mark length was obtained for the optical disk with the following structure: PC-substrate (0.6 mm)/ ZnS-SiO_2 (170 nm)/ $\text{PtO}_{1.6}$ (4 nm)/ ZnS-SiO_2 (40 nm)/AIST (60 nm)/ ZnS-SiO_2 (20 nm) [5.58, 5.59].

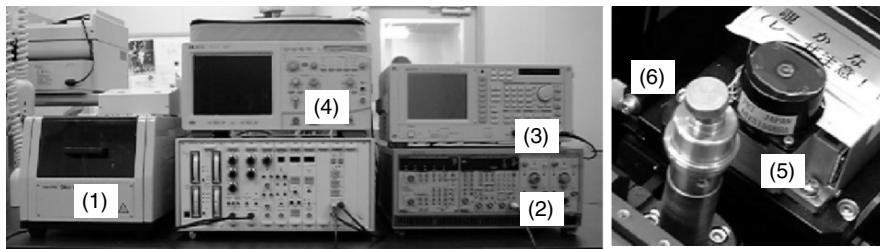
The third is a huge change in the refractive index generated in a focused laser spot. Tominaga et al. [5.60] have proposed a ring aperture formed by ferroelectric catastrophe in AgInSbTe recording medium. This superresolution aperture can be observed between 350°C and 400°C, resulting in a second phase transition from a hexagonal to a rhombohedral structure. This type optical disk consists of PC-substrate (0.6 mm)/ ZnSiO_2 (130 nm)/ AgInSbTe (40 nm)/ ZnSiO_2 (100 nm) [5.61]. Mask layer does not required.

Sb-super-RENS(Aperture Type)

Here, write and read mechanism of super-RENS optical disk of PC-substrate (0.6 mm)/ SiN (170 nm)/Sb (15 nm)/ SiN (30 nm)/ GeSbTe (15 nm)/ SiN (20 nm) is presented by the results obtained from the experiments in various read/write conditions and theoretical analyses for a six-layer film reflectivity.

Experimental setup and read/write conditions

Figure 5.39 shows the conventional experimental apparatus consists of an optical disk tester (Pulstec Industrial Co., Ltd) with a wavelength of $\lambda = 826$ nm laser diode and an NA = 0.5 objective lens. Figure 5.40 shows a typical super-RENS disk using an Sb mask layer with an objective lens. A near-field aperture



(1) Optical disk tester (Pulstec:DDU-1000)
 (2) Function generator (Tektronix:TM5006)
 (3) Oscilloscope (HP:Infinium54820ZA)
 (4) Spectrum analyzer (ADVANTEST:R3132)

(5) Optical head
 (6) Spindle

Fig. 5.39. Conventional experimental apparatus consists of an optical disk tester with laser diode ($\lambda = 826$ nm) and objective lens ($NA = 0.5$)

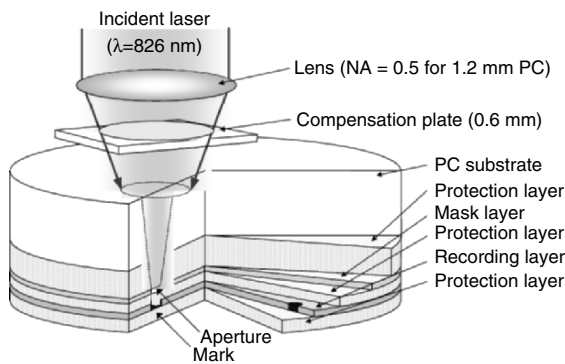


Fig. 5.40. Typical super-RENS disk medium using Sb mask layer. Optical diffraction limit for detection $\lambda/4NA$ is 413 nm

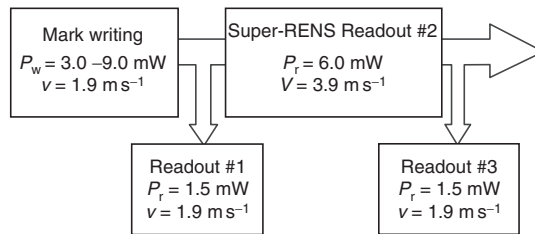
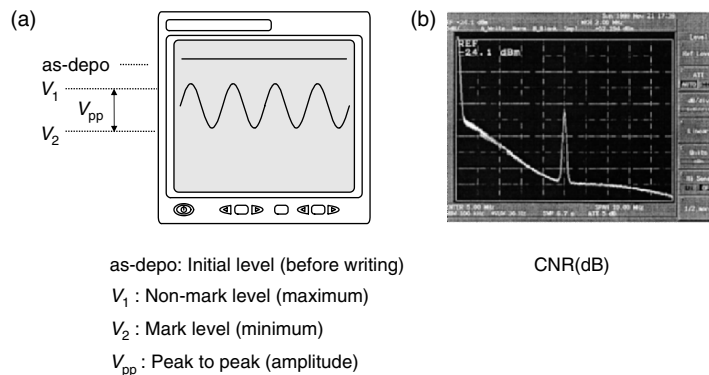
is generated in the center portion of the laser spot. Optical diffraction limit for detection, $\lambda/4NA$, of our experiment is 413 nm. Table 5.6 shows the disk configuration and the parameters of materials for the medium.

In order to determine the amorphous level of the mask and recording layers in super-RENS readout, we measured write power dependence of signal amplitude with an oscilloscope and CNR with a spectrum analyzer. They were measured for two conditions, just after writing with read power of $P_r = 1.5$ mW (readout #1) and the super-RENS readout with $P_r = 6.0$ mW (readout #2) as shown in Fig. 5.41. Readout #3 with $P_r = 1.5$ mW is for reference. We compared these two signals (readout #1 and readout #2) in Fig. 5.42 and estimated the phase change levels of the medium.

First, read power dependence of CNR for various mark length written at the power of 7.0 mW for the medium velocity of 1.9 m s^{-1} is shown in Fig. 5.43. For long marks (1,000–3,000 nm), CNRs are high and almost independent of

Table 5.6. Medium configuration of aperture-type super-RENS disk

layer	material	thickness (nm)	phase	optical constant	
				<i>n</i>	<i>k</i>
substrate	PC	0.6×10^6	—	1.56	0
protective layer	SiN	170	—	2.35	0
mask layer	Sb	15	crystal	3.52	5.48
			amorphous	4.21	3.2
protective layer	SiN	30	—	2.35	0
recording layer	GeSbTe	15	crystal	3.97	4.41
			amorphous	4.29	2.09
protective layer	SiN	20	—	2.35	0

**Fig. 5.41.** Experimental analysis scheme to determine amorphous levels of both mask and recording layers for super-RENS disk**Fig. 5.42.** Two measured signals; signal amplitude with oscilloscope (a) and CNR with spectrum analyzer (b)

read power. For short marks (200–400 nm) less than diffraction limit, the signals appeared at the read power more than 5.0 mW. We define Sb-super-RENS read power as 6.0 mW.

Wright power (recording level) consideration

Figure 5.44 shows a write power dependence of signal amplitude measured for readout#1. Complete amorphous means the signal level that marks are

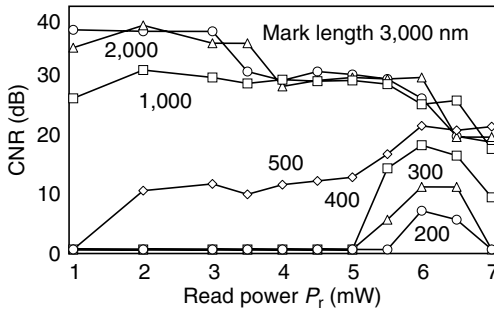


Fig. 5.43. Read power dependence of CNR for various mark lengths written at power of 7.0 mW for medium velocity of 1.9 m s^{-1}

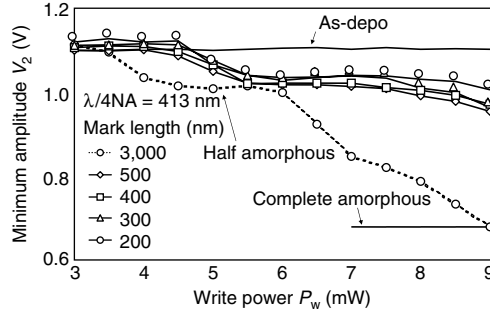


Fig. 5.44. Write power dependence of signal amplitude measured for readout #1

written many times on one track until the signal level become saturated. For long marks of 3,000 nm the signal level changes (decreases) clearly both the write power 3.5 mW and 6.5 mW from as-depo to amorphous and reaches two states of halfway amorphous and complete amorphous. It is not clear for short marks of 200–500 nm, but the signal level changes (decreases) at 5.0 and 9.0 mW. This is because that the marks are much smaller than the laser spot size.

Figure 5.45 shows a write power dependence of CNR measured for readout #2. For long marks of 3,000 nm, CNR increases drastically at the write power 6.5 mW, which corresponds to the write power of Fig. 5.44. Figure 5.46 shows typical signals for as-depo ($P_r = 1.5 \text{ mW}$), just after writing ($P_r = 1.5 \text{ mW}$), and super-RENS ($P_r = 6.0 \text{ mW}$) at the write power of $P_w = 6.0 \text{ mW}$ and $P_w = 9.0 \text{ mW}$. These signal levels obtained experimentally agree well with those obtained theoretically from the reflectivity calculation for a six-layer thin film super-RENS. From these results, we confirm that the Sb-super-RENS has two states; one is due to the change of only mask layer (halfway amorphous), the other due to the change of both mask and recording layer (complete amorphous).

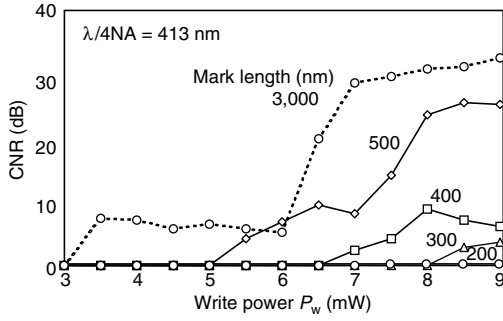


Fig. 5.45. Write power dependence of CNR measured for readout #2

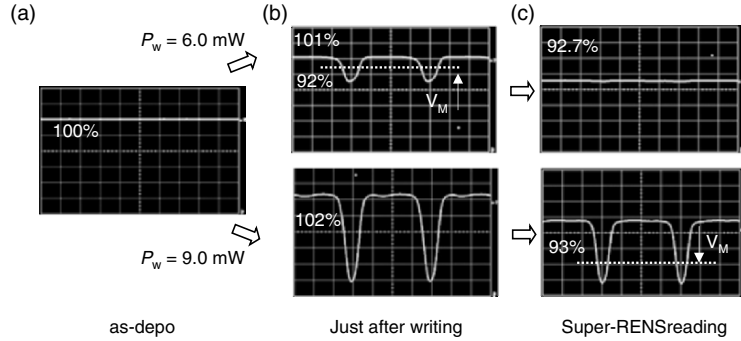


Fig. 5.46. Typical signal levels for (a) as-depo state ($P_r = 1.5$ mW), (b) just after writing ($P_r = 1.5$ mW), and (c) super-RENS readings at write powers of $P_w = 6.0$ mW and $P_w = 9.0$ mW

Aperture-type super-RENS working model

Figure 5.47 shows a model of working mechanism for the super-RENS obtained from the experimental results given earlier:

1. In the case of sufficient write power ($P_w = 8.0\text{--}9.0$ mW for 300 nm mark), the heat reaches the lower recording layer, and both mask and recording layers change from as-depo to amorphous (Fig. 5.47b). After super-RENS readout, the mask layer is crystallized uniformly but small high temperature region behaves the aperture just like a superresolution technique (Fig. 5.47c).
2. In the case of insufficient write power ($P_w = 3.0\text{--}7.5$ mW for 300 nm mark), the heat dose not reach the recording layer, and only upper mask layer change from as-depo to amorphous (Fig. 5.47d). After super-RENS readout, the signal does not appear because there are no marks on recording layer (Fig. 5.47e).

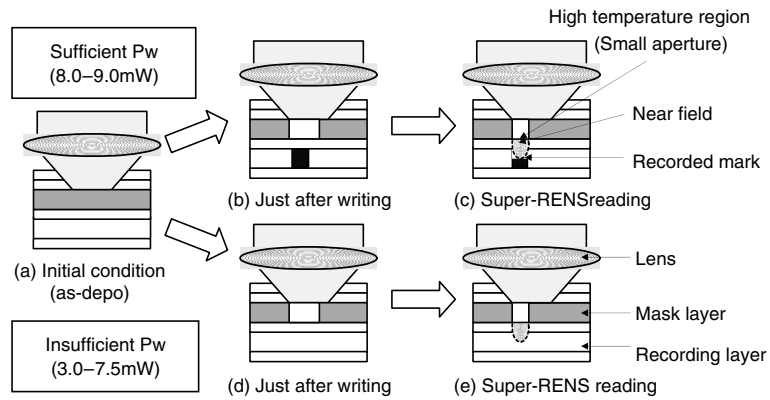


Fig. 5.47. Working mechanism for aperture-type super-RENS disk obtained from experimental results. The disk moves from right to left

In summary, both mask and recording layers change from as-depo to amorphous in write process and the mask layer uniformly changes to amorphous in read process is presented. According to the conventional superresolution mechanism, the very small high temperature region in the focused spot behaves as an aperture and makes it possible to detect marks less than diffraction limit on the recording layer.

Ag-Super-RENS (Scattered Type)

In this paragraph, following read/write mechanism for the scattered-type super-RENS optical disk using a silver oxide (AgO_x) mask layer will be presented experimentally: The AgO_x mask layer has five possible states depending on the input laser power; AgO_x (as-depo), uniformly dispersed Ag particles (after the initialization of 3.5 mW), Ag cluster (4.0–5.0 mW), Ag diffusion (5.5–7.5 mW), and Ag ring structure (greater than 8.0 mW) for an objective lens numerical aperture of $\text{NA} = 0.5$, a laser wavelength of $\lambda = 826 \text{ nm}$ and a medium velocity of 2 m s^{-1} . On the other hand, the GeSbTe recording layer has states; crystal, halfway amorphous, completely amorphous and gas bubble associated with Ag particles. At the superresolution read power (4 mW), the mask layer will have Ag ring structure that increases both the CNR and the resolution limit.

A scattered-type super-RENS disk using a silver oxide (AgO_x) mask layer has been proposed to improve the CNR markedly. The small metal particles in the gas bubble pit formed in write process enhanced the near field (surface plasmon on the particles) as shown in the upper figure of Fig. 5.48. Ho et al. found that the functional structure [5.55] of AgO_x depends on the write power as shown in the lower figure. The aggregated Ag nanocluster (having high reflectivity due to Ag dots) efficiently scatters the near field and the Ag ring (having high transmission due to a nanoaperture) not only confines the input

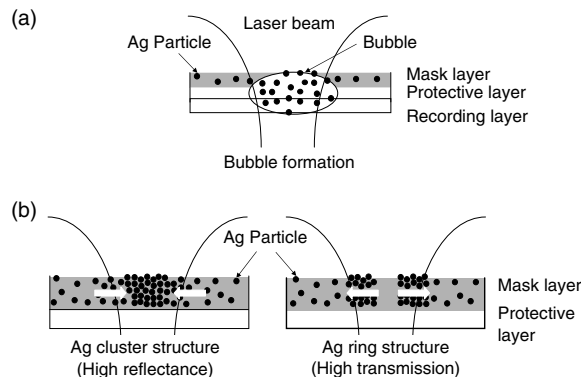


Fig. 5.48. Bubble pit formation and functional structures of scattered-type super-RENS disk using AgO_x mask layer [5.55]

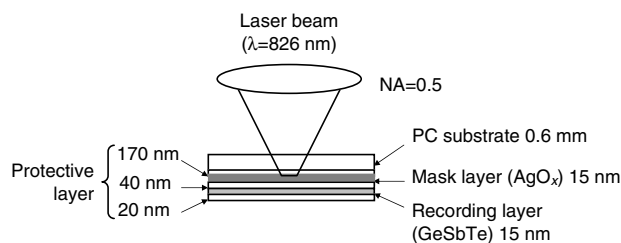


Fig. 5.49. Configuration for super-RENS optical disk using AgO_x mask layer

laser beam as that it is thin, but also enhances the scattering field. Kataja et al. numerically studied the AgO_x super-RENS phenomena using a 2-D FDTD method [5.56]. They indicated that an AgO_x super-RENS structure can be produced beyond the diffraction limit resolution when the aperture surrounded by small Ag particles that were formed and filled with a low index material such as O_2 .

In the following, the read/write mechanism of a super-RENS with the structure: PC-substrate (0.6 mm)/ ZnSiO_2 (170 nm)/ AgO_x (15 nm)/ ZnSiO_2 (15 nm)/ GeSbTe (15 nm)/ ZnSiO_2 (20 nm) is described along with results obtained from experiments under various conditions. The smallest mark formation of 50 nm length owing to the optical pulses with a reduced duty ratio is also presented.

Initialization effect

To explain the super-RENS mechanism directly and clearly, the read/write characteristics have been scrutinized experimentally. The configuration for a super-RENS optical disk using an AgO_x mask layer is shown in Fig. 5.49. The optical disk parameters and read/write conditions are shown in Table 5.7.

Table 5.7. Parameters of materials for super-RENS disk using AgO_x mask layer

layer	material	thickness (nm)	phase	optical constant	
				<i>n</i>	<i>k</i>
substrate	PC	0.6×10^6	—	1.56	0
protective layer	ZnSiO_2	170	—	2.25	0.01
mask layer	AgO_x	15	AgO_2 Ag particle	28 0.04	0.08 6.99
protective layer	ZnSiO_2	30	—	2.25	0.01
recording layer	GeSbTe	15	crystal amorphous	4.29 3.97	2.09 4.41
protective layer	ZnSiO_2	20	—	2.25	0.01

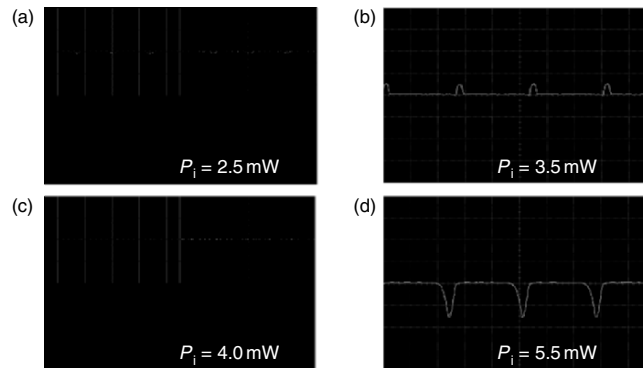
**Fig. 5.50.** Effect of initialization laser power P_i on reproduced signals

Figure 5.50 shows the reproduced signals (normalized with as-depo level V_i) at different initializations of laser power P_i for an as-depo medium. The reproduced signal V_i (mark) at the read power $P_r = 1 \text{ mW}$ changes in ways such as the following: becomes small negative at $P_i = 2.5 \text{ mW}$ (a), becomes maximum positive at $P_i = 3.5 \text{ mW}$ (b), becomes nearly zero at $P_i = 4 \text{ mW}$ (c), and gradually increases to negative as P_i increases (d). This variation generated by the written mark is shown in greater detail by the curve “mark” in Fig. 5.51. This figure shows the effect of initialization on an as-depo medium of the super-RENS disk. The mark reflectivity V_2 , normalized with as-depo reflectivity V_i , changes from (a) a small negative to zero to (b) positive to (c) zero to (d) increases to negative and then becomes saturated as the laser power increases.

This phenomenon corresponds to (a) the little decrease in reflectivity due to the little amorphous process in GeSbTe and then cancellation due to the increase in reflectivity with the AgO_x decomposition (Ag particle), (b) fully decomposed Ag particles, (c) cancellation due to the half amorphous process of GeSbTe, (d) the decrease in reflectivity due to the completely amorphous

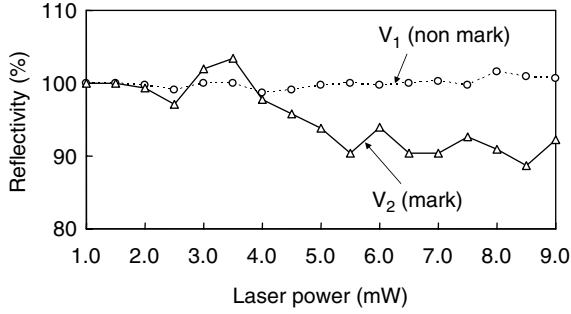


Fig. 5.51. Initialization effect on as-depo medium of the scattered type super-RENS disk with read power of 1 mW, medium velocity of 2 m s^{-1} , and mark length of 3,000 nm

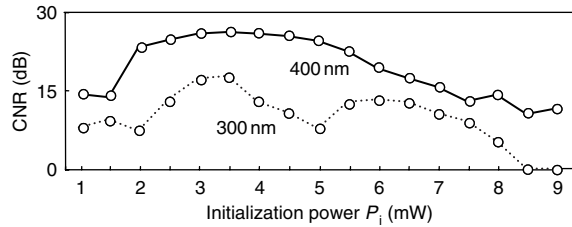


Fig. 5.52. Relationship between CNR of super-RENS readout ($P_r = 4 \text{ mW}$) and initialization laser power P_i , with mark length as parameter

process in GeSbTe. The maximum positive of the laser power of 3.5 mW shows that the AgO_x is fully decomposed to Ag particles and O_2 , both of which are uniformly dispersed in the mask layer. On the other hand, the nonmark reflectivity V_2 remains constant because thermal interference due to the successive laser pulses does not occur for long (3,000 nm) marks.

Figure 5.52 shows the relationship between the CNR for the super-RENS readout ($P_r = 4 \text{ mW}$) and the initialization laser power P_i , mark length as a parameter. We define $P_i = 3.5 \text{ mW}$ as the initialization laser power where the CNR for the short mark (under diffraction limit) reaches maximum. The maximum CNR corresponds to a reproduced signal maximum at $P_i = 3.5 \text{ mW}$ in Fig. 5.51, where fully decomposed Ag particles are dispersed in the mask layer.

Figure 5.53 shows the effect of initialization on the CNR for the super-RENS readout, with write power P_w as a parameter. The CNR with initialization (b) is higher and less dependent on P_w than that without initialization (a). Moreover, we can detect a mark length of 200 nm (duty ratio 50%) because with initialization the resolution increases.

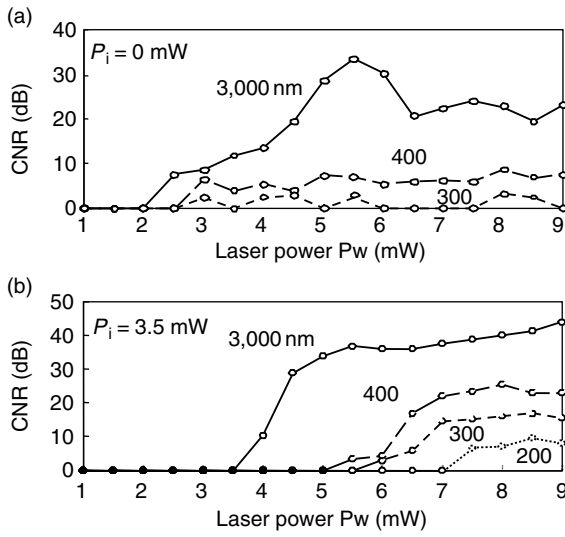


Fig. 5.53. Effect of initialization on CNR for super-RENS readout ($P_r = 4 \text{ mW}$), with write power P_w as parameter

Write power dependence

To determine the amorphous level of the recording layer, we measured write power dependence of signal amplitude V_{pp}/V_i and the CNR for the initialized medium. Here, $V_{pp} = V_1 - V_2$, and V_i is the as-depo level. They were measured for two conditions, immediately after writing (observed at $P_r = 1 \text{ mW}$) and at super-RENS readout (observed at $P_r = 4 \text{ mW}$). We compared the two signals and estimated the phase level (signal) and the noise level of the medium.

Figure 5.54 shows the relationship between CNR, V_{pp}/V_i , and write power P_w at the read power of $P_r = 1 \text{ mW}$. Figure 5.55 shows the relationship between CNR, V_{pp}/V_i , and write power P_w at $P_r = 4 \text{ mW}$ mark length is a parameter. Figure 5.54 shows that a dip appears for every mark length. This phenomenon occurs because reflectivity decreases as the half amorphous process for middle P_w , but it increases as the Ag cluster process for high P_w . Then the CNR becomes constant for high P_w . This suggests that the noise level increases for high P_w because the reflectivity (signal level) was found to increase with the completely amorphous process as P_w increases, as shown in the lower figure. We also found that the signal remains constant between 5.5 and 7.5 mW for a long mark at $P_r = 1 \text{ mW}$. This suggests that some changes occurred in the mask layer between 5.5 and 7.5 mW.

In the case of the super-RENS readout ($P_r = 4 \text{ mW}$), we found that every dip disappears as shown in the upper figure of Fig. 5.55. Moreover, we found that the signal increases as P_w increases due to the completely amorphous process, as shown in the lower figure. We confirm that the constant signal level

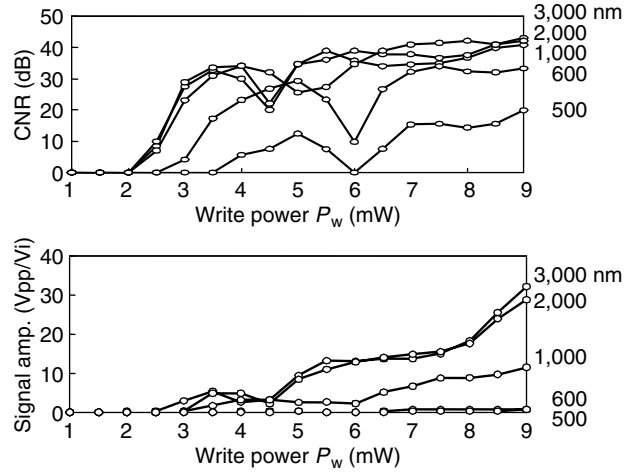


Fig. 5.54. Relationship between CNR, V_{pp}/V_i and write power P_w for read power of $P_r = 1$ mW, with mark length as parameter

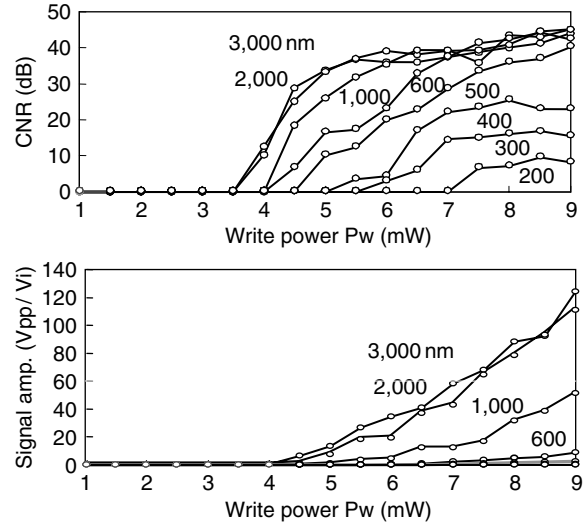


Fig. 5.55. Relationship between CNR, V_{pp}/V_i and write power P_w for read power of $P_r = 4$ mW (super-RENS readout), with mark length as parameter

between $P_w = 5.5$ and 7.5 mW, which appears in the lower figure of Fig. 5.54, is a result of the reflectivity decreasing as the Ag cluster is decomposed and diffused due to the great heat generated at the continuous read power of $P_r = 4$ mW. We define the optimum write power as $P_w = 8.5$ mW, at which the CNR for the shortest mark of 200 nm reaches maximum as shown in the upper figure of Fig. 5.55.

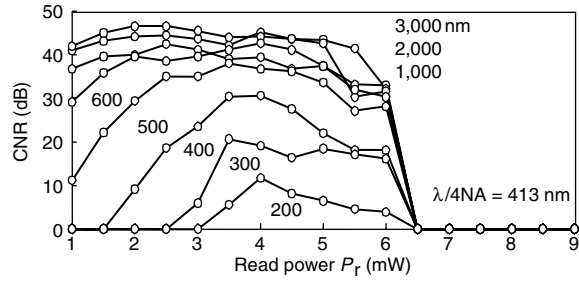


Fig. 5.56. Read power dependence on CNR of mark written at power of $P_w = 8.5$ mW, with mark length as parameter

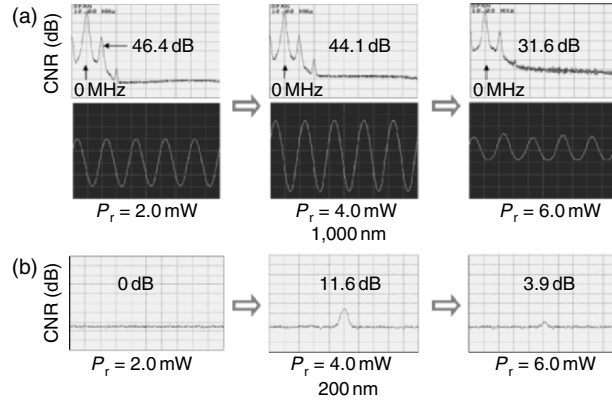


Fig. 5.57. Read power dependence on signal amplitude and spectrum for mark lengths of 1,000 nm with 10 dB div^{-1} and 1 MHz div^{-1} (a), and 200 nm with 10 dB div^{-1} and 10 kHz div^{-1} (b), with read power P_r as parameter

Read power dependence

Figure 5.56 shows the read power P_r dependence on the CNR of the mark written at the power of $P_w = 8.5$ mW, where mark length is a parameter. From the figure, it is evident that signals (400–200 nm) appear beyond the diffraction limit and the highest CNR of each mark length can be obtained at $P_r = 4$ mW. On the other hand, CNRs are high and almost independent from P_r for long marks (1,000–3,000 nm). All the signals disappear at read powers greater than $P_r = 6.5$ mW because the amorphous mark and the bubble pit are erased due to the continuous large P_r . We define the optimum super-RENS read power as 4 mW.

Figure 5.57 shows the read power dependence on the signal spectrum and the amplitude for mark lengths of 1,000 nm (a), and 200 nm (b), where read power P_r as a parameter. Both the signal spectrum and the signal amplitude increase at $P_r = 4$ mW. On the other hand, we find that noise increases at

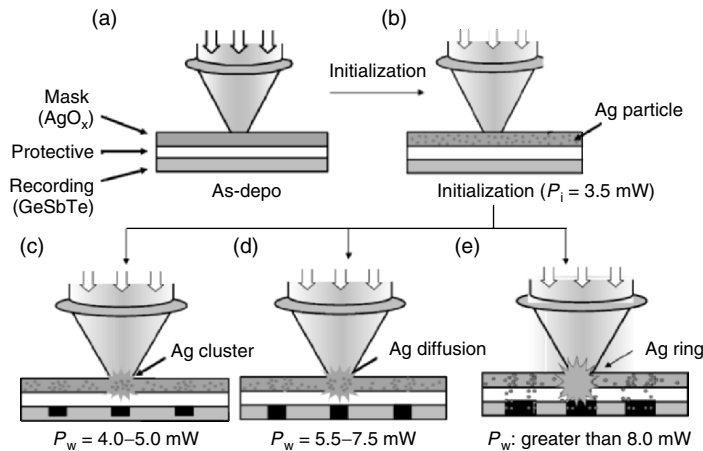


Fig. 5.58. Proposed working mechanism of super-RENS using AgO_x mask layer

$P_r = 6 \text{ mW}$ in the spectrum in the upper right figure and the signal amplitude decreases due to the degradation of the resolution (Ag cluster size increases).

Scattered type super-RENS working mechanism

On the basis of these results, we propose a model for an Ag-super-RENS mechanism. Figure 5.58 shows the states just after writing ($P_r = 1 \text{ mW}$) for both the mask layer and the recording layer, with write power P_w as a parameter. The working mechanism for the Ag-super-RENS is as follows. Both the mask and the recording layer have five possible states depending on the write power P_w (a) as-depo, (b) Ag particles uniformly dispersed and crystallized (after initialization $P_i = 3.5 \text{ mW}$), (c) Ag cluster and half amorphous ($P_w = 4\text{--}5 \text{ mW}$), (d) Ag diffusion and completely amorphous ($P_w = 5.5\text{--}7.5 \text{ mW}$), and (e) Ag ring and bubble pit (greater than $P_w = 8 \text{ mW}$). The mask layer for the super-RENS readout ($P_r = 4 \text{ mW}$) has an Ag ring structure, and the aperture is filled with O_2 , which increases both the CNR and the resolution limit.

Optical pulse duty dependence

To realize a short mark length, we illuminated thermally isolated optical pulses (having decreased duty ratio). Figure 5.59 shows the relationship between reflectivity V_1 (non-mark), V_2 (mark), and mark length for the write power of $P_w = 8.5 \text{ mW}$ with the super-RENS readout ($P_r = 4 \text{ mW}$); the optical pulse duty ratio as a parameter. The signal amplitude $V_{pp} = V_1 - V_2$ increases as the duty ratio decreases, which means the amorphous level difference between mark and nonmark increases because the difference in temperature increases due to the longer time separation between the laser pulses. Figure 5.60 shows the relationship between CNR and mark length for the super-RENS readout, optical pulse duty ratio as a parameter ($P_w = 8.5 \text{ mW}$). The reproduced signal

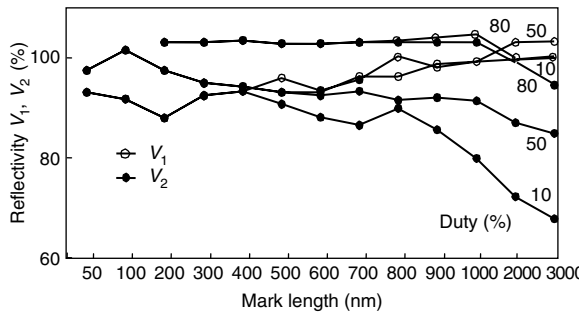


Fig. 5.59. Relationships between reflectivity V_1 (non-mark), V_2 (mark), and mark length for super-RENS readout ($P_r = 4 \text{ mW}$), with optical pulse duty as parameter

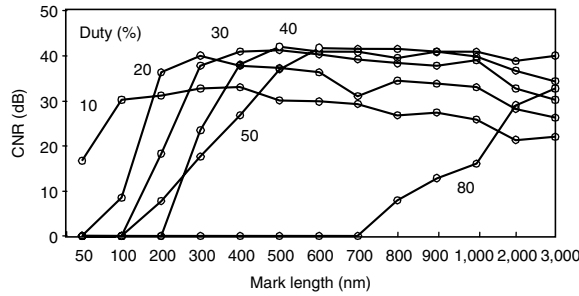


Fig. 5.60. Relationship between CNR and mark length for super-RENS readout ($P_r = 4 \text{ mW}$), with optical pulse duty as parameter

mark length becomes shorter as the optical pulse duty ratio decreases, and reaches 50 nm (CNR = 17 dB) at the duty ratio of 10%.

In summary, the scattered-type super-RENS using $\text{ZnSiO}_2/\text{AgO}_x/\text{ZnSiO}_2/\text{GeSbTe}/\text{ZnSiO}_2$ has the following characteristics:

1. The mask layer and the recording layer have five possible states depending on the write power P_w : as-depo, Ag particles uniformly dispersed and crystallized (after initialization), Ag cluster and half amorphous, Ag diffusion and completely amorphous, and Ag ring and bubble pit.
2. The mask layer for the super-RENS readout has an Ag ring structure, and the aperture is filled with O_2 , which increases both the CNR and the resolution limit.
3. The smallest mark length of 50 nm is reproduced at 17 dB by decreasing the optical pulse duty ratio of 10% under the experimental condition of $\lambda/4\text{NA} = 413 \text{ nm}$.

Problems

- 5.1.** How is the force $F = 2kT/d$ (due to Brownian motion) dependence on the diameter d of a microsphere? The microsphere is suspended in water, where k is the Boltzman constant, and T is 298 K.

5.2. Simulate the scattered light of the evanescent field generated by the attenuated total reflection at the prism (refractive index 1.6) to air interface. A plane wave with a wavelength of 800 nm is incident at an angle of 45° and the induced evanescent field is scattered by the sharpened metal probe of the curvature of 20 nm, where the distance between the probe tip and the prism surface is 15 nm.

5.3. The drag force F_{drag} acting on a metal sphere (diameter d) moving at the constant speed of v in the medium can be expressed by Eq. (5.23) [5.11]

$$F_{\text{drag}} = 3\pi\mu dv \left\{ 1 + \frac{9d}{32} \left(\frac{1}{D} - \frac{1}{H-D} \right) \right\}, \quad (5.23)$$

where μ is the viscosity of the medium, H is the height of the sample chamber and D is the distance between the sphere and the wall surface of the chamber. The viscosity μ varies with the temperature T as shown by

$$\log_{10} \mu = -1.64779 + \frac{262.37}{T + 273.15 - 133.98}. \quad (5.24)$$

How is the drag force dependent on the trapping position (particle-to-wall distance) (a) and medium temperature (b)?

5.4. The van der Waals force F_v between the particle and the wall is expressed as the Hamaker approximation shown by (5.25) [5.26], where H is the Hamakar constant, a is the radius of the particle, δ is the shortest distance between the particle and the wall.

$$F_v = -\frac{H}{6} \left[\frac{a}{\delta^2} + \frac{a}{(\delta+2a)^2} - \frac{1}{\delta} + \frac{1}{\delta+2a} \right]. \quad (5.25)$$

How is the van der Waals force dependent on the distance between the particle and the wall?

5.5. The electrostatic force acting on a particle is expressed as the Hogg approximation shown by (5.26) [5.26], where (ψ_1, ψ_2) are the potentials of the particle and the wall, $1/\kappa$ is the thickness of the electric double layer and ε is the dielectric constant of the medium

$$F_S = \pi\varepsilon a \left[2\psi_1\psi_2 \ln \left\{ \frac{1 + \exp(-\kappa\delta)}{1 - \exp(-\kappa\delta)} \right\} + (\psi_2^2 + \psi_1^2) \ln \{1 - \exp(-2\kappa\delta)\} \right]. \quad (5.26)$$

How is the electrostatic force dependent on the distance between the particle and the wall?

Answers, Hints and Solutions

Chapter 1

A1.1 There are several aspects in comparing the fabrication methods for microstructures: productivity, thickness, structure, and material used. Photolithography and LIGA will be used for mass production, but photoforming will be used for small-scale production and also for fabricating a complicated 3-D structure. An EBL, which has high resolution and does not require masks, will be used for fabricating microstructures less than $1\text{ }\mu\text{m}$ thick. Photolithography will be used for fabricating microstructures less than several $10\text{ }\mu\text{m}$, and LIGA less than several $100\text{ }\mu\text{m}$. The latter two require the use of masks for the etching. Groups III–V compound materials are used to integrate an LD and a PD.

A1.2 A sacrificed layer is the layer that is etched away, whereby the microstructure is undercut, leaving it freely suspended (see Sect. 1.2.1).

A1.3 Friction-less and contact sticking-free structures are needed for optical MEMS because of the increase of the surface effect. Refer to the scaling law (see Sect. 1.3.1).

A1.4 The moment of inertia of the mirror is $I_1 = \rho ab^3t/12I_2$ with a 50% reduction in the dimensions is $I_2/I_1 = (0.5)(0.5)^3(0.5) = 3.1\%$.

A1.5 Response time is proportional to [mass/frictional force], i.e., $[L^3/L^2] = [L]$, which leads to faster response as L decreases.

A1.6 See Sect. 1.5.

A1.7 There will be two development directions when device/system size decreases: the number of functions will decrease (commercialization-oriented direction), and the number of functions will increase (research-oriented direction). See Sect. 1.5.

Chapter 2

A2.1 See Fig. A.1.

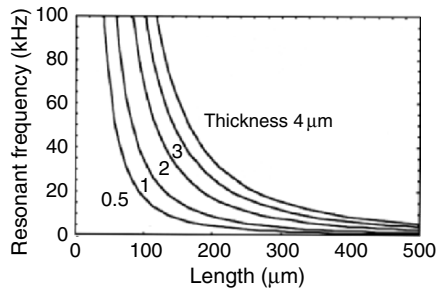


Fig. A.1. Relationship between the cantilever resonant frequency f_0 and the length l , with thickness t as a parameter

A2.2 See Fig. A.2.

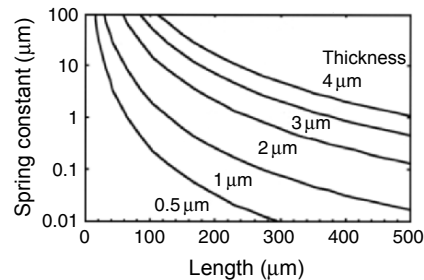


Fig. A.2. Relationship between the cantilever spring constant K and the length l , with thickness t as a parameter

A2.3 Since the LD facet reflectivity R_2 facing the medium is greatly reduced by an antireflection coating to improve the signal-to-noise ratio, the light

output P_1 (PD side) differs from P_2 (medium side). The light output ratio for a complex cavity laser is calculated using effective reflectivity R_2^{eff} instead of laser facet reflectivity R_2 , as shown [2.34]

$$\frac{P_2}{P_1} = \sqrt{\frac{R_1}{R_2^{\text{eff}}}} \frac{(1 - R_2^{\text{eff}})}{(1 - R_1)}.$$

Figure A.3 shows the calculated results for a high-reflection coated facet $R_1 = 0.70$. It is found that $P_2/P_1 = 5$ for $R_2 = 0.01$ and $R_3 = 0.3$ with $h = 2\text{ }\mu\text{m}$. While, for a cleaved facet $R_1 = 0.32$, $P_2/P_1 = 1.5$ for $R_2 = 0.01$ and $R_3 = 0.3$ with $h = 2\text{ }\mu\text{m}$.

$$h = 2\text{ }\mu\text{m}.$$

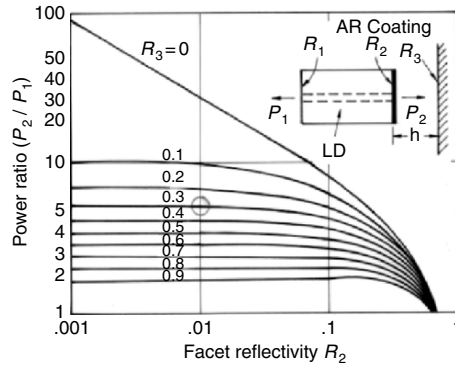


Fig. A.3. Relationships between the power ratio and the medium side LD facet reflectivity R_2 for $R_1 = 0.7$ with $h = 2\text{ }\mu\text{m}$, medium reflectivity R_3 as a parameter.

A2.4 There will be two ideas: one is a fine microactuator, such as a PZT, on the slider or on the arm of the main actuator. An electric actuator, such as a laser beam deflector, will be preferable to a mechanical actuator, such as a PZT.

A2.5 A 1.3- μm long-wavelength InGaAsP LD is used because it is stable and oxidation-free in air and its spot diameter (near field) is mainly constrained by the shape of the ridged waveguide. The oxidation-free characteristics are very important, especially when the LD is used at a high power output for thermal writing.

A2.6 Contamination may be a problem for removable media, but it can be avoided if we apply some kind of wiping mechanism and head lifting mechanism.

Chapter 3

A3.1 See Fig. 3.2 and Table 3.1 in Sect. 3.1.

A3.2 Consult the following procedure:

1. decompose the beam into individual rays with appropriate intensity and direction
2. trace individual rays
3. find the angle $\theta_1(r, \beta)$ incident to the microsphere of a ray entering the objective lens aperture at an arbitrary point (r, β)
4. compute the Fresnel transmission T and reflection R coefficients at the incident point
5. compute the trapping efficiencies $Q_s(r)$ and $Q_g(r)$, for that ray
6. integrate the contribution of all rays within the convergent angle
7. compute total trapping efficiency using $Q_t = \sqrt{Q_s^2 + Q_g^2}$

A3.3 See Fig. 3.15.

A3.4 First, we find the incident angle $\theta_1(r, \beta)$ of a ray entering the aperture of the objective lens at an arbitrary point (r, β) as shown in Fig. 3.12a. The ray makes an angle α to the xy plane and also makes an angle γ to the y -axis as shown in Fig. 3.12b. Then the angles become

$$\alpha = \tan^{-1} \left(\frac{R_m}{r} \cot \Phi_m \right),$$

$$\gamma = \cos^{-1}(\cos \alpha \cos \beta).$$

Since $r_0 \sin \theta_1(r, \beta) = s \sin(\gamma)$, then the incident angle becomes

$$\theta_1(r, \beta) = \sin^{-1}(s \sin(\tan^{-1} \left(\frac{R_m}{r} \cot \Phi_m \right) \cos \beta)),$$

where R_m is the radius of the objective lens, Φ_m is the maximum convergent angle, s is the distance from the laser focus to the center of the microsphere.

Next, the trapping efficiencies $Q_s(r)$ and $Q_g(r)$ are computed by the vector sum of the contributions of all rays within the convergent angle in the same manner described in Example 3.4. See Fig. 3.13b.

A3.5 See Fig. 3.16.

A3.6 See Fig. A.4.

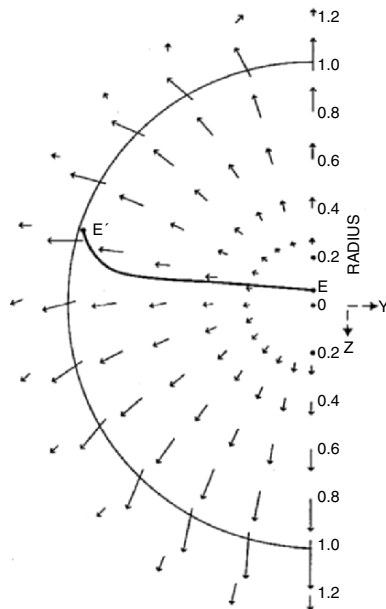


Fig. A.4. Magnitude and direction of total trapping efficiency (optical pressure force) for a microspore of relative refractive index of 1.2 at arbitrary focal position in the yz plane. A circularly polarized laser beam uniformly fills the objective aperture of NA = 1.25 [6.4]

A3.7 The discrepancy between theoretical and experimental results comes from the fact that the trapping position moves upward due to the gravitational force, which decreases Q_t as shown in Fig. A.5. Expected trajectory of the trapping (focus) position in the polystyrene are shown by 1: for a diameter

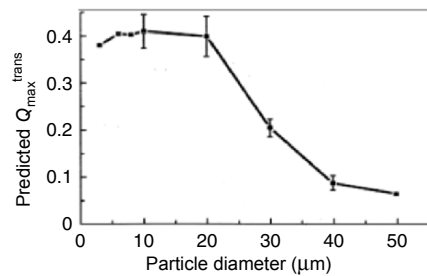


Fig. A.5. Dependence of predicted Q_{\max}^{trans} on sphere diameter for polystyrene, which is derived from experimental data of Fig. 3.32. Q_{\max}^{trans} decreases as diameter increases

less than $20\text{ }\mu\text{m}$; 2: for the diameter of $30\text{ }\mu\text{m}$; and 3: for a diameter greater than $40\text{ }\mu\text{m}$, as shown in Fig. A.6.

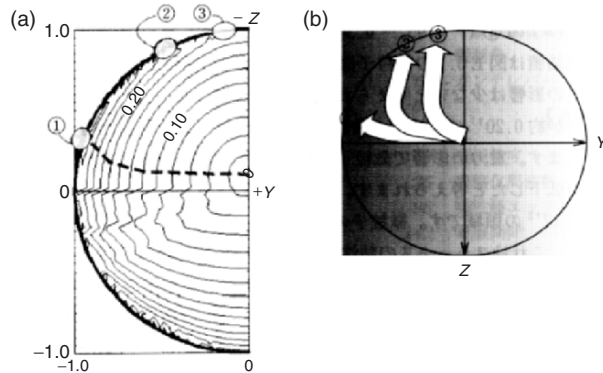


Fig. A.6. Contour lines for total trapping efficiency Q_t of polystyrene particle; broken line indicates along which Q_t is purely horizontal (a). Expected trajectory of trapping position; 1: for diameter less than $20\text{ }\mu\text{m}$, 2: for diameter of $30\text{ }\mu\text{m}$, 3: for diameter greater than $40\text{ }\mu\text{m}$ (b)

Chapter 4

A4.1 Figure A.7 shows the shape of a three-wing shuttlecock rotor. Optical pressure F_α exerted at part α generates torque in the normal rotation direction (a), but optical pressure F_β exerted at part β generates torque in the reverse rotation direction (b).

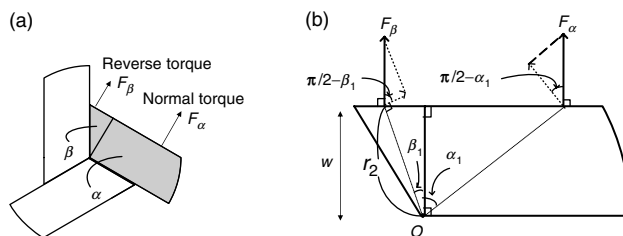


Fig. A.7. Optical torques induced in three-wing rotor. Not only normal torque but also reverse torque is generated.

To obtain a higher torque, the reverse torque should be changed to be 0 or to be in the normal direction by varying the side wall angle β_2 , as shown in Fig. A.8a, and the normal torque should be increased by varying the side wall angle α_2 , as shown in Fig. A.8b. From the 2-D simulation results shown in the figures for the rotor and medium conditions listed in Table 4.1, $\beta_2 = 130^\circ$ and $\alpha_2 = 100^\circ$ are found to lead to the shape shown in Fig. A.9.

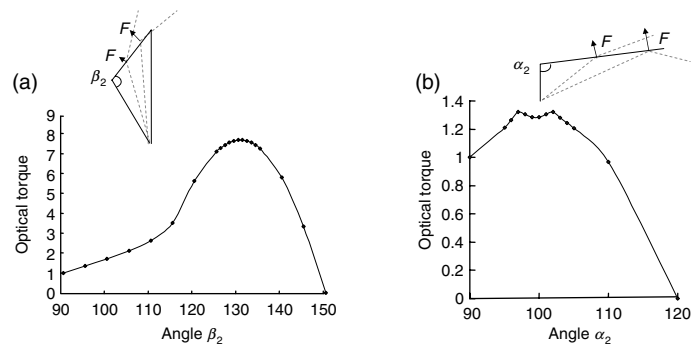


Fig. A.8. Relationship between optical torque and side wall angle β_2 (a), and side wall angle α_2 (b), both simulated in two dimension for simplicity

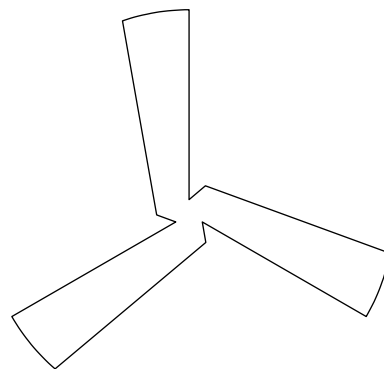


Fig. A.9. Improved shape of the three-wing shuttlecock rotor with $\beta = 130^\circ$ and $\alpha_2 = 100^\circ$ for the rotor of $n_2 = 1.6$, $d = 20\text{ }\mu\text{m}$, $t = 10\text{ }\mu\text{m}$, $w = 5\text{ }\mu\text{m}$, and medium $n_1 = 1.33$

A4.2 See Fig. A.10.

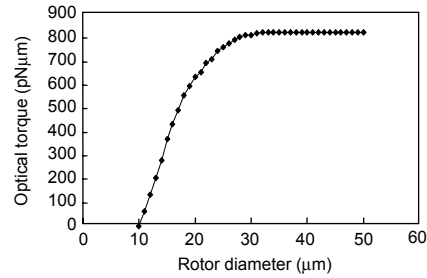


Fig. A.10. Optical torque dependence on diameter of rotor with four wings

A4.3 See Fig. A.11.

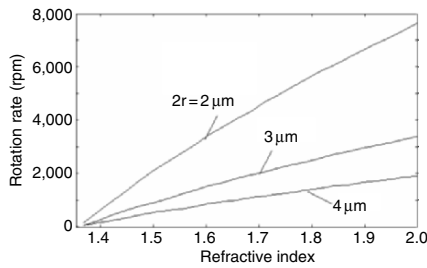


Fig. A.11. Rotation rate dependence on refractive index of cylindrical optical rotor with slope angle of 45°

A4.4 See Figs. A.12 and A.13.

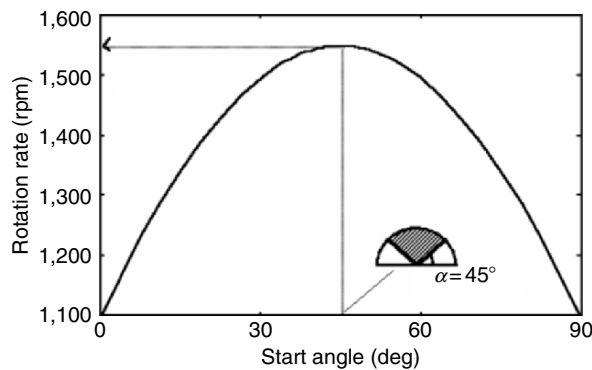


Fig. A.12. Relationship between rotation rate and starting angle α of the slope. The span of the slope forms from α to $\alpha + 90^\circ$

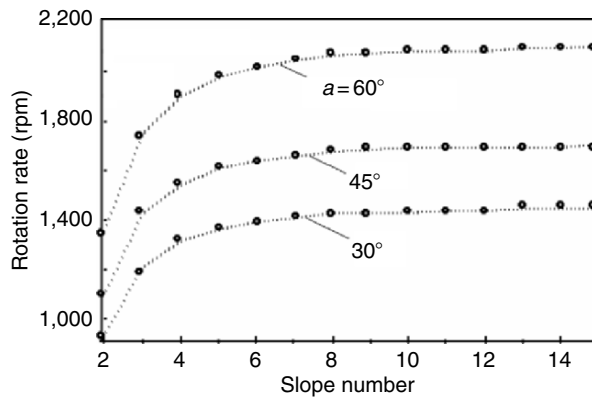


Fig. A.13. Rotation rate and number of slopes of the cylindrical rotor with slope angle of $a = 30^\circ$, 45° , and 60°

A4.5 See Fig. A.14. Optical mixer rotates due to the torque exerted on the slope upon parallel beam illumination, making the objective lens unnecessary.

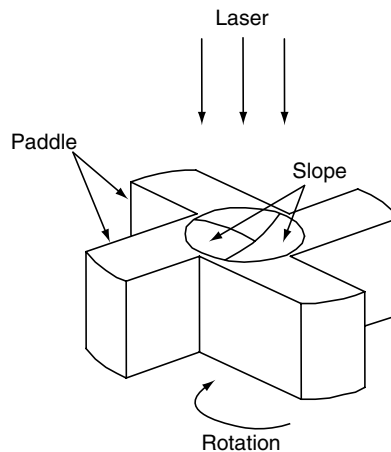


Fig. A.14. Optical mixer suitable for used in a microchannel of future μ -TAS

Chapter 5

A5.1 Figure A.15 shows a simulated result, indicating that the force decreases inversely proportional to the particle diameter (a), and linearly increases with temperature (b). At less than 10 nm in diameter, it reaches the piconewton (pN) order

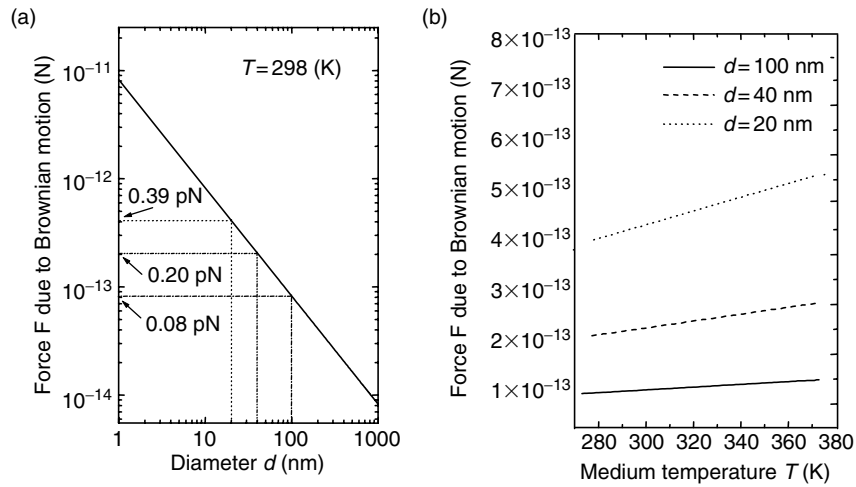


Fig. A.15. Relationships between force due to Brownian motion and diameter of microsphere (a), and temperature of medium (b)

A5.2 See Fig. A.16 and [5.20].

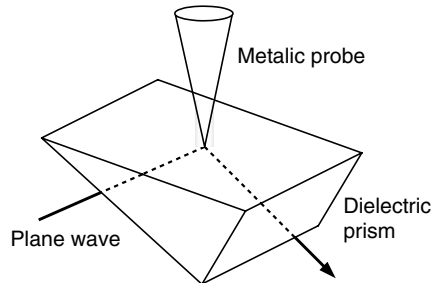


Fig. A.16. 3-D configuration of system for calculation of scattered light by sharpened metal probe [5.20]

A5.3 See Fig. A.17.

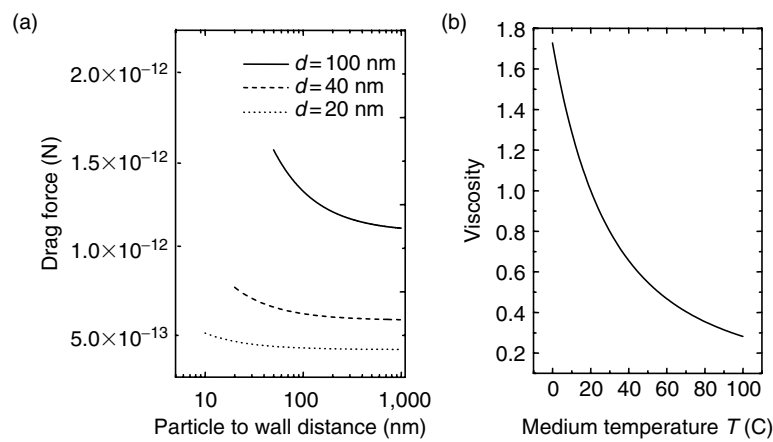


Fig. A.17. Drag force dependence on diameter of microsphere moving at constant speed of v in water (a), and viscosity dependence on temperature of medium (b)

A5.4 See Fig. A.18.

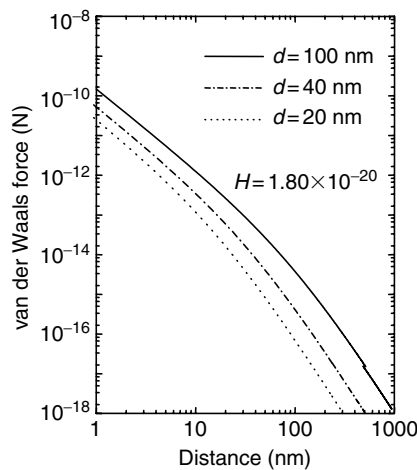


Fig. A.18. van der Waals force dependence on distance between particle and wall

A5.5 See Fig. A.19.

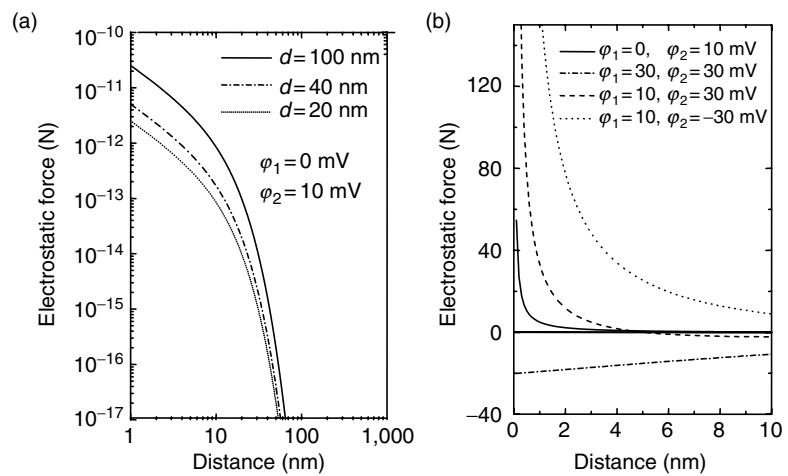


Fig. A.19. Electrostatic force dependence on distance between particle and wall

References

Chapter 1

- 1.1 Bustillo JM, Howe RT, Muller RS (1998) Surface micromachining for microelectromechanical systems. Proc IEEE 86:1552–1574/Madou MJ (2002) Fundamentals of microfabrication. CRC, London
- 1.2 Fan LS, Tai YC, Muller RS (1988) IC-processed electrostatic micromotors. In. Griffing B, Sodini C (eds) Technical digest of the 1988 IEEE Int Elect Devices Meeting IEEE:666–669, San Francisco USA
- 1.3 Solgaard O, Ford JE, Fujita H, Herzig HP (eds) (2002) IEEE J Select Top Quantum Electron Opti MEMS 8/Solgaard O, Talghadert J, Toshiyoshi H, Kopola H (eds) (2004) IEEE J Select Top in Quantum Electron Opt Microsyst 10
- 1.4 Szuromi P (1993) Micromechanical photonics. Science 260:733
- 1.5 Hornbeck LJ (1993) Current status of the digital micrometer device (DMD) for projection television applications. In. Thompson M (ed) Technical digest of the 1993 IEEE Int Elect Devices Meeting IEEE:381–384. Piscataway NJ USA/Kessel PFV, Hornbeck LJ, Meier RE, Douglass MR (1998) A MEMS-Based Projection Display. Proc IEEE 86:1687–1704
- 1.6 Lin LY, Goldstein EL, Tkach RW (1998) Free-space micromachined optical switch with submilisecond switching time for large-scale optical cross connects. IEEE Photon Tech 10:525–527
- 1.7 Aksyuk VA, Pardo F, Carr D, Greywall D, Chan HB, Simon ME, Gasparyan A, Shea H, Lifton V, Bolle C, Arney A, Frahm R, Paczkowski M, Haueis M, Ryf R, Neilson DT, Kim J, Giles CR Bishop D (2003) Beam-steering micromirros for large optical cross-connects. J Lightwave Tech 21:634–642
- 1.8 Imamura T, Katayama M, Ikegawa Y, Ohe T, Koishi R, Koshikawa T (1998) MEMS-based integrated head/actuator/slider for hard disk drive. IEEE/ASME Trans Mechatron 3:166–174

- 1.9 Yee Y, Nam HJ, Lee SH, Bu JU, Jeon YS, Cho SM (2000) PZT actuated micromirror for nano-tracking of laser beam for high-density optical data storage. Proc MEMS, Miyazaki Japan, 435–440
- 1.10 Chiou PY, Ohta A, Wu MC (2004) Toward all optical lab-on-a-chip system: optical manipulation of both microfluids and microscopic particles. Proc SPIE 5514:73–81
- 1.11 Suzuki K, Shimoyama I, Miura H, Ezura Y (1992) Proc MEMS, Travemunde, 190–193,
- 1.12 Furuya A, Shimokawa F, Matuura T, Sawada R (1994) J Micromech Microeng 4:67
- 1.13 Cox JA, Zook JD, Ohnstein T (1995) Proc SPIE 2383:17–24
- 1.14 Uenishi Y, Tanaka H, Ukita H (1995) AlGaAs/GaAs micromachining for monolithic integration of micromechanical structures with laser diodes. IEICE Trans Electron E78-C:139–145
- 1.15 Hjort K et al (1997) Demands and solutions for an indium phosphide based micromechanically tunable WDM photo detectors. Int Conf on Optical MEMS and Their Applications Nara Japan: 39–44
- 1.16 Sugihwo F, Larson MC, Harris JS (1997) Low threshold continuously tunable vertical-cavity surface-emitting lasers with 19.1 nm wavelength range. Appl Phy Lett 70:547–549
- 1.17 Ukita H, Uenishi Y, Tanaka H (1993) A photomicrodynamic system with a mechanical resonator monolithically integrated with laser diodes on gallium arsenide. Science 260:786–789
- 1.18 Paesler MA, Moyer PJ (1996) Near-field optics. John Wiley and Sons Inc, New York
- 1.19 Novotny L, Bian RX, Xie XS (1997) Theory of nanometric optical tweezers. Phys Rev Lett 79:645–648
- 1.20 Lin LY, Shen JL, Lee SS, Wu MC (1996) Realization of novel monolithic free-space optical disk pickup heads by surface micromachining. Opt Lett 21:155–157
- 1.21 Noell W, Clerc PA, Dellmann L, Guldmann B, Herzig HP, Manzardo O, Marxer CR, Weible KJ, Dändliker R, Rooij N (2002) Applications of SOI-based optical MEMS. IEEE J Select Top Quantum Electron Opt MEMS 8:148–154
- 1.22 Mehregany M, Bart SF, Tavrow LS, Lang JH, Senturia SD, Schlecht MF (1990) A study of three microfabricated variable-capacitance motors. Sens Actuat A21:73–179
- 1.23 Tay FEH, van Kan JA, Watt F, Choong WO (2001) A novel micromachining method for the fabrication of thick-film SU-8 embedded micro-channels. J Micromech Microeng 11:27–32
- 1.24 Becker EW et al (1986) Fabrication of microstructures with high aspect ratios and great structural heights by synchrotron radiation lithography galvanoformung and plastic molding (LIGA process). Microelectron Eng 4:35–56

- 1.25 Cox JA, Zook JD, Ohnstein T, Dobson DC (1995) Optical performance of high aspect LIGA gratings. SPIE 2383:17–24
- 1.26 Nishi N, Katoh T, Ueno H, Konishi S, Sugiyama S (1999) 3-Dimensional micromachining of PTFE using synchrotron radiation direct photo-etching. Proc Int Sym Micromechatron and Hum Sci 93–98
- 1.27 Nakamoto T, Yamaguchi K, Abraha PA, Mishima K (1996) Manufacturing of three-dimensional micro-parts by UV laser induced polymerization. J Micromech Microeng 6:240–253
- 1.28 Ikuta K, Maruo S, Kojima S (1998) New micro stereo lithography for freely movable 3D micro structure – Super IH process with submicron resolution -. Proc MEMS: 290–295
- 1.29 Maruo S, Ikuta K, Hayato K (2001) Light-driven MEMS made by high-speed two-photon microstereolithography. Technical Digest of the MEMS, Interlaken Switzerland, 954–957
- 1.30 Sun HB, Kawata S (2003) Two-photon laser precision microfabrication and applications to micro-nano devices and systems. J Lightwave Tech 21:624–633
- 1.31 Obi S, Gale MT, Gimkiewicz C, Westenföfer S (2004) Replicated optical MEMS in sol–gel materials. IEEE J Select Top Quantum Electron Opt Microsyst 10:440–444
- 1.32 Feynman R (1993) Infinitesimal machinery. J MEMS 2:4–14/Krim J (2005) Friction at the nano-scale. Phys World 18:31–34
- 1.33 Asada N, Matsuki H, Minami K, Esashi M (1994) Silicon micro-machined two-dimensional galvano optical scanner. IEEE Trans Mag 30:4647–4649
- 1.34 Akimoto K, Uenishi Y, Honma K, Nagaoka S (1997) Proc MEMS, Nagoya Japan: 66–69
- 1.35 Chauvel D, Haese N, Rolland PA, Collard D, Fujita H (1997) A micro-machined microwave antenna integrated with its electrostatic spatial scanning, Proc MEMS, Nagoya Japan: 84–89
- 1.36 Uenishi Y, Tsugai M, Mehregany M (1995) Micro-opt-mechanical devices fabricated by anisotropic etching of (100) silicon. J Micromech Microeng 5:305–312
- 1.37 Tabib-Azar M (1995) Integrated optics microstructures and sensors. Kluwer Academic Publishers
- 1.38 Wu MC (1997) Micromachining for optical and optoelectronic systems. Proc IEEE 85:1833–1856
- 1.39 Marom DM, Doerr CR, Basavanhally NR, Cappuzzor M, Gomez L, Chen E, Wong-Foy, A Laskowski E (2004) Wavelength-selective 1×2 switch utilizing a planar lightwave circuit stack and a MEMS micro-mirror array. Proc Optical MEMS, Takamatsu Japan: 28–29
- 1.40 Yamamoto T, Yamaguchi J, Takeuchi J, Shimizu A, Sawada R, Higurashi E, Uenishi Y (2004) A three-dimensional micro-electro-mechanical system (MEMS) optical switch module using low-cost highly accurate polymer components. Jpn J Appl Phys 43:5824–5827/

- Sawada R, Higurashi E, Shimizu A, Maruno T (2001) Single crystalline mirror actuated electrostatically by terraced electrodes with high-aspect ratio torsion spring, Okinawa, Japan: 23–24
- 1.41 Tsai J, Huang S, Wu MC (2004) High fill-factor two-axis analog micro-mirror array for $1 \times N^2$ wavelength-selective switches. Proc Opt MEMS, Takamatsu Japan: 101–104
- 1.42 Talghader JH (2002) Shape control and heat transfer in optical MEMS, IEEE LEOS Newsletter August: 3–8
- 1.43 Rooij NF, Noell W (2001) Opportunities of Optical MEMS in telecommunication, advanced instrumentation and life science. Proc Optical MEMS, Okinawa Japan: 3–3
- 1.44 Maeda T, Terao M, Shimano T (2003) A review of optical disk systems with blue–violet laser pickups. Jpn J Appl Phys 42:1044–1051
- 1.45 Katayama R (2003) Blue/DVD/CD compatible optical head technologies, Technical Digest of International Symposium on Optical Memory, Nara Japan: 216–217
- 1.46 Iwami K, Ono T, Esashi M (2003) Electrostatic actuator integrated optical near-field bow-tie probe for high transmission efficiency. 12th Int Conf on Solid State Sensors Actuators and Microsystems (Transducers'03), Boston USA: 548–551
- 1.47 Lee A, Fair RB (eds) (2004) Special Issue on Biomedical Applications for MEMS and Micro-Fluidics. Proc IEEE 92:3
- 1.48 Reyes DR, Iossifidis D, Auroux PA, Manz A (2002) Micro total analysis systems. Anal Chem 74:2623–2651
- 1.49 Stroock AD, Dertinger SKW, Ajdari A, Mezic I, Stone HA, Whitesides GM (2002) Chaotic mixer for Micro-channels. Science 295:647–651
- 1.50 Ukita H, Kanehira M (2002) A shuttlecock optical rotator – Its design fabrication and evaluation for a micro-fluidic mixer. IEEE J Select Top Quantum Electron Opt MEMS 8:111–117
- 1.51 Webster JR, Burns MA, Burke DT, Mastrangelo CH (2000) Electrophoresis system with integrated on-chip fluorescence detection. Proc MEMS, Miyazaki Japan: 306–310
- 1.52 Maillefer D, Gamper S, Frehner B, Balmer P, Lintel HV, Renaud P (2001) A high-performance silicon micro-pump for disposable drug delivery systems. Technical Digest of MEMS, Interlaken Switzerland: 413–416
- 1.53 Yaga Y and Esashi M (2004) Biomedical microsystems for minimally invasive diagnosis and treatment. Proc IEEE 92:98–114
- 1.54 Nogomori W, Irisa K, Ando M, Naruse Y (1997) A laser-powered micro-gripper. Proc MEMS, Nagoya Japan: 267–271
- 1.55 Sato M, Shimokawa F, Makihara M, Nishida Y (1997) Two types of thermo-capillary optical switches. Int Conf Optical MEMS and Their Applications, Nara Japan: 56–61
- 1.56 Akuto K, Takahashi M, Kato N, Ogata T (1994) Extended Abstracts 94–2:239, Fall Meeting Miami Beach FL USA

- 1.57 Lee JB, Chen Z, Allen MG, Rohatgi A, Arya R (1994) A high voltage solar cell array as an electrostatic MEMS power supply. Proc MEMS, Oiso Japan: 331–336
- 1.58 Sakakibara T, Izu H, Shibata T, Takahashi S, Tarui H, Hirano H, Shibata K, Kiyama S, Kawahara N (2001) Multi-source power supply system using micro-photovoltaic devices combined with microwave antenna. Technical Digest of MEMS, Interlaken Switzerland: 192–195
- 1.59 Ashkin A (2000) History of optical trapping and manipulation of small-neutral particle atom and molecules. IEEE J Select Top Quantum Electron 6:841–856
- 1.60 Friese MEJ, Rubinsztein-Dunlop H, Gold J, Hagberg P, Hanstorp D (2001) Optically driven micromachine elements. Appl Phy Lett 78:547–549
- 1.61 Harada T, Yoshikaw K (2002) Mode switching of an optical motor. Appl Phy Lett 81:4850–4852
- 1.62 Higurashi E, Ukita H, Tanaka H, Ohguchi O (1994) Rotational control of micro-objects by optical pressure. Proc MEMS, Oiso Japan: 291–296
- 1.63 Ukita H, Nagatomi K (2003) Optical tweezers and fluid characteristics of an optical rotator with slopes on the surface upon which light is incident and a cylindrical body. Appl Opt 42:2708–2715
- 1.64 Galajda, P Ormos P (2001) Complex micromachines produced and driven by light. Appl Phy Lett 78:249–251
- 1.65 Maruo S, Ikuta K, Hayato K (2001) Light-driven MEMS made by high-speed two-photon microstereolithography. Technical Digest of MEMS, Interlaken Switzerland: 954–957
- 1.66 Ukita H, Takada K and Itoh Y (2004) Experimental and theoretical analyses of 3-D micro-flows generated by an optical mixer, Proc SPIE Opt Sci Technol 5514:704–711
- 1.67 Ukita H (2004) A tunable laser diode with a photothermally driven integrated cantilever and related properties. IEEE J Select Top Quantum Electron Opt Microsyst 10:622–628
- 1.68 Sawada R, Ohguchi O, Mise, K Tsubamoto M (1994) Fabrication of advanced integrated optical micro-encoder chips. Proc MEMS, Oiso Japan: 337–342
- 1.69 Ukita H, Katagiri Y, Nakada H (1991) Flying head read/write characteristics using a monolithically integrated laser diode/photodiode at a wavelength of $1.3\text{ }\mu\text{m}$, Proc SPIE Opt Data Storage 1499:48–262
- 1.70 Higurashi E, Sawada R, Ito T (2003) An integrated laser blood flowmeter. J. Lightwave Tech 21:591–595
- 1.71 Katagiri Y, Ukita H (1990) Ion beam sputtered $(\text{SiO}_2)_x(\text{Si}_3\text{N}_4)_{1-x}$ antireflection coating on laser facet produced using O_2-N_2 discharges. Appl Opt 29:5074–5079
- 1.72 Ukita H, Tanabe Y, Okada A (2004) Improved photothermal deflection design of an integrated microbeam for application to an external-cavity tunable laser diode. Smart Mater Struct 13:970–975

- 1.73 Wise KD, Anderson DJ, Hetke JF, Kipke DR (2004) Wireless implantable Microsystems: high-density electronic interfaces to the nervous system. *Proc IEEE* 92:76–97
- 1.74 Fukuzawa K, Tanaka Y, Akamine S, Kuwano H, Yamada H (1995) Imaging of optical and topographical distributions by simultaneous near field scanning optical/atomic force microscopy with a microfabricated photocantilever. *Appl Phys Lett* 78:7376–7381
- 1.75 Shao Y, Dickensheets DL, Himmer P (2004) 3-D MOEMS mirror for laser beam pointing and focus control. *IEEE J Select Top Quantum Electron Opt Mycrosyst* 10:528–535
- 1.76 Perregaux G, Gonseth S, Debergh P, Thiebaud JP, Vuilliomenet H (2001) Arrays of addressable high-speed optical microshutters, Technical Digest of MEMS, Interlaken Switzerland: 232–235
- 1.77 Kaneko T, Mitsumoto N, Kawahara N (2000) A new smart vision system using a quick-response dynamic focusing lens. *Proc MEMS*, Miyazaki Japan: 461–466

Chapter 2

- 2.1 Kim JY, Hsieh HC (1992) An open-resonator model for the analysis of a short external-cavity laser diode and its application to the optical disk head. *Lightwave Tech* 10:439–447
- 2.2 Rodrigo PJ, Lim M, Saloma C (2001) Optical-feedback semiconductor laser Michelson interferometer for displacement measurement with directional discrimination. *Appl Opt* 40:506–513
- 2.3 Berger JD, Zhang Y, Grade DJ, Lee H, Hrinya S, Jerman H, Fennema A, Tselikov A, Anthon D (2001) External cavity diode lasers tuned with silicon MEMS. *IEEE LEOS Newslett Oct*
- 2.4 Larson MC, Harris JS (1996) Wide and continuous wavelength tuning in a vertical-cavity surface-emitting laser using a micromachined deformable-membrane mirror. *App Phys Lett* 68:891–893
- 2.5 Sugihwo F, Larson MC, Harris JS (1998) Simultaneous optimization of membrane reflectance and tuning voltage for tunable vertical cavity lasers. *App Phys Lett* 72:10–12
- 2.6 Okada M (2004) Wavelength tuning characteristics of vertical cavity surface emitting laser diodes with an external short cavity. *Opt Rev* 11:193–198/Cole GD, Bjorlin ES, Chen Q, Chan CY, Wu S, Wang CS, MacDonald NC, Bowers JE (2005) MEMS-tunable vertical-cavity SOAs. *IEEE J Quantum Electron QE-41:390–407*
- 2.7 Uenishi Y, Tsugai M, Mehregany M (1995) Hybrid-integrated laser-diode micro-external mirror fabricated by (110) silicon micromachining. *Electr Lett* 31:965–966
- 2.8 Liu AQ, Zhang X, Murukeshan VM, Lu C, Cheng TH (2002) Micro-machined wavelength tunable laser with an extended feedback model. *IEEE J Select Top Quantum Electron* 8:73–79

- 2.9 Sidorin Y, Howe D (1998) Some characteristics of an extremely-short-external-cavity laser diode realized by butt coupling a Fabry–Perot laser diode to a single-mode optical fiber. *Appl Opt* 37:3256–3263
- 2.10 Rupercht PA, Brandenberger JR (1992). *Opt Commun* 93:82
- 2.11 Uenishi Y (1997) Development of Optical Micro Mechanical Devises by Micromachining, Ph.D. thesis, Osaka University: 12–34 (in Japanese)
- 2.12 Asada M, Suematsu Y (1985) Density-matrix theory of semiconductor lasers with relaxation broadening model and gain-suppression in semiconductor lasers. *IEEE J Quantum Electron QE-21:434–442*
- 2.13 Ukita H, Karaki Y (2004) A wavelength and spectrum measurement of an extremely-short-external-cavity laser diode by precisely controlling slider flying height. *Opt Rev* 11:188–192
- 2.14 Katagiri Y, Ukita H (1990) Ion beam sputtered $(\text{SiO}_2)_x(\text{Si}_3\text{N}_4)_{1-x}$ antireflection coating on laser facets produced by using $\text{O}_2\text{--N}_2$ discharges. *Appl Opt* 29:5074–5079
- 2.15 Liu JY, Yamaguchi I (2000) Surface profilometry with laser diode optical feedback interferometer outside optical benches. *Appl Opt* 39:104–107
- 2.16 Ukita H, Katagiri Y, Fujimori S (1989) Supersmall flying optical head for phase change recording media. *Appl Opt* 28:4360–4365
- 2.17 Ukita H, Uenishi Y, Tanaka H (1993) A photomicrodynamic system with a mechanical resonator monolithically integrated with laser diodes on gallium arsenide. *Science* 260:786–789
- 2.18 Kataja K, Aikio J, and Howe D (2002) Numerical study of near-field writing on a phase-change optical disk. *Appl Opt* 41:4181–4187
- 2.19 Uenishi Y, Tanaka H, Ukita H (1995) AlGaAs/GaAs micromachining for monolithic integration of micromechanical structures with laser diodes. *IEICE Trans Electron* E78-C:139–145
- 2.20 Hjort K, Streubel K, Viktorovitch P (1996). Optical MEMS and Their Applications 45, Keystone
- 2.21 Pruessner MW, King TT, Kelly DP, Grover R, Calhoun LC, Ghodssi R (2003) Mechanical property measurement of InP-based MEMS for optical communications. *Sens Actuat A-105:190–200*
- 2.22 Stemme G (1991) Resonant silicon sensors. *J Micromech Microeng* 1:113–125
- 2.23 Muro H, Hoshino S (1991). IEICE J74-C-II:421–425 (in Japanese).
- 2.24 Tabib-Azar M, Leave JS (1990). *Sens Actuat A21–23:229*
- 2.25 Uenishi Y, Isomura Y, Sawada R, Ukita H, Toshima T (1988) Beam converging laser diode by taper ridged waveguide. *Electr Lett* 24:623–624
- 2.26 Salathe R, Voumard C, Weber H (1974) Rate equation approach for diode lasers. *Opto-electronics* 6:451–463
- 2.27 Eguchi N, Tobita M, Ogawa M (1990) An 86 mm Magneto-optical disk drive with compact and fast-seek time optical head. *Conf Digest of Optical Data Storage: 2–5*

- 2.28 Kaminow IP, Eisenstein G, Stulz LW (1983) Measurement of the modal reflectivity of an antireflection coating on a superluminescent diode. *IEEE J Quantum Electron* 19:493–495
- 2.29 Marti O, Ruf A, Hipp M, Bielefeldt H, Colchero J, Mlynek J (1992) Mechanical and thermal effects of laser irradiation on force microscope microbeams. *Ultramicroscopy* 42–44:345–350
- 2.30 Chu WH, Mehregany M, Muller RL (1993) Analysis of tip deflection and force of a bimetallic microbeam microactuator. *J Micromech Microeng* 3:4–7
- 2.31 Born M, Wolf E (1970) Principles of optics p.62, Pergamon, Oxford
- 2.32 Mito I et al (1985) Natl Conf Rec. IEICE 881:4–5 (in Japanese).
- 2.33 Ukita H, Katagiri Y (1993) Optimum reflectivity design of laser diode facets and a recording medium for an integrated flying optical head. *Jpn J Appl Phys* 32 11B:5292–5300
- 2.34 Ettenberg M, Sommers HS, Kressel Jr H, Lockwood HF (1971) *Appl Phys Lett* 18:571–573

Chapter 3

- 3.1 Stimler M, Slawsky ZI (1964) Torsion pendulum photometer. *Rev Scient Instrum* 35:311–313
- 3.2 Ashkin A (1970) Acceleration and trapping of particles by radiation pressure. *Phys Rev Lett* 24:156–159
- 3.3 Wright WH, Sonek GJ, Tadir Y, Berns MW (1990) Laser trapping in cell biology. *IEEE J Quantum Electron* 26:2148–2157
- 3.4 Ashkin A (1992) Forces of a single-beam gradient laser trap on a dielectric sphere in the ray optics regime. *Biophys J* 61:569–582
- 3.5 Weber G, Greulich KO (1992) Manipulation of cells organelles and genomes by laser microbeam and optical trap. *Int Rev Cytol* 133:1–41
- 3.6 Masuhara H (ed) (1994) Microchemistry. Elsevier, Amsterdam
- 3.7 Simon A, Libchaber A (1992) Escape and synchronization of a Brownian particle. *Phys Rev Lett* 68:3375–3378
- 3.8 Higurashi E, Ukita H, Tanaka H, Ohguchi O (1994) Optically induced rotation of anisotropic microobjects fabricated by surface micromachining. *Appl Phys Lett* 64:2209–2210/Higurashi E, Ukita H, Tanaka H, Ohguchi O (1994) Rotational control of microobjects by optical pressure. *Proc MEMS, Oiso Japan*:291–296.
- 3.9 Misawa H, Sasaki K, Koshioka M, Kitamura N, Masuhara H (1992) Multibeam laser manipulation and fixation of microparticles. *Appl Phys Lett* 60:310–312
- 3.10 Wright WH, Sonek GJ, Berns MW (1993) Radiation trapping forces on microshperes with optical tweezers. *Appl Phys Lett* 63:715–717
- 3.11 Felgner H, Muller O, Schliwa M (1995) Calibration of light forces in optical tweezers. *Appl Opt* 34:977–982

- 3.12 Constabl A, Kim J, Mervis J, Zarinetchi F, Prentiss M (1993) Demonstration of a fiber-optical light-force trap. *Opt Lett* 18:1867–1869
- 3.13 Lyons ER, Sonek GJ (1995) Demonstration and modeling of a tapered lensed optical fiber trap. *SPIE* 2383:186–198
- 3.14 Sidick E, Collins SD, Knoesen A (1997) Trapping forces in a multiple -beam fiber-optic trap. *Appl Opt* 36:6423–6433
- 3.15 Taguchi K, Atsuta K, Nakata T, Ikeda M (1999) Experimental analysis of optical trapping system using tapered hemispherically lensed optical fiber. *Opt Rev* 6:224–226/Sano T, Ukita H (2005) Analyses of an off-axial optical trapping by a solitary optical fiber. *Trans Inst Electr Eng Jpn MSS-04–13* (in Japanese):61–66
- 3.16 Emery R, Kobayashi T, Suzuki A (1997) *Opt Lett* 22:816–818
- 3.17 Higurashi E, Sawada R, Ito T (1999) Optically induced angular alignment of trapped birefringent microobjects by linearly polarized light. *Phy Rev E* 59:3676–3681
- 3.18 Ukita H, Saitoh T (1999) Optical micro-manipulation of beads in axial and lateral directions with upward and downward-directed laser beams. *LEOS'99* (IEEE Lasers and Electro-Optics Society 1999 Annual Meeting) 169–170, San Francisco USA
- 3.19 Ashkin A, Dziedzic JM, Bjorkholm JE, Chu S (1986) Observation of a single-beam gradient force optical trap for dielectric particles. *Opt Lett* 11:288–290
- 3.20 Sato S, Higurashi E, Taguchi Y, Inaba H (1991) Achievement of laser fusion of biological cell using UV pulsed dye laser beams. *Appl Phys* B54:531–533
- 3.21 Furukawa H, Yamaguchi I (1998) Optical trapping of metallic particles by a Gaussian beam. *Opt Lett* 23:26–218
- 3.22 Gahagam H, Swartzlander GA (1998) Trapping of low-index microparticles in an optical vortex. *J Opt Soc Am* B15:524–534
- 3.23 Ashkin A, Dziedzic JM, Yamane T (1987) Optical trapping and manipulation of single cells using infrared laser beams. *Nature* 330:769–771
- 3.24 Block SM, Blair DF, Berg HC (1989) Compliance of bacterial flagella measured with optical tweezers. *Nature* 338:514–518
- 3.25 Svoboda K, Schmidt CF, Schnap BJ and Block SM (1993) Direct observation of kinesin stepping by optical trapping interferometry. *Nature* 365:721–727
- 3.26 Ishijima A, Kojima H, Funatsu T, Tokunaga M, Higuchi H, Tanaka H, Yanagida T (1998) Simultaneous observation of individual ATPase and mechanical events by a single myosin molecule during interaction with actin. *Cell* 92:161–171
- 3.27 Misawa H, Koshioka M, Sasaki K, Kitamura N, Masuhara H (1991) Three-dimensional optical trapping and laser ablation of a single polymer latex particle in water. *J Appl Pyhs* 70:3829–3836
- 3.28 Barber PW, Chang RK (1988) Optical effects associated with small particles. World Scientific, Singapore

- 3.29 Misawa H, Fujisawa R, Sasaki K, Kitamura N, Masuhara H (1993) Simultaneous manipulation and lasing of a polymer particle using a CW 1064 nm laser beam. *Jpn J Appl Phys* 32:L788–L790
- 3.30 Sasaki K, Fujisawa H, Masuhara H (1997) Optical manipulation of a lasing microparticle and its application to near-field microspectroscopy. *J Vac Sci Technol B15:2786–2790*
- 3.31 Sugiura T, Okada T, Inoue Y, Nakamura O, Kawata S (1997) Gold-bead scanning near-field optical microscope with laser-force position control. *Opt Lett* 22:1663–1665
- 3.32 Ukita H, Uemi H, Hirata A (2004) Near field observation of a refractive index grating and a topographical grating by an optically-trapped gold particle. *Opt Rev* 11:365–369
- 3.33 Miwa M, Misawa H, Araki H, Yoshimura T (1995) Laser manipulation technique and its role in study of micromachine. *Proc Int Symp on Microsystems Intelligent Materials and Robots:67*, Sendai Japan
- 3.34 Yamamoto A, Yamaguchi I (1995) Measurement and Control of optically induced rotation of anisotropic shaped particles. *Jpn J Appl phys* 34:3104–3108
- 3.35 Omori R, Sawada K, Kobayashi T, Suzuki A (1996) Optical trapping of ThO₂ and UO₂ particles using radiation pressure of a visible laser light. *J Nucl Sci and Technol* 33:956–963
- 3.36 Omori R, Kobayashi T, Suzuki A (1997) Observation of a single-beam gradient-force optical trap for dielectric particles in air. *Opt Lett* 22:816–818
- 3.37 Grier DG (2003) A revolution in optical manipulation. *Nature* 424:810–816
- 3.38 Leach J, Sinclair G, Yao E, Courtial J, Padgett MJ, Jordan P, Cooper J, Laczik J (2004) Crystal-like structures within holographic optical tweezers. *IEEE LEOS Newslett April:7–8*
- 3.39 Padgett MJ, Leach J, Sinclair G, Courtial J, Yao E, Gibson G, Jordan P, Cooper J, Laczik J (2004) Three-dimensional structures in optical tweezers. *Proc SPIE* 5514:371–378
- 3.40 Hoogenboom JP, Vossen DLJ, Moskalenko CF, Dogterom M, van Blaaderen A (2002) Pattering surfaces with colloidal particles using optical tweezers. *Appl Pys Lett* 80:4828–4830
- 3.41 Ito S, Yoshikawa Y, Masuhara H (2001) Optical pattering and photochemical fixation of polymer nanoparticles on glass substrates. *Appl Pys Lett* 78:2566–2568

Chapter 4

- 4.1 Sugiura T, Kawata S, Minami S (1990) Optical rotation of small particles by a circularly-polarized laser beam in an optical microscope. *J Spectrosc Soc Jpn* 39:342 (in Japanese)

- 4.2 Sato S, Ishigure M, Inaba H (1991) Optical trapping and rotational manipulation of microscopic particles and biological cells using high-order mode Nd:YAG laser beams. *Electron Lett* 27:1831–1832
- 4.3 Higurashi E, Ukita H, Tanaka H, Ohguchi O (1994) Optically induced rotation of micro-objects fabricated by surface micromachining. *Appl Phy Lett* 64:2209–2210
- 4.4 Yamamoto A, Yamaguchi I (1995) Measurement and control of optically induced rotation of anisotropic shaped particles. *Jpn J Appl Phys* 34:3104–3108
- 4.5 Gauthier RC (1995) Ray optics model and numerical computation for the radiation pressure micromotor. *Appl Phy Lett* 67:2269–2271
- 4.6 Ukita H, Nagatomi K (1997) Theoretical demonstration of a micro-rotator driven by optical pressure on the light incident surface. *Opt Rev* 4:447–449 / Ukita H and Nagatomi K (2003) Optical tweezers and fluid characteristics of an optical rotor with slopes on the surface upon which light is incident and a cylindrical body. *Appl Opt* 42:2708–2715
- 4.7 Luo ZP, Sun YL, An KN (2000) An optical spin micromotor. *Appl Phy Lett* 76:1779–1781
- 4.8 Gauthier RC, Tait RN, Mende H, Pawlowicz C (2001) Optical selection manipulation trapping and activation of a microgear structure for application in micro-optical-electromechanical systems. *Appl Opt* 40:930–937
- 4.9 Friese MEJ, Dunlop HR (2001) Optically driven micromachine elements. *Appl Phy Lett* 78:547–549
- 4.10 Galajda P, Ormos P (2001) Complex micromachines produced and driven by light. *Appl Phy Lett* 78:249–251
- 4.11 Larsen UD, Rong W, Telleman P (1999) Design of rapid micromixers using CFD. *Transducers'99*, Sendai Japan: 200–203
- 4.12 Nagumo K, Ogami Y, Nagatomi K, Ukita H (2000) Investigation on mixing performance by a shuttlecock optical micro-rotor. *Proc Int Symp Transport Phenomena and Dynamics of Rotating Machinery ISROMAC-8*, Hawaii USA: 452–457
- 4.13 Ogami Y, Nishikawa K, Ukita H (2005) Study on the mixing performance of a microoptical rotor by CFD. *Trans Jpn Soc Mech Eng* 71:2434–2441 (in Japanese)
- 4.14 Katsuhara T, Ued Y, Miyazak D, Matsushita K, Yamada K, Yotsuya T (2001) Micro-rotators fabricated by photolithography. *Proc SPIE* 4440:277–284
- 4.15 Akagi D, Takada K, Ukita H (2005) Fabrication of three-wing mixers and their application to liquid mixing in a microchannel. *Trans Inst Electr Eng Jpn MSS-05–30:51–56* (in Japanese)
- 4.16 Higurashi E, Sawada R, Ito T (1998) Optically induced rotation of trapped microobjects about an axis perpendicular to the beam axis. *Appl Phys Lett* 72:2951–2953
- 4.17 Galajda P, Ormos P (2000) Complex micromachines produced and driven by light. *Appl Phys Lett* 78:249–251

- 4.18 Ukita H and Kanehira M (2002) A shuttlecock optical rotator – its design fabrication and evaluation for a micro-fluidic mixer. In. Solgaard et al. (eds) IEEE Select Top in Quantum Electron on Opt MEMS 8:111–117
- 4.19 Ukita H, Takada K, Itoh Y (2004) Experimental and theoretical analyses of three-dimensional microflows generated by an optical mixer. Proc SPIE 5514:704–711
- 4.20 Freymuth P (1993) Flow visualization in fluid mechanics. Rev Sci Instrum 64:1–18
- 4.21 Stroock AD, Dertinger SKW, Ajdari A, Mezic I, Stone HA, Whitesides GM (2002) Chaotic mixer for Microchannels. Science 295:647–651
- 4.22 Lee YK, Deval J, Tabeling P, Ho CM (2001) Chaotic mixing in electrokinetically and pressure driven micro flows. Technical Digest of the MEMS, Interlaken Switzerland: 483–486
- 4.23 Dodge A, Jullien MC, Lee YK, Niu X, Okkels F, Tabeling P (2004) An example of a chaotic micromixer: the cross-channel mixer. C. R. Physique 5, Elsevier, Amsterdam: 557–563
- 4.24 Kitamori T (2001) Thermal lens microscope for non-fluorescent single molecule determination and its role in integrated chemical systems on microchip. Proc Opt MEMS, Okinawa Japan: 153–154
- 4.25 Burns MA, Johnson BN, Brahmasandra SN, Hndique K, Webster JR, Krishnan M, Sammarco TS, Man PM, Jones D, Heldsinger D, Mastangelo CH, Burke DT (1998) An Integrated nanoliter DNA analysis device. Science 282:484–487
- 4.26 Balslev S, Bilenberg B, Geschke O, Jorgensen AM, Kristensen A, Kutter JP, Mogensen KB, Snakenborg D (2004) Fully integrated optical system for Lab-on-a-chip applications. Technical Digest of the MEMS: 89–92

Chapter 5

- 5.1 Raether H (1988) Surface plasmons on smooth and rough surfaces and on gratings. In: Föhler GH (ed) Springer Tracts in Modern Physics vol 111. Springer, Berlin Hidelberg New York London Paris Tokyo
- 5.2 Paesler MA, Moyer PJ (1996) Near-field optics. John Wiley and Sons Inc, New York
- 5.3 Ohtsu M (ed) (1998) Near-field nano/atom optics and technology. Springer, Berlin Hidelberg New York London Paris Tokyo
- 5.4 S. Kawata S (ed) (2001) Near-field optics and surface plasmon polaritons. Springer, Berlin Hidelberg New York London Paris Tokyo
- 5.5 Inoue Y, Kawata S (1994) Near-field scanning optical microscope with a metallic probe tip. Optics Lett 19:159–161
- 5.6 Novotny L, Bian RX, Xie XS (1997) Theory of nanometric optical tweezers. Phys Rev Lett 79:645–648

- 5.7 Okamoto T, Yamaguchi I (1999) Field enhancement by a metallic sphere on dielectric substrates. *Opt Rev* 6:211–214.
- 5.8 Sugiura T, Okada T, Inoue Y, Nakamura O, Kawata S (1997) Gold-bead scanning near-field optical microscope with laser-force position control. *Opt Lett* 22:1663–1665
- 5.9 Pohl DW, Denk W, Lanz M (1984) Optical stethoscopy: Image recording with resolution of $\lambda/20$. *Appl Phys Lett* 44:651–653
- 5.10 Fischer UC, Dürig UT, Pohl DW (1998) *Appl Phys Lett* 52:249.
- 5.11 Betzig E, Trautman JK (1992) Near-field optics: Microscopy spectroscopy and surface modification beyond the diffraction limit. *Science* 257:189–195
- 5.12 Hecht B, Bielefeldt H, Inoue Y, Pohl DW, Novotny L (1997) Facts and artifacts in near-field optical microscopy. *J Appl Phys* 81:2492–2498
- 5.13 Mamin HJ, Ried RP, Terris BD, Rugar D (1999) High-density data storage based on the atomic force microscope. *Proc IEEE* 87:1014–1027
- 5.14 Tabata O, Ikawa T, Hasegawa M, Tsuchimori M, Kawata Y (2001) Nanofabrication induced by near-field exposure from a nanosecond laser pulse. *Appl Phys Lett* 79:1366–1368
- 5.15 Uno T (1998) Finite difference time domain method for electromagnetic field and antenna analyses. Coronasha, Tokyo (in Japanese)/Taflove A, Hagness SC (2000) Computational electrodynamics the finite-difference time-domain method. Artech House, Boston
- 5.16 Yee KS (1966) Numerical solution of initial boundary value problems involving Maxwell's equations in isotropic media. *IEEE Trans Antennas and Propagation* 14:302–307
- 5.17 Mur G (1981) Absorbing boundary conditions for the finite-difference approximation of the time-domain electromagnetic field equations. *IEEE Trans Electromagnetic Compatibility* 23:377–382
- 5.18 Berenger JP (1994) A perfectly matched layer for the absorption of electromagnetic waves *J Comput Phys* 114:185–200
- 5.19 Mansuripur M, Zakharian AR, Moloney JV (2004) Transmission of light through small elliptical aperture (part 1). *Optics Photonics News* March:38–43/(part 2). *Opt Photon News April*:44–48.
- 5.20 Furukawa H, Kawata S (1998) Local field enhancement with an apertureless near-field-microscope probe. *Opt Commun* 148:221–224
- 5.21 Malmqvist L, Hertz HM (1992) Trapped particle optical microscopy. *Opt Commun* 94:19–24
- 5.22 Fukuzawa K, Tanaka Y, Akamine S, Kuwano H, Yamada H (1995) Imaging of optical and topographical distributions by simultaneous near field scanning optical/atomic force microscopy with a microfabricated photocantilever. *Appl Phys Lett* 78:7376–7381
- 5.23 Gu M, Ke PC (1999) Image enhancement in near-field scanning optical microscopy with laser-trapped metallic particles. *Opt Lett* 24:74–76

- 5.24 Ukita H, Uemi H, Hirata A (2004) Near Field Observation of a Refractive Index Grating and a Topographical Grating by an Optically Trapped Gold Particle. *Opt Rev* 11:365–369
- 5.25 Ukita H, Saitoh T (1999) Optical Micro-Manipulation of Beads in Axial and Lateral Directions with Upward and Downward-Directed Laser Beams. In: Harder E (ed) IEEE Lasers and Electro-Optics Society Annual Meeting LEOS'99 1: San Francisco USA, 169–170
- 5.26 Okuyama K (1985) Interaction between two particles. *Funtai Kogaku* 22:27–51 (in Japanese).
- 5.27 Felgner H, Muller O, Schliwa M (1995) Calibration of light forces in optical tweezers. *Appl Opt* 34:977–982
- 5.28 Hill KO, Malo B, Bilodeau F, Johnson DC, Albert J (1993) Bragg gratings fabricated in monomode photosensitive optical fiber by UV exposure through a phase mask. *Appl Phys Lett* 62:1035–1037
- 5.29 Krenn JR, Dereux A, Weeber JC, Bourillot E, Lacroute Y, Goudonnet JP (1999) Squeezing the optical near-field zone by plasmon coupling of metallic nanoparticles. *Phys Rev Lett* 82:2590–2593
- 5.30 Wang MD, Yin Y, Landick R, Gelles J, Block SM (1997) Stretching DNA with optical tweezers. *Biophys J* 72:1335–1346
- 5.31 Hesselink L (2000) Ultra-High-Density Data Storage. Communication of the ACM 43:33–36 / Technical Digest of International Symposium on Optical Memory and Optical Data Storage (ISOM/ODS 2005), Hawaii USA
- 5.32 Concerning the coaxial read/write holographic memory or holographic versatile disc (HVD) visit <http://www.optware.co.jp/english/tech.htm>
- 5.33 Tominaga J, Nakano T, Atoda N (1998) An approach for recording and readout beyond the diffraction limit with an Sb thin film. *Appl Phys Lett* 73:2078–2080
- 5.34 Betzig E, Trautman JK, Wolfe R, Gyorgy EM, Finn PL (1992) Near-field magneto-optics and high density data storage. *Appl Phys Lett* 61:142–144
- 5.35 Nakano M, Kawata Y (2003) Compact confocal readout system for three-dimensional memories using a laser feedback semiconductor laser. *Opt Lett* 28:1356–1359
- 5.36 Yasuda K, Ono M, Aratani K, Fukumoto A, Kaneko M (1993) Pre-mastered optical disk by superresolution. *Jpn J Appl Phys* 32:5210–5213/Kaneko M, Aratani K, Fukumoto A, Miyaoka S (1994) IRISTER-Magneto optical disk for magnetically induced superresolution. *Proc IEEE* 82:544–553
- 5.37 Maeda T, Treao M, Shimano T (2003) A review of optical disk systems with blue-violet laser pickups. *Jpn J Appl Phys* 42:1044–1051
- 5.38 Wu Y, Chong CT (1997) Theoretical analysis of a thermally induced super-resolution optical disk with different readout optics. *Appl Opt* 36:6668–6677

- 5.39 Sukeda H, Saga H, Nemoto H, Itou Y, Haginoya C, Matsumoto T (2001) Thermally assisted magnetic recording on flux-detectable RE-TM media. *IEEE Trans Mag* 37:1234–1238
- 5.40 Bhushan B, Fuchs H, Hosaka S (eds) (2004) *Applied Scanning Probe Methods*. Springer, Berlin Heidelberg New York: 390–428
- 5.41 Ukita H, Katagiri Y, Uenishi Y (1987) Readout Characteristics of Micro-optical Head Operated in Bi-stable Mode. *Jpn J Appl Phys Suppl* 26:111–116
- 5.42 Partovi A, Peale D, Wuttig M, Murray CA, Zydzik G, Hopkins L, Baldwin K, Hobson WS, Wynn J, Lopata J, Dhar L, Chichester R, Yeh JHJ (1999) High-power laser light source for near-field optics and its application to high-density optical data storage. *Appl Phys Lett* 75:1515–1517
- 5.43 Chen F, Zhai J, Stancil DD, Schlesinger TE (2001) Fabrication of very small aperture laser (VSAL) from a commercial edge emitting laser. *Jpn J Appl Phys* 40:1794–1795
- 5.44 Kataja K, Aikio J, Howe DG (2002) Numerical study of near-field writing on a phase-change optical disk. *Appl Opt* 41:4181–4187
- 5.45 Hirota K, Milster TD, Shimura K, Zhang Y, Jo JS (2000) Near-field phase change optical recording using a GaP hemispherical lens. *Jpn J Appl Phys* 39:968–972
- 5.46 Ueyanagi K, Tomono T (2000) Proposal of a near-field optical head using a new solid immersion mirror. *Jpn J Appl Phys* 39:888–891
- 5.47 Zijp F, Mark MB, Lee JI, Verschuren CA, Hendriks BHW, Balistreri MLM, Urbach HP, As MAH (2004) Near field read-out of a 50 GB first-surface disk with NA = 1.9 and a proposal for a cover-layer incident dual-layer near field system. *Optical Data Storage*:222–224
- 5.48 Challenner WA, McDaniel TW, Mihalcea CD, Mountfield KR, Pelhos K, Sendur LK (2003) Light delivery techniques for heat-assisted magnetic recording. *Jpn J Appl Phys* 41:981–988
- 5.49 Barnes WL, Dereux W, Ebbesen TW (2003) Surface plasmon subwavelength optics. *Nature*, 424:824–830
- 5.50 Liu WC, Tsai DP (2002) Optical tunneling effect of surface plasmon polaritons and localized surface plasmon resonance. *Phys Rev B* 65:15423-1–15423-5
- 5.51 Tsai DP, Yang CW (2000) Dynamic aperture of near-field super resolution structure. *Jpn J Appl Phys* 39B:982–983
- 5.52 Tagashira T, Ukita H (2001) A proposal for a read/write mechanism of a transparent-aperture type super-RENS optical disk. *ISOM 2001 TOYAMA Satellite Technical Digest*:74–75
- 5.53 Wei J, Gan F (2003) Thermal lens model of Sb thin film in super-resolution near-field structure. *Appl Phys Lett* 82:2607–2609
- 5.54 Kikukawa T, Tachibana A, Fujii H, Tominaga J (2003) Recording and readout mechanisms of super-resolution near-field structure disc with silver-oxide layer. *Jpn J Appl Phys* 42:1038–1039

- 5.55 Ho FH, Chang HH, Lin YH, Chen BM, Wang SY, Tsai DP (2003) Functional structure of AgO_x thin film for near-field recording. *Jpn J Appl Phys* 42:1–5
- 5.56 Kataja K, Olkkonen J, Akiko J, Howe D (2004) Numerical study of the AgO_x super resolution structure, *Jpn J Appl Phys* 43:160–167
- 5.57 Ukita H, Ueda Y, Sasaki M (2005) Read/write mechanism for a scattered type super-RENS using an AgO_x mask layer and the smallest mark reproduced. *Jpn J Appl Phys* 44:197–121
- 5.58 Kikukawa T, Nakano T, Shima T, Tominaga J (2002) Rigid bubble pit formation and huge signal enhancement in super-resolution near-field structure disk with platinum-oxide layer. *Appl Phys Lett* 81:4697–4699
- 5.59 Kim J, Hwang I, Yoon D, Park I, Shin D, Kikukawa T, Shima T, Tominaga J (2003) Super-resolution by elliptical bubble formation with PtO_x and AgInSbTe layers. *Appl Phys Lett* 83:1701–1703
- 5.60 Tominaga J, Shima T, Kuwahara M, Fukaya T, Kolobov A, Nakano T (2004) Ferroelectric catastrophe: beyond nanometer-scale optical resolution. *Nanotechnology* 15:411–415
- 5.61 Kuwahara M, Shima T, Kolobov A, Tominaga J (2004) Thermal origin of readout mechanism in light-scattering super-resolution near-field structure disk. *Jpn J Appl Phys* 43:L1–L10

Index

- μ -TAS, 163
3-D microstructures, 7, 152
3-D recording, 193
3-D trapping, 131
 O_2 RIE, 151
 $(SiO)_x(Si_3N_4)_{1-x}$, 63
 AgO_x , 204
Au/Si₃N₄/Au, 68
- a-SiN:H (hydrogenated amorphous silicon nitride), 66
absorbing boundary conditions (ABCs), 173
accelerometers, 3
actin filament, 114
actin–myosin interaction, 115
adhesion, 149
Auger electron spectroscopy, 66
Ag cluster, 208
Ag nanocluster, 204
Ag nanoparticle, 199
Ag particles, 207
Ag ring, 204, 211
Ag-Super-RENS, 204
AgInSbTe, 199
agitation, 153
agitation efficiency, 161
AgOx decomposition, 206
air bearing, 42
air gap, 50
Al-coated fiber probe, 196
aligning, 103
AlN slider, 64
- amount of reagent, 165
anisotropic etching, 3
antireflection, 68
antireflection coating design, 71
antireflection-coated (ARC), 63, 76
antireflection-coated LD, 45, 64
aperture probe, 180
aperture-type super-RENS, 203
apertureless probe, 180
apertureless scattering probe, 168
applications of optical tweezers, 113
artifact problem, 185
as-depo, 202
Ashkin, 83
aspect ratio, 5
ATPase, 114
attachment error, 42, 43
attenuated total reflection (ATR), 167
average flux amount, 159
axial trapping efficiency, 90, 92
- bacteria, 113
bacterial flagella, 113
baking, 149
beam expander, 104
beam waist, 36, 93, 123, 128
beam waist position, 131
beat frequency, 26
beyond the diffraction limit, 190
bimetallic MC, 69
bimorph, 68
bimorph design, 68
bio MEMS, 18

- blade of grass, 83
 blood flow sensor, 25
 Blue ray, 17
 bow-tie probe, 18
 bow-tie antenna, 197
 broken microobject, 121
 Brownian motion, 111, 212
 Brownian movement, 106
 brush tip recording, 193
 BTB, 164
 bubble pit, 211
 bubble pit formation, 205
 bulk micromachining, 3, 16
 buoyant force, 88
 carrier density, 40
 carrier to noise ratio (CNR), 198
 cavity length, 33
 CCD camera, 104
 CD, 193
 central differences, 170
 CFD, 143
 CFX, 136
 chamber, 104
 chaotic flow, 163
 chaotic-like mixing, 163
 circularly polarized light, 86
 cleaved fiber trap, 109
 CMP, 14
 color aberration, 188
 comb-drive actuator, 12
 commercial computational fluid dynamics, 136
 commercialization, 29
 compact disc (CD), 17
 compatible optical head, 17
 completely amorphous, 206
 complex cavity, 60
 compliance, 113
 composite cavity LD, 42
 composite cavity signal, 52
 conceptual frameworks, 1
 constant distance mode, 180
 constant height mode, 180
 contact start/stop (CSS), 66
 continuity equation, 137
 continuous wave YAG, 115
 contour lines, 138
 contour map, 72
 convection, 147
 convective mixing, 165
 convergence angle, 90
 corner prisms, 182
 correlation, 158
 counterpropagating coaxially aligned optical fibers, 98, 110
 coupling coefficient, 36, 61
 Courant condition, 173
 coverslip, 104
 creep, 181
 crescent-shaped region, 193
 cross-channel mixers, 163
 cross-sectional shape, 152
 curvature, 70, 95
 cutoff frequency, 180
 cylindrical body, 124
 cylindrical optical rotor with slopes, 127
 cylindrical PZT, 181
 cylindrical-body drag force, 144
 deep reactive ion etching (DRIE), 17
 deformation, 11
 depth of focus, 130
 design tradeoffs, 76
 dichroic mirror, 104
 diffraction limit for detection, 200
 diffraction limit resolution, 117
 diffraction-limited spot, 193
 diffractive effect, 112
 diffusion, 18
 diffusion coefficient, 146
 digital micromirror device (DMD), 14
 digital versatile disk (DVD), 17
 discrepancy, 105, 108
 discrete block format (DBF), 61
 dispersed Ag particles, 204
 dissymmetrical microobjects, 121
 distributed feedback laser diode (DFB LD), 26
 donut, 133
 downward-directed, 103
 drag force, 104, 138, 213
 DVD, 193
 dye, 194
 dynamic range, 182
 edge-emitting LD, 22, 50
 effective reflectivity, 35, 61

- effective reflectivity variation, 41
 electric field, 169
 electrodeposition, 6
 electromagnetic, 26
 electromagnetic force (EM) model, 85
 electromagnetic interaction, 178
 electron beam lithography (EBL), 5
 electrostatic, 26
 electrostatic force, 14, 213
 equilibrium position, 109
 ESEC configuration, 41
 etch-stop layer, 10
 etched mirror, 10–11
 evaluation criteria, 77
 evanescent field, 167
 evanescent light, 114
 excitation light, 54
 exposure time, 150
 external mode frequency, 38
 external-cavity LD, 35
 external-cavity-length, 35, 42
 extinction coefficient, 118
 extremely short-external-cavity
 (ESEC), 197
 extremely short-external-cavity laser
 diodes (ESEC LDs), 31, 39, 42,
 51, 58
 fabrication conditions, 149
 fabrication methods, 2
 feedback control, 29
 feedback light effects, 44
 ferroelectric catastrophe, 199
 Feynman, 11
 field enhancement, 178, 184
 fine positioning, 183
 finite difference time domain (FDTD),
 169, 205
 finite volume method, 137
 five-layer MC, 74
 five-wing rotor, 161
 flagella filament, 113
 flagella motor, 113
 flow-in, 140
 fluorescence, 114, 164
 flux amount, 139, 159
 flying head, 58
 flying height, 42
 flying optical head, 24
 focus error signal, 181
 focused laser beam, 123, 128
 free end, 70
 free spectral ranges, 39
 free-space micro-optical elements, 13
 free-space permittivity, 176
 frequency spectra, 55
 frequency-locked fringe pattern, 48
 Fresnel formula, 72, 125
 friction-less, 11
 friction-less mechanism, 49
 full width at half-maximum, 47
 full widths half-maximum (FWHM),
 24, 59
 future outlook, 26
 GaAlAs LD (LD#2), 59
 GaAs, 10
 GaAs substrate, 51
 gain spectrum, 39
 gain spectrum range, 40
 gallium arsenide (GaAs), 2
 gap, 180
 gas bubble, 199
 Gaussian, 133
 GeSbTe, 198, 204
 giant magnetoresistive (GMR), 196
 glass, 105
 glass slide, 104
 glycerol, 155, 188
 gold particle probe, 184
 gradient force, 88, 112, 123
 gravitational force, 104
 gravity force, 88
 gray-scale image, 184
 grid system, 145
 groove edge, 192
 group III–V compounds, 2, 49
 gyros, 3
 half amorphous, 206
 half-wavelength, 51
 half-wavelength interval, 40
 Halley's comet, 81
 Hamaker approximation, 213
 heat-assisted magnetic recording
 (HAMR), 197
 heavy particle, 105
 high reflectivity, 60

- high-speed camera, 153
 Hogg approximation, 213
 holographic optical tweezers, 119
 holography, 193
 hotplate, 149
 hybrid, 29
 hysteresis, 181
- immersion oil, 104
 incident angle, 92, 93
 indium phosphide (InP), 2
 InGaAsP LD (LD#1), 59
 Initialization, 205
 InP, 10, 51
 inspection time, 165
 internal forces, 69
 internal mode frequency, 38
 intersection point, 99
 isolated optical pulses, 211
 isotropic etching, 3
- junction-up, 59
 just after writing, 202
- kinesin stepping, 113
 kinetic energy of light, 20
- L_{ex} , 36
 Labs-on-a-chip, 163
 laminar flow, 11
 laser beam profiles, 92
 laser diode (LD), 32
 laser noise, 62
 laser scanning micromanipulation, 83
 lasing condition, 38
 lasing wavelengths, 40
 layer-by-layer, 8
 LD efficiency, 77
 LD-PD chip, 59
 leapfrog, 170
 LED, 22
 lensed fiber trap, 109
 lensless flying optical head, 197
 LIGA, 6
 light beam profiles, 133
 light output, 44
 light output difference, 60
 light output ratio, 78, 79
 light particle, 105
- light processing, 12
 linear actuator, 58
 liquid particles, 83
 living cells, 83, 112
 localized surface plasmons, 198
 low reflectivity, 60
 low-index microobjects, 112
- magnetic field, 169
 manipulating, 103
 mark, 211
 mask function, 195
 mask layer, 193, 194
 Maxwell's equation, 169
 maximum flux amount, 159
 maximum gain spectrum, 40
 maximum trapping efficiency, 107, 118
 MC deflections, 54
 measurement, 29
 medium density variation, 157
 medium reflectivity, 60
 MEMS motor, 124
 mesh numbers, 145
 metallic needle, 179
 metallic oxide, 118
 metallic particles, 156
 metalorganic vapor phase epitaxy (MOVPE), 10, 51
- micro-XYZ stage, 13
 micro/nanoobject, 81
 microassembly, 30
 microassembly system, 119
 microcantilever (MC), 10, 50
 microchannel, 18, 163
 microchemical conversion system, 115
 microconfocal optical scanning microscope (m-COSM), 19
 microfabrication, 119
 microflow, 162
 microflow visualization, 157
 microgear, 124
 micromechanical photonics, 1, 26
 micromechanical reflector, 31
 micromirrors, 16
 micromixer, 19
 micromotor, 3
 microphotoforming, 151
 microstrip antenna, 12
 micrototal analysis system, 18

- Mie regime, 85
- milk fat colloid, 154
- miniaturization, 11
- minimum axial trapping power, 104
- mitochondria, 113
- mitochondrion, 83
- mixing, 18
- mixing efficiency, 144
- mixing rate, 146
- mode interval, 33, 46, 47
- modulation transfer function (MTF), 195
- molding, 6
- molecular devices, 29
- moment of inertia, 70
- moments, 69
- momentum change per second, 85
- momentum of light, 85
- monolithic, 29
- monolithic integration, 10, 21
- multi mode, 46
- Mur ABCs, 173
- myosin, 114
- NA, 93
- NA control, 18
- nanoparticle assembly, 120
- NaOH, 164
- Navier–Stokes equation, 137
- ND filter, 104
- near field, 167
- near field recording, 193
- near-future optical disk, 193
- negative pressure, 142
- next-generation DVD, 193
- non-mark, 211
- nonpropagating conditions, 167
- number of functions, 29
- numerical aperture, 93
- oblique angle, 123
- oblique illumination, 154
- oblique incident, 101
- off-axial distance, 100
- off-axial trapping, 98, 101
- off-resonant frequencies, 68
- on-chip actuator, 18
- on-chip Mach-Zehnder interferometer, 13
- optical, 26
- optical box, 186
- optical cavities, 117
- optical constant, 118
- optical disk tester, 199
- optical encoder, 23
- optical fiber trapping, 97
- optical fiber with a sharpened end, 167
- optical heads, 17
- optical MEMS, 1, 26
- optical method, 157
- optical mixer, 124, 163
- optical motors, 124
- optical pressure, 20, 26, 81, 85, 125
- optical pressure force, 120
- optical pulse duty, 211
- optical rotors, 21, 121
- optical spring constant, 112
- optical switches, 16
- optical torque, 125
- optical tweezers, 81
- optical-fiber tweezers, 97
- optically switched laser head, 58, 76, 197
- optically trapped gold particle, 176
- OSL, 58, 197
- out-of-plane micro-Fresnel lens, 13
- output variation, 64
- oxygen reactive ion-beam etching, 151
- p-polarization, 86
- packing, 30
- parabolic ray model, 106
- paraffin wax, 83
- parallel beam, 127
- particle manipulation, 83
- particle pattern formation, 83
- particle transport, 118
- pattern tracking algorithm, 158
- patterning, 5
- perfect conductor, 173
- perfect conductor sphere, 176
- perfectly matched layer (PML), 173
- permissible read power, 78
- permittivity, 176
- phase change, 194
- phase change medium, 59
- phase difference, 53
- phase mask, 188

- photo-electric, 26
 photo-electrochemical, 26
 photocantilever, 180
 photochemical reaction, 117
 photoelectric effect, 20
 photoelectrochemical effect, 20
 photoforming, 7, 151
 photoforming conditions, 152
 photolithography, 3, 149
 photon tunneling, 117
 photopolymerization, 8
 photothermal, 26
 photothermal deflection, 68
 photothermal effect, 20
 photothermal excitation, 52
 photothermally driven MC, 67
 photovoltaic microdevice, 20
 phthalocyanine, 57
 piezoelectric, 26
 piezoelectric transducer (PZT), 181
 pinhole, 186
 planar light waveguide circuit (PLC),
 188
 planar lightwave circuits (PLCs), 16
 PMT, 186
 point-spread function, 195
 polarizability, 186
 polyimide, 150
 polysilicon, 3, 16
 polystyrene, 105
 power margin, 78
 pressure, 137, 142
 pressure perturbations, 163
 pressure sensors, 3
 probe vertical displacement, 193
 probing technologies, 2

 Q-switched YAG, 117
 quarter-wave plate, 104

 ray optics (RO) model, 85
 ray tracing, 128
 Rayleigh regime, 85
 reactive dry-etching (RIBE), 51
 reactive ion beam etching (RIBE), 2, 4,
 24, 59
 read power dependence, 210
 recognition, 29
 reflectivity coating (HRC), 76

 reflectivity difference, 77
 refractive index, 118, 190
 refractive index grating, 188
 relative refractive index, 186
 reliability, 158
 remote power supply, 29
 replication, 10
 reproducibility, 180
 research-oriented, 29
 residual stress, 11, 16
 resin, 8
 resolution, 8
 resonant field, 117
 resonant frequency, 55, 68, 79
 resonant MC, 52
 resonant mode, 117
 resonant sensor, 22, 52
 reverse torque, 136
 Reynolds number, 11, 138
 ringlike microobject, 112
 rotary actuator, 58
 rotating, 103
 rotation rate, 122, 132
 rotational direction, 121
 rough positioning, 183
 round trip, 38
 round-trip number dependence, 174

 s-polarization, 86
 S-shape curve, 182
 Sacrificed layer, 149
 sacrificial layer, 14
 sample chamber, 154, 186
 sample surface, 190
 sampled servo, 61
 Sb mask layer, 199
 Sb-super-RENS, 199
 scaling laws, 11
 scanning electron microscopy (SEM),
 190
 scanning near-field microscopy, 168
 scanning near-field optical microscopy
 (SNOM), 117
 scanning velocity, 188
 scattered-type super-RENS, 212
 scattering force, 88, 123
 search size, 158
 selective etching, 11
 sharpened optical fiber, 179

- shearing stress, 138, 142
- shuttlecock optical rotor, 124
- shuttlecock optical rotor with slopes, 135
- side-mode suppression ratio, 47
- signal amplitude, 211
- SIL, 197
- silicon (Si), 2
- silicon dioxide (SiO_2), 4, 122
- silicon-nitride (SiN), 66
- silicon-on-insulator, 2
- silver oxide (AgO_x) mask layer, 204
- simple assembly, 29
- single mode, 46
- single peak, 192
- single-beam gradient-force optical trap, 83
- single-beam gradient-force optical trapping, 112
- SIT camera, 115
- skin depth, 180
- slider, 42
- sliding mesh, 137
- slope angle, 127
- sloped top, 123
- slopes, 124
- small aperture, 173, 179
- small metallic sphere, 179
- SNOM image (scattered light intensity), 190
- SNR, 62
- SOI, 17
- sol-gels, 10
- solar radiation pressure, 81
- solid immersion lens/solid immersion mirror (SIM), 197
- solid particles, 83
- solidification, 7
- solitary fiber, 110
- solitary LD, 32
- space derivatives, 170
- space increment, 170
- spacing, 59, 62
- spectral structure, 46
- spectroscopic data, 180
- spectroscopy, 117
- spectrum line width, 47
- spectrum peak shift, 41
- spherical aberration, 188
- spherical aberration correction, 18
- spinner, 151
- split peaks, 191
- SPM storage, 196
- spring constant, 79
- stacking, 7
- sticking-free, 11
- stirred flow, 165
- straight ray model, 106
- streamlines, 138, 141
- stripping, 3
- strongly focused laser beam, 112
- SU-8, 4, 148
- SU-8 rotors, 162
- super-RENS, 198
- super-RENS readout, 208
- superresolution, 193
- superresolution near-field structure (super-RENS), 193
- surface active agent, 155
- surface micromachining, 3, 14
- surface plasmon, 184
- surface property, 180
- surface-emitting LD, 22
- syringe pumps, 164
- tangential vector, 96
- taper-ridged waveguide, 24, 59
- tapered lensed optical fiber, 94–95, 100
- tapered optical fiber, 175
- thermal energy, 106
- thermal expansion, 54
- thermal expansion coefficients, 69
- thin resin film, 151
- three-layer MC, 69
- three-wing rotor, 149, 161
- threshold current, 44
- threshold gain, 33
- Ti:sapphire laser, 8
- tight convergence, 90
- time derivatives, 170
- time increment, 170
- time-step dependence, 174
- time-stepping expressions, 171
- tip deflection, 70
- tip probe, 179
- TM (p-polarized) plane wave, 173
- topography, 190
- torque efficiency, 131

- torque force, 123
- torsion pendulum, 82
- total trapping efficiency, 120
- tracers, 155
- track error signals, 61
- tracking groove, 190
- trajectory, 120
- transmission efficiency, 198
- transmittance efficiency, 104
- transverse components of the momentum, 86
- transverse trapping efficiency, 90, 120
- transverse trapping power, 106, 187
- trapping, 81
- trapping efficiency, 87, 90
- trapping force, 128
- tribology, 30
- tunable infrared (IR) filter, 7
- tunable LD, 21, 76
- two-dimensional (2-D) trapping, 128
- two-liquid mixing, 166
- two-photon absorption, 8
- U-shaped LD, 23
- ultrahigh density optical storage, 193
- unfocused (parallel) laser beam, 123
- uniformly filled, 133
- upward-directed, 185
- urethane, 8
- using up-ward-directed, 104
- UV light, 149
- V-grooves, 3
- vaccum, 81
- van der Waals force, 213
- vane, 81
- variable parameter, 95
- vector theory, 169
- velocity, 137
- vertical cavity surface-emitting laser (VCSEL), 50
- vertical components of the momentum, 87
- very small aperture laser (VSAL), 197
- vibration amplitude, 54
- viscosity, 188, 213
- visualization, 153
- wall force, 106
- wavelength division multiplexing (WDM), 16
- wavelength tuning, 45
- wavelength tuning range, 46
- wet-etching, 11
- windmill effect, 121
- wing number, 148
- wiring, 30
- with the gold particle, 191
- without the gold particle, 192
- working mechanism, 203, 211
- write power dependence, 208
- X-ray lithography, 6
- Y-shaped microchannel, 145
- Yee algorithm, 170
- yield strength, 57
- yoke, 14
- Young's moduli, 69